

**Keeping in Touch:
Visualising and Perturbing
Photorespiratory Organelle
Proximity in Plants**

**Anna-Lena Falz
2023**

KEEPING IN TOUCH: VISUALISING AND PERTURBING PHOTORESPIRATORY
ORGANELLE PROXIMITY IN PLANTS

Dissertation
zur
Erlangung des Doktorgrades (Dr. rer. nat.)
der
Mathematisch-Naturwissenschaftlichen Fakultät
der
Rheinischen Friedrich-Wilhelms-Universität Bonn

vorgelegt von
ANNA-LENA FALZ
aus
Moers, Deutschland

Bonn, 2023

Angefertigt mit Genehmigung der Mathematisch-Naturwissenschaftlichen Fakultät
der Rheinischen Friedrich-Wilhelms-Universität Bonn

Gutachter: Prof. Dr. Andreas Meyer

Gutachterin: Prof. Dr. Ute C. Vothknecht

Tag der Promotion: 03.08.2023

Erscheinungsjahr: 2023

This thesis has been carried out under additional supervision of:

Prof. Dr. Stefanie Müller-Schüssele
Molecular Botany
Technische Universität Kaiserslautern

Contents

Abbreviations	VII
--------------------------------	------------

Summary	XIII
--------------------------	-------------

Chapter I

Introduction	1
1 Membrane contact sites as a platform for organellar communication	1
2 Defining the structural and functional characteristics of MCS	2
3 Experimental evidences for organellar contact sites in plants	4
3.1 Together but still separate: The spatial organisation of organelles	4
3.2 Identified plant MCS components - the ER as most characterised player	5
3.3 The impact of MCS on plant development and growth	7
3.4 Lipid trafficking at MCS	8
3.5 The unique nature of plants: Organellar cooperation as need for effective photosynthesis under ambient light conditions	9
3.6 The potential role of MCS in photorespiration	10
4 Techniques for investigating MCS in plants	12
4.1 Identification of novel MCS components	12
4.2 Measuring organelle tethering forces	14
4.3 Microscopy techniques to monitor MCS	15
4.4 Detecting and monitoring MCS by usage of fluorescent sensors	16
4.4.1 Usage of split fluorescent protein systems to investigate MCS	16
4.4.2 FRET/FLIM reporters as dynamic approach for visualising MCS	21
4.5 Perturbing organellar interaction	23
5 Objectives of this work	24

Chapter II

Methods	25
1 Technical equipment and consumables	25
2 Plant methods	28
2.1 Plant material	28
2.2 Transient transformation of tobacco plants	29
2.3 Plant growth on agar plates	29
2.4 Plant growth on soil	29

CONTENTS

2.5	Stable transformation of Arabidopsis	30
2.6	Selection of transformed Arabidopsis plants	30
2.6.1	T ₁ seeds: Selection on soil	30
2.6.2	T ₂ seeds: Segregation pattern	31
2.6.3	T ₃ seeds: Verification of homozygous plants	31
2.7	Seed germination efficiency	34
2.8	Seedling phenotyping on agar plates - root growth	34
2.9	Heat stress on agar plates	34
2.10	Phenotyping on soil under normal light	35
2.11	Phenotyping on soil under high light	35
2.12	Dark-induced leaf senescence	35
2.13	Anthocyanin extraction	35
2.14	Pulse Amplitude Modulation (PAM) fluorometry	36
2.15	Oxygen consumption of leaf tissue	36
2.16	Pollen staining	37
2.17	Silique imaging	37
2.18	Vacuum infiltration and MitoTracker staining	37
3	Microbiological methods	37
3.1	Bacterial strains	37
3.2	Bacterial growth	38
3.3	Transformation of electro-competent <i>A. tumefaciens</i>	38
3.4	Transformation of chemical competent <i>E. coli</i>	39
3.5	Plasmid isolation from <i>E. coli</i>	39
4	Molecular biological techniques	40
4.1	DNA extraction from Arabidopsis plants	40
4.2	RNA extraction from Arabidopsis	40
4.3	Complementary DNA synthesis	40
4.4	Oligonucleotides	40
4.5	Polymerase chain reaction	48
4.6	DNA agarose gel electrophoresis and DNA purification	49
4.7	Quantification of RNA and DNA concentration	49
4.8	DNA sequencing	49
4.9	Digestion of DNA with restriction endonucleases	49
4.10	Cloning of the inducible pInd 2in1 vector system using Greengate cloning	50
4.11	Generation of rBiFC, saGFP and FRET/FLIM expression constructs by Gateway cloning	52
5	Dexamethasone induction of pInd vector system	58
6	Calculation of FP-based reporter sizes	59
7	Fluorescence microscopy methods	60

CONTENTS

	7.1 Monitoring of chloroplast-peroxisomes proximity and movement . . .	60
	7.2 Localisation and topology control using BiFC sensors	63
	7.3 Monitoring organellar proximity with BiFC sensors	63
	7.4 Monitoring organellar proximity with FRET/FLIM sensors	64
Chapter III		
	Results	67
1	Influence of light on the proximity between chloroplasts and peroxisomes . .	67
1.1	Establishment of an automatically performed Python-based segmentation process	67
1.2	Verifying the Python-based surface-to-surface proximity quantification	72
1.3	Proximity analysis between chloroplasts and peroxisomes in three model plant species under different photosynthetic conditions	76
2	Assessment of targeting and topology of fusion proteins for proximity reporters	79
2.1	Known ER-PM contact site proteins as fusion protein	81
2.2	MCS-unspecific OE, MOM and PerM protein or protein domains as fusion protein	83
3	Characterisation of splitFP sensor systems for the visualisation of MCS in plants	87
3.1	Assessment of BiFC sensor system fused to non-interacting and homogeneously distributed proteins of OE, MOM and PerM	87
3.1.1	Specificity of fluorescence pattern of splitYFP transiently expressed in <i>N. tabacum</i>	88
3.1.2	Distance: Influence of linker length to bridge different distances between organellar membranes on BiFC signal distribution . .	92
3.1.3	Comparison of splitFP sensor systems	94
3.2	Testing the BiFC system using known interacting and non-interacting MCS proteins at EPCS	96
4	Generation and verification of a 2in1 inducible vector system (pInd) for fluorescent protein (FP) sensor systems	99
4.1	Cloning of pInd vectors for split fluorescent proteins (splitFP) and Förster resonance energy transfer (FRET)/ FLIM systems	99
4.2	Verification of the dexamethasone induction of 2in1 pInd vector	103
5	FRET/FLIM as a putative tool to visualise the dynamics of MCS	109
5.1	Determination of FLIM measurement range	109
5.2	Suitability verification of FRET/FLIM sensor system to monitor dynamic MCS	111
6	Perturbing organelle interactions	117
6.1	Effects of synthetic tethering on cellular organisation in plant cells . .	117

CONTENTS

6.1.1	Peroxisomal cluster formation in <i>N. benthamina</i> and <i>N. tabacum</i> cells overexpressing the synthetic tether construct	117
6.1.2	Cluster formation of peroxisomes and elongated mitochondria in synthetic tether lines	118
6.2	Synthetic tethers – influence on the plant performance tested in transgenic <i>A. thaliana</i> T ₃ plants	125
6.2.1	No distinct trend in terms of germination and root growth of seedlings	125
6.2.2	Rolled leaf and early senescence phenotype in synthetic tether lines	127
6.2.3	Inconsistently altered reproductive development in synthetic tether lines	130
6.3	Photosynthetic performance and respiration of synthetic tether plants	134
6.4	Synthetic tethers – influence on the plant performance under stress conditions	136
6.4.1	Increased resilience to heat in seedling in roots	136
6.4.2	Higher susceptibility to high light stress in adult plants than in young plants	137

Chapter IV

Discussion	143
1 Inconclusive trend of the chloroplast-peroxisome proximity	143
1.1 The Python-based proximity analysis pipeline enabled a high-throughput analysis	143
1.2 Minor but probably critical changes in the experimental setup lead to results different to already published data	145
2 Fluorescent probes for the visualisation of MCS: challenges and possibilities .	147
2.1 Suitability of splitFP as proximity reporter system needs further investigation	148
2.2 Unaltered lifetime of FRET/FLIM-based proximity sensors at putative MCS	152
2.3 Limitations of FP-based proximity sensors used for MCS visualisation	153
3 Perturbing the proximity of photorespiratory organelles lead to sever phenotypic and physiological alterations	157
3.1 Tether overexpression potentially interfere with organellar proliferation, fusion and autophagy	159
3.2 The biological relevance of MCS regarding photorespiration needs further investigation	160
3.3 Impact of synthetic tethering on germination	162

CONTENTS

3.4	Assessment of possible correlations between the synthetic tether phenotype and altered oxidative phosphorylation	163
3.5	Synthetic tethering potentially causes alterations in signalling cascades	164
3.6	Potential interdependency of anthocyanin biosynthesis and synthetic tethering	165
Chapter V		
	Conclusion and outlook	167
	Bibliography	169
	Appendix	XV
	Supplemental information	XVII
	List of Figures	XXXIII
	List of Tables	XXXIX
	Acknowledgements	XLI
	General statement	XLIII

CONTENTS

Abbreviations

Abbreviation	Meaning
1C	1 component
2C	2 component
2D / 3D	2 / 3 dimensional
2OG	2-oxoglutarate (α -ketoglutaric acid)
2PG	2-phosphoglycolate
35sT	cauliflower mosaic virus 35S terminator
3PGA	3-phosphoglycerate
aa	amino acid
<i>A. tumefaciens</i>	<i>Agrobacterium tumefaciens</i>
ANOVA	analysis of variance
AOX	alternative oxidase
<i>A. thaliana</i>	<i>Arabidopsis thaliana</i>
ATP	adenosine triphosphate
Basta	glufosinate ammonium
BiFC	Bimolecular Fluorescence Complementation
bZIP	basic region-leucine zippers
c_c/c_t	proximity ratio between chloroplasts with peroxisomal contact to the total number of the respective organelle
C ₂ A/C ₂ B	calcium-binding domains
CaMV35S	cauliflower mosaic virus 35S promoter
CaMV35Sm	minimal CaMV 35S promoter
CB cycle	calvin benson cycle
<i>ccdB</i>	gyrase inhibitor gene
cDNA	complementary DNA
CFP	cyan fluorescent protein
CHUP1	Chloroplast Unusual Positioning 1
CLSM	confocal laser scanning microscopy
CmR	chloramphenicol acetyltransferase resistance gene
CO ₂	carbon dioxide
Col-0	<i>Arabidopsis thaliana</i> ecotype Columbia 0 (wild type)
cytD	cytochalasin D

Abbreviation	Meaning
DCMU	3-(3,4-dichlorophenyl)-1,1-dimethylurea
ddFP	dimerisation dependent fluorescent protein
ddH ₂ O	double distilled water
dex	dexamethasone
DF	degree of freedom, distance filter
DGDG	digalactosyldiacylglycerol
DMSO	dimethyl sulfoxide
dNTP	deoxynucleotide solution mix
dSTORM	direct Stochastic Optical Reconstruction Microscopy
EGB	early biosynthesis genes
EM	electron microscopy
EMCS	ER-mitochondria contact sites
EPCS	ER-PM contact site
ER	endoplasmic reticulum
ESyt	extended synaptotagmins
ETC	electron transport chain
EtOH	Ethanol
FA	fatty acid
FAB	flavonoid/anthocyanin biosynthesis
Fd	ferredoxin
FL	full length
FLIM	fluorescence lifetime imaging
FP	fluorescent protein
FRAP	fluorescence recovery after photobleaching
FRET	Förster Resonance Energy Transfer
F_V/F_M	maximum quantum yield of photochemistry of PSII
fw	forward
FW	fresh weight
g	multiples of the earth's gravitational acceleration
GFP	green fluorescent protein
GFP ₁₋₁₀ /GFP ₁₁	fragments of saGFP
glu	glutamate
GR	rat glucocorticoid receptor
H ₂ O ₂	hydrogen peroxide
HA-tag	hemagglutinin epitope tag
HL	high light
Hpyr	hydroxypyruvate

Abbreviations

Abbreviation	Meaning
HyPer2	fluorescent H ₂ O ₂ sensor
IE	inner envelope
IF	image filter
IPTG	Isopropyl-D-1-thiogalactopyranoside
LacZ	Z gene of lac operon, codes for β -galactosidase
latB	latrunculin B
LB-medium	lysogeny broth-medium
LD	lipid droplet
LEF	linear electron transport
LGB	late biosynthesis genes
LhG4	transcription activator consisting of a high-affinity DNA binding mutant of the lac repressor and the transcription activation domain-II of GAL4 of <i>Saccharomyces cerevisiae</i>
LIPA	LD-PM ADAPTOR
MCS	membrane contact sites
MDH	malate dehydrogenases
MDS	mitochondrial dysfunction stimulon
MERC reporter	mitochondria-ER contact site reporter
MES	2-(N-morpholino) ethanesulfonic acid
MIM	mitochondrial inner membrane
MIP	maximum intensity projection
MOM	mitochondrial outer membrane
MS/MS	tandem mass spectrometry
MS-medium	Murashige-Skoog-medium
MSP	major sperm protein
MVB	multivesicular body
myc-tag	myc epitope tag
<i>N. benthamiana</i>	<i>Nicotiana benthamiana</i>
<i>N. tabacum</i>	<i>Nicotiana tabacum</i>
NAD ⁺	nicotinamide adenine dinucleotide (oxidised)
NADH	nicotinamide adenine dinucleotide (reduced)
NADP ⁺	nicotinamide adenine dinucleotide phosphate (oxidised)
NADPH	nicotinamide adenine dinucleotide phosphate (reduced)
NET3C	NETWORKED 3C
N _{FRET} /N ₀	ratio of the number of interacting and non-interacting molecules
NL	normal light
NPQ	non-photochemical quenching

Abbreviation	Meaning
ns	not significant
nYFP, cYFP	N-/C-terminal fragment of splitYFP
O ₂	oxygen
OD600	optical density at 600 nm
OE	outer envelope
OEP7	<i>A. thaliana</i> outer envelope protein 7
OXPPOS	oxidative phosphorylation
p_c/p_t	proximity ratio between peroxisomes with chloroplastidic contact to the total number of the respective organelle
PAM	Pulse Amplitude Modulation fluorometry
PCR	polymerase chain reaction
PD	plasmodesmata
PED1	peroxisomal defective 1
PerM	peroxisomal membrane
PEX10	peroxin 10
PLAM	plastid-associated membranes
PM	plasma membrane
pOp6	chimeric promoter pOp consisting of two ideal lac operators, repeated 6 times
PpPEX3N	N-terminal domain of <i>P. patens</i> Peroxin 3
PpPEX3N(GGSGG) ₁₃	PpPEX3N plus an additional linker
PpTOM20C	C-terminal domain of <i>P. patens</i> translocase of the outer membrane
Ψ	sphericity
PSI	photosystem I
PSII	photosystem II
px-ck	peroxisomal CFP marker line (ecotype Col-0)
rBiFC	ratiometric BiFC
rev	reverse
RFP	red fluorescent protein
RFU	relative fluorescence unit
RGB	red-green-blue colours
ROI	region of interest
ROS	reactive oxygen species
RT	room temperature
RuBisCO	ribulose 1,5-bisphosphate (RuBP) carboxylase/oxygenase
RuBP	ribulose 1,5-bisphosphate
saGFP	self-assembling GFP

Abbreviations

Abbreviation	Meaning
SDP1	SUGAR DEPENDENT 1
SIM	structured illumination microscopy
SLDP	LD-localised SEED LD PROTEIN
SMP	synaptotagmin-like, mitochondria protein domain
SPLICS	split-GFP-based contact site sensor
splitFAST	fluorescence-activating and absorption-shifting tag
STED microscopy	super-resolution stimulated emission depletion microscopy
SYT	synaptotagmins
SYT1	Synaptotagmin 1
$t_{1/2}$	half-life
T ₁ , T ₂ , T ₃	first, second, third generation of transgenic lines
τ_1	fast lifetime component (2C)
τ_2	slow lifetime component (2C)
τ_m	mean lifetime
TCA	Trichloroacetic acid, tricarboxylic acid cycle
TCSPC	time-correlated single photon counting
T-DNA	transfer DNA
TEM	transmission electron microscopy
TF	transcription factor
TGD	trigalactosyldiacylglycerol
TGN	ER-trans-Golgi
TM	transmembrane domain
TOM	Translocase of the outer membrane
v/v	volume per volume
Vac	vacuole
VAMP	vesicle-associated membrane protein
VAP	VAMP-associated proteins
w/v	weight per volume
WT	wild-type
χ^2 -value	Chi-square value
xGal	5-bromo-4-chloro-3-indolyl- β -D-galactopyranoside
Y(II)	quantum yield of PSII
YFP	yellow fluorescent protein

Summary

Organelles within cells are typically depicted as isolated structures, but increasing evidence shows that they are interconnected via specific membrane contact sites (MCS). While MCS research in mammals and yeast is gaining importance, MCS are less explored in plants. Photorespiration is a metabolic process that occurs across three organelles in plants: chloroplasts, peroxisomes and mitochondria. Whereas this process is well studied on the molecular level, only little is known about the relevance of inter-organelle contacts. The aim of this study was to elucidate the significance of organelle interactions and to determine how MCS are linked to plant growth and performance with the photorespiratory organelles as a model. We addressed this question with three main experimental approaches: 1) quantifying the proximity between chloroplasts and peroxisomes under different photosynthetic conditions, 2) testing potential dynamic or irreversible reporter systems for organelle proximity, and 3) manipulating the spatial organisation of cells by introducing a synthetic tether construct.

Previous reports evidenced physical associations and an increased interaction rate between the photorespiratory organelles in response to light in *A. thaliana*. We developed an automated high-throughput Python-based analysis pipeline for the quantification of organelle proximity. We used confocal z-stacks of cells with fluorescently labelled organelles and performed analyses in three model plant species. We were not able to replicate the findings of previous reports using manual image analysis or the Python-based analysis pipeline, potentially due to minor but critical changes in the experimental setup.

Secondly, we tested potential fluorescence-based proximity reporters, based on Bimolecular Fluorescence Complementation (BiFC) or Förster Resonance Energy Transfer/Fluorescence Lifetime Imaging (FRET/FLIM). We successfully targeted the potential proximity reporters to the cytosolic face of the photorespiratory organelles. Using splitYFP-based proximity sensors, we found unspecific homogeneous organelle membrane labelling, whereas the investigation of organelle positioning revealed tethering between peroxisomes and chloroplasts. Moreover, we created an inducible 2in1 gateway vector system (pInd) to test the suitability of self-assembling GFP (saGFP) and to enable inducible expression in transgenic lines. Testing the expression of a saGFP-based proximity sensor between chloroplasts and peroxisomes transiently in *N. tabacum*, we found a peroxisomal membrane labelling with increased GFP signal at putative MCS. Using FRET/FLIM-based proximity sensors, controls mimicking 100% and no organelle interaction were established, while dynamic imaging did not reveal a decrease in fluorescence lifetime at putative MCS between chloroplasts and peroxisomes.

The third approach involved introducing a synthetic tether to disturb the spatial organisation of the photorespiratory organelles. We were able to obtain transgenic *A. thaliana* lines showing curly leaves, impaired growth, an accelerated senescence, and a reduced high light tolerance including decreased anthocyanin accumulation. On cellular level, the overexpression of the synthetic tether resulted in the formation of spherical peroxisomal clusters, where mitochondrial structures also accumulated.

I Introduction

1 Membrane contact sites as a platform for organellar communication

In eukaryotes, cell compartmentalisation allows cells to separate biochemical functions and environments. However, this spatial subdivision also creates the need for a specific exchange of metabolites, proteins and information among the compartments. One very prominent example in plants is the photorespiration recycling a toxic metabolite across chloroplasts, peroxisomes and mitochondria [1].

Organelles in cell biology textbooks are commonly portrayed as isolated compartments whose close proximity to one another is largely due to spatial limitations. This assumption is invalidated by the growing evidence that a network of specific organellar membrane contact sites (MCS) exists [2]. These MCS serve as platform for an effective organellar communication [3, 4], which in turn facilitates a rapid response to fluctuating environmental conditions (references in Scorrano *et al.*, Baillie *et al.* [5, 6]). In addition, MCS are reported to be of relevance for the regulation of the positioning and number of various organelles within cells [7–9].

Alternatives for a direct molecular exchange between organelles are transient fusion-fission dynamics (e.g. "kiss-and-run" in mitochondria [10]) or vesicles transport [5]. However, both alternative processes involve the fusion of organellar membranes. This distinguishes them from MCS, where by definition membranes retain their identity without fusion [5, 6].

First indications of the possible existence of MCS were found in animal cells in the 1950s [11, 12]. In plants, transmission electron microscopy (TEM) indicated as well a close proximity between organelles [13]. However, these evidences were not pursued any further, since MCS existence was difficult to imagine based on the state of knowledge at this time [5]. The research field of MCS started to gain interest, when first functional evidences for MCS were found [5], including Ca^{2+} transfer [14], as well as phospholipid biosynthesis and transfer between mitochondria and the endoplasmic reticulum (ER) [15]. Since then, multiple MCS with highly specialised functions have been identified in yeast and mammals, while MCS research in plants has been less advanced so far.

2 Defining the structural and functional characteristics of MCS

In order to be able to identify MCS, measurable criteria need to be determined (adapted from Baillie *et al.* 2020 [6]). MCS can be defined regarding their spatial and structural characteristics [5, 6, 16], while those criteria alone cannot provide any proof for the formation of a functional MCS. A further difficulty is that different types of MCS can occur between the same organellar pair, which are in turn unique in their function, spatial arrangement, dynamics and lipid/protein composition [6, 16]. Both the spatial characteristics and the functionality are interdependent and therefore need to be equally considered and explored in order to gain a better understanding of MCS [6].

MCS are widely described as regions of physical but transient interactions between organelles within a distance of 10 nm - 30 nm without membrane fusion [5, 6]. However, also larger tethering distances up to 325 nm have been found between the plasma membrane (PM) and mitochondria in yeast [17]. Since the organellar proximity is strongly dependent on size and arrangement of tether proteins, a defined distance cannot function as the only criterion for the identification of MCS [6]. It may also be based on random collisions of organelles [18], especially in plant cells, where the large vacuole compresses the cytoplasm plus organelles to a relatively small percentage of the cell [6].

Another spatial characteristic worth taking a closer look at, is the contact surface area of MCS. The total area of a specific MCS can be influenced by variations in size or/and the MCS abundance profile [6]. The contact surface area was found to change in response to abiotic or biotic stresses [19–21], or also during different developmental stages [22]. Furthermore, MCS are not permanent but transient structures, which is why duration and frequency of their formation is important to consider. However, quantifying the dynamics of MCS is a technical challenge, which is likely the reason why it has been less studied so far [6].

Since proximity is no proof for a functional MCS, additional parameters need to take into account. At MCS, organelles are connected by tether proteins. Thus, real physical interaction can be confirmed by measuring the tethering force between organelles [6]. The biophysical evidence for a MCS can be gathered using optical tweezers [23–25] or femtosecond laser's generated shock waves [26], which enable the measurement of the separation force (for detail see introduction section 4.2. figure 4 B). A direct molecular exchange between the respective organelles supports the functionality of MCS [26–28], albeit this exchange is not automatically a proof for a MCS. However, it can serve as an additional reference to the aforementioned characteristics [6].

MCS differ in their lipid and protein composition compared to the surrounding membrane regions [5, 6, 16, 30]. These highly specialised micro-environments are essential to fulfil the functions of the respective MCS. Even between the same pair of organelles, multiple and functionally distinct types of MCS can occur consisting of unique lipid and protein compositions [6, 16]. Proteins being enriched at MCS fulfil different functions (reviewed in

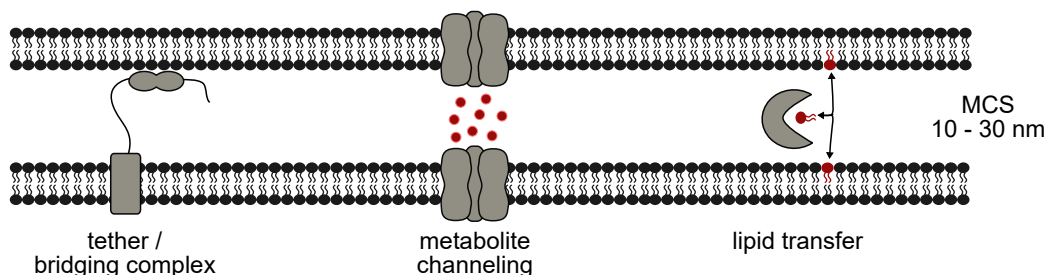


Figure 1: Schematic representation of putative MCS proteins and their functions.

The distance between organelles range typically within 10 nm to 30 nm at MCS, although larger tethering distances have been also reported [5, 6, 17]. Tether proteins, as SYT1 [29], or bridging complexes are essential for the maintenance and stabilisation of organellar interaction sites. There is evidence that MCS serve as platforms for metabolite channelling (e.g. photorespiration [1]) and lipid transfer [3] originated from different organelles.

[5, 31]) as indicated in figure 1. Scorrano *et al.* subdivided MCS proteins in four classes regarding their function, whereas it is important to mention that one protein can belong to more than one class [5]. The first class is defined as "structural proteins" including tether proteins or bridging complexes, which are responsible for the structural arrangement and maintenance of MCS. Helle *et al.* clearly defined five criteria, which a MCS tether should fulfil [31]: 1) its presence at MCS, 2) providing a tethering force between adjacent organelles, 3) increase in MCS size or number, when the tether protein is overexpressed, and that deletion of the tether should lead to 4) abolition of the organellar contact and 5) change in the physiological processes performed at this MCS [31]. Tether proteins can simultaneously function as active spacer [5]. This was proven investigating the 3D architecture of extended synaptotagmins (ESyt)-mediated ER-PM contact sites (EPCS) in mammalian cell culture by cryo-electron tomography. In cells, overexpressing individual ESyts, the distance between ER and PM correspond to the amino acid (aa) length of the cytosolic region of the overexpressed tether protein (19–22 nm, [32]).

The second class is classified as "functional proteins" and is directly responsible to fulfil the specific function of the respective contact site. They facilitate the transfer of lipids, proteins, ions or metabolites (figure 1) and/or ROS signalling [33] (reviewed in [5]). For instance, under phosphate deficiency, MCS between chloroplasts and mitochondria are thought to be the platform for the transport of specific galactolipids synthesised in chloroplasts to mitochondria in *A. thaliana* [3, 27, 34, 35]. "Regulatory proteins", the third protein class, can regulate the functionality of a MCS by affecting the activity of proteins, for instance through phosphorylation [5, 36]. The fourth protein class is termed as "sorter/recruitment proteins" and work to determine the proteome and lipidome at MCS by recruiting, repelling or sorting the proteins and lipids [5].

In summary, the spacial and structural characteristics can serve as evidence for MCS, but need to be linked to MCS functionality. The complexity and interdependence of the structural and functional categories makes MCS difficult to identify.

3 Experimental evidences for organellar contact sites in plants

MCS in mammals and yeast are well explored (reviewed in [5]), whereas the MCS research field in plants has been only slowly gaining attention. This is surprising, since the additional organelle in plants, the chloroplasts, as well as the necessary metabolite processes resulting from photosynthesis point towards a strong demand of organellar exchange, possibly via MCS. So far, plant metabolic pathways, which involve enzymes of distinct organelles, have been well investigated on biochemical level, whereas the putative role of MCS remains enigmatic (for instance photorespiration, introduction section 3.5).

This section concentrates on evidences in the MCS research field in plants, focusing on the unique nature of plants but also making the link to conserved functions in other organisms (overview figure 2).

3.1 Together but still separate: The spatial organisation of organelles

The intra-cellular membrane system functions as diffusion barriers. Various soluble substances, such as metabolites, ROS and ions/anions, but also proteins are actively or passively transported through membranes creating sub-cellular components with a unique composition of reaction components [37]. Therefore, a single organelle can be considered as an individual functional unit, as also recently extensively described for plant mitochondria [38].

Besides metabolic processes, compartmentalisation is also essential for maintenance of local redox environments. All organelles create redox networks, which is needed for scavenging of ROS, repairing ROS-induced damage and also metabolic control [37, 39]. Under stress conditions, it is possible that the local redox status of one compartment spread to others, as shown in J. M. Ugalde *et al.* from chloroplast to cytosol under photo-oxidative stress [40]. An effective organellar communication is essential during stress for instance via chloroplast-to-nucleus retrograde signalling cascades. Caplan *et al.* showed that stromule-nuclear association increases in *A. thaliana* as immune response, where proteins and possibly H_2O_2 from chloroplasts are transferred to the nucleus. They suggested these connections to be involved in retrograde signalling [19] (figure 2). A direct evidence for the transfer from H_2O_2 from chloroplasts-to-nucleus under photo-oxidative stress was given two years later by using a genetically encoded fluorescent H_2O_2 sensor (HyPer2) [41].

From these examples, it becomes clear that organellar interaction can, on the one hand, be transient and influenced by external conditions and that, on the other hand, the cellular spatial organisation influences the function, dynamics and homeostasis of the organelles. The spatial organisation includes positioning, movement and the number of organelles [6]. Whereas in yeast and animals dis-organisation of MCS is known to be linked to diseases, respiratory deficiency and ageing [42, 43], the research field in plants is less advanced yet.

Organellar movement and positioning are dependent on an interplay between MCS as

communication platform and the cytoskeleton. This is responsible for an active motor-driven and independent movement including the separation of organelles (reviewed in [24]). It is widely accepted that correlating movements of two adjacent organelles may indicate a physical interaction between them (reviewed in [2, 24]). In mammalian and yeast cells, ER tubules remain connected with endosomes, peroxisomes and mitochondria as they move within the cell (reviewed in [2]). Linked organellar dynamics have also been visualised in plants, for instance the light-avoidance mechanism of nucleus and chloroplasts [44]. The photorelocation of chloroplasts is known to be an actin-based mechanism inducing chloroplast attachment to the PM probably via chloroplast unusual positioning 1 (CHUP1) protein [45–47]. The physical association between nuclei and chloroplasts was shown to be essential for a linked organellar dynamic [44] and might facilitate retrograde or anterograde signalling [48]. Another linked organellar dynamic in *A. thaliana* has been identified between peroxisomes and ER, where ER tubule dynamics are closely related with peroxule extension [49] (figure 2).

ER tubule dynamics were shown to correlate with mitochondria dynamics in the moss *Physcomitrella patens* and in *A. thaliana* [50, 51] (figure 2). In yeast and animal cells, EMCS were found to be sites of mitochondrial fission [2, 52] regulating the number and size of those. A similar scenario can be suggested for plants, as in *P. patens* and *A. thaliana* ER tubules are located at mitochondrial constriction sites [50, 51]. However, the mechanistic proof of EMCS being involved in mitochondrial fission is still missing [53]. Evidences that mitochondria tethering to the ER does not only influence mitochondrial fission but also fusion was found in a recent publication [9]. Miro2 was identified to be essential for tethering mitochondria to the ER and promote mitochondrial fusion in *N. tabacum* pavement cells.

3.2 Identified plant MCS components - the ER as most characterised player

In all eukaryotes, the ER is a highly dynamic structure and the largest membrane-bound organelle [55], which serves many functions in the cell metabolism [56]. Therefore, it is not surprising that the potential role of ER regarding MCS has been intensively studied. The ER has been identified to function as a key player in the interactive, organellar network [2]. In mammalian and yeast cells, MCS of the ER to other organelles such as mitochondria, vacuoles, Golgi, lipid droplets and PM have been identified and investigated in detail (reviewed in [2, 33, 55, 57]).

In plants, the potential role of the ER being a key player in MCS formation has been acknowledged as well [22, 58–60]. The ER was also studied in terms of physical interactions to other organelles (see introduction section 4.2 for method details) identifying ER-Golgi [61, 62], ER-chloroplasts [30] and ER-mitochondria [9] associations. In addition, there are further evidences for physical interaction between ER-peroxisomes [49, 63] (figure 2).

In 2015, the first plant MCS tether protein has been identified at EPCS [29]. Thus, it is

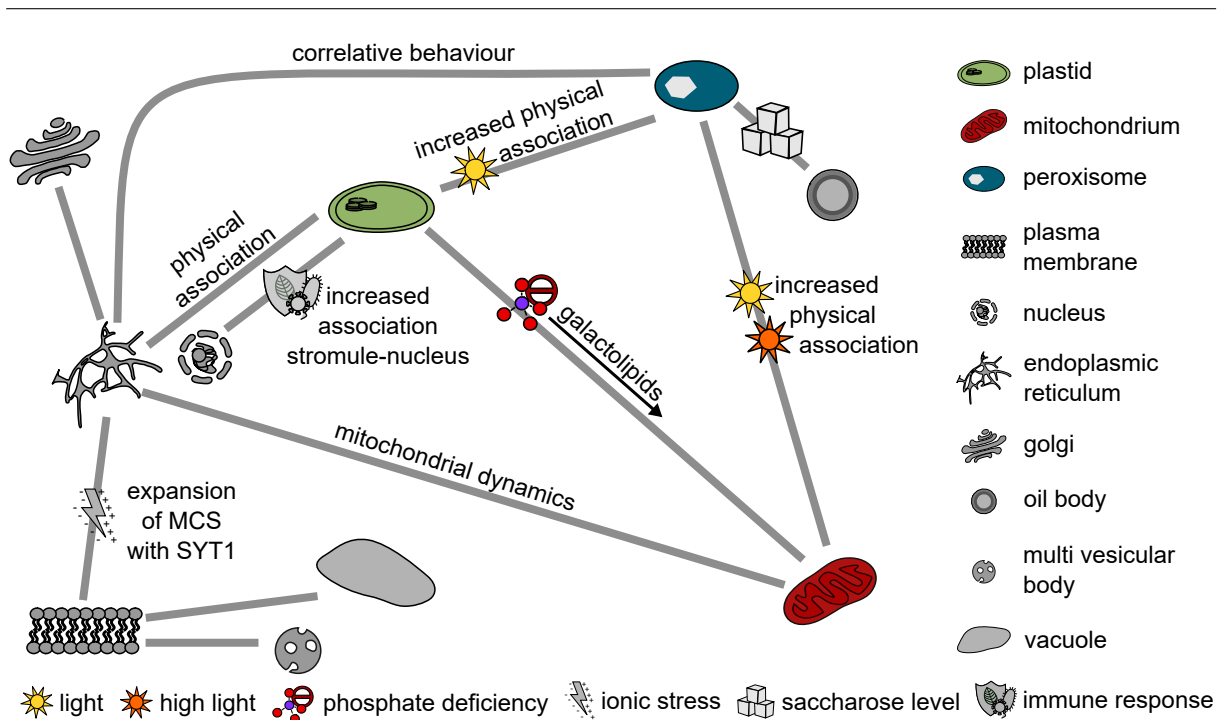


Figure 2: Schematic overview of known organellar interaction in plants.

The symbols of the edges reflect the conditions, under which an interaction have been described, whereas the text explains the experimental evidence. Modified from Falz & Müller-Schüssele 2021 [37] (based on [3, 6, 19, 21, 25–27, 49–51, 54], for further information see text).

not surprising that EPCS in plants are the most explored MCS [29, 58, 64]. Components of plant MCS are likely to be evolutionary conserved [60] (see introduction section 4.1 for further detail). This is also true in the case of EPCS, where homology research, using known mammalian and yeast MCS components as basis, resulted in the identification of two EPCS protein families [60], namely the vesicle-associated membrane protein (VAMP)-associated proteins (VAP) [58, 64] and the tether protein family synaptotagmins (SYT) [29].

A. thaliana VAP proteins consist of a C-terminal transmembrane (TM) domain targeted to the ER membrane and a N-terminal major sperm protein (MSP) domain, which is responsible for protein–protein interaction [65]. The best-characterised protein of this family in *A. thaliana* is VAP27-1 [60], which was identified as plant homolog [58] of the EPCS protein Scs2 in yeast [66, 67]. It was identified in 2014 to be part of a complex at EPCS [58] consisting of three components: 1) VAP27-1, 2) NETWORKED 3C (NET3C), a member of the plant-specific Networked (NET) superfamily of actin-binding proteins [68] and 3) actin and microtubule networks [58]. VAP27-1 interacts with NET3C localising to punctual ER-PM-associated areas, whereas F-actin and microtubules regulate the turnover of NET3C and VAP27-1, respectively [58].

Shortly after the discovery of VAP27-1 and NET3C, another EPCS component has been identified, namely SYT1 [29]. SYT1 belongs to a five member gene-family in *Arabidopsis* termed SYT [69, 70]. They have been identified as plant homologs of yeast tricalbin membrane tethers and mammalian extended synaptotagmins (E-SYT) [29, 71]. Those homologs

and the plant SYT family share a similar modular structure [29, 72]. Proteins of the plant SYT family consist of a N-terminal TM domain followed by a plant synaptotagmin-like mitochondria proteins (SMP) domain and two C-terminal calcium-binding domains (C₂A/C₂B). The TM of SYT1 mediates ER-anchoring, whereas the positively charged C₂A/C₂B domain is responsible for PM association by binding negatively charged phospholipids [29, 60, 69, 70, 73, 74]. Pérez-Sancho *et al.* investigated the impact of SYT1-mediated EPCS on the ability to cope with mechanical stress in *A. thaliana* [29]. They found SYT1 co-localising with the former described VAP27-1 EPCS and contributing to PM stabilisation through mechanical reinforcement of the contact sites [29]. Contradictory to those findings, a publication of 2016 reported that SYT1 and VAP27 do not co-localise but form distinct EPCS which are nevertheless always adjacent to each other [16]. Albeit the disagreement regarding the distinct protein localisation, both studies agree that SYT1 is responsible for stabilising the VAP27-mediated EPCS [16, 29]. Both EPCS proteins, VAP27-1 and SYT1 are also localised to plasmodesmata (PD) [64, 75]. PD are structurally unique in plants forming cytoplasmic channels including ER and PM. They connect plant cells across the cell wall and function therefore as main pathway for the inter-cellular communication [60, 76–78].

The known MCS proteins offer the possibility to investigate them regarding their function or screen for putative further interaction partners. In this context, VAP27-1-mediated EPCS were found to be involved in endocytosis via ArEH1/Pan [79] or clathrin [80], and lipid droplet formation via SEIPIN isoforms [81]. Additionally, VAP27-1 has been identified to be not only part of EPCS but also of ER-mitochondria contact sites (EMCS) [82]. EMCS serve as platform for multiple physiological activities, for instance lipid metabolism, autophagy, mitochondrial dynamic and Ca²⁺ transfer [9, 42, 51, 52, 83, 84]. Nevertheless, the protein compositions and the functionality of EMCS in plants are poorly understood compared to yeast and mammalian cells [82]. In a very recent study in plants, novel components of EMCS have been identified [82]. TraB1 is a mitochondrial outer membrane (MOM) protein, which interacts with VAP27-1 but also with ATG8 regulating mitochondrial degradation [82, 85]. Thus, the authors suggested that TraB1 is important for mitochondrial function by regulating the formation of EMCS, whereas these are likely to regulate mitophagy [82].

3.3 The impact of MCS on plant development and growth

The life cycle of higher plants starts with the seeds, which contain a far developed plant embryo in a dormant state. During germination, the mobilisation and breakdown of storage lipids are crucial, since they provide the primary source of energy in the form of generated products [54]. The storage lipids are located in lipid droplets (LD, also termed as oil bodies) and converted to fatty acids (FAs). After a translocation into the peroxisomes, FAs are broken down during the β -oxidation to acetyl-CoA, which is further processed to succinate glyoxylate cycle or citrate by the citrate synthase [86–89]. Both succinate and citrate can

serve as substrate for the mitochondrial metabolism [86–88, 90]. A kick-start of mitochondrial respiration is essential for an effective germination delivering metabolic and energy intermediates. These are important for cell expansion and plant cell physiology in general [90]. Thus, an effective germination relies on an interplay between LD, peroxisomes and mitochondria. While there is no proof of a physical interaction between peroxisomes and mitochondria during germination, a physical interaction between peroxisomes and LD was identified being mediated by PED3 as anchor protein [54] (figure 2).

In addition, MCS have recently been shown to play a role during post-germinative seedling growth [91]. LD provide energy and carbon, which are required for early seedling development. In *A. thaliana* a LD-PM tethering complex was identified consisting of PM-localised LD-PM ADAPTOR (LIPA) and LD-localised SEED LD PROTEIN (SLDP) 1 and SLDP2 [91]. The authors of this study suggested that this complex is essential for the anchoring of a subset of LDs to PM during the early seedling development [91].

Also, aberrant expression of the previously described EPCS proteins VAP27-1 and SYT1 were shown to affect the plant development [64, 74]. Both, an overexpression or a RNAi-line of VAP27-1 has defects in root hair development [64], while the null mutant *syt1-2* shows a slightly impaired root growth at seedling age resulting in a lower fresh weight [74].

3.4 Lipid trafficking at MCS

Organellar membranes consist of specific lipid assemblies. Since only some organelles generate specific lipids, they need to be transported from the location of their synthesis to their final destination. The role of MCS in lipid trafficking during plant development and stress response is extensively reviewed by Michaud & Jouhet [3]. In this section, we will only highlight two potential MCS located protein complexes being involved in lipid transfer.

Plants are unique in having an additional endosymbiotic organelle beside the mitochondria, namely the chloroplasts. While in yeast and animals, FAs are generated in the cytosol, their synthesis in plants takes mainly place in the chloroplasts [35, 92]. FAs function as building blocks for lipid biosynthesis as glycerolipids including digalactosyldiacylglycerol (DGDG) [35, 92]. DGDG are also synthesised in the chloroplasts [3]. Under standard growth conditions, they remain mainly in the chloroplasts, while they are massively exported to mitochondria, vacuoles and the PM under phosphate (Pi) starvation [27, 93, 94]. Whereas the role of MCS remains unknown for the DGDG transport from chloroplasts to PM and the vacuole, a simultaneous increase in chloroplasts-mitochondria contact under Pi starvation indicates that the transfer of DGDG between these organelles takes place at MCS [27], (figure 2). Lipid remodelling during Pi starvation is crucial: The phospholipids, which are located at the mitochondrial inner membrane (MIM), can be degraded to provide phosphate [34] and they are replaced by DGDG [27, 93, 94]. In *A. thaliana*, MIC60 was identified as a component of a mitochondrial transmembrane lipoprotein complex tethering MIM to MOM by inter-

acting with TOM40. MIC60 contributes simultaneously to the import of those galactoglycerolipids from chloroplasts as to the export of phospholipids from the mitochondria [34]. Although some proteins have been identified that establish contact between MIM and MOM, the mechanism underlying lipid transfer between chloroplasts and mitochondria remains unclear [3].

Similar also applies to another protein complex being located at the outer envelope (OE) and the inner envelope (IE) of the chloroplasts. The trigalactosyldiacylglycerol (TGD) complex transfers precursor lipids from the OE to the IE, which are synthesised in the ER [3, 95]. While the transport between the outer and inner membrane of the chloroplasts is identified, the transfer from ER to OE has not yet been proven [3]. Albeit both mentioned protein complexes are only partly identified, they have a huge potential being located at MCS and even function as tethering complex between the respective organellar pair.

3.5 The unique nature of plants: Organellar cooperation as need for effective photosynthesis under ambient light conditions

During photosynthesis, light energy is converted to chemical energy in chloroplasts by CO₂ fixation generating O₂ as a byproduct. The linear electron transport (LEF) is driven by light energy and convert water to nicotinamide adenine dinucleotide phosphate (NADPH). The LEF is coupled with a proton accumulation in the thylakoid lumen generating an electrochemical gradient, which in turn drives the synthesis of adenosine triphosphate (ATP). These reducing agents in turn fuel carbon fixation and sugar biosynthesis in the calvin benson (CB) cycle during the light-independent reaction (reviewed in [96]).

In their natural environment, plants are exposed to daily changes between fluctuating light and darkness. This is why plant cells need to be able to switch from an autotrophic to a heterotrophic metabolism. Balancing photosynthetic processes is important, since a lack of regulation may cause an imbalance in redox equivalents leading to the accumulation of the reducing power [96–100]. This can lead to an over-reduction of the plastoquinone pool [101] and the production of reactive oxygen species (ROS), which in turn can damage DNA, lipids or proteins including the photosynthetic machinery [97, 98, 102]. Thus, photochemical reactions have to be tightly regulated and adapted efficiently in reaction to changes in the light energy [96, 99, 100]. To ensure an efficient adaption, plants developed several mechanisms including the regulation of the light harvesting (for instance chloroplast relocation: [103]) or non-photochemical quenching (NPQ) [104]. These two examples concerned only chloroplasts, while excess electrons can also be exported from the chloroplasts [105]. For that, an effective communication and dynamic interaction between chloroplasts and other organelles are necessary to prevent the photosynthetic machinery from over-reduction and photoinhibition. The redistribution of reducing agents can be achieved through malate valves, for example [106, 107].

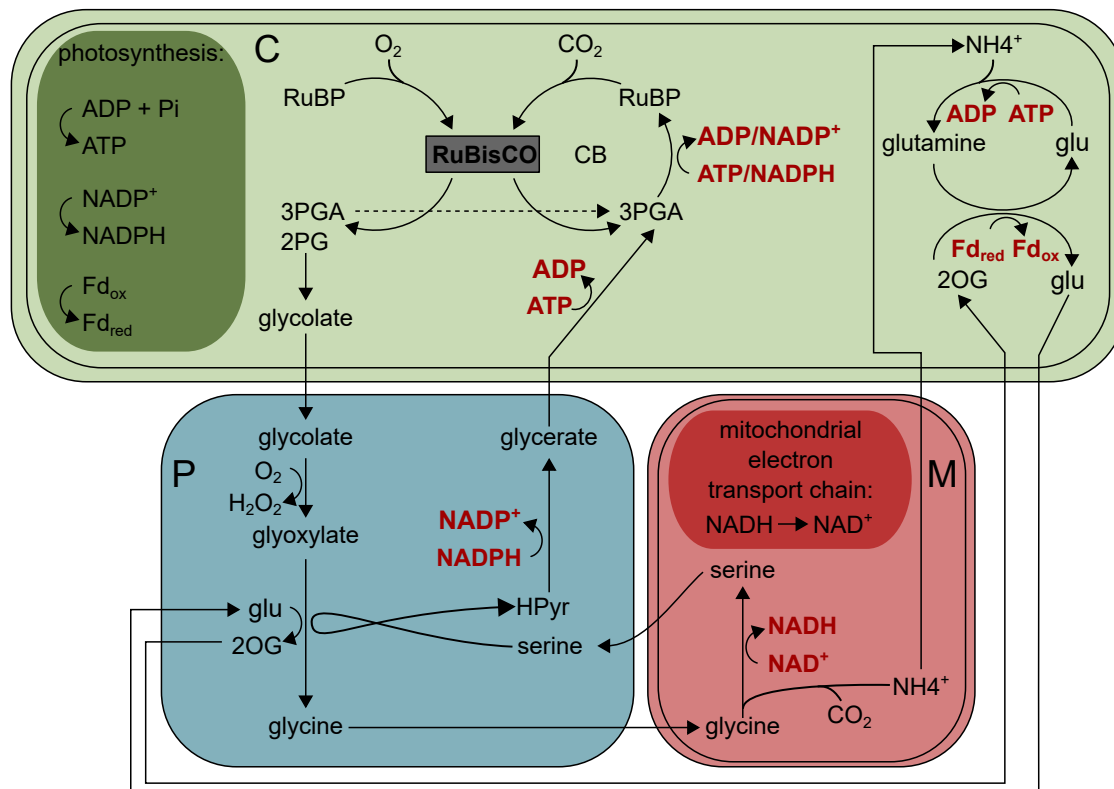


Figure 3: Simplified schemata of photorespiratory metabolism.

Oxygenase activity of ribulose 1,5-bisphosphate (RuBP) carboxylase/oxygenase (RuBisCO) lead to generation of 3-phosphoglycerate (3PGA) and the dead-end metabolite 2-phosphoglycolate (2PG). 2PG accumulation is prevented by photorespiration recycling 2PG to 3PGA across chloroplasts (C), peroxisomes (P) and mitochondria (M), which re-enters the calvin benson (CB) cycle. Photorespiration requires energy in form of ATP and reducing equivalents NAD(P)H and Fd_{red} (marked in red), which are mainly derived from the light reaction of photosynthesis. In addition, the two amino acids serine and glycine are synthesised during photorespiration. Oxidised form of ferredoxin (Fd_{ox}); reduced form of ferredoxin (Fd_{red}); glutamate (glu); 2-oxoglutarate (2OG); hydroxyppyruvate (HPyr); nicotinamide adenine dinucleotide (phosphate) (NAD(P)H); adenosine triphosphate (ATP). Adapted and modified from [110, 111].

The malate valve is a carbon flux-based export pathway linking the cellular energy and redox homeostasis to photosynthesis and the chloroplastidic redox potential [105, 108]. It plays a role in balancing ATP/NAD(P)H ratio across chloroplasts, mitochondria, peroxisomes and the cytosol (reviewed in [107]). Live monitoring of NADH/NAD⁺, pH and MgATP²⁻ dynamics with genetically encoded fluorescence biosensors revealed that photosynthetic activity influences the physiology of other cell compartments as cytosol and mitochondria [105].

3.6 The potential role of MCS in photorespiration

Photorespiration is one of the best studied metabolic pathway that occurs across organelles, namely chloroplasts, peroxisomes and mitochondria [1, 109]. Whereas proteins and the metabolic flux of photorespiration are well studied, only little is known about the potential role of inter-organellar contacts. The question needs to be addressed, if the interplay between chloroplasts, peroxisomes and mitochondria is additionally mediated by transient, specific MCS.

Photorespiration represents the recycling mechanism of the toxic component 2-phosphoglycolate (2PG). 2PG is generated, when oxygen (O_2) substitutes carbon dioxide (CO_2) as substrate for ribulose 1,5-bisphosphate (RuBP) carboxylase/oxygenase (RuBisCO) in the first reaction of photosynthetic CO_2 fixation [1, 112] (figure 3). It involves eight core enzymes, which are distributed across chloroplasts, peroxisomes and mitochondria (in detail reviewed in [1, 109, 110]). To maintain photorespiration, ATP and reducing equivalents are required. Thus, photorespiration has been considered to be an energy-losing process, making it a prime target for crop improvement [113–115]. However, this pathway is integrated into a central metabolism network [116], and modifications in photorespiration affects for instance nitrate uptake and assimilation [117, 118], or the functionality of the mitochondrial TCA cycle [119] (figure 3). Without recycling 2PG into 3-phosphoglycerate (3PGA), which re-enters the CB cycle, photosynthesis would quickly collapse, since 2PG acts as inhibitor of at least 2 CB enzymes [1, 112, 120]. Additionally, two important amino acids are generated during the photorespiratory metabolism, namely glycine and serine (figure 3, [110]).

First evidences that MCS between the photorespiratory organelles are likely, were given by TEM images showing the photorespiratory organelles often close proximity to each other (for instance [13, 121]). Although a close proximity of organelles is no prove of a functional MCS [6], there were further indications for the existence of an organellar contact. In 2003, an interdependency between chloroplastidic and peroxisomal positioning has been identified in *A. thaliana* mesophyll cells [47]. In addition, the PerM located peroxin 10 (PEX10) was suggested to be required for peroxisome-chloroplast connectivity and an effective flux of the photorespiratory metabolites [122]. PEX10 defective mutants display a defect in photorespiration. Furthermore, the peroxisomes in PEX10 defective mutants are increased in number and form clusters, while those are not adjacent to chloroplasts [122].

The proof for a physical interaction between chloroplasts and peroxisomes could be provided by biophysical techniques. The connectivity between chloroplasts and peroxisomes was tested in living tissue using optical tweezers [25] or a femtosecond laser pulse technique [26] (for detail see introduction section 4.2). Peroxisomes were found to be associated to chloroplast via peroxules in tobacco epidermal cells [25]. In *A. thaliana* mesophyll cells, a greater force is required to detach peroxisomes from chloroplasts under light compared to the dark conditions [26] (figure 2). The association of both organelles was shown to be actin-independent [25], while the dissociation is driven by F-actin [26].

The role of the interdependency between the interaction of the photorespiratory organelles and light, was also investigated by Jaipargas *et al.*. They found that high light induces peroxule formation with mitochondria clustering around these [20]. An additional functional link between chloroplast, peroxisome and mitochondria proximity, and light as stimulus was revealed by Oikawa *et al.*. They investigating the organellar interaction and morphology under different photosynthetic conditions. They found peroxisomes to be more elongated alongside the chloroplasts under light conditions compared to darkness, where

those are shaped more spherical. Also the interaction between the photorespiratory organelles was increased under light conditions [26] (figure 2).

In summary, physical interactions between peroxisomes and chloroplasts have been proven, as well as a light dependent proximity between all three photorespiratory organelles. Even though the exchange between organelles was demonstrated to be necessary for photorespiration, neither all of the involved metabolite transporters nor some MCS components have been identified yet [1, 116]. Nevertheless, considering the results of previous studies, MCS are very likely to be involved in photorespiration to ensure effective flux of metabolites.

4 Techniques for investigating MCS in plants

After providing a measurable definition of MCS (section introduction 2) and providing an overview about experimental evidences for MCS in plants (section introduction 3), this section summarises techniques that have been already used or offer great potential in the plant MCS research (after [6]).

4.1 Identification of novel MCS components

Proteins with specific functions are enriched at MCS [21, 29, 123]. In mammalian and yeast cells a lot of MCS proteins are already identified and characterised with respect to their function (see review [33]). Since contact sites are likely to be evolutionary conserved, screening for plant orthologs of mammalian or yeast MCS proteins is one potential way to identify putative candidates in plants [60]. In Pérez-Sancho *et al.* an ortholog of mammalian and yeast families of ER-PM anchors SYT1 (further information see introduction section 3.2) was identified as an EPCS anchor protein in *A. thaliana* [29].

Another possibility to screen for MCS compositions is to investigate contaminants during organelle isolation. The underlying assumption is, that physical interaction at MCS leads to a co-purification of associated organellar membranes. These contaminants can be in turn identified by mass spectrometry [126]. The same principle could be implemented for complexome data sets. This proteomic technique is developed for a systematic characterisation and an identification of protein complexes. Before performing the identification of the organellar proteome, the protein complexes get separated by a blue native page and one lane is dissected from top to bottom into equally sized slices. Proteins of each individual slice are identified via mass spectrometry and clustered according to profile similarity. Thus, complexomes provide information not only about the abundance of a protein but also about the complexes in which they are likely to occur and their interaction partners [127]. Rugen *et al.* used a complexome analysis to study the changes of mitochondrial complexes in the absence and presence of light [128]. This data set may be of special interest regarding

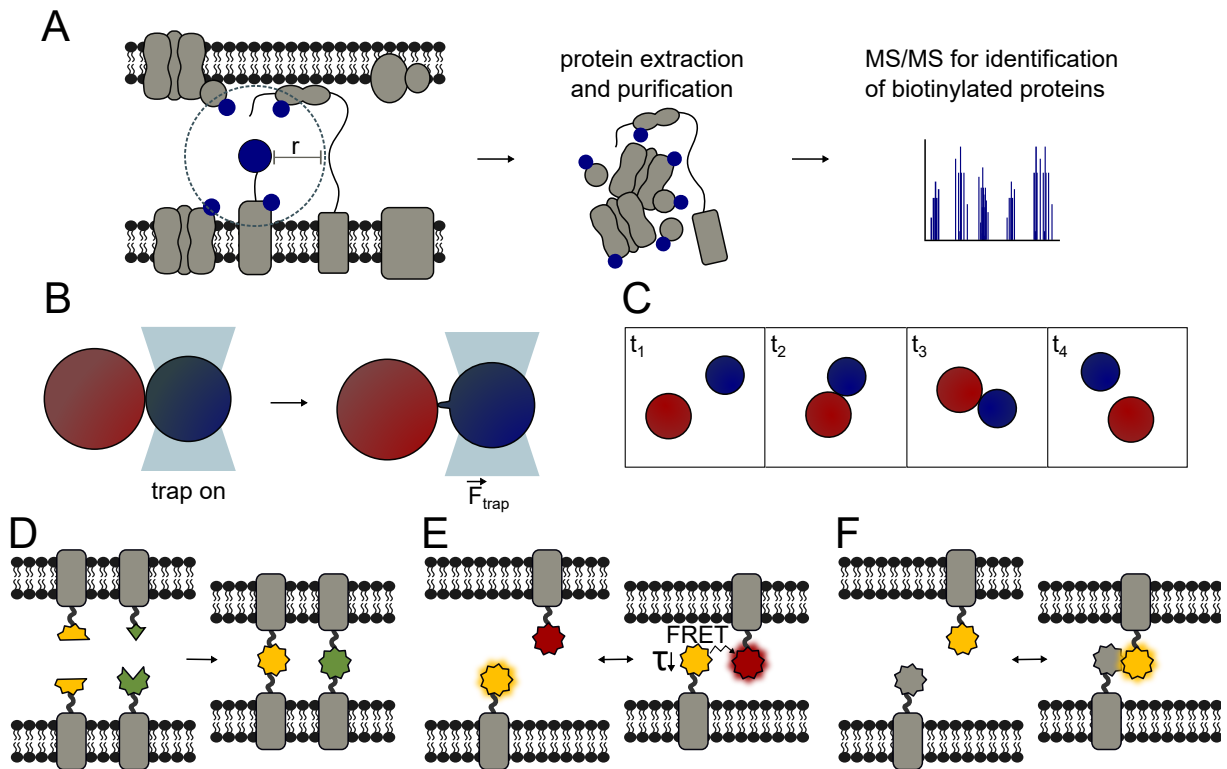


Figure 4: Putative techniques for the identification and characterisation of organelle-organelle interaction.

A: Certain proteins are enriched at MCS as SYT1 at the contact site of endoplasmic reticulum (ER) and plasma membrane (PM) [29]. If an MCS-specific protein is known, proximity labelling with a biotin ligase as BioID could be performed. This biotin ligase is fused to the known MCS-protein and could label proteins within a radius of ~ 10 nm with a biotin group [124], [125]. **B:** Optical tweezers to confirm physical interaction between organelles. In Gao *et al.* an increase of physical interaction between peroxisomes (blue) and chloroplasts (red) were detected in the light compared to dark conditions [25]. **C:** Using microscopy time series, the frequency and duration of organelle interactions could be detected. **D, E, F:** Different fluorescent sensor approaches could be used to visualise MCS. **D:** The Bimolecular fluorescence complementation (BiFC, yellow) or self assembly GFP (saGFP, green) sensor systems consist of two split protein fragments of the respective FP. Both fragments mature if the distance between them is less than ~ 10 nm and form a fully emitting FP. This approach is irreversible. **E:** For an reversible approach FRET pairs (Förster resonance energy transfer) can be fused to membrane proteins of organelles of interest. Contact can be detected either via a changed FRET ratio of donor and acceptor or a decrease in fluorescence lifetime (τ). **F:** Dimerisation dependent FP (ddFP) is a reversible approach and emit fluorescent signal only if both interact. Modified from Baillie *et al.* 2020 [6].

photorespiration, which is a light dependent process and involves chloroplasts, peroxisomes and mitochondria ([129], further information see introduction section 3.6).

Not only the protein but also the lipid content of contact sites can be investigated using co-purification during organelle isolation. Andersson *et al.* isolated specifically chloroplasts-associated membranes (PLAM) from pea protoplasts and analysed their lipid composition as well as the enzymatic activity [30]. They found an activity of ER associated enzymes in the PLAM fraction as well as a lipid composition and a polypeptide profile, which differed from the chloroplast envelope but showed a similarity to the ER membrane [30].

If one MCS component is already known, there are additional techniques to identify further candidates as GFP-trap pull-down assays [123]. Another promising approach is proximity labelling. Adjacent proteins are labelled with a biotin group within a radius of approximately 10 nm [124], followed by a separation by streptavidine affinity binding of biotinylated proteins and identification via mass spectrometry (figure 4 A). Two probes have

been commonly used for proximity labelling: 1) A modified biotin ligase BirA of *Escherichia coli*, termed BioID [130, 131], or an engineered soybean ascorbate peroxidase APEX2 [132, 133]. Both probes have been also utilised to investigate MCS in mammalian cells identifying novel components of EPCS [134, 135] and EMCS [133]. Also split variants of both probes have been used for the investigation of MCS in mammalian cells. For the reassembly of the split fragments a protein-protein interaction is essential, which increase the specificity for the proximity based labelling (APEX [136], BioID [137]).

So far, BioID assays have been conducted in rice protoplasts [138] and *A. thaliana* leaf tissue [139], albeit not for the study of MCS proteins. One possible reason of its rare usage might be the slow kinetics leading to a labelling time of 18 h or even longer to have enough material of biotinylated proteins for proper quantification. Another issue for the application in plants is the preferential working temperature of BioID enzymes of 37°C [140], which is higher than the normal environmental growing temperature for plants. Recently, Branon *et al.* published a biotin ligase derived from directed evolution of BirA in yeast, called TurboID [141]. This enzyme has its maximal activity at 30°C and a improved kinetics compared to BioID [125, 141]. Arora *et al.* first established TurboID in plant model systems as tomato, tobacco, and *A. thaliana* [125]. The potential of this technique in plants can also be seen in the rapid increase of publications in the last 2 years using TurboID [142–144].

4.2 Measuring organelle tethering forces

The presence of MCS in plants has also been investigated by biophysical methods, examining the physical association between organelles. Oikawa *et al.* used an intense femtosecond laser pulse technique to analyse the adhesion between peroxisomes and chloroplasts in *A. thaliana* mesophyll cells [26]. Shock waves are generated and propagate from the laser focal point across the interfaces. The impulsive force leads to a rearrangement of the cellular compartments and is used for calculating the pressure, which is required to detach peroxisomes from chloroplasts. The physical interaction between the same organelles has also been investigated with optical tweezers in *N. tabacum* [25]. This technique provides the possibility to trap single organelles with a submicron precision and manipulate its position (figure 4 B). The chloroplast-associated peroxisomes are trapped and subsequently moved away from the chloroplasts resulting in peroxule formation. After releasing the trap the recovery displacement of the peroxisomes has been quantified [25]. Optical tweezers have also been used to analyse the physical attachment of ER-chloroplast in pea and *A. thaliana* [30], of ER-Golgi in *A. thaliana* [62], CASP proteins [61] and ER-mitochondria in *N. tabacum* [9].

4.3 Microscopy techniques to monitor MCS

MCS are usually defined as regions of organelle proximity within a distance of 10 to 30 nm, though also larger tethering distances has been described [5, 17]. The organellar proximity is not sufficient as exclusive criterion to confirm a physical interaction. This needs to be considered in particular in adult plants, where the turgor of the central vacuole ensures that the remaining contents of the cell are compressed [6]. In addition, other evaluation criteria must also be considered, such as the contact area [21], the duration and frequency of the organellar contacts [25, 26]. As indicated in figure 4 C, the frequency and duration of organellar interaction can be obtained from microscope time series. Correlation of the movement and the mutual impact of the organellar dynamics could be visualised by a simultaneous expression of fluorescent proteins (FP) targeted at the respective organelles [44, 49, 63]. Based on these criteria, meaningful considerations can be made, especially when effects of various environmental treatments [20, 26, 44] or altered expression levels of known or putative tether proteins are included ([50]: ER-mitochondria, [64]: ER-PM).

Valm *et al.* used a variety of available fluorophores simultaneously expressed in yeast to reveal an organellar interactome of six different compartments [145]. In addition, confocal laser scanning microscopy (CLSM) using FPs has emerged as a preferred method to investigate organelle-organelle interaction in plants (see references in [6]). Fluorescence recovery after photobleaching (FRAP) has contributed to get a better understanding of dynamics and mobility of already known MCS located proteins [16, 21, 29, 58]. Commonly, CLSM can also allow conclusions to be drawn about the organellar interaction. One approach is to record time series to investigate organelle dynamics [26, 49]. Another option is 3D remodelling of confocal image stacks to identify possible relationships between neighbouring organelles [63]. However, the resolution of CLSM is limited with a pixel size larger than the defined size of MCS with less than 30 nm. Thus, respective organellar membranes may still be separated further than the presumed distance at MCS, even if the FP signal of organellar membranes is within the same pixel [6, 37].

One way to overcome the resolution issue is the usage of electron microscopy (EM) techniques. These techniques are much more accurate for the quantification of the organellar distance than CLSM images, since their resolution range in a nm-scale [19]. However, disadvantages of EM are that they are low throughput and that sample fixation is required, which is accompanied by losing the possibility for dynamic visualisation of MCS (see review [6]). Where MCS protein components are known, fusion to FP allow an immunogold labelling for EM to specifically label MCS [29, 54, 64]. In *A. thaliana*, immunogold labelling with different particle sizes was used to investigate the localisation of the known EPCS proteins SYT1 and VAP27-1 in detail. SYT1 and VAP27-1 do not co-localise and are associated with distinct EPCS that are, however, directly adjacent to each other [16]. Not only the localisation of SYT1 was investigated by EM, but also its role in the extension of EPCS [21]. SYT1 was labelled with a

FP and compared to the localisation of a Mapper-GFP, which non-selectively labels EPCS [21, 146]. The principle of the EPCS Mapper was adapted from a EPCS Mapper for human cells, which is composed of an internal GFP within the ER lumen, an ER transmembrane domain (TM), a linker and a C-terminal polybasic domain, which enables an electrostatic interaction with the PM [21, 146]. Under ionic stress EPCS containing SYT1 increased [21] (figure 2).

To guarantee both, a better resolution and the possibility of visualising dynamics, super-resolution imaging techniques have become more attractive. These techniques use various innovative approaches to overcome the diffraction limit in light microscopy and therefore enable the visualisation of biological structures within a typical range of 10-70 nm (see review [147]). So far, only Knox *et al.* investigated the desmotubules of ER in primary plasmodesmata using the super resolution technique structured illumination microscopy (SIM) in *A. thaliana* [148]. It was demonstrated in mammalian cells that super resolution is a promising tool for investigating MCS. For instance, SIM and direct Stochastic Optical Reconstruction Microscopy (dSTORM) were used to analyse protein clusters at EMCS [149].

4.4 Detecting and monitoring MCS by usage of fluorescent sensors

Förster resonance energy transfer (FRET, section 4.4.2), dimerisation dependent GFP and split fluorescent reporter systems Bimolecular fluorescence complementation (BiFC, section 4.4.1) (figure 4 D-F) convert proximity directly into a fluorescent signal. Those sensors have been insensitively used to investigate protein-protein interactions (reviewed in [150]). In addition, these sensors have been applied extensively to study MCS in mammals and yeasts, while their use in plants has been less frequent [4, 59, 151–157]. On the one hand, those sensors were combined with organellar membrane targeting to investigate the organellar proximity (for instance [151]). On the other hand, the reporters were used to screen for interacting proteins at MCS (for instance [154]). The following section will introduce the reporters including their characteristics, how they have been applied in MCS investigation, and potential applications.

4.4.1 Usage of split fluorescent protein systems to investigate MCS

BiFC has emerged as a key technique for the visualisation of protein-protein interaction. It is based on a splitFP, which is composed of two non-fluorescent peptides. Those peptides are normally fused to putative protein interaction partners [158–160]. If these two non-fluorescent peptide fragments come into close proximity, the chromophore reassembles to a functional FP, which in turn is able to emit a fluorescent signal [161].

In 2000, the reassembly of two splitGFP fragments to a functional GFP was first described both, *in vitro* and *in vivo* in *Escherichia coli* [162]. The GFP was dissected between the amino acid (aa) residues 157 and 158 and fused to anti-parallel leucin zippers [163]. These in turn mediated the reassembly of the GFP through their non-covalent association [162, 163]. Two years later, C.-D. Hu *et al.* investigated the reassembly of a splitYFP fused to Jun and Fos do-

I. INTRODUCTION

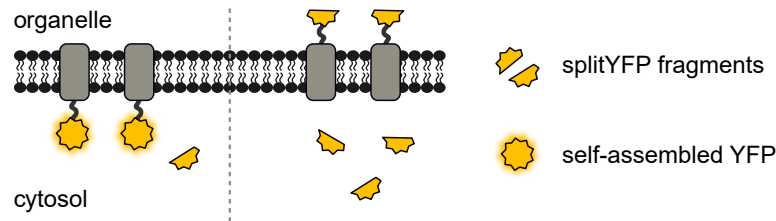


Figure 5: Schemata of topology assay using the splitYFP reporter system after Zamyatnin Jr *et al.* [165].

Either the N- or the C-terminal fragment of splitYFP (nYFP, cYFP) is fused to an organellar membrane protein of interest, whereas the complementary fragment is expressed in the cytosol. Only if the FP-tag is orientated towards the cytosol, both fragments are able to reconstitute to a functional YFP (see left). Otherwise, if the nYFP- or cYFP-tag is facing towards the luminal organellar side, the maturation could not occur resulting in no fluorescence signal.

mains of basic region-leucine zippers (bZIP) *in vitro* [159]. As the former described splitGFP, the YFP was dissected in approximately equally sized N- and C-terminal fragments between 154 aa and 155 aa. Based on the kinetics of the BiFC reassembly, the following was hypothesised: Jun and Fos reversibly form a complex within a half-life $t_{1/2} \leq 1$ s, followed by the irreversible reassembly of YFP within $t_{1/2} \leq 60$ s and the fluorophore maturation itself within $t_{1/2} \leq 3000$ s [159]. The formation of a stable complex enables the detection of weak and transient interactions on the one hand, but on the other hand eliminates the possibility to detect subsequent dynamic shifts [161]. Although the irreversibility of the maturation has been well proven and documented, in some publications BiFC was still reported to be reversible (see references in [164]).

In plant cells and under constitutive expression, splitYFP was shown to be capable of non-assisted interactions [165]. Zamyatnin Jr *et al.* took advantage of this property to elucidate the topology of integral membrane proteins or verify sub-cellular localisation [165]. The concept of the topology assay is shown in figure 5: One fragment is expressed in the cytosol, whereas the other fragment is fused to the N- or C-terminus of the membrane protein of interest. A maturation of the YFP fragments can only occur, if both splitYFP fragments are located on the same side of the membrane.

In 2005, Cabantous *et al.* published another soluble and self-associating GFP (self-assembling GFP, from here on saGFP), which was engineered for *in situ* protein tagging and localisation [166]. In contrast to splitYFP [159] and splitGFP [161], the saGFP is independent on a protein-protein interaction [166]. The reporter is divided between 214 aa and 215 aa, resulting in the unequally sized GFP₁₋₁₀ (1-214 aa, β -barrel₁₋₁₀) and GFP₁₁ (215-230 aa, β -barrel₁₁). The fragments are derived from a superfolder GFP and were both genetically engineered to overcome insolubility [166].

In general, the application of splitFP reporters is challenging, since the same expression level of both fragments is required for a reliable readout. This can be ensured by simultaneously expressing both fragments under the same promoter. Otherwise, different copy numbers and variations in expression levels might lead to false positive or negative artefacts [150, 160]. Grefen & Blatt developed a ratiometric BiFC (rBiFC) 2in1 cloning system [160]:

The simultaneous expression of two genes of interest fused to splitYFP fragments (based on EYFP, [167]) and a cytosolic expression control mRFP [168] allows a quantification of the BiFC signal. Since the vector system was designed for a transient expression by *Agrobacterium tumefaciens* mediated transformation in plants, the cytosolic mRFP also serves as transformation control, even if no BiFC signal can be detected [160].

In the context of MCS, BiFC was shown to be a suitable tool for studying organellar interaction and proximity (references see table 2). The two BiFC reporter techniques splitYFP and saGFP were applied in these studies (figure 4 D). The saGFP reporters were used to investigate the proximity between the ER to various organelles [151, 152, 169]. SplitYFP, on the one hand, was applied to verify protein-protein interactions at MCS [154, 170, 171]. Shai *et al.* for instance performed a systematic mapping of putative tether proteins between peroxisomes and mitochondria in yeast using splitYFP and uncovered two protein candidates [154]. On the other hand, splitYFP reporters have been applied to induce artificial tethering between ER-PM or PM-tonoplasts [59, 155] or to investigate EMCS in response to ER stress [153].

The distance between organelles at MCS can alter between different organelle pairs and between different MCS of the same organelle pair. Several studies, which explored MCS using BiFC-based reporter systems, included additional linkers to be able to investigate different distances (table 3). Cieri *et al.* developed a saGFP-based contact site sensor (SPLICS) with a short and a long linker. They show a different FP signal distribution for narrow and wide distance between ER and mitochondria. The relevance that the reporter need to be able bridge the natural organellar distance became clear in Z. Yang *et al.* (mitochondria-ER contact sites (MERC) reporter) [172]. While for the MERC reporter without a linker no FP signal could be detected, adding two different linkers resulted in a FP signal [172]. Especially in plants, where little is known about the distance between organelles at MCS, investigating proximity with different distances is important to consider. In T. Li *et al.* a combinatorial reporter set for the visualisation of MCS between the ER and mitochondria, chloroplasts or PM in plants was published [152]. Neither in *A. thaliana* protoplasts nor in *N. benthamiana* leaves a signal was detected without an additional linker for all three combinations. Adding a linker by either multiple fusions of GFP₁₁ or by adding a GS-linker, the signal increased proportional to the size of the reporter [152].

When using BiFC reporter systems, their irreversibility needs to be taken into account, since it leads to a limitation in mapping or quantifying of the subsequent dynamics. Tao *et al.* pointed out, that the usage of BiFC for the investigation of MCS is accompanied by risks, since artificial tethering might include the potential of an altered cell structure and membrane organisation. For that reason, the experimental controls must be carefully chosen and the results critically reviewed. However, the artificial tethering effect could also be used specifically to perturb organelle interaction. In plants, this was performed by Tao *et al.* [59] and Tao *et al.* [155] between ER-PM and ER-tonoplast/multivesicular bodies (MVB), respectively.

There is a need of reversible techniques for the visualisation of organellar proximity to

I. INTRODUCTION

Table 2: Publications using Bimolecular fluorescence complementation (BiFC) for the investigation of organellar interaction.

Endoplasmic reticulum (ER), mitochondrial outer membrane (MOM), outer envelope (OE), plasma membrane (PM), peroxisomal membrane (PerM), lipid droplet (LD), vacuole (Vac), multivesicular body (MVB).

Technique	Organellar membrane	Outcome	Organism	Ref.
saGFP	ER-MOM	SPLICS: saGFP-based sensor for narrow and wide organelle juxtapositions.	Human (cell culture)	[151]
	ER-MOM MOM-Vac MOM-PerM PerM-Vac Vac-LD PerM-ER MOM LD LD-ER	Visualising multiple inter-organellar contact sites using the organelle-targeted split-GFP system.	<i>S. cerevisiae</i>	[169]
	ER-OE ER-MOM ER-PM	Reporter set for the visualisation of MCS between ER and other organelles	<i>N. benthamiana</i> , <i>A. thaliana</i> (transiently)	[152]
splitYFP	ER-MOM	Specific BiFC signal between Mmm1 and Atg8 proteins	<i>S. cerevisiae</i>	[170]
	ER-MOM	ER-MOM associations increase in response to tunicamycin induced ER stress.	Human, mouse, monkey (cell culture)	[153]
	PerM-MOM	Systematic mapping of candidates: Identification of tethering candidates between PerM-MOM.	<i>S. cerevisiae</i>	[154]
	ER-PM	Artificial tethering of ER-PM with PM membrane proteins (peripheral, integral (synthesis over ER)).	<i>N. benthamiana</i> (transiently)	[59]
	PM-tonoplast / MVB	Artificial tethering of PM-tonoplast/MVB with PM peripheral membrane proteins.	<i>N. benthamiana</i> (transiently)	[155]
	OE-MOM	Verification of glycolytic enzymes for substrate channeling complex between chloroplasts and mitochondria.	<i>A. thaliana</i> (transiently)	[171]

Table 3: Overview of publications using Bimolecular fluorescence complementation (BiFC) to study different distances at MCS.
Endoplasmic reticulum (ER), mitochondrial outer membrane (MOM), outer envelope (OE), plasma membrane (PM).

Ref.	Organism	Organellar membranes	Sensor method + linker/ spatial information	Distance readout
[153]	Human, mouse, monkey (cell culture)	ER-MOM	<u>splitVenus:</u> cVenus: ER MOM:nVenus No linker: Largest measurable distance 10 nm.	Distance between ER and mitochondria between 6 – 10 nm.
[151]	Human (cell culture)	ER-MOM	<u>saGFP:</u> saGFP-based contact site sensor (SPLICS _{S/L}): MOM:GFP ₁₋₁₀ ER:S/L:GFP ₁₁ (S: short linker; L: long linker) 1) SPLICS _S : 8 - 10 nm 2) SPLICS _L : 40 - 50 nm	Signal proportional to linker length. FP signal differs for SPLICS _{S/L} .
[172]	Human (cell culture)	ER-MOM	<u>saGFP:</u> Mitochondria-ER contact sites (MERC) reporter: GFP ₁₋₁₀ -ER Mito-(+/-linker)GFP ₁₁ 1) no linker 2) short linker ~3 nm 3) long linker ~10 nm	Signal proportional to linker length.
[152]	<i>Nicotiana benthamiana</i> , <i>A. thaliana</i> (transient)	ER-MOM ER-OE ER-PM	<u>saGFP:</u> saGFP-based MCS reporter: GFP ₁₋₁₀ :ER OE:GFP ₁₁ MOM:GFP ₁₁ PM: GFP ₁₁ 1) increasing length via multiple GFP ₁₁ (1/2/4x) (6.12 nm/GFP ₁₁) 2) GS-linker (3nm) 4.2 -24.48 nm	Signal increases with length of protein, either due to GS-linker or multiple GFP ₁₁

overcome the issue of irreversibility of the BiFC sensor system and therefore the risk of manipulation of cellular structures. One promising possibility is the split fluorescent reporter Fluorescence-activating and absorption-shifting tag (splitFAST) [173]. SplitFAST was designed for real-time visualisation of the formation and dissociation of protein-protein interactions in human cell culture and is a reversible split fluorescent reporter [173]. Albeit this reporter system has not been tested in the context of MCS, the described criteria of splitFAST makes it a promising tool for the dynamic study of MCS in mammalian but also in plant cells [6].

4.4.2 FRET/FLIM reporters as dynamic approach for visualising MCS

Similar to splitFAST, FRET is a fully reversible reporter technique (figure 4 E). Within the FRET pair, the emission spectra of donor FP need to overlap with the absorption spectra of the acceptor FP. Thus, a physical phenomenon can take place, where a donor FP in its excited state transfers its excitation energy to a neighbouring acceptor FP, which in turn emits a fluorescent signal [174, 175] (figure 4 E). The energy transfer normally takes place within a distance of 3-10 nm [174]. Its efficiency depends on the distance between the donor and acceptor fluorophores and the specific Förster radius of the respective FRET pair (see references in [174, 176]). Compared to the irreversible BiFC reporters, FRET sensors offer the ability to monitor transient interactions in a real time context [177].

On the one hand, FRET can be detected by observing the ratio between acceptor and donor fluorescence intensity (see references in [150]). The fluorescence ratio readout is strongly dependent on equal donor and acceptor concentrations [150, 178]. Addressing the need for the equal expression levels of the FRET pair fused to the proteins of interest, Hecker *et al.* developed a binary FRET 2in1 cloning system for plants [177]. However, spectral bleed-through of the donor and photobleaching can additionally interfere with the fluorescence ratio readout. On the other hand, FRET can be detected by monitoring the fluorescence lifetime of the donor using fluorescence lifetime imaging (FLIM). The FLIM method is unaffected by the aforementioned criteria and might be a more robust detection method [150, 178, 179]. However, it must be considered that FLIM can require an imaging time of several seconds per image, dependent on the experimental setup [6].

One detection method for FLIM is the time-correlated single photon counting (TCSPC), which is a very sensitive technique offering a picosecond resolution and an extremely high precision for recording low-level light signals [179]. TCSPC exploits the circumstance that the light intensity of weak signals with a high repetition rate is usually so low that the probability of detecting more than one photon in a signal period is negligible [179]. The principle and the analysis opportunities of TCSPC are depicted in figure 6. During the measurement, the donor molecules of the sample are excited by a pulsed laser in a MHz repetition rate. The expected fluorescence decay resembles a waveform (figure 6 A), which represents the probable photon distribution. For each detected photon the arrival time of the respective detector pulse in the signal period is collected. After several signal periods, the distribution

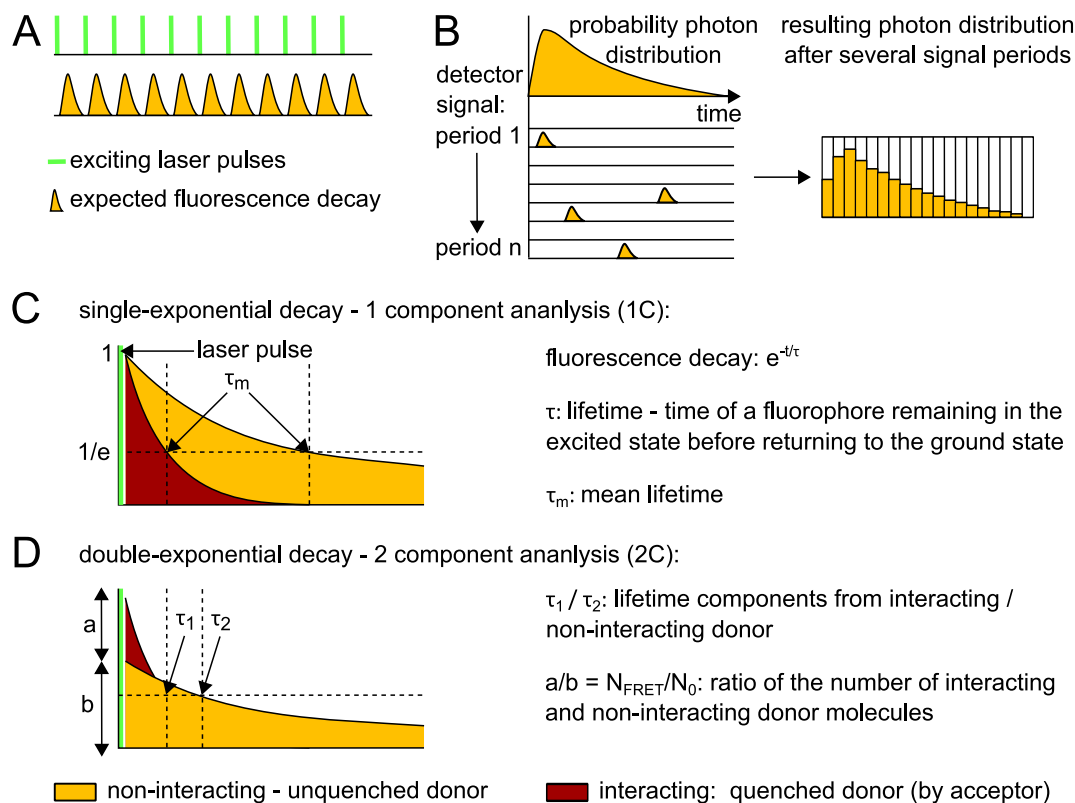


Figure 6: Principle of time-correlated single photon counting (TCSPC) and the fluorescence lifetime (FLIM) analysis.

A, B: Detection of the fluorescence decay by TCSPC. Excitation pulse sequence of defined MHz pulse repetition rate and the expected fluorescence waveform (A). However, the expected waveform need to be considered as a probability distribution of the photons, whereas actual the signal consists of a few pulses representing a single photon randomly distributed over the time axis (B). For each detected photon, the arrival time of the respective detector pulse in the signal period is recorded. The probability detecting a photon in one signal period is a relatively low. Thus, only after many signal periods, the number of detected photons is sufficient, calculating the photon distribution over time, which in turn represents the expected waveform. **C, D:** Analysis of the FLIM parameters based on the fluorescence decay. The lifetime of the FRET/FLIM donor can be either analysed with a 1 component (1C) (C) or 2 component (2C) (D) analysis. The donor τ_m of the interacting and therefore quenched donor molecule is decreased compared to the non-interacting one. Usage of the double exponential decay analysis provides besides the lifetimes τ_1 and τ_2 of the interacting and non-interacting donor molecules, respectively, also the intensity factors (amplitudes), a and b, of the 2C. The ratio of a and b (N_{FRET}/N_0) represents the number of interacting and non-interacting molecules. Modified from Becker 2014 [179].

of photons over time can be calculated representing the expected waveform (figure 6 B).

The counted photon distribution can be analysed using a single-exponential (figure 6 C) or double-exponential decay (figure 6 D). FRET leads to a highly effective quenching of the donor fluorescence and therefore to a reduction of the donor lifetime. Single exponential decay analyses are particularly useful for identifying areas where FRET occurs. Using the 1 component (1C) analysis, the mean lifetime (τ_m) of the donor is distinctly decreased compared to that of the non-interacting, unquenched donor FP. τ_m is composed of non-interacting and interacting donor molecules, where the respective separated lifetimes can not be reflected in a 1C analysis. This information can be generated by using a double-exponential decay model for the analysis, resulting in a slow (τ_2) and a fast (τ_1) lifetime component from non-interacting, unquenched and from interacting, quenched donor molecules, respectively. Besides τ_1 and τ_2 , the 2C analysis also provides amplitudes (intensity factors), a and b, of both decay components. Based on those amplitudes, the ratio of the

number of interacting and non-interacting molecules (N_{FRET}/N_0) can be calculated.

In plants, FRET/FLIM reporters have been used to investigate protein-protein interactions at MCS. Osterrieder *et al.* applied a FRET-FLIM sensors to detect interactions between specific protein partners at MCS within Golgi stacks [180]. Additionally, a protein-protein interaction between EPCS proteins VAP27-1 and NET3C was confirmed in *N. benthamiana* [58]. In mammals, ER-trans-Golgi (TGN) and EMCS have been studied by using FRET-based approaches. In both cases, rapamycin-inducible FRET systems were applied [4, 157, 181]. Rapamycin induction leads to dimerisation of so called FRB and FKBP12 modules, which are fused to both FP and organelles, and therefore stabilise the contact [4, 182].

Another reversible sensor technique, which can also be applied for the investigation of MCS, is the dimerisation-dependent FP (ddFP) (figure 4 F). It is composed of a pair of non-fluorescent FP-derived monomers, which are able to form a fluorescent heterodimer. The reporter is reversible, but only produces a low fluorescence signal levels [6, 183]. Nevertheless, the sensor has already proven useful for studying the interactions between membrane-associated proteins of the EMCS in mammalian cells [183].

In conclusion, a diverse toolbox is available to study MCS or identify novel protein components.

4.5 Perturbing organellar interaction

Besides visualisation, another possibility to explore MCS is to perturb their formation or organelle dynamics, and verify the impact on the cellular and phenotypic levels. There are two ways to achieve a perturbation of MCS formation.

A change in the expression level of known MCS components by either overexpression or knockout/knockdown may lead to altered spatial or functional characteristics of MCS. As an example in plants, the overexpression of VAP27-1, a known EPCS protein, was shown to increase EPCS area. Overexpression and knockdown of VAP27-1 and VAP27-3 in *A. thaliana* lead to defects in the root hair development [64].

Secondly, artificial tethering can be conducted to keep organelles in close proximity to each other. However, it is not known if the proximity would automatically induce the recruitment of functional MCS proteins or these areas remain without natural and specified functionality. By using a synthetic tether protein, the famous ER-mitochondria encounter structure (ERMES) was discovered [42]. To identify proteins being involved in EMCS in yeast, Kornmann *et al.* screened for mutants, whose phenotype could be complemented by an artificial tether protein. Also in plants, artificial tethering was applied in two BiFC studies [59, 155]. Here the expression of the artificial tether construct led to tethering between ER-PM, PM-tonoplast or PM-multivesicular bodies but the authors did not investigate the biological relevance of the perturbation [59, 155].

5 Objectives of this work

While MCS in mammalian and yeast have been already broadly investigated, the research field in plants is less advanced. Photorespiration is a metabolic pathway, which operates across three organelles: chloroplasts, mitochondria and peroxisomes. Whereas this process is well studied on the molecular level, only little is known about the relevance of inter-organelle contacts. The aim of this study was to elucidate organelle-organelle interactions using the photorespiratory metabolism as a model, and to reveal how MCS are linked to plant growth and performance. We addressed this question using three main experimental approaches:

- 1) The first key objective of this study is to test if the proximity between chloroplasts and peroxisomes differs under light and dark conditions. In previous reports, there is evidence for an increase in the interaction rate of the three photorespiratory organelles and physical association under light conditions compared to dark conditions in *A. thaliana* [25, 26]. To extend the information content to the aforementioned studies, we will perform an organelle proximity analysis in *A. thaliana*, *N. tabacum* and *P. patens* using fluorescently labelled organelles. For the analysis, we aim to develop a transparent and automated high-throughput Python-based analysis process.

- 2) The second key objective of this work is to establish novel *in vivo* proximity sensor systems in plants. We test the suitability of BiFC and FRET/FLIM reporter systems to visualise MCS using *in vivo* imaging. Those sensor systems convert proximity directly into a fluorescent signal [6]. In theory, this would make them in combination with organelle membrane targeting to a promising tool for MCS visualisation. The targeting will be achieved using membrane proteins or protein domains of the three photorespiratory organelles, which are not specifically located at MCS and do not interact with each other. The aim is to test if those generated proximity sensors are suitable to detect organelle proximity in plants.

- 3) The third key objective of this work is to manipulate the natural spatial organisation of a cell by introducing a synthetic tether construct cross-linking the photorespiratory organelles. We aim to generate stable *A. thaliana* synthetic tether lines expressing the synthetic organelle tether (1) constitutively or (2) inducibly. On the one hand, those transgenic plants should be investigated on the cellular level regarding organelle positioning and morphology. On the other hand, we want to study effects of organelle positioning on the plant physiology including germination, growth, photosynthetic performance and coping with stress conditions as high light.

II Methods

1 Technical equipment and consumables

General chemicals were purchased from AppliChem (www.applichem.com), Duchefa (www.duchefa-biochemie.com), Merck (www.merckmillipore.de), Roth (www.carlroth.com) and Sigma-Aldrich (www.sigmaaldrich.com). General plastic ware as falcons and tubes was purchased from Sarstedt (www.sarstedt.com) and VWR (de.vwr.com). Micropore™ tape was purchased from 3M (www.3mdeutschland.de).

Table 4: Technical equipment

Equipment	Manufacturer
A1000 plant growth chamber	Conviron, www.conviron.com
Airstream® Class II Biological Safety	ESCO, www.escoglobal.com
Analytical Balance Summit SI-234	Denver Instrument, www.denverinstrument.com
Beckman Centrifuge Avanti® J-26-XP	Beckman, www.beckmancoulter.com
Beckman Rotor JA-10	Beckman, www.beckmancoulter.com
C1000™ Thermal cycler	Bio-Rad, www.bio-rad.com
C1000™ Thermal cycler Reaction Module 48W	Bio-Rad, www.bio-rad.com
Canon CanoScanLide 700F	Canon, www.canon.de
Canon EOS 1100D EF-S digital camera	Canon, www.canon.de
CLARIOstar® plate reader	BMG, www.bmglabtech.com
Electroporator MicroPulser™	Bio-Rad, www.bio-rad.com
Eppendorf BioPhotometer Plus	Eppendorf, www.eppendorf.de
Eppendorf Centrifuge 5424 R	Eppendorf, www.eppendorf.de
Eppendorf Centrifuge 5430	Eppendorf, www.eppendorf.de
Eppendorf Thermomixer™ Comfort	Eppendorf, www.eppendorf.de
Eppendorf Thermomixer™ Compact	Eppendorf, www.eppendorf.de
Gel documentation MF-ChemiBIS 2.0	DNR Bio-Imaging Systems, www.dnr-is.com
Incubators 28°C Ecotron Typ ET25-TA-RC	INFORS HT, www.infors-ht.com
Incubators 37°C Ecotron Typ ET25-TA-00	INFORS HT, www.infors-ht.com

(continued)

Table 4: (continued)

Equipment	Manufacturer
INTAS ECL Chemostar imager	INTAS, www.intas.de
Labculture [®] Vertical laminar flow cabinet	ESCO, www.escoglobal.com
Leica DCF425C camera	Leica, www.leica-microsystems.com
Leica M165FC stereomicroscope	Leica, www.leica-microsystems.com
Magnetic Stirrer MR Hei-Mix L	Heidolph, www.heidolph-instruments.de
Metrohm pH-meter 827 pH lab	Metrohm, www.metrohm.com
Nanodrop [™] 2000c	Thermo Scientific, www.thermoscientific.com
Orbital platform shaker Unimax 1010	Heidolph, www.heidolph-instruments.de
Oxygraph Clark-type oxygen electrode	Hansatech Instruments,
pH-Meter FE20 – FiveEasy [™]	Mettler Toledo, www.mt.com
Plant growth chambers	Jan Weiler GmbH, www.jan-weiler.de
POLARstar [®] Omega plate reader	BMG, www.bmglabtech.com
Precision Balance TP1502	Denver Instrument, www.denverinstrument.com
S1000 [™] Thermal Cycler	Bio-Rad, www.bio-rad.com
S1000 [™] Thermal Cycler Reaction Module 96W	Bio-Rad, www.bio-rad.com
T100 [™] Thermal Cycler	Bio-Rad, www.bio-rad.com
Compact TCSPC System	Becker & Hickl GmbH, www.becker-hickl.com
TKA LabTower EDI water purification system	Thermo Electron LED, www.thermofisher.com
UV-lamp, portable	M&S, www.m-und-s-laborgeraete.de
Vacuum concentrator Savant [®] DNA 120	Thermo Scientific, www.thermofisher.com
Vortex mixers	Scientific Industries, www.scientificindustries.com
Zeiss Axio Observer Z1 Zeiss	Zeiss, www.zeiss.de
Zeiss confocal microscope LSM780	Zeiss, www.zeiss.de
Zeiss Plan-Apochromat 63x/1.40 Oil DIC M27	Zeiss, www.zeiss.de

II. METHODS

Table 5: Enzymes used in this study

Enzyme	Manufacturer
Gateway [®] BP clonase II enzyme mix	Invitrogen [™] www.thermoscientific.com
Gateway [®] LR clonase II enzyme mix	Invitrogen [™] www.thermoscientific.com
Proteinase K	Invitrogen [™] www.thermoscientific.com
FastDigest Eco31I (BsaI)	ThermoScientific, www.thermoscientific.com
FastDigest NcoI	ThermoScientific, www.thermoscientific.com
FastDigest Eam1105I	ThermoScientific, www.thermoscientific.com
FastDigest SacI	ThermoScientific, www.thermoscientific.com
FastDigest KpnI	ThermoScientific, www.thermoscientific.com
T4 DNA ligase (5 U/μL)	ThermoScientific, www.thermoscientific.com
Phusion [®] High-Fidelity DNA Polymerase (2 U/μL)	ThermoScientific, www.thermoscientific.com
Taq [™] DNA Polymerase	New England Biolabs [®] , www.neb.com

Table 6: Specific materials and kits used in this study.

Kits/materials	Manufacturer
NucleoSpin [®] Plasmid	Macherey-Nagel, www.mn-net.com
NucleoSpin [®] RNA	Macherey-Nagel, www.mn-net.com
NucleoSpin [®] Gel and PCR Clean-up	Macherey-Nagel, www.mn-net.com
RevertAid First Strand cDNA Synthesis	Thermo Scientific, www.thermofisher.com
Q5 [®] Site-Directed Mutagenesis	New England Biolabs [®] , www.neb.com
MitoTracker [™] Orange	Invitrogen [™] www.thermoscientific.com
MitoTracker [™] Green FM	Invitrogen [™] www.thermoscientific.com

Table 7: Software used in this study.

Software	Manufacturer
Fiji	www.fiji.sc, Schindelin et al., 2012; Rueden et al., 2017
FinchTV v. 1.4.0 sequence viewer	PerkinElmer, www.geospiza.com/ftvdlinfo.html
GraphPad Prism 7.0a	GraphPad Software, www.graphpad.com
Icy	de Chaumont <i>et al.</i> [184], icy.bioimageanalysis.org
Imaris (version 9.2.1, surface module)	Oxford Instruments, imaris.oxinst.com
Inkscape: Open Source Scalable Vector Graphics Editor	www.inkscape.org
Leaf Lab tool (Version 1.4.1)	Prof. M. Fricker, Wagner et al 2015
Leica Application Suite	Leica, www.leica-microsystems.com
MatLab-based ratiometric imaging software	Prof. M. Fricker, www.markfricker.org
Microsoft Office 2016	Microsoft, www.microsoft.com
Oxytherm Plus v. 1.02	Hansatech Instruments, www.hansatech-instruments.com
Python (version 3.7.6/ 3.7.9 64 bit)	www.python.org
Redox Ratio Analysis (RRA)	markfricker.org
RootNav	[185], sourceforge.net/projects/rootnav/files/?source=navbar
SerialCloner 2.6.1	SerialCloner, serialbasics.free.fr
VSCodium (version 1.52.1)	vscodium.com
ZEN 2011 black and blue edition	Zeiss, www.microscopy.zeiss.com

2 Plant methods

2.1 Plant material

Plant experiments were either performed in transiently transformed *Nicotiana benthamiana* / *tabacum* leaves or in stable *Arabidopsis thaliana* lines.

Stable *Arabidopsis* sensor lines, which were generated in the background of the ecotype Columbia-0 (Col-0) wild-type (WT) and peroxisomal CFP marker line px-ck (NASC: N16259, px = peroxisome, c = CFP, k = kanamycin, [186], ecotype Col-0) (2.5), are listed in table 8, 9,

27 (page 119) and 28 (page 120) with their respective segregation pattern.

2.2 Transient transformation of tobacco plants

A pre-culture of *Agrobacterium tumefaciens* AGL1 or GV3101 cells harbouring fluorescent sensor constructs was grown in 5 – 10 mL LB medium under appropriate antibiotic selection at 28°C for 24 h. The pre-culture was used to start a fresh culture in 10-20 mL LB medium with respective antibiotics with an OD of 0.1. When the actively growing culture is in the exponential phase between an OD₆₀₀ of 0.8 and 1.0, cells were harvested by centrifugation at 3500 g for 4 min. The pellets were washed two times with sterile deionised water before cells were resuspended in deionised water to an OD₆₀₀ of 0.05 - 0.2. *N. benthamiana* or *N. tabacum* leaves of 4 – 6 week-old plants were infiltrated and imaged after 1 – 3 d incubation.

2.3 Plant growth on agar plates

If not indicated otherwise, Petri dishes containing 25 mL of prepared standard growth medium (1/2 Murashige and Skoog medium (MS; [187]), 0.05% MES (w/v), 0.1% (w/v) sucrose, 0.8% (w/v) agar, pH 5.7 adapted with KOH). Arabidopsis seeds were surface sterilised by incubating for 7 min in 1 mL 70% (v/v) ethanol and centrifuged for 1 min at 10.000 g. The supernatant is removed and the seeds are washed 2 times with 1 mL sterile water before transferring them on Petri dishes. After the plates are sealed with Parafilm and stratified for at least 2 d in the dark at 4°C, the plates were transferred to long day growth conditions (16 h 75-100 $\mu\text{mol m}^{-2} \text{s}^{-1}$ at 22°C, 8 h darkness at 18°C). Experiment dependent, plants were grown in a vertical or horizontal position.

2.4 Plant growth on soil

3 - 5 Arabidopsis seeds were placed on water-imbibed Jiffy-7 (peat swelling pellets) or squared pots and stratified for at least 2 d at 4°C at high humidity covered them with a transparent plastic dome. After stratification they were transferred to the growth cabinet (16 h, 100–120 $\mu\text{mol m}^{-2} \text{s}^{-1}$ at 22°C, 8 h darkness at 18°C, humidity 50%), still covered by a transparent plastic dome during the first week to ensure high humidity during germination. Plants were thinned out 14 – 21 d after germination to one plant per Jiffy. For experimental approaches one Jiffy-7 was transferred to a squared pot filled with a soil mixture (Floradur B-seed, Perlite Perligran 0-6 and quartz sand in a ratio of 10:1:1, respectively). For floral dip or seed propagation three Jiffies were combined in a round pot containing the soil mixture. For phenotyping on soil see section 2.10.

2.5 Stable transformation of Arabidopsis

Arabidopsis plants were grown on soil as described in section 1.2.3. The primary inflorescence branch was removed by cutting to induce growing of secondary stems to increase the number of inflorescence branches.

To generate stable Arabidopsis lines floral dip transformation method established by Clough & Bent [188] was used. A pre-culture of *Agrobacterium tumefaciens* AGL1 or GV3101 cells harbouring fluorescent sensor constructs was grown in LB medium under respective antibiotic selection at 28°C 140 - 180 rpm overnight. The pre-culture was used to inoculate a main culture of 400 mL with fresh medium. It was grown until an OD₆₀₀ of 0.8-1.0 and Cells were harvested by centrifugation at 5000 g for 10 min. The cells were carefully resuspended in floral dipping solution (5% (w/v) sucrose and 0.02% (v/v) surfactant Silwet L-77) by pipetting or shaking to a final OD₆₀₀ of 0.8 - 1.0. After the flower buds were dipped into the culture for 20 - 30 s, the plants were incubated for 16-24 h in the dark at room temperature (RT) and high humidity. Afterwards plants were returned to standard growth conditions for seed harvesting and screening for positively transformed plants.

2.6 Selection of transformed Arabidopsis plants

2.6.1 T₁ seeds: Selection on soil

In this work, all generated stable lines harbouring fluorescent sensors with Basta as plant selection marker. T₁ seeds of dipped plants (see section 2.5) and background lines as control were transferred to round pots with soil mixture, stratified for at least 2 d at 4°C and cultivated under standard growth conditions as described in section 2.4. 5-7 day-old seedlings were sprayed with a Basta solution (240 mg/L glufosinate ammonium, Bayer, stock solution: 200 g/L, liquid). Spraying was repeated 3 d afterwards. If 7 d after the first spraying the control lines (Col-0, px-ck) were dead, survivors of T₁ plants can be transferred to Jiffies. Otherwise spraying with the Basta solution was repeated until all seedlings of the control lines are dead. At an age of 4 to 6 weeks survivors were first screened for fluorescence with a Leica M165 FC stereomicroscope. This is equipped with a Leica DFC425 C camera for imaging and GFP filters with 470/40 nm and 525/50 nm as well as DsRED filter with 545/30 nm and 620/60 nm for excitation and for emission, respectively. The fluorescent, transgenic T₁ seedlings were verified by using a Zeiss confocal microscope LSM780 screening for YFP and RFP signal (settings similar to section 1.3). Jiffies of verified T₁ plants were transferred to pots for proliferation of seeds. The T₁ generation is uniformly heterozygous for the inserted fluorescent sensor constructs.

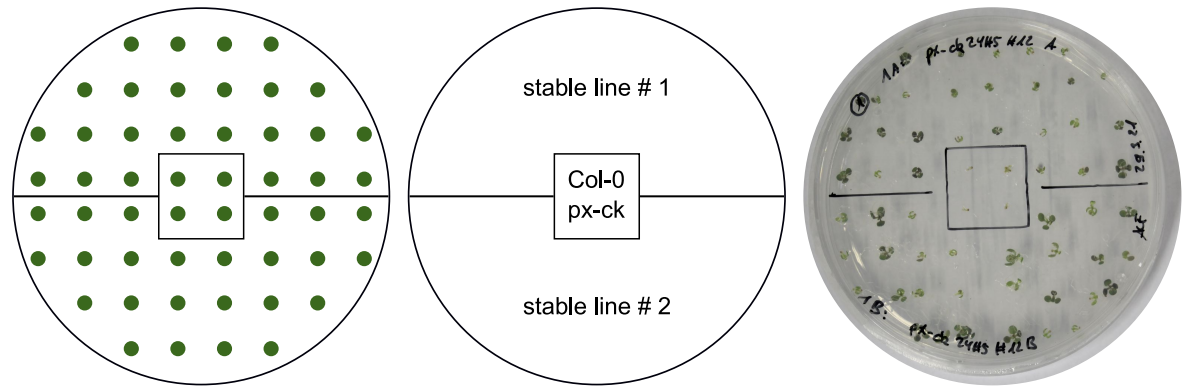


Figure 7: Plate design for Basta selection on plates.

Seeds were applied to plates with 1/2 MS medium including 10 µg/mL glufosinate ammonium for Basta selection. Right image is a representative image after 14 d, where seedlings of the background line placed in the centre are dead and two investigated lines show a distribution of dead and survived seedlings.

2.6.2 T₂ seeds: Segregation pattern

For the assumption of one T-DNA insertion event, the T₂ generation should segregate according to Mendel in a 1:2:1 pattern (Col-0/px-ck: hemizygous: homozygous). In order to select lines with only one insertion event, the segregation pattern of T₂ plants were investigated on plates with 1/2 MS medium with 10 µg/mL glufosinate ammonium (Fluka, 45520-100MG) as plant selection marker (plate design see figure 7). After the plates were sealed with Parafilm and stratified for at least 2 d in the dark at 4°C, the plates were transferred to long day growth conditions (16 h 75 – 100 µmol photons m⁻² s⁻¹ at 22°C, 8 h darkness at 18°C) in a horizontal position. After 10 – 14 d segregation pattern could be detect and verified. Survivors of T₂ generation were transferred to Jiffies in pots for phenotyping experiments or seed propagation.

2.6.3 T₃ seeds: Verification of homozygous plants

Since homozygous and heterozygous T₂ plants for the sensor construct cannot be distinguished by their fluorescence or resistance, the propagation of T₃ plants is obligatory to identify homozygous T₂ plants. T₃ seeds were either transferred directly to soil and sprayed with Basta solution as described in section 1.2.5.1 or were selected on plates (see section 1.2.5.2). Seeds of heterozygous T₂ plants should show a segregation pattern of 3:1 survivor to dead seedlings, whereas seed of homozygous T₂ plants do not show a segregation, thus all T₃ seedlings survive the Basta selection. Only seeds of homozygous T₂ plants were used for phenotyping experiments.

Table 8: Segregation pattern of all tested independent Arabidopsis lines in T₂ generation on plates with Basta selection.

For one T-DNA insertion event in the second generation (T₂) a segregation pattern of 1:3 is expected, which was used as reference for the Chi-square value (χ^2 -value). The segregation pattern is mathematically defined as survivor divided by total amount of seedlings. All lines with a p-value ≤ 0.05 were defined as significant different (sig. dif.) to the expected. As degree of freedom DF = 1 was used, since two different phenotypic observations (survivor, dead) could be quantified.

Independent Ara- bidopsis line	Survivor	Dead	Segregation pattern [%]	χ^2 -value	Sig. dif.
Tether lines:					
Col-0 24#5 #11	37	11	77.08	0.12	no
Col-0 24#5 #16	39	10	79.59	0.64	no
Col-0 24#5 #31	38	10	79.17	0.51	no
Col-0 24#5 #47	34	14	70.83	0.40	no
Col-0 24#5 #48	44	4	91.67	17.45	yes
px-ck 24#5 #12	44	1	97.78	107.45	yes
px-ck 24#5 #31	32	14	69.57	0.64	no
px-ck 24#5 #38	42	5	89.36	10.20	yes
px-ck 24#5 #39	40	10	80.00	0.78	no
px-ck 24#5 #40	35	14	71.43	0.31	no
FLIM lines:					
Col-0 20#1 #20	43	6	87.76	7.42	yes
Col-0 20#1 #26	34	15	69.39	0.73	no
Col-0 20#1 #34	48	0	100.00	3.00	no
Col-0 20#1 #41	37	12	75.51	0.01	no
Col-0 20#1 #48	36	11	76.60	0.07	no
px-ck 20#1 #11	4	44	8.33	279.27	yes
px-ck 20#1 #25	34	11	75.56	0.01	no
px-ck 20#1 #29	37	11	77.08	0.12	no
Col-0 84#2 #9	65	6	91,55	10.37	yes
Col-0 84#2 #12	49	21	70.00	0.93	no
Col-0 84#2 #15	56	16	77.78	0.30	no
Col-0 84#2 #16	48	23	67.61	2.07	no
Col-0 84#2 #30	61	11	84.72	3.63	yes
px-ck 84#2 #5	57	17	77.03	0.16	no
px-ck 84#2 #4	69	2	97.18	18.63	yes
px-ck 84#2 #35	56	18	75.68	0.02	no
Col-0 48#1 #20	50	23	68.49	1.65	no
px-ck 48#1 #21	57	15	79.17	0.67	no
px-ck 48#1 #22	45	20	69.23	1.15	no
px-ck 48#1 #23	66	5	92.96	12.21	yes
px-ck 48#1 #24	53	20	72.60	0.22	no

II. METHODS

Table 9: Segregation pattern of independent Arabidopsis lines in T₃ generation on Basta plates.

Independent Arabidopsis line	Survivor	Dead	Segregation pattern [%]
Col-0 24#5 #11A	31	8	79.49
Col-0 24#5 #11B	32	10	76.19
Col-0 24#5 #11C	28	0	100.00
Col-0 24#5 #11D	17	7	70.83
Col-0 24#5 #11E	22	7	75.86
Col-0 24#5 #11F	28	0	100.00
Col-0 24#5 #11G	22	6	78.57
Col-0 24#5 #11H	26	0	100.00
Col-0 24#5 #11I	28	0	100.00
Col-0 24#5 #11J	25	3	89.29
Col-0 24#5 #16A	22	4	84.62
Col-0 24#5 #16B	19	4	82.61
Col-0 24#5 #16C	32	0	100.00
Col-0 24#5 #16D	22	6	78.57
Col-0 24#5 #16E	23	4	85.19
Col-0 24#5 #16F	24	4	85.71
Col-0 24#5 #16G	20	8	71.43
Col-0 24#5 #16H	18	9	66.67
Col-0 24#5 #16I	28	0	100.00
Col-0 24#5 #16K	28	0	100.00
px-ck 24#5 #12A	28	0	100.00
px-ck 24#5 #12B	28	0	100.00
px-ck 24#5 #12C	30	1	96.77
px-ck 24#5 #12D	18	9	66.67
px-ck 24#5 #12E	17	10	62.96
px-ck 24#5 #12F	25	2	92.59
px-ck 24#5 #12G	27	0	100.00
px-ck 24#5 #12H	31	0	100.00
px-ck 24#5 #12I	29	0	100.00
px-ck 24#5 #12J	27	2	93.10
px-ck 24#5 #31/29A	21	7	75.00
px-ck 24#5 #31/29B	24	5	82.76
px-ck 24#5 #31/29C	23	4	85.19
px-ck 24#5 #31/29D	21	8	72.41
px-ck 24#5 #31/29E	21	6	77.78

(continued)

Table 9: (continued)

Independent Arabidopsis line	Survivor	Dead	Segregation pattern [%]
px-ck 24#5 #31/29F	30	0	100.00
px-ck 24#5 #31/29G	28	0	100.00
px-ck 24#5 #31/29H	24	5	82.76
px-ck 24#5 #31/29I	25	6	80.65
px-ck 24#5 #31/29J	21	6	77.78

2.7 Seed germination efficiency

Synchronised Arabidopsis seeds were harvested from plants, which were grown under standard conditions and surface sterilised as described in section 2.3. Seeds were transferred on Petri dishes containing 25 mL of 1/2 MS media (see section 1.2.2) with and without sucrose. In order to control plate effects, seeds of different mutant lines were grown on the same Petri dish as the control lines (Col-0, px-ck).

Germination efficiency was determined daily at the same time point for 5 d by usage of a stereomicroscope to investigate the appearance of radicle penetrating endosperm and testa (see thesis [189], figure 22).

2.8 Seedling phenotyping on agar plates - root growth

Arabidopsis seeds were sterilised and stratified as described in section 2.3. Seedlings were vertically grown on standard medium for 5 d. To avoid plate effects, 6 seedlings from the genetic background plant and corresponding mutant line were placed side-by-side on one plate. Plates were sealed with Micropore tape and photographically documented at indicated time points. Increase of primary root was quantified by using Fiji (www.fiji.sc; [190, 191]).

2.9 Heat stress on agar plates

Arabidopsis seedlings were grown as described in section 2.3 and 2.8. To avoid plate effects, 6 seedlings from the genetic background plant and corresponding mutant line were placed side-by-side on one plate. The primary root length of 7-day-old seedlings were marked prior to the incubation of the plate for 25 min at 43 °C in a waterbath. The agar site of the plate was facing towards the water. Control plates were incubated for 25 min in the dark at RT. 4 d after the heat stress treatment the root length was recorded by a photo and quantified by the software RootNav [185].

2.10 Phenotyping on soil under normal light

Arabidopsis plants were grown on standard medium in plates for up to 7 d or in round pots and single plants were transferred carefully to squared pots. The plants were maintained at standard conditions (16 h 100–120 $\mu\text{mol photons m}^{-2} \text{s}^{-1}$ at 22°C, 8 h darkness at 18°C, humidity 50%). For the analysis of the leaf rosette area photos from a top position were taken and analysed using a custom Leaf Lab tool (Version 1.4.1) as described in Wagner *et al.* [192]. To analyse the shift from vegetative to generative growth the time point, where the primary inflorescence is 1 cm, was documented. The height of the primary inflorescence was measured with a ruler.

2.11 Phenotyping on soil under high light

Arabidopsis plants were grown as described in methods section 2.10. Plants were maintained at standard conditions (16 h 100–120 $\mu\text{mol photons m}^{-2} \text{s}^{-1}$ at 22°C, 8 h darkness at 18°C, humidity 50%) prior to the experiments. 2 week or 5 week-old plants were transferred to high light conditions (16 h 350 $\mu\text{mol photons m}^{-2} \text{s}^{-1}$ at 22°C, 8 h darkness at 18°C). In the stress experiments the HL treatment was applied for 4 d followed by 4 d of recovery (standard growth conditions). The photosynthetic yield (methods section 2.14), the anthocyanin content (methods section 2.13) and fresh weight was investigated.

2.12 Dark-induced leaf senescence

Dark induced leaf senescence assays were performed as described in F. Li *et al.* [193]. The third and the fourth rosette leaves of 4 week-old Arabidopsis plants were individually covered with aluminium foil for 5 d (figure 8). The degree of greenness is used as an indicator of the progression of senescence. This was quantified based on the pixel-wise division of green by red color intensity obtained from RGB-encoded images with Fiji (www.fiji.sc; [190, 191].)

2.13 Anthocyanin extraction

For anthocyanin analysis, the extraction and quantification method was adapted from Richter *et al.*, Lohmann *et al.*, Lotkowska *et al.* [194–196]. 30 mg fresh leaf material of 6 week-old plants was harvested in 2 mL safety lock tubes with one small metal ball and one glass ball. For 3 week-old plants, the whole rosettes of the seedlings were harvested (~4.5–15.0 mg). Samples were immediately frozen in liquid nitrogen and temporarily stored at -80°C for at least 24 h. Afterwards, frozen samples were disrupted by using a TissueLyser II (Qiagen) at 30 Hz for 1 min 30 s, whereby the adapters were pre-cooled to -80°C. The frozen powder was



Figure 8: Leaves covered individually in aluminium foil for senescence assay.

resuspended vigorously in 1 mL or 350 μL extraction buffer (18% [v/v] 1-propanol, 81% [v/v] H_2O_{dd} , 1% [v/v] HCl 37%) for 6 week-old or 3 week-old samples, respectively. Samples were heated at 98°C for 3 min, incubated at RT in the dark for 2 h and centrifuged at 13200 g at RT for 20 min. Absorbance was detected at 535 nm and 650 nm with a Nanodrop spectrophotometer (Thermo Scientific). The relative anthocyanin content was calculated as following (after [194]):

$$\frac{A_{537} - 0.25 * A_{650}}{FW[g]} \quad (1)$$

2.14 Pulse Amplitude Modulation (PAM) fluorometry

For the PAM experiments stable Arabidopsis plants were grown under standard growth conditions or treated with HL (see methods section 2.4 and 2.14). Plants were dark adapted for at least 45 min prior measuring the photosynthetic activity by using a JUNIOR-PAM (Heinz Walz GmbH) [197]. For the experiment, a predefined program “induction curve + recovery” (IC + Recov) was performed under high light (HL) conditions with an actinic light intensity of $250 \mu\text{mol m}^{-2} \text{s}^{-1}$ (Act. Int. 6) for 200 s followed by a recovery phase of 45 min 50 s in the dark. The chosen parameters were the photochemical quantum yield of photosystem II (PSII) (Y(II)), non-photochemical fluorescence quenching (NPQ) and the maximum quantum yield of photochemistry of PSII (F_V/F_M).

2.15 Oxygen consumption of leaf tissue

Respiration of leaf discs was analysed using a Clark-type oxygen electrode (Oxytherm, Hansatech) with an adapted method from Kühn *et al.* 2015 [198]. The electrode was prepared and calibrated according to manufacturer’s instruction. Arabidopsis plants were dark adapted for at least 30 min at RT. Three leaf discs were cut out (70 mm diameter) of different areas and

leaves per plant ([199]) and directly placed in the darkened Oxytherm chamber containing 1 mL H_2O_{dd} . Oxygen consumption was measured in the dark at 20°C for at least 30 min. Afterwards the leaf discs were carefully wiped dry, and the fresh weight was determined. Oxygen consumption was calculated in $mmol O_2 \text{ min}^{-1} \text{ g FW}^{-1}$.

2.16 Pollen staining

Pollen staining was performed similar to J.-M. Ugalde *et al.* [200] and Peterson *et al.* [201]. Pollen grains of 8 week-old plants were coloured with premixed ALEXANDER's Staining Solution (MORPHISTO GmbH) in a dilution of 1:20 with water, which marks the cytoplasm in magenta-red with acid fuchsine and the pollen cell wall in green with Malachite Green. Alive pollen grains look as magenta-red circles with a green envelope, whereas dead pollen grains lost their cytoplasm and look smaller and only green.

2.17 Silique imaging

Siliques of 8 week-old Arabidopsis plants were transferred to microscope slides. The valves were carefully dissected along the replum on one side and stick to the object glass. Images were taken with a Leica M165 FC stereomicroscope stereomicroscope.

2.18 Vacuum infiltration and MitoTracker staining

Vacuum infiltration was performed for the application of pharmacological and control treatments in *N. tabacum* and Arabidopsis leaves. Therefore, leaves or leaf slices of 1 - 2 cm were submerged into a 2 mL Eppendorf tube containing the respective solution. Tubes were transferred into Vacuum concentrator Savant[®] DNA 120 (Thermo Scientific, www.thermofisher.com) and leaves were vacuum-infiltrated for 3 min. If the leaves /leaf slices were not fully infiltrated, the vacuum infiltration was repeated. For staining mitochondria with MitoTracker orange or Mitotracker Green FM (500 nM), the leaves were dark incubated for 15 - 20 min prior imaging.

3 Microbiological methods

3.1 Bacterial strains

All *Escherichia coli* and *Agrobacterium tumefaciens* strains, which are used in this work, are listed in table 10.

Table 10: Bacteria strains. *E. coli* strains are chemical competent and *A. tumefaciens* strains electro-competent.

Bacterial strain	Genotype
<i>E. coli</i> DB3.1	F ⁻ <i>gyrA462 endA1</i> Δ (<i>sr1-recA</i>) <i>mcrB mrr hsdS20</i> (r _B ⁻ m _B ⁻) <i>ara-14 galK2 lacY1 proA2 rpsL20</i> (Sm ^R) <i>xyl5</i> Δ <i>leu mtl1</i> λ ⁻ (Invitrogen)
<i>E. coli</i> DH5 α	F ⁻ Φ 80 <i>lacZ</i> Δ M15 Δ (<i>lacZYA-argF</i>) U169 <i>recA1 endA1</i> <i>hsdR17</i> (r _K ⁻ , m _K ⁺) <i>phoA supE44 thi-1 gyrA96 relA1</i> λ ⁻ (Stratagene)
<i>E. coli</i> TOP10	F ⁻ <i>mcrA</i> Δ (<i>mrr-hsdRMS-mcrBC</i>) Φ 80 <i>lacZ</i> Δ M15 Δ <i>lacX74</i> <i>recA1 araD139</i> Δ (<i>ara-leu</i>)7697 <i>galU galK rpsL</i> (Str ^R) <i>endA1</i> <i>nupG</i> (Invitrogen)
<i>A. tumefaciens</i> AGL-1	AGL-0 (C58 pTiBo542) <i>recA::bla</i> , T-region deleted Mop(+) Cb(R). AGL-0 background based on EHA101 with T-region deleted (Δ <i>aph</i>) (Rif ^R , Amp ^R) [202]
<i>A. tumefaciens</i> GV3101	C58,Ti pMP90 (pTiC58DT-DNA), Nopaline (Rif ^R , Gent ^R) (Lifeasible, www.lifeasible.com)

3.2 Bacterial growth

Bacteria strains were cultivated in liquid LB medium (Lysogeny broth: 1% (w/v) tryptone, 0.5% (w/v) yeast extract, 1% (w/v) NaCl, pH 7 with NaOH) [203] at 120 – 160 rpm and 28°C for *A. tumefaciens* and 37°C for *E. coli*. For growing them on plates, 2% (w/v) agar was added to LB medium before autoclaving. Corresponding sterile-filtered antibiotics (see table 11) were added after autoclaving in appropriate concentrations. For blue-white selection additional sterile-filtered X-Gal (5-bromo-4-chloro-3-indolyl- β -D-galactopyranoside) and IPTG (isopropyl- β -D-thiogalactoside) were added in appropriate amount.

For long-time storage, glycerol stocks were generated by mixing 400 mL of an overnight culture and 600 mL 80% sterilised glycerol, freezing in liquid nitrogen and storing at -80°C.

3.3 Transformation of electro-competent *A. tumefaciens*

All used *A. tumefaciens* strains are electro-competent and were transformed by using a Micropulser electroporator (Bio-Rad Laboratories) according to manufacturer's protocol. 40 μ L of cells were thawed on ice and 1-20 ng plasmid were added. After 5 min incubation on ice, the cell-plasmid mix were transferred in a cold electroporation cuvette. Immediately after a pulse of 2.500 V for 5 ms 500 μ L of 28°C preheated LB medium was added to the bacteria solution in the cuvette and transferred back to an Eppendorf tube. The bacteria were

II. METHODS

incubated for 2 – 3 h at 28°C before plating them on agar plates with appropriate antibiotics.

Table 11: Stock and working concentrations of antibiotics and additional selection markers.

Antibiotic/selection marker	Abbr.	Stock concentration [mg/mL] / *[mM]	Working concentration [mg/mL] / *[mM]
Ampicillin	amp	100	100
Gentamycin	gent	50	50
Kanamycin	kan	50	50
Rifampicin	rif	50	50
Spectinomycin	spec	100	100
5-bromo-4-chloro-3-indolyl- β - D-galactopyranoside	X-Gal	20	40
isopropyl- β -D-thiogalactoside	IPTG	*100	*0.1

3.4 Transformation of chemical competent *E. coli*

All used *E. coli* strains were chemically competent and transformed via heat-shock.

For generating chemical competent cells, an *E. coli* culture was grown to an OD₆₀₀ of 0.4. 400 mL of the cell culture were centrifuged for 10 min at 2500 g at 4°C, the supernatant was discarded and the pellet resuspended on ice in 50 mL 50 mM MgCl₂. Cells were pelleted at 2800 g at 4°C and resuspended on ice in 40 mL 100 mM CaCl₂. After an incubation of 20 min on ice, cells were pelleted at 2800 g at 4°C and resuspended in 1 mL 85 mM CaCl₂ containing 15% (v/v) glycerol. Aliquots of 100 μ L cells were frozen in liquid nitrogen.

100 μ L of *E. coli* cells were thawed on ice for about 10 min and 1-20 ng plasmid or cloning reaction were added. After an incubation of 30 min on ice cells were heat-shocked at 42°C for 45 s and directly transferred to ice for 2 min. 300 μ L of preheated LB were added to the cells and the mix were incubated at 37°C under shaking conditions. After 1 h cells were plated on LB plates with respective antibiotic selection. For blue-white selection X-Gal and IPTG (see table 11) were added in the plate medium.

3.5 Plasmid isolation from *E. coli*

Plasmid DNA was isolated with the NucleoSpin[®] Plasmid kit (Macherey-Nagel, www.mn-net.com) according to the manufacturer's protocol. For the elution deionised water was used instead of the elution buffer.

4 Molecular biological techniques

4.1 DNA extraction from Arabidopsis plants

DNA was extracted with a short version of a protocol described in Edwards *et al.* 1991 [204] and Hu and Lagarias 2020 [205]. Rosette leaves from 4-8 week-old plants were transferred to 1.5 mL tubes, 200 μ L Edwards buffer (200 mM Tris-HCl pH 7.5, 250 mM NaCl, 25 mM EDTA and 0.5% (w/v) SDS) and leaves were disrupted manually by usage of a small plastic pestle. Afterwards 200 μ L isopropanol was added and gently mixed by inverting the samples followed by centrifugation at 15000g for 5 min. The supernatant was discarded and the pellet air-dried. The pellet was dissolved in 100 μ L deionised water and centrifuged at 15000 g for 1 min. From the supernatant 1-1.5 μ L was used for a PCR with a total volume of 20 μ L.

4.2 RNA extraction from Arabidopsis

RNA was isolated from rosette leaves of 3-5 week-old plants. After collection, leaves were frozen in liquid nitrogen and disrupted in a TissueLyser II (Qiagen) at 30 Hz twice for 10 s, whereby the adapters need to be pre-chilled to -86°C. RNA was isolated using the NucleSpin RNA isolation kit (Macherey-Nagel) according to manufacturer's instruction. Concentration of isolated RNA was quantified with a Nanodrop spectrophotometer and quality was verified on an agarose gel.

4.3 Complementary DNA synthesis

For reverse transcription of isolated mRNA to complementary DNA (cDNA), the RevertAid First Strand cDNA Synthesis Kit (Thermo Scientific) was used according to manufacturer's instructions. 1 μ L RNA and 0.5 μ L of Oligo (dT)18 and Random Hexamer primer each were used for the first strand cDNA synthesis. According to the manufacturer's protocol, the cDNA (20 μ L) was diluted to 25 ng/ μ L and used as template for cloning PCRs.

4.4 Oligonucleotides

Lyophilised salt-free primers were ordered from Eurofins Genomics (www.eurofinsgenomics.eu). After resuspension in H₂O to a stock concentration of 100 μ M, primers were stored at -20°C. For polymerase chain reactions (PCR) and sequencing experiments, stocks were 1:10 diluted to a working concentration of 10 μ M.

II. METHODS

Table 12: Primers for Gateway cloning. Bold uppercase letters: **GGGG + attB1/attB2/attB3/attB4-site**, lowercase letters: Glycin-alanin linker, uppercase letters: Gene specific sequence. No. corresponds to primer stock number.

No.	Primer	Sequence
4505	B3_L_toc34_fw	GGGGACAAC TTTGTATAATAA AGTT GGAggtggaggtggagctGCAGCTTTGC AAACGCTTC
4506	B2_toc34_rev	GGGGACCACT TTTGTACAAGAA AGC TGGGT TCAAGACCTTCGACTTGCTA AACC
4507	UTR_toc34_fw	TAAGGATTTGTGTCCATGGC
4508	UTR_toc34_rev	CTCGTGTCCACA ACTCAAGA
4509	B1_pex10_fw	GGGGACAAG TTTGTACAAAA AGC AGGCT TAAATGAGGCTTAATGGGGA T
4510	B4_L_pex10_rev	GGGGACAAC TTTGTATAGAAA AGTT GGGT GagctccacctccAAAATCAGAAT GATACAAACAA
4511	UTR_pex10_fw	AAAGAAACGATGAGGCTTAAT
4512	UTR_pex10_rev	CCATTGTGCCTAAAA ATCA
4522	B1_chupN(1-25)_fw	GGGGACAAG TTTGTACAAAA AGC AGGCT TAAATGTTTGTCCGGATAGG GTT
4523	B4_chup1N(1-25)_L_rev	GGGGACAAC TTTGTATAGAAA AGTT GGGT GagctccacctccGGGTTAACGT TGAGCCG
4526	B3_L_TOC34C_fw	GGGGACAAC TTTGTATAATAA AGTT GGAggtggaggtggagctTGGATTCCCAA TCTGTTCAA
4527	B2_TOC34C_rev	GGGGACCACT TTTGTACAAGAA AGC TGGGT TCAAGACCTTCGACTTGCTA
4546	B3_Chup1N_fw	GGGGACAAC TTTGTATAATAA AGTT GGAATGTTTGTCCGGATAGGGTT
4547	B2_Chup1N_L_rev	GGGGACCACT TTTGTACAAGAA AGC TGGGT GagctccacctccGGGTTAACG TTGAGCCG
4548	B1_CFP_fw	GGGGACAAG TTTGTACAAAA AGC AGGCT TAAatggtgagcaagggcgag

(continued)

Table 12: (continued)

No.	Primer	Sequence
4549	B2_CFP-SKL_rev	GGGGACCACTTTGTACAAGAAAGC TGGGTTCAAAGCTTAGA cttgtacagct cgtccatgcc
4562	B3_OEP7N_fw	GGGGACAACCTTTGTATAATAAAGTT GGAATGGGAAAACTTCGGGA
4563	B2_OEP7N_L_rev	GGGGACCACTTTGTACAAGAAAGC TGGGT GagctccacctccGTCTTTGGTT GGGTCAGATT
4600	B3_L_AtTOM5_fw_noATG	GGGGACAACCTTTGTATAATAAAGTT GG AggtggaggtggagctGTGAACAACG TTGTCTCT
4601	B2_AtTOM5_rev	GGGGACCACTTTGTACAAGAAAGC TGGGTTCAA ACTCCCATGAGATC
4602	attB3_AtPECT1N_fw	GGGGACAACCTTTGTATAATAAAGTT GGAATGGTTTGGGAGAAAGAGAA
4603	attB2_L_AtPECT1N	GGGGACCACTTTGTACAAGAAAGC TGGGT GagctccacctccTCGTTTTCTC AAAATGCG
4604	B3_L_MIRO2C_fw	GGGGACAACCTTTGTATAATAAAGTT GG AggtggaggtggagctGAGACAGAGT CAGGAAGAAG
4605	B2_MIRO2C_rev	GGGGACCACTTTGTACAAGAAAGC TGGGTTCAAGCATTCTTCCTTGC
4606	UTR-PECT1N_fw	TGTTTCGTAAGCAAAAATG
4607	UTR-PECT1N_rev	AAGCATATAGCTCTATCAGTC
4608	UTR_MIRO2C_fw	AATCTCTCCGATGATGCTCG
4609	UTR_MIRP2C_rev	GGCAAAAAGCTTCAAGCATT
4610	UTR_AtTOM5_fw	TCAGCAGCAAGATGGTGAAC
4611	UTR_AtTOM5_rev	TTCTTCTTCTCAAACCTCCCA
4692	4692_B3_L_TOM20-2_F	GGGGACAACCTTTGTATAATAAAGTT GG AggtggaggtggagctATGGAGTTCT CTACCGCCG
4693	4693_B2_L_Pect1(FL)(noStop)_rev	GGGGACCACTTTGTACAAGAAAGC TGGGT GagctccacctccGTCTCCGGA CACAAACGAC

(continued)

II. METHODS

Table 12: (continued)

No.	Primer	Sequence
4694	4694_!B3_L_Pect1N	GGGACAACCTTTGTATAATAAAGTT GGAggtggaggtggagctATGGTTTGGG AGAAAGAGAA
4695	4695_!B2_Pect1N(Stop)_rev	GGGACCACTTTGTACAAGAAAGC TGGGTT CATCGTTTTTCTCAAATGC G
4696	4696_B3_L_Miro1C_fw	GGGACAACCTTTGTATAATAAAGTT GGAggtggaggtggagctGAGACCGAAG CAGGCAA
4697	4697_B2_Miro1(Stop)_rev	GGGACCACTTTGTACAAGAAAGC TGGGTT CAGGCAGACGAGCTCTT
4698	4698_B3_L_Miro1(FL)_fw	GGGACAACCTTTGTATAATAAAGTT GGAggtggaggtggagctATGGCGAGAT ACGCTGCT
4699	4699_B3_L_Miro2(FL)_fw	GGGACAACCTTTGTATAATAAAGTT GGAggtggaggtggagctATGATGCTCG GTGAAAAG
4700	4700_B3_L_OMP85_fw	GGGACAACCTTTGTATAATAAAGTT GGAggtggaggtggagctATGGCGAATC CGACGGAG
4701	4701_B2_OMP85(Stop)_rev	GGGACCACTTTGTACAAGAAAGC TGGGTT CAGGACGAAGCAGAGAAT GTC
4702	4702_B3_OMP85(Start)_fw	GGGACAACCTTTGTATAATAAAGTT GATGGCGAATCCGACGGAG
4703	4703_B2_OMP85(noStop)_rev	GGGACCACTTTGTACAAGAAAGC TGGGTT GagctccacctccGGACGAAGC AGAGAATGTCAAG
4704	4704_B3_L_RRG_fw	GGGACAACCTTTGTATAATAAAGTT GGAggtggaggtggagctATGGGTAAAT GGAGAGCAG
4705	4705_B2_RRG(Stop)_rev	GGGACCACTTTGTACAAGAAAGC TGGGTT CAGAGTGAAGCTCCTGC
4706	4706_B3_RRG(Start)_fw	GGGACAACCTTTGTATAATAAAGTT GATGGGTAAATGGAGAGCAGTAG

(continued)

Table 12: (continued)

No.	Primer	Sequence
4707	4707_B2_RRG(noStop)_rev	GGGGACCACTTTGTACAAGAAAGC TGGGTGagctccacctccGAGTGAAGC TCCTGCGGA
4708	4708_B2_L_OEP7(FL)(noStop)_rev	GGGGACCACTTTGTACAAGAAAGC TGGGTGagctccacctccCAAACCCTCT TTGGATGTG
4709	4709_B1_pex11d_fw	GGGGACAAGTTTGTACAAAAAAGC AGGCTTAATGGGGACGACGTTAGA TG
4710	B4_Pex11d(noStop)_L_rev	GGGGACAACCTTTGTATAGAAAAGTT GGGTGagctccacctccGGGTGTTTTG ATCTTGGG
4711	4711_B1_pex14_fw	GGGGACAAGTTTGTACAAAAAAGC AGGCTTAatggcaactcatcagcaa
4712	4712_B4_Pex14(noStop)_L_rev	GGGGACAACCTTTGTATAGAAAAGTT GGGTGagctccacctccgttcccttctggctg at
4713	4713_B1_L_Pex14_fw	GGGGACAAGTTTGTACAAAAAAGC AGGCTTAagtgagggtggagctATGGCAA CTCATCAGCAA
4714	4714_B4_Pex14_rev	GGGGACAACCTTTGTATAGAAAAGTT GGGTTTAGTTCCCTTCCTGGCT
4747	B1_cYFP_fw	GGGGACAAGTTTGTACAAAAAAGC AGGCTTAatggacaagcagaagaacgg
4748	B4_cYFP_rev	GGGGACAACCTTTGTATAGAAAAGTT GGGTGctactgtacagctcgtcca
4749	Syt5.2_seq_500_fw	ATTTGTGATAAGCTATGGAC
4750	Syt5.2_seq_1037_fw	TTTGTTCACCTCCAAAGAT
4842	B1_35sT_F	GGGGACAAGTTTGTACAAAAAAGC AGGCTGATGAgcaaaaatcaccagtctctc tc
4843	B4_35sT_rev	GGGGACAACCTTTGTATAGAAAAGTT GGGTtactggatttggtttagga

(continued)

II. METHODS

Table 12: (continued)

No.	Primer	Sequence
4844	B3_L_OEP7_fw	GGGACAACCTTTGTATAATAAAGTT GGAggtggaggtggagctATGGGAAAAA CTTCGGGA
4845	B2_OEP7_Stop_rev	GGGACCACCTTTGTACAAGAAAGC TGGGTT CACAAACCCTCTTTGGATG TG
4917	attB1_L_SYT1C_fw	GGGACAAGTTTGTACAAAAAAGC AGGCTT AggtggaggtggagctCTTGTAG TTCCAATCCTTGACC
4918	attB4_SYT1C(Stop_rev	GGGACAACCTTTGTATAGAAAAGTT GGGT GTCAAGAGGCAGTTCGCCAC
4919	attB1_Start_SYT1C_fw	GGGACAAGTTTGTACAAAAAAGC AGGCTT AATGCTTGTAGTTCCAATC CTTGACC
4920	attB4_SYT1C(noStop)_rev	GGGACAACCTTTGTATAGAAAAGTT GGGT GagctccacctccAGAGGCAGTT CGCCACTC
4921	attB1_L_NET3C_fw	GGGACAAGTTTGTACAAAAAAGC AGGCTT AggtggaggtggagctGTTAGAG AAGAGGAGAAATCGAGA
4922	attB4_NET3C_Stop_rev	GGGACAACCTTTGTATAGAAAAGTT GGGT GCTAAAGGACCTTGTTGCCA TC
4923	attB4_NET3C_Stop_rev	GGGACAACCTTTGTATAGAAAAGTT GGGT GCTAAAGGACCGCGGCCA T
4924	B3_L_VAP27_fw	GGGACAACCTTTGTATAATAAAGTT GGAggtggaggtggagctAGTAACATCGA TCTGATTGG
4925	B2_VAP27_rev	GGGACCACCTTTGTACAAGAAAGC TGGGTTT ATGTCCTCTTCATAATGT ATC
4983	attB2_L_SYT1N_rev	GGGACCACCTTTGTACAAGAAAGC TGGGT GagctccacctccGGTCTTAGG CCAGAGATACAT

(continued)

Table 12: (continued)

No.	Primer	Sequence
4984	attB1_SYT1_fw	GGGGACAAGTTTGTACAAAAAAGC AGGCTTAATGGGCTTTTTTCAGTACG AT
4985	attB4_L_SYT1N_rev	GGGGACAAC TTTGTATAGAAAAGTT GGGTGagctccacctccGGTCTTAGGC CAGAGATACAT
4986	attB3_L_SYT1C_fw	GGGGACAAC TTTGTATAATAAAGTT GGAggtggaggtggagctCTTGTAGTTCC AATCCTTGACC
4987	attB2_SYT1C(Stop)_rev	GGGGACCACTTTGTACAAGAAAGC TGGGTTCAAGAGGCAGTTCGCCAC

Table 13: Primers for Greengate cloning. **GGTCTC**: Eco31I (BsaI) endonuclease recognition site, **NNNN**: module specific overhang for Greengate cloning, lowercase: module specific sequence. No. corresponds to primer stock number.

No.	Primer	Sequence
4735	C_cYFP_R1R4_BiFC_fw	AACAGGTCTCAGGCTatggacaagcaga agaacgg
4736	D_35sT_rev	AACAGGTCTCACTGAtcactggattttggt ttag
4737	C_R1_BiFC_FRET_fw	AACAAGGCTgaacaagttgtacaaaaaa
4738	C_tagRFP_R1R4_FRET_fw	AACAAGGCTatggtgagtaaaggtgaaga
4739	E_R3_BiFC_FRET_fw	AACAGGTCTCACTGctggcaactttgtag aataaa
4740	F_35sT_rev	AACAGGTCTCATAGTtactggattttggt ttag
4741	E_nYFP_R3R2_fw	AACAGGTCTCACTGCatggtgagcaagg gcgag

Table 14: Primers for Q5 mutagenesis *ccdB* gene. Lowercase letter reflect Q5 mutagenesis site from g to a in order to remove Eco31I (BsaI) recognition site in *ccdB* gene. No. corresponds to primer stock number.

No.	Primer	Sequence
4742	Q5SDM_R1R4_ccdB_ohne_BsaI_fw	CCAGTGTGCCaGTCTCCGTTA
4743	Q5SDM_R1R4_ccdB_ohne_BsaI_rev	CCATATCGGTGGTCATCATG

II. METHODS

Table 15: Primers for DNA sequencing, colony PCR or genotyping only. No. corresponds to primer stock number.

No.	Primer	Sequence
335	M13 u	GTAAAACGACGGCCAGT
689	pDONR201-Seq-For	TCGCGTTAACGCTAGCATGGATCTC
690	pDONR201-Seq-Rev	GTAACATCAGAGATTTTGAGACAC
1490	35S_fwd	GCAAGTGGATTGATGTGATATC
4016	nYFP_F	actacaacagccacaacg
4017	cYFP_R	cttgatgccgttcttctg
4036	tagRFP_seq_R	ggtgattattgacagttccctcc
4627	BiFC_CC_nYFP_rev	atgaacttcagggtcagc
4628	FRET_CC_mVenus_rev	tgaactgtggccgttta
4629	nYFP_rev	cgttgtggctgtttagt
4804	GK-pGGC-incl-sp6-T7-fw	ggaattgtgagcggataaca
4805	GK-pGGC-incl-sp6-T7-rv	CACGACGTTGTAAAACGACG
4810	pEntry_GG_seq_rev_3533	AAATACCGCACAGATGCGTAAG
4811	pEntry_GG_seq_fw_1927	CCTTTGAGTGAGCTGATACCG
4812	pEntry_GG_seq_fw_1998	GAAGAGCGCCCAATACGCAAAC
4839	35sT_2in1_rev	cactggattttggttttagga
4840	pMA_M13_fw	TTGTAAAACGACGGCCAGT
4841	pMA_M13_rev	GGAAACAGCTATGACCATGT
4852	BastaR_seq_rev	ttgacgatggtgcagacc
4853	GR-LhG4_seq_fw	acggtccgaacctcataaca
4854	CmR_seq1_rev	tttaaaaaggccgtaatatcca
4855	CmR_seq2_rev	tccagtgattttttctccat
4856	cYFP_seq_fw	cccgacaaccactacctgag
4857	pGGInt_ALF_seq_fw	ggcctttttgcgtttctaca
4858	pGGInt_ALF_seq_rev	acgctaccttgccatgttt
4859	GGsaGFP_seq_fw	aggtggaagtATGCGTGACC
4860	tagRFP_seq_fw	attgcgacttacctccaagc
4886	GGsaGFP_seq_rev	GGTCACGCATacttccacct
4887	CmR_seq1_fw	tggatattacggcctttttaa
4934	GFP1-10_seq_fw	tctcggacacaaactggagt
4935	GFP1-10_seq_rev	agcacgcgtcttgatttcc
4936	GFP11_seq_rev	TCCCAGCAGCATTACGTA

4.5 Polymerase chain reaction

For PCR two different protocols were conducted. For cloning, the proof reading Phusion High Fidelity DNA polymerase (New England Biolabs) were used in a 20 μ L standard reaction containing 4 μ L 5x Phusion GC buffer, 0.4 μ L 10 mM dNTPs, 1 μ L forward primer (10 pM), 1 μ L reverse primer (10 pM), 1 μ L template (25 ng/ μ L cDNA), 0.2 μ L Phusion high fidelity DNA polymerase and 12.4 μ L H₂O. The thermocycler conditions are described in below (table 16)

Table 16: Phusion PCR thermocycler conditions.

Steps	Temperature [°C]	Time [s]	
Initial Denaturation	98	30	
Denaturation	98	10	x 35
Annealing	60-70	30	
Extension	72	15-30 / kb	
Final Extension	72	600	
Hold	12		

For primers with a template unspecific overhang and an annealing temperature of 72°C a two step PCR protocol was performed (table 17).

Table 17: Two step PCR thermocycler conditions.

Steps	Temperature [°C]	Time [s]	
Initial Denaturation	98	30	
Denaturation	98	10	x 5
Annealing	60-70	30	
Extension	72	15-30 / kb	
Denaturation	98	10	x 5
Annealing + Extension	60-70	15-30 / kb	
Final Extension	72	600	
Hold	12		

For colony or genotyping PCR the Tag DNA polymerase was used in a standard reaction containing 2 μ L 10x ThermoPol buffer, 0.4 μ L 10 mM dNTPs, 0.4 μ L forward primer (10 pM), 0.4 μ L reverse primer (10 pM), 0.1 μ L Taq DNA polymerase, 16.7 μ L deionised water. Either a colony or extracted DNA served as template for the PCR. The thermocycler conditions are described in table 18.

Annealing temperatures of primers were calculated with the NEB Tm Calculator (tmcaltulator.neb.com).

II. METHODS

Table 18: Taq DNA polymerase PCR thermocycler conditions.

Steps	Temperature [°C]	Time [s]	
Initial Denaturation	95	30	
Denaturation	95	30	x 35
Annealing	48-60	30	
Extension	68	30-60 / kb	
Final Extension	68	720	
Hold	12		

4.6 DNA agarose gel electrophoresis and DNA purification

DNA fragments from PCR or enzymatic digest were separated via agarose gel electrophoresis. DNA samples were supplemented with 6x DNA loading buffer (final concentration: 0.05% (w/v) bromophenol blue, 0.05% (w/v) xylene cyanole and 8% (v/v) glycerol) before loading on the agarose gel. The Gel was prepared with TAE (40 mM Tris-Acetate, 1 mM EDTA, pH 8.3), 1-2% (w/v) agarose and 40 µL/L HDGreen Plus (Intas). As base pair length standard, GeneRuler™ DNA Ladder Mix (www.thermoscientificbio.com) was used. Electrophoresis was performed at 80-150 V for 30 min to 1 h 30 min. Gel documentation was done with the gel documentation chamber MF-ChemiBIS 2.0.

DNA purification was done with the NucleoSpin® Gel and PCR clean-up system kit from Macherey-Nagel (www.mn-net.com) according to the manufacturers' protocol.

4.7 Quantification of RNA and DNA concentration

Concentrations of plasmids, genomic DNA, RNA and fragments of PCR or digest reactions were quantified with a Nanodrop spectrophotometer.

4.8 DNA sequencing

DNA sequencing was either performed by Eurofins (www.eurofinsgenomics.eu) or Microsynth (www.microsynth.ch) to verify the sequence of PCR products or the correct assembly of vectors.

4.9 Digestion of DNA with restriction endonucleases

For DNA digestion, FastDigest enzymes from Thermo Fisher Scientific (www.thermofisher.com) were used. Digestion was performed in 15-30 µL final volume using 1-2 U of enzyme per 1 µg DNA. Buffer, temperature and incubation time were applied according to manufacturer's instructions. The digest was either verified on an agarose gel or used for further cloning steps.

4.10 Cloning of the inducible pInd 2in1 vector system using Greengate cloning

The 2in1 pInd vector system was cloned using the Greengate technique. Greengate cloning was performed as described in Lampropoulos *et al.* 2013 [206]. They designed the GreenGate system for generation of plant transformation constructs. It based on the Golden Gate technique and the enzyme BsaI (Eco31I), which is a type IIS enzyme.

For the 2in1 pInd vector system, individual modules were generated as indicated in figure 31 after the protocol of Lampropoulos *et al.* 2013 [206]. Therefore, the nucleotides 5´-AACAGGTCTC-A-NNNN(nn)-3´ were added to the forward primer. GGTCTC is the BsaI recognition site. AACAA is added as a placeholder, since the BsaI does not cut when the restriction site is at the ends of the PCR products. NNNN represents the module specific overhang and (nn) represents needed nucleotides to stay in the reading frame with the adjacent module. To the reverse primer 5´-AACAGGTCTC-A-NNNN-3´ were added, while NNNN represents the reverse complement of the module specific overhang (primer see table 13). Table 19 shows an overview of all individual generated constructs with respective information including the templates and the stock number of the primer. After amplification via PCR and gel purification of the desired fragment, the product and the respective empty pEntry were digested with BsaI. Both digestions were purified, ligated with T4 DNA ligase for 1 h at RT or overnight at 4°C and after heat inactivation transformed in *E. coli* strains. For the constructs containing a *ccdB* expression cassette DB3.1 cells were used, whereas for the other constructs *ccdB* sensitive DH5 α or TOP10 *E. coli* strains were used. Colonies were checked by colony PCR (methods section 4.5). The plasmids of verified colonies were purified (methods section 3.5) and sequenced (methods section 4.8).

Table 19: Individual pEntry modules for Greengate cloning of 2in1 pInd vector system. *¹: pEntry modules were synthesised by Thermo Fisher. *²: Mutagenesis of template was necessary in order to remove unwanted BsaI recognition site in *ccdB* encoding region.

Tagged protein	Empty pEntry	Fwd. primer	Rev. primer	Product size [bp]	Template
I:A-pOP6Cam35Sm-B	*1	*1	*1	432	pSW180a - pOp6 [207]
II:D-pOP6Cam35sM-E	*1	*1	*1	432	pSW180a - pOp6 [207]
IV:C-R1R4-GFP11-Stop-35sTD	*1	*1	*1	1102	[160, 208]
V:E-GFP1-10-R3R2-35sT-F	*1	*1	*1	1604	[160, 208]

(continued)

II. METHODS

Table 19: (continued)

Tagged protein	Empty pEntry	Fwd. primer	Rev. primer	Product size [bp]	Template
VI:E-R3R2-GFP1-10-Stop-35sT-F	*1	*1	*1	1616	[160, 208]
E-R3-lacZ-R2-nYFP-Stop-35sT-F	pGGE000	4739	4740	1403	BiFC CC [160]
E-nYFP-R3-lacZ-R2-35sT-F	pGGE000	4741	4740	1423	BiFC NC [160]
E-R3-lacZ-R2-mVenus-Stop-35sT-F	pGGE000	4739	4740	1603	FRET CC [177]
E-mVenus-R3-lacZ-R2-35sT-F	pGGE000	4741	4740	1704	FRET NC [177]
C-(puffer)-R1-CanR-ccdB-R4-cYFP-Stop-35sT-D	pGGC000	4737	4736	2307	BiFC NC [160] mutagenised *2
C-cYFP-R1-CanR-ccdB-R4-35sT-D	pGGC000	4735	4736	2311	BiFC NN [160] mutagenised *2
C-R1-CmR-ccdB-R4-tagRFP-Stop-35sT-D	pGGC000	4737	4736	2700	FRET NC [177] mutagenised *2
C-tagRFP-R1-CmR-ccdB-R4-35sT-D	pGGC000	4738	4736	2776	FRET NN [177] mutagenised *2

Since more than six pEntry modules were needed for the 2in1pInd vector system, an intermediate cloning step was necessary. The Greengate cloning kit also includes intermediate vectors to generate two constructs on one T-DNA. Different intermediate vectors were generated as indicated in figure 31 A after the protocol from Lampropoulos *et al.* 2013 [206]. The Greengate reaction was performed the respective empty intermediate vector (pGGM000/pGGN000) as destination vector for the pEntry modules. Therefore 1.5 μL of each module (concentration approximately 100 - 150 $\text{ng}/\mu\text{L}$) were mixed with 1 μL of the digested and purified intermediate vector, 1.5 μL FastDigest buffer, 1.5 μL ATO (10 mM), 1 μL T4 DNA ligase (30 $\text{u}/\mu\text{L}$) and 1 μL FastDigest Eco31I (BsaI) in a total volume of 15 μL . The Greengate reaction conditions are shown in table 20. For generating intermediate vectors, fresh T4 and ATP were added after the 50 cycles and incubated for 1 h at RT prior heat inactivation. 6 μL of the reaction were used for transforming *E. coli* (methods section 3.4). Colonies were checked by colony PCR (methods section 4.5), purified and verified by digesting those with SacI, KpnI and BsaI. Positive intermediate clones were combined in a final Greengate reaction using the

destination vector pGGZ001.

Table 20: Greengate reaction conditions.

Temperature [°C]	Time [min]	
37	5	x 50
16	5	
50	5	
80	5	

Table 21: 2in1 pInd destination vectors, which were generated in this study.

Vector	Clone number
pGGM001 saGFP_CC	#7.1
pGGM004:splitYFP_NC	#1.1
pGGM003:splitYFP_CC	#4.1
pGGM006:FRET_NC	#1.3
pGGM005:FRET_CC	#3.1
pGGN000:LhGR	#1
pInd splitYFP NC	#1
pInd splitYFP CC	#2
pInd saGFP CC	#2
pInd FRET NC	#1
pInd FRET CC	#1

4.11 Generation of rBiFC, saGFP and FRET/FLIM expression constructs by Gateway cloning

The Gateway cloning technology is based on λ -phage recombination sites. For generating the rBiFC, saGFP and FRET/FLIM-based sensor constructs, a 2in1 MultiSite Gateway system developed by Grefen & Blatt was used [160]. The pDest vector for the FP-based sensor systems have two Gateway cassettes. Therefore, two different donor vectors, pDONR221 P3P3 or pDONR221 P1P4, were used to generate pEntry L1L4 or pEntry L3L2 via BP reaction. One pEntry221 L1L4 and one pEntry221 L3L2 were recombined with the respective pDest of the 2in1 cloning systems (rBiFC [160], FRETvr [177]: see table 22, self generated pInd system: see table 21) via LR reaction.

II. METHODS

Table 22: Gateway vectors used as donor or destination vector.

Vector	Provided by	Ref.
pBiFC NC	Christopher Grefen, Ad- dgene (plasmid #105112)	[160], www.n2t.net/addgene:105112
pBiFC CC	Christopher Grefen Ad- dgene (plasmid #105114)	[160], www.n2t.net/addgene:105114
pBiFC NN	Christopher Grefen, Ad- dgene (plasmid #105111)	[160], www.n2t.net/addgene:105111
pBiFC CN	Christopher Grefen, Ad- dgene (plasmid #105113)	[160], www.n2t.net/addgene:105113
pFRET NC	Christopher Grefen, Ad- dgene (plasmid #105123)	[177], www.n2t.net/addgene:105123
pFRET CC	Christopher Grefen, Ad- dgene (plasmid #105117)	[177], www.n2t.net/addgene:105117
pFRET NN	Christopher Grefen, Ad- dgene (plasmid #105126)	[177], www.n2t.net/addgene:105126
pFRET CN	Christopher Grefen, Ad- dgene (plasmid #105120)	[177], www.n2t.net/addgene:105120
pDONR221 P1P4	Invitrogen	www.thermofisher.com
pDONR221 P3P2	Invitrogen	www.thermofisher.com

Generating pEntry clone Gene transcripts encoding selected fusion candidates were enriched using primers that add attB Gateway recombination sites (table 12). PCR fragments were purified and recombined into pDONR by the BP reaction. Therefore the respective pDONR (75 ng), the calculated amount of PCR product (equation 2; i = insert; v = vector; m = mass; kb = kilobase) and 0.5 μ l PB II clonase were mixed and incubated for 1 h at RT. After inactivation of the BP reaction via proteinaseK (0.5 μ L, 10 min, 37°C), bacteria were transformed. pEntry colonies were verified via colony PCR followed by pEntry plasmids purification and verification via sequencing. All used candidate protein/protein domains and generated pEntry clones are listed in table 23.

$$m(i) = (m(v) * kb(i)) / kb(v) \quad (2)$$

Table 23: Proteins or protein domains used for 2in1 FP-based sensor systems as candidates. *¹: provided by Stefanie Müller-Schüssele.

Protein of origin	FL or chosen protein domain	Organelle membrane	FP-fusion site	pDONR221	Ref.
PpPEX3 Pp1s16_308V	PpPEX3N, PpPEX3N(GGSGG) ₁₃ , M1-A50 (+/-linker)	PerM	C-terminal	P1P4	* ¹
AtOEP7 AT3G52420	FL	OE	C-terminal N-terminal	P3P2	[209]
TOM20-2 AT1G27390	FL	MOM	N-terminal	P3P2	[210, 211]
PpTOM20 Pp1s15_226V6.1	PpTOM20C, P161- R204	MOM	N-terminal	P3P2	* ¹
VAP27-1 AT3G60600	FL	ER	N-terminal	P3P2	[58]
NET3C AT2G47920	FL	PM	N-terminal	P1P4	[58]
SYT1 At2g20990	SYT1C, L244-S541	PM	C-terminal N-terminal	P1P4	[29]
PEX11b AT3G47430	FL	PerM	C-terminal	P1P4	[212]
PEX11d AT2G45740	FL	PerM	C-terminal	P1P4	[212]
PEX10 At2g26350	FL	PerM	C-terminal	P1P4	[122, 213]
CHUP1 AT3G25690	CHUP1N, M1-P25	OE	C-terminal	P3P2	[214]
TOC34 AT5G05000		OE	N-terminal	P3P2	[215]
TOC34 AT5G05000	TOC34C, W231-S313	OE	N-terminal	P3P2	[215]
Miro1 At5g27540	MIRO1C, E602-A648	MOM	N-terminal	P3P2	[216]
Miro2 At3g63150	MIRO2C, E599-A643	MOM	N-terminal	P3P2	[216]
SYT1 At2g20990	SYT1N, M1-T243	ER	C-terminal	P3P2	[29]

(continued)

II. METHODS

Table 23: (continued)

Protein of origin	FL or chosen protein domain	Organellar membrane	FP-fusion site	pDONR221	Ref.
VAP27-1 (T59/60A) AT3G60600	FL	ER	N-terminal	P3P2	[58]
NET3C(K211) AT2G47920	FL	PM	N-terminal	P1P4	[58, 68]

Generating pExpression clones One pEntry221 L1L4 and one pEntry221 L3L2 were recombined with the respective pDest of the 2in1 cloning system (rBiFC [160], FRETvr [177], self generated pInd system) via LR reaction. For the 2in1 LR reaction a molecular ratio of 1:2:2. Therefore, 50 ng pDest, the calculated amount of both pEntry plasmids (equation 2; i = pEntry vector; v = destination vector; m = mass; kb = kilobase) and LR II clonase were mixed and incubated overnight at RT. After inactivation of the LR reaction via proteinaseK (0.5 μ L, 10 min, 37°C), DH5 α or TOP10 bacteria were transformed. pExpression colonies were verified via blue white selection and colony PCR followed by pExpression plasmids purification and verification via digest or sequencing. All generated pExpression clones, which were generated during this work, are listed in table 24.

Table 24: Generated Gateway expression clones for FP-based sensor systems. All plasmids were generated during the project by Stefanie Müller-Schüssele, Andrea Wübben, Alexa Brox or Anna-Lena Falz.

Vector tem	sys-	Proteins used	LR No	Error-free clone	Outcome tobacco:
pBiFC NC		PpPEX3N; 35sT	14	#3	PerM YFP signal
pFRET NC		AP1sp; PpTOM2C	18	#3	OE, MOM mVenus signal, negative control for FRET/FLIM
pBiFC NC		PpPEX3N; PpTOM20C	19	#2	YFP signal in PerM, OE, MOM
pFRET NC		PpPEX3NtagRFPlinker mVenusPpTOM20C	24	#5	Co-localisation of tagRFP and mVenus signal, PerM + OE signal
pBiFC NC		PEX11b; 35sT	25	#50	PerM YFP signal

(continued)

Table 24: (continued)

Vector tem	sys- Proteins used (B1B4; B3B2)	LR No	Error-free clone	Outcome tobacco
pBiFC NC	35sT35sP; TOC34C	26	#1	No YFP signal in transformed cells (cytosolic RFP control), pEntryL1L4 35sT35sP was subsequently found out to be non-functional
pBiFC NC	35sT35sP; TOC34	27	#1	No YFP signal in transformed cells (cytosolic RFP control), pEntryL1L4 35sT35sP was subsequently found out to be non-functional
pFRET NC	PpPEX3N, TOM5	28	#1	Cytosolic mVenus signal, PerM tagRFP signal
pBiFC NC	PpPEX3N, TOM5	29	#1	PerM YFP signal
pFRET CC	PpPEX3N; OEP7(noStop)_L	48	#1	OE mVenus signal (many stro-muli), PerM tagRFP signal
pFRET NC	PpPEX3N; MIRO2C	49	#1	PerM tagRFP signal, Miro2C probably MOM (mVenus), but not verified by MitoTracker staining
pBiFC NC	PEX11d; 35sT	50	#1	PerM YFP signal
pFRET CC	PpPEX3N; OEP7N	54	#1	OE mVenus signal (many stro-muli), PerM tagRFP signal
pFRET CC	PEX11d; PECT1FL	59	#1	Probably MOM mVenus signal (not verified by MitoTracker staining), PerM tagRFP signal
pBiFC NC	PpPEX3N(GGSGG) ₁₃ ; PpTOM20C	74	#1	PerM, OE YFP signal
pFRET NC	PpPEX3N(GGSGG) ₁₃ ; PpTOM20C	75	#2	Weak OE, MOM mVenus signal, PerM tagRFP signal
pBiFC NN	35sT; 35sT	76	#1	Cytosolic YFP + RFP signal
pBiFC NC	cYFP35sT; 35sT	77	#1	Cytosolic YFP + RFP signal
pBiFC NN	35sT; OEP7_Stop	78	#1	Cytosolic YFP + RFP signal

(continued)

II. METHODS

Table 24: (continued)

Vector	sys-	Proteins used (B1B4; B3B2)	LR No	Error-free clone	Outcome tobacco
pBiFC CN		35sT; OEP7(noStop)_L	79	#2	OE YFP signal
pBiFC CC		PpPex3N; OEP7(noStop)_L	82	#1	PerM YFP signal, weak OE YFP signal
pBiFC CC		PpPex3N(GGSGG) ₁₃ ; OEP7(noStop)_L	83	#2	PerM YFP signal, weak OE YFP signal
pFRET CC		PpPex3N(GGSGG) ₁₃ ; OEP7(noStop)_L	84	#2	PerM tagRFP signal, OE mVenus signal
pBiFC NN		35sT; PpTOM20C	85	#1	OE, MOM YFP signal (verified by MitoTracker)
pBiFC NC		SYT1C_L; 35sT	88	#4	Weak YFP signal, cytosolic or PM (both)
pBiFC NN		L_SYT1C; 35sT	89	#1	Weak YFP signal, cytosolic or PM (both)
pBiFC NC		PpPex3N(GGSGG) ₁₃ ; 35sT	90	#1	PerM YFP signal
pBiFC NN		NET3C; 35sT	91	#1	Cytosolic RFP (expression control), no YFP signal
pBiFC NN		35sT; VAP27	92.2	#2	ER YFP signal
pBiFC NN		NET3C; VAP27	93.2	#2	Cytosolic RFP (expression control), no YFP signal
pInd CC	saGFP	PpPEX3N; OEP7(noStop)_L	94	#1.1	Weak PerM GFP signal
pInd CC	saGFP	PpPEX3N(GGSGG) ₁₃ ; OEP7(noStop)_L	95	#1	PerM GFP signal
pInd CC	splitYFP	PpPEX3N; OEP7(noStop)_L	96	#6	Weak PerM YFP signal
pFRET NC		PpPEX3N; PpTOM20C	98	#1	-
pInd NC	FRET	PpPEX3N(GGSGG) ₁₃ ; PpTOM20C	99	#1	-
pBiFC NN		NET3C(N222A/K223A); 35sT	100	#1	Cytosolic RFP (expression control), no YFP signal
pFRET NN		NET3C; VAP27	104	#17	No tagRFP signal, ER mVenus signal

(continued)

Table 24: (continued)

Vector tem	sys- B3B2)	Proteins used (B1B4; LR No	Error-free clone	Outcome tobacco
pFRET NN	NET3C(N222A/K223A); VAP27	111	#1	No tagRFP signal, ER mVenus signal
pBiFC NC	SYT1C-L; VAP27	112	#1	-
pBiFC NN	L-SYT1C; VAP27	113	#1	ER YFP signal

5 Dexamethasone induction of pInd vector system

The dexamethasone induction of the pInd vector system was performed in the transient system *N. tabacum*. Leaves were infiltrated with the respective pInd construct 2 d or 5 d prior the induction assay. *N. tabacum* leaf discs (diameter 6.3 mm) were submerged upside down in a 96-well plate prefilled with imaging buffer (10 mM MES, pH 5.8, 5 mM KCl, 10 mM CaCl₂, 10 mM MgCl₂) and incubated for 1 h in the dark.

Prior the experiment, the buffer was replaced by fresh buffer. The CLARIOstar[®] plate reader was used to monitor the dexamethasone induction of the pInd vector system (see methods section 4.10 and 4.11; results section 4).

After 5 cycles dexamethasone or control solution (buffer + DMSO) was added to start the induction (as indicated in the respective experiment). Fluorescence of RFP, GFP or YFP was recorded at 25°C with top optics and orbital shaking at 500 rpm for 5s prior each measurement cycle (RFP: excitation: 540-20 nm; emission: 580-20 nm; excitation: 540-20 nm (RFP), 482 nm (saGFP, splitYFP); emission: 580-20 nm (RFP) 530-20 nm (saGFP), 540-20 nm (splitYFP)).

6 Calculation of FP-based reporter sizes

Table 25: Calculation of FP-based reporter sizes. The values for splitYFP are similar to those for saGFP. The longer linker (GGSGG)₁₃ adds additional 23.3 nm to the FP-based sensors.

vector	Features	Nucleotides	amino acids	size [nm]	sensor size [nm]
BiFC NC	nYFP + cYFP	secondary structure	secondary structure	4.20	17.17 + 15.12 = 32.28
	HA-tag + Myc (inclusive remaining sequence)	69 + 90	23 + 30	8.28 + 10.80	
	attB-sites	24 + 24	8 + 8	2.88 + 2.88	
	short linker	15 + 12	5 + 4	1.80 + 1.44	
BiFC CC	nYFP + cYFP	secondary structure	secondary structure	4.20	17.88 + 15.12 = 33.00
	HA-tag + Myc (inclusive remaining sequence)	78 + 90	26 + 30	9.36 + 10.80	
	attB-sites	24 + 24	8 + 8	2.88 + 2.88	
	short linker	15 + 12	5 + 4	1.80 + 1.44	
FRET NC/ FRET CC	mVenus + tagRFP	secondary structure	secondary structure	4.20 + 4.20	11.04 + 11.04 = 22.08
	remaining sequence	18 + 18	6 + 6	2.16 + 2.16	
	attB-sites	24 + 24	8 + 8	2.88 + 2.88	
	short linker	15 + 12	5 + 4	1.80 + 1.44	

7 Fluorescence microscopy methods

All fluorescence microscope imaging experiments were performed using a confocal laser scanning Zeiss LSM780 microscope and a $\times 10$ (Plan-Apochromat, 0.3 N.A.), $\times 40$ (C-Apochromat, 1.20 N.A., water immersion) or $\times 63$ lens (Plan-Apochromat, 1.40 N.A., oil immersion) and for FLIM additional a Compact TCSPC System (Becker&Hickl).

7.1 Monitoring of chloroplast-peroxisomes proximity and movement

Imaging: The experimental setup was adapted from Oikawa *et al.* 2015 [26]. In this study, peroxisomes and chloroplasts of *N. tabacum* pavement cells, *A. thaliana* mesophyll cells and *P. patens* protonema cells were investigated regarding their proximity to each other under different photosynthetic conditions. Therefore, *N. tabacum* leaves were infiltrated with the peroxisomal marker construct pSS02:CFP-SKL or stable peroxisomal marker lines of *A. thaliana* (px-ck, CFP) and *P. patens* (HPR-Citrine #3, citrine) were used. Fluorescence of CFP and citrine was excited 405 nm (Diode 405-30) and 488 nm and the emission was collected between 467-487 nm and 508-535 nm, respectively. Chloroplasts were detected via chlorophyll fluorescence, which was excited at 488 nm and collected between 686-735 nm. Z-stacks were recorded with 15-20 layers and 1 μm distance between the layers.

The experimental setup is shown in figure 10 A & B. Leaves or leaf slices of *A. thaliana* and *N. tabacum* were vacuum infiltrated with DCMU (20 μM), cytD (20 μM) or water as control. DCMU is an inhibitor of PSII [26], while cytD is a cytoskeleton inhibitor [26]. Afterwards, the leaf material was dark adapted for 30 min followed by either imaging of the dark sample or a transfer to light conditions (20 $\mu\text{mol photons m}^{-2} \text{ s}^{-1}$) for 1.5-3 h. *P. patens* protonema tissue was 45 min dark adapted followed by imaging or the pharmaceutical treatments plus transfer to light conditions for 1.5-3 h. Differently to higher plants oryzalin (10 μM) was used as cytoskeleton inhibitor.

Analysis process: In order to be able to verify the chloroplast-peroxisome-interaction rate per cell, cells were cropped using the analysis software Icy [184]. Z-stacks were loaded into Icy, the cells were marked using the transmitted light channel, cropped in 3D and exported as a tiff file. It was important not to change the histograms of the raw data. The proximity of chloroplasts and peroxisomes of the cropped cells were analysed using an automatic Python-based analysis pipeline developed in this study. The used Python packages are listed in table 26 and the analysis was executed via VSCodium using the Python version 3.8.2/ 3.7.6 64 bit. The Python-based analysis pipeline is composed of a parameter file (parameter.py) and five linked but individually executable scripts. The parameter file includes general settings for the analysis procedure and information about the raw data (1-5), settings for the segmentation (6-7) and settings for the calculation of the interaction rate (8) (figure 9).

II. METHODS

```
1 import numpy as np
2 import os
3 #####
4 # #
5 # #     ####
6 # #     ####
7 # #     ####
8 # #     ##### CHANGE THIS
9 # #     #####
10 # #     ####
11 # #     ##
12 # #
13 # #####
14 #
15 # General settings
16 #
17 # List of all folders to be analyzed
18 # separate folders with a comma
19 FOLDERS = [
20     "Folder1",
21     "Folder2",]
22 # The subdirectory in each folder where results are saved
23 OUTPUTDIR = "output"
24 # The number of CPU cores used for analysis, e.g. 4. If you set CORES to "0"
25 # then **ALL** cores will be used. When using all cores, the analysis is faster
26 # but blocks the whole PC. If you use a laptop set the number of cores half of
27 # the available number of cores! Otherwise you risk overheating
28 CORES = 12
29 # Set the channel indices for peroxisomes and chloroplasts. Indices start at 0.
30 CHANNEL_PEROXISOMES = 0
31 CHANNEL_CHLOROPLAST = 2
32 # Pixel/Voxel resolution
33 VOXEL = np.array((0.208, 0.208, 1.0)) # (x, y, z) in um
34 #
35 # Settings for script 1, proximity analysis
36 #
37 # Filters for peroxisomes
38 imageFilterPeroxisome = 1
39 distanceFilterPeroxisome = 1
40 # Filters for chloroplasts
41 imageFilterChloroplast = 1.5
42 distanceFilterChloroplast = 2.5
43 #
44 # Settings for script 3, data compilation
45 #
46 # The threshold below which a distance is considered as contact
47 THRESHOLD = 0.208 * 0
48 #####
49 # #
50 # #     ##
51 # #     ####
52 # #     #####
53 # #     ##### CHANGE THIS
54 # #     ####
55 # #     ####
56 # #     ####
57 # #
58 # #####
59
```

Figure 9: Parameter file for the Python-based analysis pipeline.

Green code is commented (#) and serves only as an explanation. Numbers indicate parameters, which can be individually adapted for each analysis. 1-5, General setting: 1) List of folders to be analysed containing the cropped z-stacks. 2) Subdirectory in each folder, where results are saved. 3) The number of CPU cores used for the analysis. 4) Channels of peroxisomes and chloroplasts of the respective raw data. 5) Voxel resolution. 6-7, Settings for script main_1_proximity_ALF.py: 6) Image and distance filter for peroxisomes. 7) Image and distance filter for chloroplasts. 8, Settings for script main_3_compile_ALF.py: 8) The distance threshold (maximal distance), which is considered as contact.

Table 26: Python packages used for the proximity Python-based analysis pipeline.

Package	Version
opencv-Python	4.5.1.48
matplotlib	3.2.0rc2
numpy	1.18.3
tifffile	2020.2.16
scipy	1.4.1
scikit-image	0.16.2
pandas	1.2.1
imagecodes	2021.1.28
seaborn	0.11.1

The scripts must be located in the same parent directory as the depicted folder in order to work.

In script “main_1_proximity_main_ALF.py” regions of interest (ROI) were identified for two selected channels and segmented to different objects. For imaging segmentation, a watershed method and two different filters were used (figure 11 A, B). The filters could be adapted manually regarding object size and shape, resolution of image (figure 9 (number 6,7)). The image filter is responsible for smoothing of inhomogeneities, whereby a larger filter corresponds to more smoothing. The distance filter is responsible for smoothing the local maxima for distorted objects, as for example chloroplasts. A larger filter corresponds to more blurring.

The voxel resolution needs also to be adapted respective to the imaging setups. Coloured images of segmented objects with a spectral colour map were generated, on which basis the distance of organelles is calculated. The formula to calculate the distance (d) in a three-dimensional space is:

$$d^2 = (X_1 - X_2)^2 + (Y_1 - Y_2)^2 + (Z_1 - Z_2)^2 \quad (3)$$

$$\sqrt{d} = \sqrt{(X_1 - X_2)^2 + (Y_1 - Y_2)^2 + (Z_1 - Z_2)^2} \quad (4)$$

In script “main_1_proximity_ALF.py” the pairwise minimal distance from centre of mass to centre of mass is calculated and an output for each individual input file as an input_file_Distance.csv file is generated. An additional output is the minimal normalised distance from centre of mass plus average radius to centre of mass plus average radius. To be able to calculate the surface to surface distance, an additional script is included, since this a very computationally intense calculation (“main_2_surface_dist_ALF.py”). As an output for each individual input file an input_file_Distance_Surface.csv file is generated.

The script “main_3_compile_ALF.py” is to compile all related .csv files to one and directly calculating the percentage of the interaction rate of peroxisomes to chloroplasts and chloroplasts to peroxisomes (p_c/p_t , c_c/c_t , organelle with contact/ organelle total) per cell based on the surface to surface distance. Therefore, a distance threshold must be included defining

the maximal distance, which is defined as contact between those two organelles.

7.2 Localisation and topology control using BiFC sensors

The topology of proteins or protein domains was verified after Zamyatnin Jr *et al.* [165]. As vector system the 2in1 rBiFC vector system was used [160], which includes an additional RFP expression control for transient expression as in *N. tabacum*. The transient transformation was performed as described in methods section 2.2 and imaged after 2 d after infiltration. If necessary for the localisation, an additional organellar marker construct was co-infiltrated or MitoTracker staining was performed (methods section 2.18). One splitYFP fragment was expressed in the cytosol, whereas the other splitYFP fragment was fused C- or N-terminal to the respective candidate protein / protein domain (figure 5). A self-assembly of both fragments only occurred if the FP-tag was fused to the cytosolic facing site of the protein. If only the RFP expression control could be detected but no YFP signal, the FP-tag was located towards the organelle inward-facing site.

Fluorescence settings were adjusted to the different spectral properties of each FP: YFP was excited at 488 nm and the emission was collected at 517-561 nm. RFP and MitoTracker orange were excited at 543 nm (HeNe543) and the emission was collected at 579-624 nm. CFP (ER, peroxisomal marker) was excited at 405 nm (Diode 405-30) and the emission was collected at 467-487 nm. Chlorophyll autofluorescence was excited at 488 nm and the emission was collected at 686-735 nm. As beam splitters following were used: MBS: MBS 488/543/633, MBS_InVis: f-MBS 405/625c and DBS1: Mirror.

7.3 Monitoring organellar proximity with BiFC sensors

Monitoring the organellar proximity via BiFC sensors was performed via a transient expression in *N. tabacum* using the rBiFC vector system of Christopher Grefen [160]. Since this vector system does not contain any plant selection marker cassette, the imaging was exclusively performed transiently in *N. tabacum* two days after infiltration. If necessary, an additional organellar marker construct was co-infiltrated or MitoTracker staining was performed (methods section 2.18). Both splitYFP/saGFP fragments were fused C- or N-terminal to the respective candidate proteins / protein domains.

The pixel dwell was set to 1.58-2.55 μ s, the averaging to 4-8-fold and the pinhole mostly to 1.5-4 Airy units. Fluorescence settings were adjusted to the different spectral properties of each FP: YFP was excited at 488 nm (Argon) and the emission was collected at 517-561 nm. GFP was excited at 488 nm and the emission was collected at 517-561 nm. RFP and MitoTracker orange were excited at 543 nm (HeNe543) and the emission was collected at 579-624 nm. CFP (ER, peroxisomal marker) was excited at 405 nm (Diode 405-30) and the emission was collected at 467-487 nm. Chlorophyll autofluorescence was excited at 488 nm (Ar-

gon) and the emission was collected at 686-735 nm. As beam splitters following were used: MBS: MBS 488/543/633, MBS_InVis: f-MBS 405/625c and DBS1: Mirror.

7.4 Monitoring organellar proximity with FRET/FLIM sensors

Imaging: Monitoring the organellar proximity via FRET/FLIM sensors was performed via a transient expression in *N. tabacum* and in stable *A. thaliana* lines using the FRET/FLIM 2in1 vector system of Christopher Grefen [177]. If necessary, an additional organellar marker construct was co-infiltrated or MitoTracker staining was performed (methods section 2.18). The donor mVenus and the acceptor tagRFP were fused C- or N-terminal to the respective candidate proteins / protein domains.

The status Zen black software needed to be rebooted to be compatible with the FLIM time-correlated single photon counting (TCSPC) application of Becker&Hickl [179]. Afterwards the TCSPC application must be started including the SPCM imaging software. FiFo Imaging were set to 512x512x256 and detector output to 70 %, which needed also to be enabled. For CLSM imaging pixel dwell was set to 1.27 μ s, the averaging to 4-fold, the pinhole mostly to 1 Airy unit and the frame size to 512x512 px. After taking a snap with the Zen black software, for FLIM detection the settings needed to be altered as fast as possible to: 1) deactivate all Tracks InTune Track, 2) frame size to max, average number to 1-fold and 3) change Mirror to Plate. Afterwards acquisition in the SPCM imaging software was started, followed by starting continuous scanning in the Zen black software. When a photon count of about 50.000 (after about 30 s) was observed, FLIM acquisition and continuous scanning was stopped. SPCM dataset was saved and send to the SPCImage software for the analysis. For continuing with Zen, Plate was changed back to Mirror.

Fluorescence settings were adjusted to the different spectral properties of each FP: CFP (ER, peroxisomal marker) was excited at 405 nm (Diode 405-30) and the emission was collected at 467-487 nm. mVenus was excited at 517 nm (InTune) and the emission was collected at 517-562 nm. tagRFP was excited at 543 nm (HeNe543) and the emission was collected at 579-624 nm. Chlorophyll autofluorescence was excited at 517 nm (InTune) and the emission was collected at 686-735 nm. As beam splitters following were used: MBS: MBS 488/543/633, MBS_InVis: f-MBS 405/520c and DBS1: Mirror/Plate.

Analysis process: For the analysis of the FLIM data the analysis software SPCImage (Becker & Hickl GmbH) was used. The settings were set to binning factor = 4 , scatter to 0 (fix) and fix shift. The values were changed by arrow keys of shift and check for the minimal χ^2 in different areas. For the 1 component (1C) analysis (single-exponential lifetime decay, figure 6 C), components were set to "1" and decay matrix was calculated with τ_m . For the 2 component (2C) analysis (double-exponential lifetime, figure 6 D), components were set to "2". The double-exponential decay model consists of a slow (τ_2) and a fast (τ_1) lifetime compon-

II. METHODS

ent from non-interacting, unquenched and from interacting, quenched donor molecules, respectively. τ_2 was set to the τ_m value of the negative control with 2575 ps (only mVenus donor, unquenched). Based on that τ_1 and the intensity factors (amplitudes), a and b of τ_1 and τ_2 , respectively, were calculated. The ratio of a and b (N_{FRET}/N_0) represents the number of interacting and non-interacting molecules.



III Results

1 Influence of light on the proximity between chloroplasts and peroxisomes

Prior to the visualisation of MCS, it is reasonable to test whether and under which conditions the proximity between the organelles of interest is enriched. In this thesis, the main focus lies on the interaction between the photorespiratory organelles, namely chloroplasts, peroxisomes and mitochondria. Since photorespiration is a light-dependent reaction [129], the correlation between the interaction of those organelles and the dependence on light has already been addressed in previous studies: Measuring the organelle tethering forces, an increased physical interaction between chloroplasts and peroxisomes under light compared to dark conditions have been identified [25, 26]. Those findings were also supported by a study of Oikawa *et al.* analysing the interaction rate between the photorespiratory organelles in *Arabidopsis mesophyll* leaf tissue [26]. They identified the interaction rate to be higher under light compared to dark conditions quantifying CLSM imaging data.

1.1 Establishment of an automatically performed Python-based segmentation process

The following section of this work aims to reproduce and verify previous findings investigating the proximity between chloroplasts and peroxisomes and developing a transparent and automatically running analysis process. The experimental setup was adapted from Oikawa *et al.* [26]: Besides light and dark treatments, they applied also DCMU and cytochalasin D (cytD) in combination with light as pharmaceutical treatments. DCMU is an inhibitor of PSII, which in turn lead to a disruption of the linear electron transport chain (LEF) mimicking dark conditions with a reduced interaction rate [26]. Since organelle positioning has been shown to be also regulated by the cytoskeleton [217–220], they investigated the impact of the active organellar motion on the organellar proximity [26]. For this purpose, they used cytochalasin D (cytD) as cytoskeleton inhibitor finding a significantly increase in peroxisome-chloroplasts contact. The aim of this section was to verify, if this findings could be reproduced not only in *Arabidopsis thaliana* but additionally in *Nicotiana tabacum* and a basal land plant species *Physcomitrella patens*.

As imaging material confocal z-stacks (15-20 layers, 1 μm distance between the layers) of all three species were recorded under the conditions described above. The chlorophyll auto-

fluorescence and a peroxisomal marker were used to visualise chloroplasts and peroxisomes, respectively. In *N. tabacum*, leaves were infiltrated with a peroxisomal CFP marker construct (pSS02:CFP-SKL) [221] 2 d prior imaging. The Agrobacterium-mediated transformation in *N. tabacum* is known to be mostly efficient in pavement cells. This was the reason, why z-stacks of pavement cells were taken as the starting material for the proximity analysis in *N. tabacum*. For the analysis in *A. thaliana* and *P. patens*, stable lines with a peroxisomal marker (*A. thaliana*: px-ck [186], CFP-SKL; *P. patens*: HPR-Citrine #3 [222]) were used. This allowed the visualisation of the organellar proximity in photosynthetic active tissue, namely in *A. thaliana* mesophyll and in *P. patens* protonema cells.

In preparation for the following analysis, individual cells of the z-stacks were cropped with Icy [184]. Figure 10 shows the maximum intensity projections (MIP) of representative, cropped z-stacks of all three species and under different conditions (experimental procedure see figure 10 A, B). The MIP consist of an overlay of the peroxisomal marker depicted in cyan and the chlorophyll autofluorescence in magenta (figure 10 C). Considering the MIP only, no obvious differences between the different treatments regarding the peroxisome-chloroplast proximity could be observed for all three species (figure 10).

To be able to verify the beforehand described impressions, the qualitative and intensity-based image information of the cropped z-stacks had to be converted into spatial information. Therefore, we developed an automatically running and easily adaptable Python-based analysis pipeline (in collaboration with Dr. Christoph Engwer). As first step of the segmentation process (figure 11 A, B), the fluorescence signals of the original grayscale images were processed by an image filter (IF), which was responsible for smoothing inhomogeneities. A larger filter value corresponded with a higher smoothing effect. Afterwards, the otsu thresholder was applied to create a binary image from the original grayscale images. For the segmentation, a distance matrix for each object (organelle) had to be calculated, whereas the pixels with the maximal distance to the background were defined as local minima (figure 11 A, white centres).

In order to be able to segment distorted objects (such as oval chloroplasts), a distance filter (DF) was added to the process. DF was responsible for smoothing local minima of distorted object (organelles). The higher DF value was, the more blurring occurred, which in turn led to a merge of two local minima to one. After defining the local minima, the watershed algorithm was applied for the finally segmentation. This algorithm is based on using the local minima as a starting point (figure 11 A, black centres) and figuratively fill them up with water. When the water level has reached the boundary of an object or meet water coming from another local minima, so-termed watershed lines serve as boundaries [224]. Based on this segmentation, the minimal pairwise surface-to-surface distances for all organelles could be calculated later on in the quantification (see results section 1.2. Considering a distance threshold, the percentage of organelles with contact within each cell was automatically quantified.

III. RESULTS

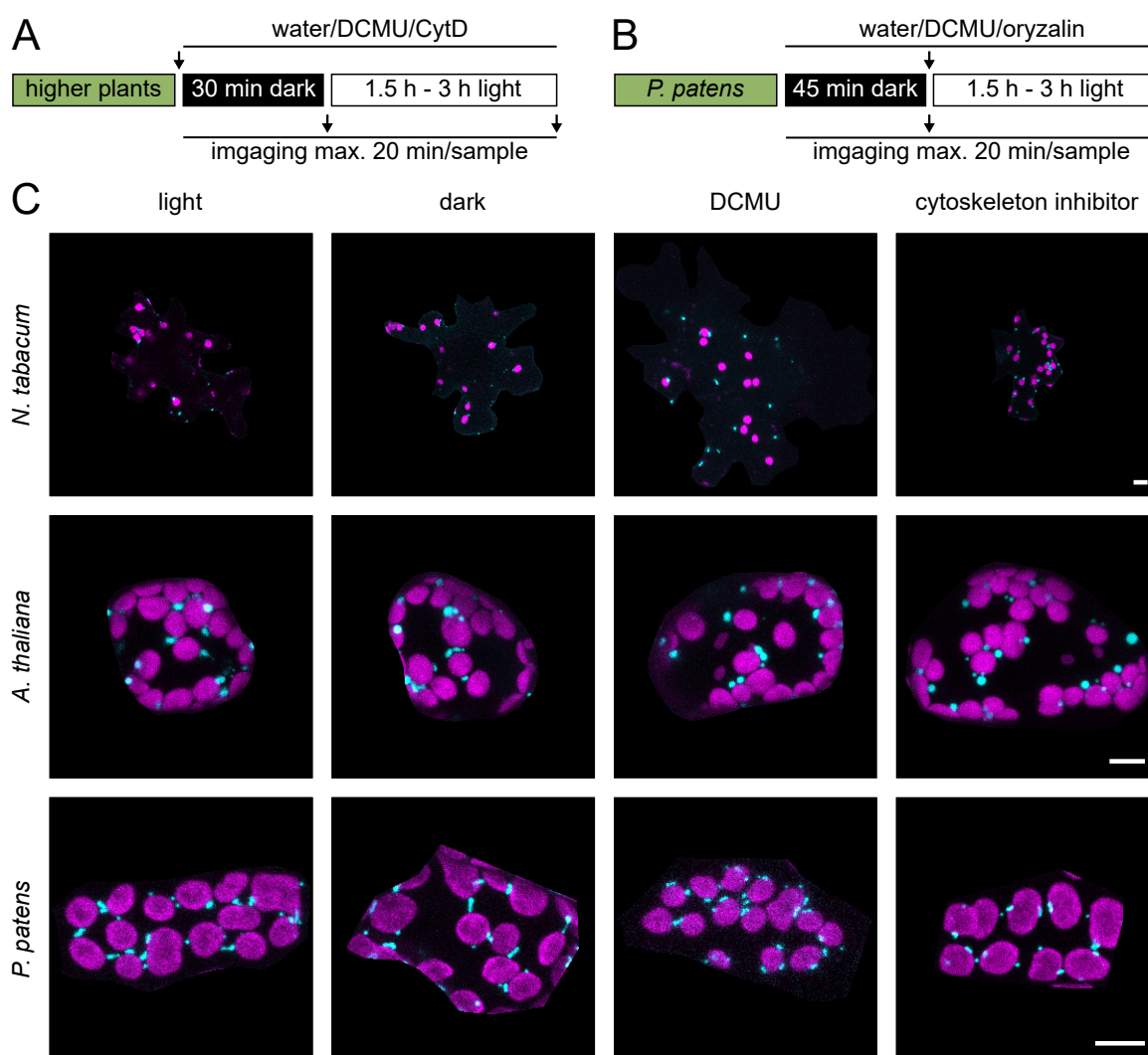


Figure 10: Maximum intensity projection (MIP) of representative z-stacks used for a chloroplast-peroxisome proximity analysis in three different species and under different photosynthetic conditions.

A, B: Experimental setup: The samples were imaged under light ($20 \mu\text{mol photons m}^{-2} \text{s}^{-1}$) and dark conditions, and after a pharmaceutical treatment under light conditions. DCMU ($20 \mu\text{M}$) is an inhibitor of photosystem II, which lead to an inhibition on of the photosynthetic electron transport chain. As second treatment either cytD ($20 \mu\text{M}$) for higher plants or oryzalin ($10 \mu\text{M}$) for *P. patens* were used as cytoskeleton inhibitors. **C:** Representative MIP images showing an overlay of chlorophyll autofluorescence (magenta) and a peroxisomal marker (cyan) in *N. tabacum* pavement, *A. thaliana* mesophyll and *P. patens* protonema tissue. *N. tabacum* was imaged 2 d after infiltration with a peroxisomal CFP marker construct (pSS02:CFP-SKL) [221]. For *A. thaliana* (px-ck, CFP-SKL [186]) and *P. patens* (HPR-Citrine #3 [222]) WT lines with a peroxisomal marker were used for the proximity analysis. Scale bar = $10 \mu\text{m}$. Raw image data of *N. tabacum* was generated as part of the supervisory relationship with Andrea Wübben [223]. Raw image data of *P. patens* was provided by Prof. Dr. Stefanie Müller-Schüssele.

The Python-based analysis pipeline has a parameter tab, where important parameters for the procedure or the analysis itself could be adjusted for differently collected data sets: 1) The list of the folders to be analysed, 2) the number of cores, which were used for the analysis, 3) the channels for peroxisomes and chloroplasts, 4) the pixel/voxel resolution, 5) IF and DF for peroxisomes and chloroplasts, and 6) the distance threshold (maximal distance), which was considered as contact. The first four parameters either belong to the analysis procedure (1, 2) or were predetermined by how the z-stacks were recorded (3, 4), whereas the filter values and the chosen distance threshold had a direct influence on the analysis and its quality (5, 6).

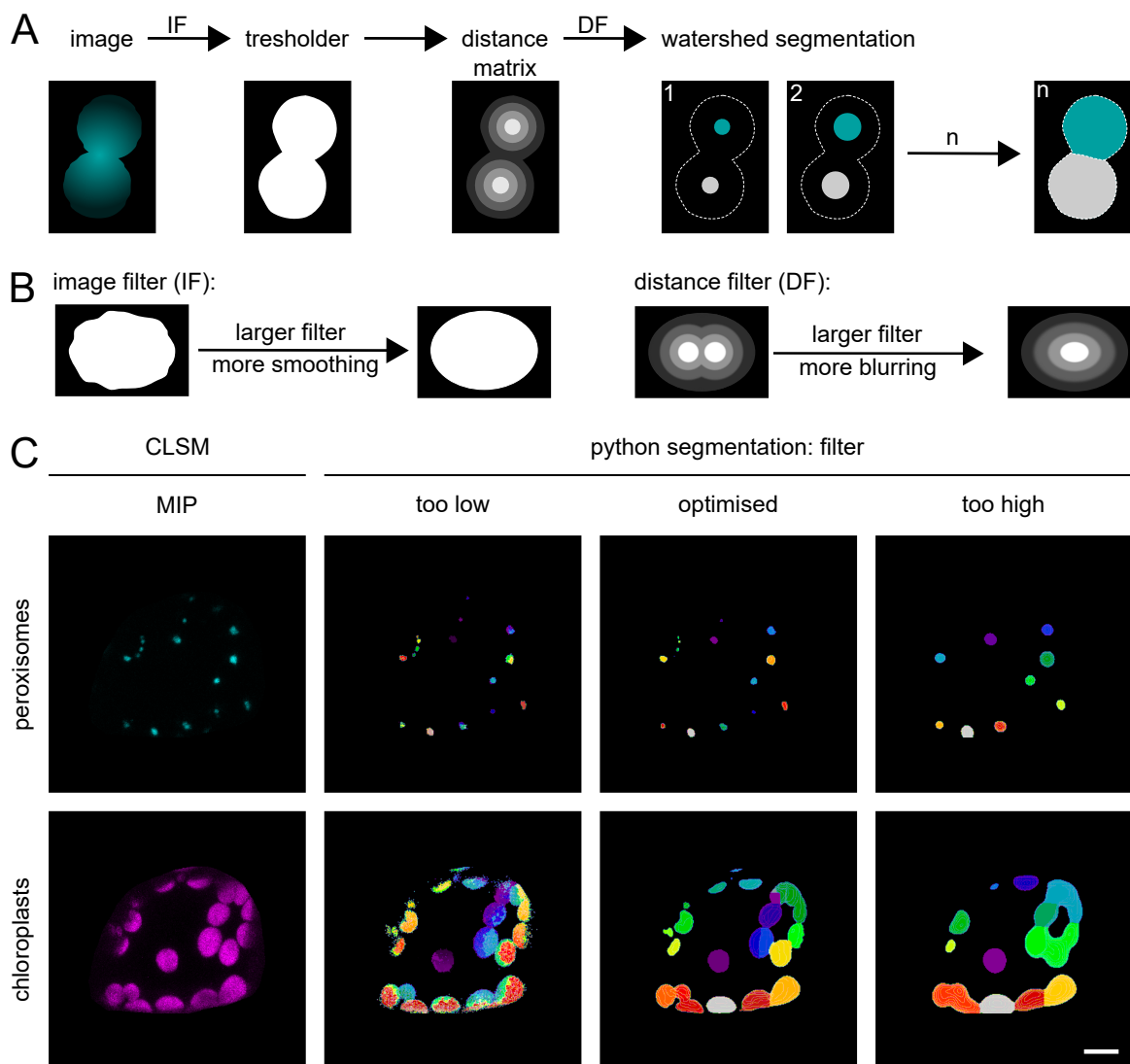


Figure 11: Segmentation of chloroplasts and peroxisomes: Procedure and setting optimisation based on the example of an *A. thaliana* mesophyll cell.

A: Organelles were segmented via Python using a otsu threshold and watershed algorithm. **B:** To optimise the segmentation two different filters were implemented in the Python-based analysis pipeline. The image filter (IF) is responsible for smoothing inhomogeneities of the objects (organelles), whereas the chosen filter value behaves proportional to the smoothing effect. The distance filter (DF) behaves also proportional and is responsible for smoothing local maximal of distorted object (organelles). **C:** Peroxisome and chloroplast segmentation of an representative *A. thaliana* mesophyll cell with differently chosen filter values. In the left column one representative MIP of the CLSM signal of peroxisomes (first row) and chloroplast (second row) are represented. In the Python-based segmentation each single object (organelle) is represented in a different colour. Too low filter values led to over-segmentation of both organelles. Too high filter led to a high number of fusion of more than one organelle and/or that the segmented objects are larger than the actual fluorescence signal. Raw image data of *N. tabacum* was generated as part of the supervisory relationship with Andrea Wübben [223]. Raw image data of *P. patens* was provided by Prof. Dr. Stefanie Müller-Schüssele.

In figure 11 C the optimisation process for the values of IF and DF is shown. In the left column the MIP of either peroxisomal CFP marker or the chlorophyll autofluorescence are presented. The other three columns show the Python-based segmentation with differently chosen filter values. Whereas too low filter values led to over-segmentation and blurred boundaries, too high filter values led to a higher number of merged organelles within one segmented object, as well as oversized objects compared to the original fluorescence signal. Using optimised filter settings, the objects of both organelles matched with the fluorescence

III. RESULTS

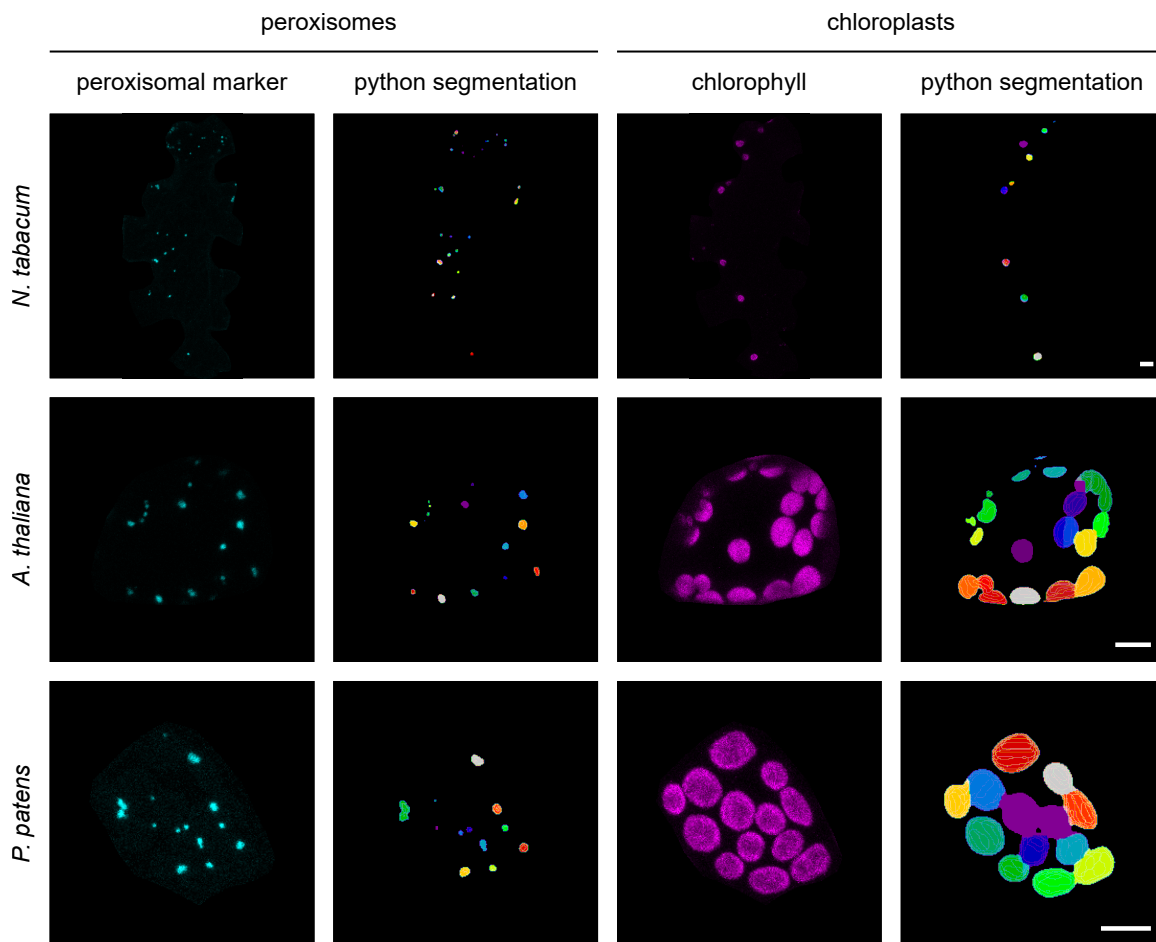


Figure 12: Segmentation of chloroplasts and peroxisomes by self-developed Python-based analysis pipeline with optimised filter settings and in three different species.

Representative 3D images of *N. tabacum* pavement, *A. thaliana* mesophyll and *P. patens* protonema tissue. Organelles were detected via a peroxisomal CFP marker (cyan) and the chlorophyll autofluorescence (magenta) and shown as maximum intensity projection (MIP). Organelles were segmented via Python using a otsu threshold and watershed algorithm. To minimise background signal and optimise the segmentation two filters were used. The image filter (IF) smooth inhomogeneities of the objects (organelles) and a distance filter (DF) smooth the local maxima for distorted objects. Larger filter values lead to a higher smoothing effect for both filters. The filters were depicted as follow: *N. tabacum* and *A. thaliana*: $IF_P = 1$, $DF_P = 1$, $IF_C = 1.5$, $DF_C = 2.5$; *P. patens*: $IF_P = 1$, $DF_P = 5$, $IF_C = 3$, $DF_C = 6$. Scale bar = 10 μm .

signal and were segmented correctly to a large extent.

The filter values had to be optimised for both organelles in all three species. The procedure was to adjust the filter values step by step and to check the quality of the segmentation manually for at least 5 z-stacks per organism. Figure 12 represents the Python-based segmentation of peroxisomes and chloroplasts alongside the original fluorescence signal exemplary in one cell of *N. tabacum*, *A. thaliana* and *P. patens*. Although the size of peroxisomes and chloroplasts were different in *N. tabacum* and *A. thaliana*, for both analysis the optimal filter settings were similar ($IF_P = 1$, $DF_P = 1$, $IF_C = 1.5$, $DF_C = 2.5$). In *P. patens* the chloroplasts were even larger (supplemental table S1) and the peroxisomes were more elongated compared to *N. tabacum* and *A. thaliana* (figure 10). This led to other filter settings than in higher plants with $IF_P = 1$, $DF_P = 5$, $IF_C = 3$ and $DF_C = 6$.

1.2 Verifying the Python-based surface-to-surface proximity quantification

After optimising the parameters for the segmentation process, the reliability of the Python-based proximity analysis itself needed to be proven. For this purpose, the Python-based analysis (figure 14 B-D) was compared to a manual evaluation (figure 14 A) of the same raw data of *N. tabacum*. Both analyses determined the proximity ratio of chloroplasts or peroxisomes in contact with the respective other organelle of one cell (chloroplasts with contact / chloroplasts total (c_c/c_t), peroxisomes with contact / peroxisomes total (p_c/p_t)).

To test, if the Python-based analysis pipeline could identify different organellar proximity ratios, two organellar tether constructs were included in the analysis in addition to the WT background. Those construct should mimic a higher proximity ratio in comparison to WT conditions (figure 13). On the one hand, artificial tethering between the mitochondrial outer membrane (MOM) and outer envelope (OE) of chloroplasts with the peroxisomal membrane (PerM) was created by using the BiFC (bimolecular fluorescence complementation) construct 19#2. The tethering effect was based on an irreversible maturation of the two non-fluorescent fragments of a splitYFP [159], both fused to different organellar membrane proteins. In our case, the fusion partners of the splitYFP fragments were truncated versions of the two *P. patens* proteins PpPEX3 and PpTOM20. PpPEX3N is the N-terminal part of the mentioned PerM protein PpPEX3 and localised to the PerM in *N. tabacum* (see results section 2). PpTOM20C is composed of the C-terminus of PpTOM20, MOM protein, and localised to the MOM and the OE (see results section 2). On the other hand, a synthetic tether construct (24#5, PpPEX3N:tagRFP:mVenus:PpTOM20C) was designed composed of the same truncated proteins flanking the FRET (Förster resonance energy transfer) pair mVenus and tagRFP, which in turn are linked by a flexible linker (schemata see figure 41 A).

The MIP of the transformed *N. tabacum* cells are represented in figure 13 under light and dark conditions. Similar to WT conditions, within the same genotype no obvious differences between light and dark treated cells could be identified (figure 10). The visual impression was that the BiFC construct 19#2 resulted in chloroplasts and peroxisomes being adjacent to each other to a higher extent than in WT cells (figure 10). The overexpression of the synthetic tether construct 24#5 led to cluster formation of peroxisomes, both in *N. tabacum* and also in *A. thaliana*. The clusters had a spherical form and were mainly not adjacent to chloroplasts (figure 13). The manual quantification of the organellar proximity (figure 14 A) supported the aforementioned impressions of the qualitative imaging data (figure 10 & 13). Within one genotype, both c_c/c_t and p_c/p_t the light and dark treatment did not differ significantly from each other (figure 14 A). However, while the organellar contact of WT and 24#5 overexpression cells were similar, overexpression of the BiFC construct 19#2 led to a significantly increase of c_c/c_t and p_c/p_t .

The Python-based analysis included various pixel-sized-based distance thresholds determining below which threshold the distance was considered as a contact (figure 14 B-D).

III. RESULTS

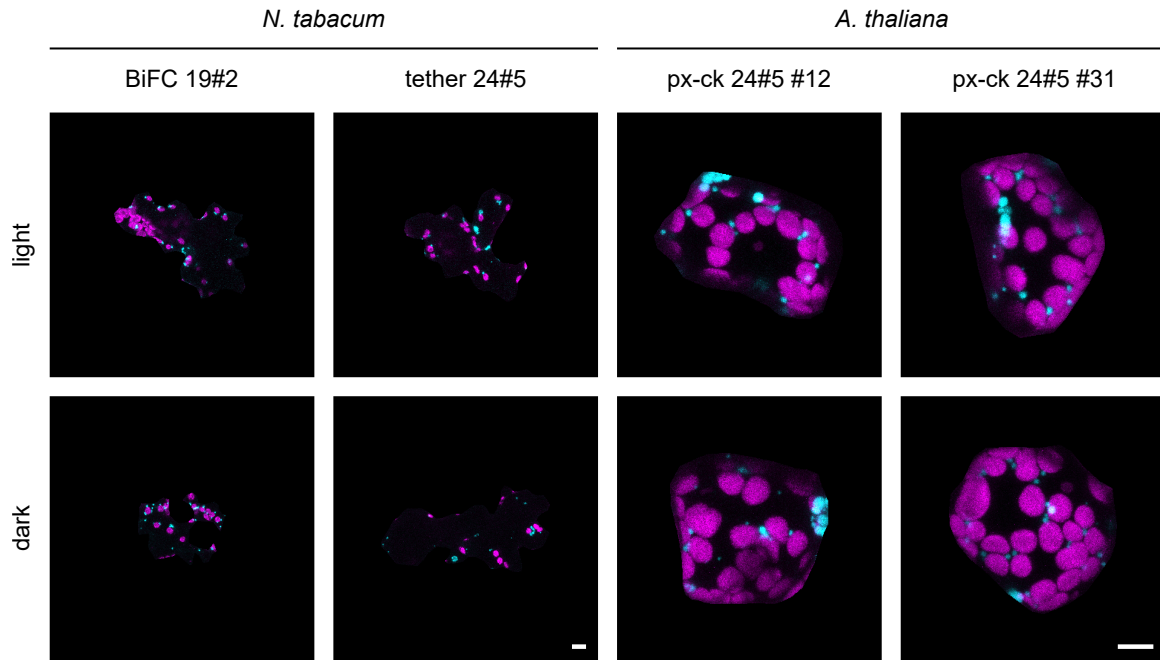


Figure 13: Maximum intensity projection (MIP) of representative cells transformed with artificial or synthetic tether constructs between chloroplasts and peroxisomes.

Representative MIP images showing an overlay of chlorophyll autofluorescence (magenta) and a peroxisomal marker (cyan) in *N. tabacum* pavement and *A. thaliana* mesophyll tissue. The samples were imaged under light ($20 \mu\text{mol photons m}^{-2} \text{s}^{-1}$) and dark conditions. Plants were transiently (*N. tabacum*) or stable (*A. thaliana*) transformed with either a BiFC (19#2, BiFC NC nYFP:PpTOM20C PpPEX3N:cYFP) or a synthetic tether construct (24#5, PpPEX3N:tagRFP:mVenus:PpTOM20C) construct. Both constructs contain PpPEX3N, a truncated version of a *P. patens* peroxisomal membrane (PerM) protein and PpTOM20C, a truncated version of a mitochondrial outer membrane (MOM) protein. In *N. tabacum*, PpPEX3N localised to the PerM in, whereas PpTOM20C localised to the MOM and the outer envelope (OE) of chloroplasts (see results section 3). In *N. tabacum*, the constructs were co-infiltrated with a peroxisomal CFP marker (pSS02:CFP-SKL) [221], whereas in *A. thaliana* stable lines with the synthetic tether construct in a WT background with a peroxisomal CFP marker (px-ck, CFP-SKL) were used for the proximity analysis. Scale bar = $10 \mu\text{m}$. Raw image data of *N. tabacum* was generated as part of the supervisory relationship with Andrea Wübben [223].

MCS are normally described to be in a range of 10-30 nm, which is smaller than the resolution limit of our CLSM imaging material with 420 nm/pixel or 208 nm/pixel for *N. tabacum* or *A. thaliana* and *P. patens*, respectively (figure 14 or 15). However, the distance threshold could not be automatically set to 0 pixels. The reason was, that instead of the organellar outer membranes, the peroxisomal matrix and chlorophyll autofluorescence were used as starting point for the segmentation. Therefore, the detected signal did not accurately reflect the real surface of the respective organelles, but was a reasonable estimate. Thus, the proximity ratio with three distance thresholds were compared, namely 0 pixels, 1 pixel and 2 pixels with $<0.42 \mu\text{m}$, $\leq 0.42 \mu\text{m}$ and $\leq 0.84 \mu\text{m}$ as maximal distance, respectively. Using the Python-based analysis pipeline and regardless of the distance thresholds being applied, the average percentages of c_c/c_t and p_c/p_t were decreased compared to those in the manual analysis (figure 14). Nevertheless the same trend as in the manual quantification could be identified: While c_c/c_t and p_c/p_t did not significantly differ from each other between light and dark treatments within the one genotype, c_c/c_t and p_c/p_t were significantly increased for the BiFC tether construct 19#2 compared to WT and 24#5 (figure 14). As the trend remained similar, the averages increased proportional with the distance threshold.

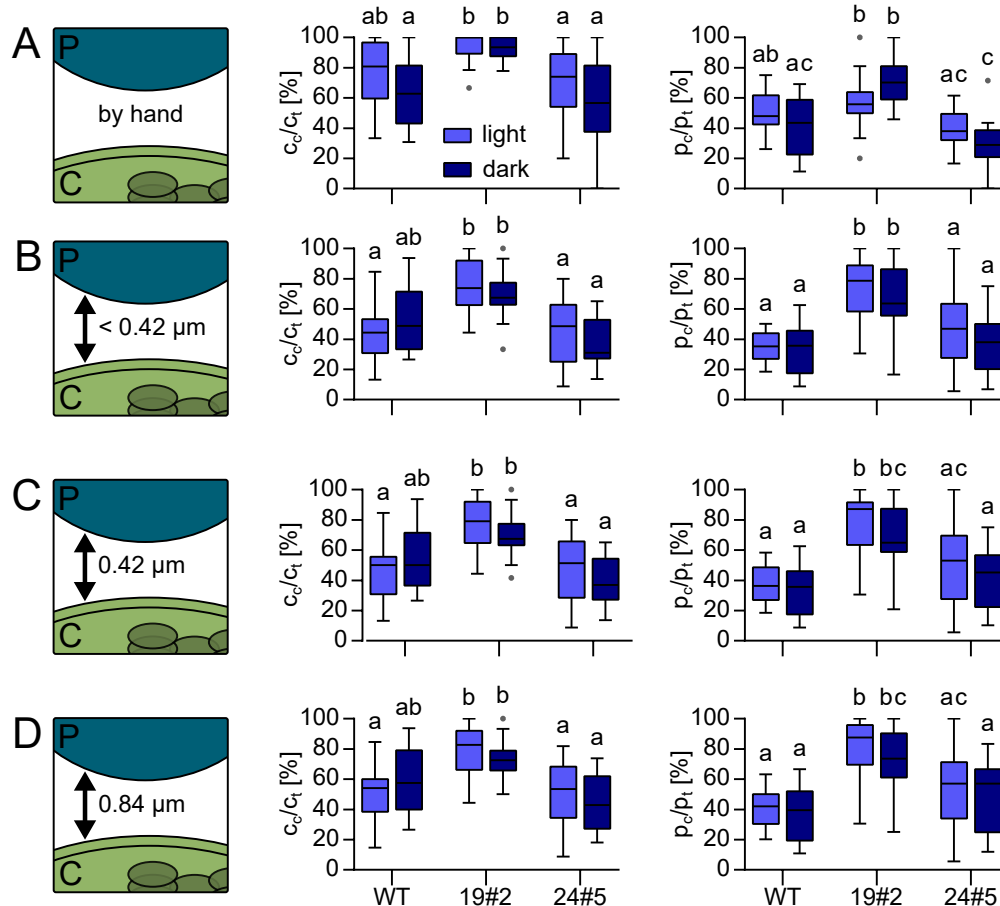


Figure 14: Quality control of self-developed Python-based proximity analysis between chloroplasts and peroxisomes in *N. tabacum* pavement cells.

WT and transiently transformed *N. tabacum* pavement cells overexpressing different artificial tether constructs were investigated regarding the proximity of chloroplasts and peroxisomes under light and dark conditions. The light treatment was performed at $20 \mu\text{mol m}^{-2} \text{s}^{-1}$ for 1.5-3 h after an dark adaption of 30 min. For the dark treatment leaf material was at least dark incubated for 30 min. One tether construct 19#2 was based on a BiFC sensor approach. The BiFC fragments (splitYFP) were either fused to truncated versions of a peroxisomal or mitochondrial (mislocalised to OE) membrane protein (PpPEX3N:cYFP nYFP:PpTOM20C). As the reassembly of the splitYFP is known to be irreversible, the matured BiFC construct could serve as an artificial tether between the photorespiratory organelles. The second tether construct 24#5 was a fusion protein PpPEX3N:tagRFP:mVenus:PpTOM20C (for further information see section 2.10). In addition all investigated plants were transiently transformed with a peroxisomal CFP marker.

The organellar proximity was either analysed manually or by using a self-developed Python-based analysis pipeline. The Python-based analysis was based on a watershed segmentation of the CFP (peroxisomes) and chlorophyll autofluorescence (chloroplasts) channel, followed by a 3D reconstruction of the z-stack. Based on the 3D reconstruction, the distance between the surfaces of chloroplasts and peroxisomes within a cell were calculated. For calibration, different distance thresholds in a range from 0 to 2 pixels ($0.42 \mu\text{m} / \text{pixel}$) were tested (B-D) and compared to the manual analysis (A). $n \geq 16$. Each replicate represents the c_c/c_t and p_c/p_t of one individual cell. Data are shown as box plot with median and Tukey whiskers. Significant differences were calculated according to 2way ANOVA with Tukey's multiple comparisons test. Raw image data of *N. tabacum* and part of the analysis was generated as part of the supervisory relationship with Andrea Wübben [223].

The comparison to the manual analysis showed that the Python-based analysis was able to reliably reproduce the same trend in *N. tabacum* with equally increasing averages proportional to the distance threshold. To ascertain if the distance threshold influences the proximity analysis in other tissues and organisms to an equal extent, an analysis was carried out on mesophyll cells of *A. thaliana* WT and two independent stable synthetic tether lines 24#5 (figure 15). In general, the average percentages of c_c/c_t and p_c/p_t did not differ between the lines or treatments except for px-ck 24#5 #31 dark with an increase in the percentage. With increasing distance threshold, the mean percentage c_c/c_t and p_c/p_t increased (figure 15) as

III. RESULTS

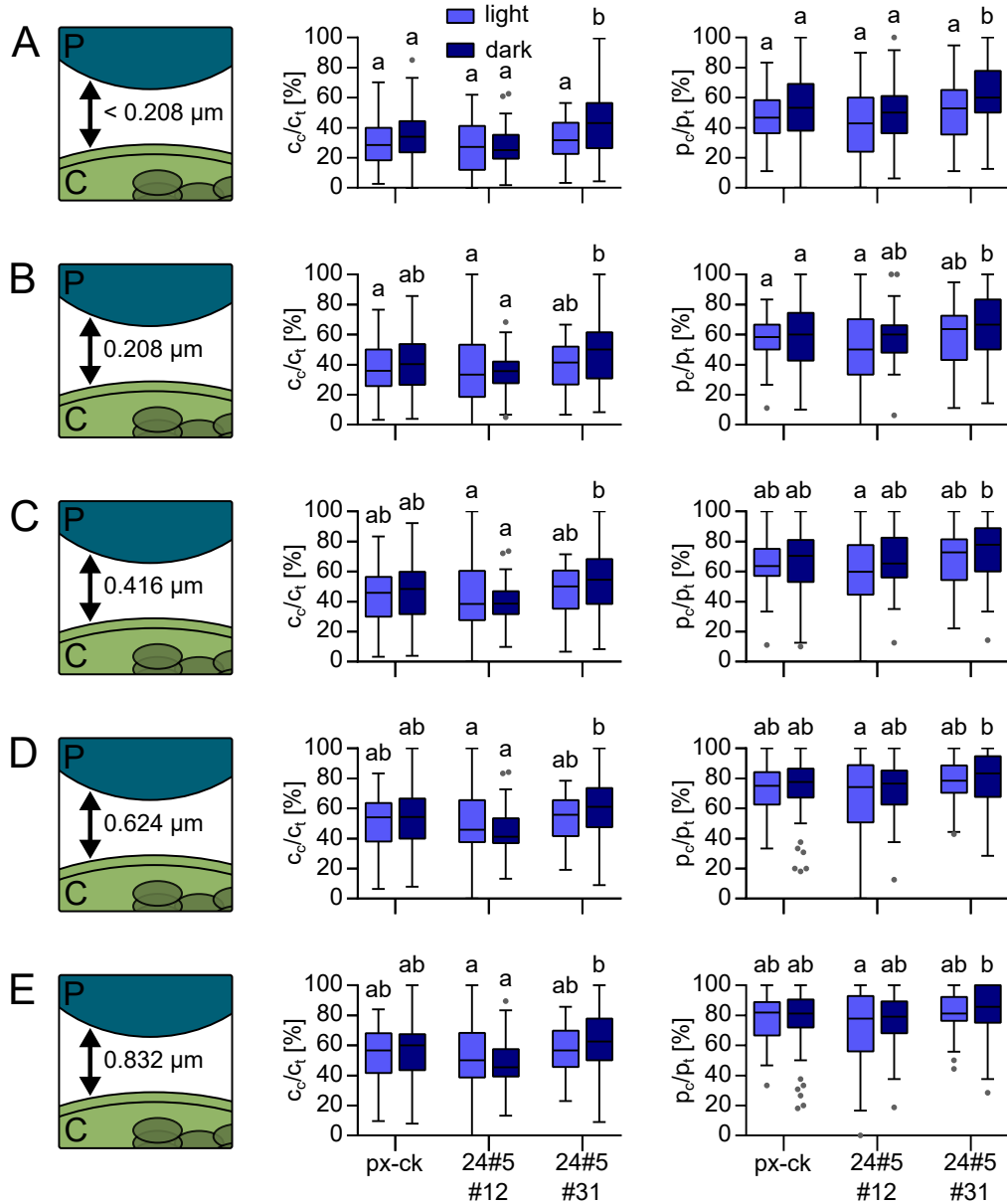


Figure 15: Quality control of self-developed Python-based analysis pipeline for the proximity analysis between chloroplasts and peroxisomes in *A. thaliana* mesophyll cells.

Mesophyll leaf material of *A. thaliana* WT px-ck and two independent T2 overexpression lines px-ck 24#5 #12 and #31 were analysed regarding the proximity of chloroplasts and peroxisomes. The tether construct 24#5 is a fusion protein PpPEX3N:tagRFP:mVenus:PpTOM20C (for further information see section 2.10). The light treatment was performed at $20 \mu\text{mol m}^{-2} \text{s}^{-1}$ for 1.5-3 h after a dark adaption of 30 min. For the dark treatment leaf material was at least dark incubated for 30 min. The organellar proximity was quantified by using a self-developed Python-based analysis pipeline. The Python-based analysis was based on a watershed segmentation of the CFP (peroxisomes) and chlorophyll autofluorescence (chloroplasts) channel, followed by a 3D reconstruction of the z-stack. Based on the 3D reconstruction, the distance between the surfaces of chloroplasts and peroxisomes within a cell was calculated. For calibration, different distance thresholds in a range from 0 to 4 pixels ($0.208 \mu\text{m} / \text{pixel}$) were tested (A-E). $n \geq 40$. Each replicate represents the c_c/c_t and p_c/p_t of one individual cell. Data are shown as box plot with median and Tukey whiskers. Significant differences were calculated according to 2way ANOVA with Tukey's multiple comparisons test.

in the analyses in *N. tabacum* (figure 14 B-D).

In summary, the quality control of the Python-based analysis revealed that we were able to reliably reproduce the same trend as a manual analysis. The distance threshold affected only the level of the mean percentages of c_c/c_t and p_c/p_t but not the general trend. Based on this findings, only one distance threshold needed to be chosen for further analyses. Thus,

we set the threshold to 0 pixels (*N. tabacum*: <0.42 μm ; *A. thaliana* & *P. patens*: <0.208 μm).

1.3 Proximity analysis between chloroplasts and peroxisomes in three model plant species under different photosynthetic conditions

After optimising the filter values, verifying the quality of the Python-based analysis pipeline, and choosing the distance threshold, the actual proximity analysis under different photosynthetic conditions was performed. As mentioned before, the proximity analysis was conducted in three different organisms and tissues, namely in *N. tabacum* pavement, *A. thaliana* mesophyll and *P. patens* protonema cells. The experimental setup was adapted from Oikawa *et al.* [26] (description see above). As cytoskeleton treatment, we used cytD (20 μM) in higher plants to inhibit the actin filament derived organellar movement (proven in supplemental figure S1), whereas oryzalin (10 μM) was chosen as microtubuli inhibitor in *P. patens*. The reason for using oryzalin in *P. patens* was, that their organellar movement is dependent on microtubuli [225].

Diagrams of the experimental setup are shown in figure 16 A and B. The proximity analysis exhibited pronounced in-homogeneities for c_c/c_t and p_c/p_t between *N. tabacum* (C), *A. thaliana* (D) and *P. patens* (E) (figure 16). In pavement cells of *N. tabacum* (figure 16 C), the mean values differed by a maximum of 37.7% for c_c/c_t and 22.4% for p_c/p_t . Both c_c/c_t and p_c/p_t were not significantly different between the light, dark and cytD treatments (c_c/c_t & p_c/p_t : light: 43.5 % \pm 17.0 % & 35.1 % \pm 9.9 %; dark: 53.2 % \pm 21.4 % & 34.0 % \pm 18.9 %; cytD: 55.7 % \pm 17.1 % & 40.3 % \pm 18.5 %). Meanwhile, the treatment with DCMU led to a significant decrease in c_c/c_t = 18.0 % \pm 14.7 % and p_c/p_t = 17.9 % \pm 15.7 % (figure 16 C).

In *A. thaliana*, the variance between the treatments was smaller than in *N. tabacum*, with c_c/c_t and p_c/p_t differing only by a maximum of 11.8 % and 2.5 %, respectively. The leaves treated with cytD and the control treatment DMSO (solvent for DCMU and cytD stock solutions) exhibited a significantly increase for c_c/c_t compared to the light, dark and DCMU treatment (light: 30.1 % \pm 14.4 %; dark: 35.2 % \pm 18.1 %; DCMU: 35.0 % \pm 15.3 %; cytD: 39.7 % \pm 16.5 %; DMSO: 41.9 % \pm 16.9 %). The mean values of p_c/p_t were generally higher (light: 47.4 % \pm 15.1 %; dark: 53.0 % \pm 22.6 %; DCMU: 54.8 % \pm 21.4 %; cytD: 52.0 % \pm 16.0 %; DMSO: 59.9 % \pm 18.0 %). Interestingly, only p_c/p_t of the control treatment DMSO was significantly increased compared to the light treatment (figure 16 D).

The mean values of the analysis in *P. patens* protonema cells were distinctly higher than those of *N. tabacum* and *A. thaliana*. The lowest average for c_c/c_t was 70.3 % (dark), while the highest averages for c_c/c_t in *N. tabacum* and *A. thaliana* were 55.7 % (cytD) and 41.9 % (DMSO), respectively. The same tendency could be also identified for p_c/p_t with the lowest average in *P. patens* at 89.1 % and the highest for *N. tabacum* and *A. thaliana* at 40.3 % and 59.9 %, respectively. Regarding c_c/c_t , only the dark treated cells showed a significant decrease compared to all other treatments (light: 91.4 % \pm 12.9 %; dark: 70.3 % \pm 19.1 %;

III. RESULTS

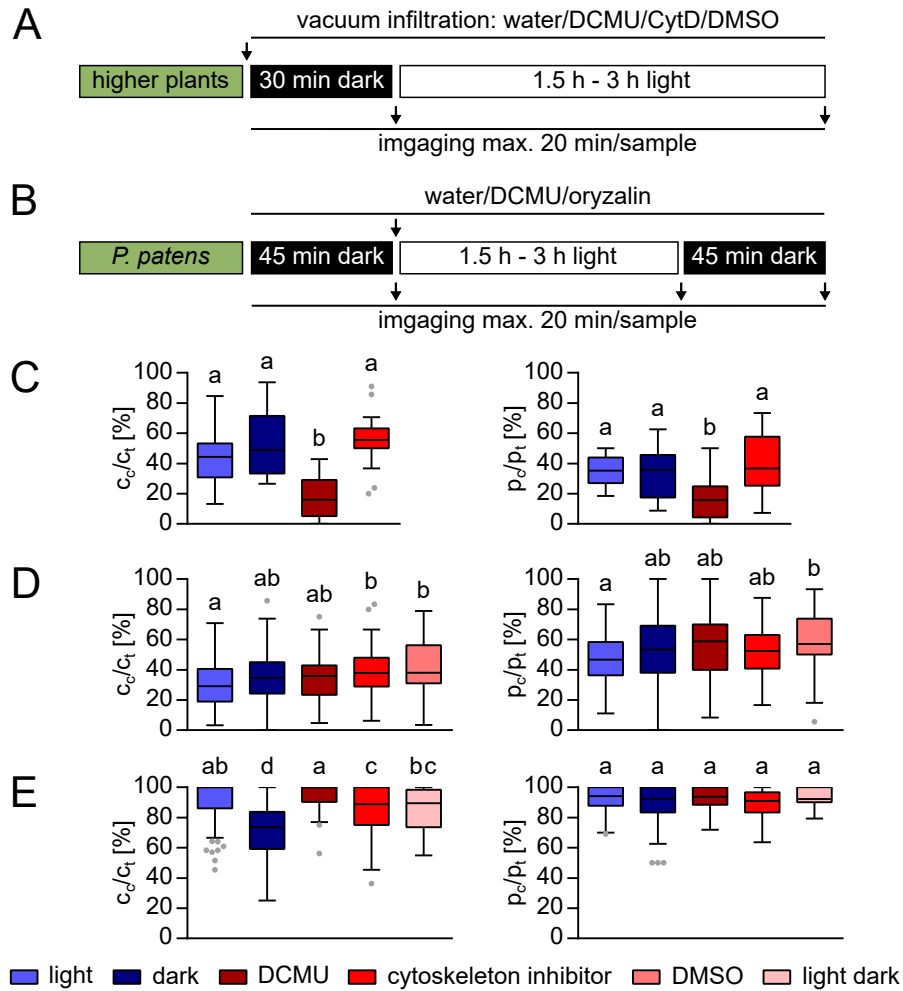


Figure 16: Proximity analysis between chloroplasts and peroxisomes under different photosynthetic conditions in *N. tabacum* (C), *A. thaliana* (D) and *P. patens* (E).

A, B: Experimental setup: light treatment was performed at $20 \mu\text{mol m}^{-2} \text{s}^{-1}$ for 1.5-3 h after a dark adaption. For the dark treatment leaf material was at least dark incubated for 30 min for higher plants (A) and 45 min for *P. patens* (D). DCMU ($20 \mu\text{M}$) functions as inhibitor of photosystem II leading to an inhibition of the photosynthetic electron transport chain. As second treatment cytoskeleton inhibitors were used to depolymerise the respective structure of the cytoskeleton, which is responsible for the active movement of the chloroplasts. In higher plants (*N. tabacum*, *A. thaliana*) cytD ($20 \mu\text{M}$) was used to depolymerise the actin filament, whereas in (*P. patens*) oryzalin ($10 \mu\text{M}$) functioned as microtubuli inhibitor. **C, D, E:** Quantification of the organellar proximity in *N. tabacum* (C), *A. thaliana* (D) and *P. patens* (E). *N. tabacum*: $n \geq 18$. *A. thaliana*: $n \geq 43$. *P. patens*: $n \geq 24$. Each replicate represents the c_c/c_t and p_c/p_t of one individual cell. Data are shown as box plot with median and Tukey whiskers. Significant differences were calculated according to One-way ANOVA with Tukey's multiple comparisons test. Distance threshold for the Python-based analysis pipeline ≤ 1 pixel. Raw image data of *N. tabacum* was generated as part of the supervisory relationship with Andrea Wübben [223]. Raw image data of *P. patens* was provided by Prof. Dr. Stefanie Müller-Schüssele.

DCMU: $95.4 \% \pm 8.1 \%$; oryzalin: $84.0 \% \pm 16.2 \%$; light dark: $85.4 \% \pm 13.8 \%$). The results of p_c/p_t showed even less variation than those of c_c/c_t with a maximum of 4.1% and no significant differences between all treatments (light: $92.6 \% \pm 7.4 \%$; dark: $89.3 \% \pm 12.8 \%$; DCMU: $93.2 \% \pm 6.7 \%$; oryzalin: $89.1 \% \pm 9.8 \%$; light dark: $92.8 \% \pm 6.2 \%$).

In summary, the proximity analysis of *N. tabacum*, *A. thaliana* and *P. patens* was not consistent between the different species. Whereas addition of DCMU led to a distinct decrease of both c_c/c_t and p_c/p_t in *N. tabacum*, in *A. thaliana* only small variations could be identified. While the average percentages of the analyses in *N. tabacum* and *A. thaliana* ranged between 17.9% and 55.9%, the lowest average in *P. patens* was 70.3%.



2 Assessment of targeting and topology of fusion proteins for proximity reporters

As a starting point for the development of specific proximity sensors (see results section 3 and 5), we verified targeting to different organellar membranes using either full-length proteins or specific domains including the targeting signals from the respective protein candidates. The procedure was to screen for candidates, where either the topology is published or predicted using bioinformatic analysis tools, and then to verify the topology transiently in *N. tabacum*. A schematic overview of all tested candidates is shown in figure 17 A.

We had to investigate the topology of the fusion candidates to guarantee cytosolic orientation of the FP-tag fusion site for the proximity reporter systems. For that, we used a BiFC approach similar the topology assay published in Zamyatnin Jr *et al.* [165] (figure 5). The truncated or the full-length candidate proteins were fused on either their N- or the C-terminal site to one fragment of the splitYFP (nYFP, cYFP) and combined with the respective cytosolic expressed splitYFP fragment. We used the published Gateway-based 2in1 ratiometric BiFC (rBiFC) vector system of Christopher Grefen ([160], figure 18 A). The simultaneous expression of both splitYFP fragments fused to the genes of interest and the cytosolic expression control RFP [168] allows a quantification of the splitYFP signal. Importantly, it is designed for the transient expression in plants, so that the cytosolic RFP serves as trans-

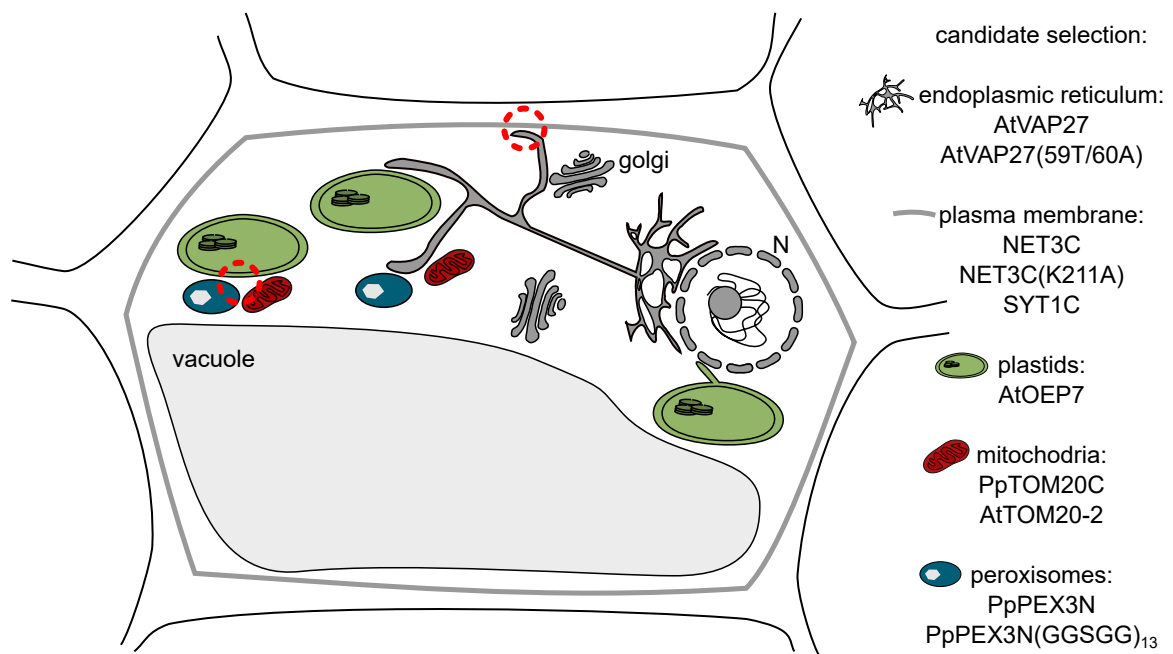


Figure 17: Schematic overview of fusion protein candidates for BiFC and FRET/FLIM reporter systems

Putative MCS of interest between endoplasmic reticulum and plasma membrane, and between plastids, peroxisomes and mitochondria are highlighted with dotted circles (red) with protein fusion candidates to label the respective (outer) organellar membranes. AtVAP27, AtVAP27(59T/60A), NET3C, NET3C(K211A), AtOEP7 and AtTOM20-2 were utilised as full length proteins, while for SYT1, PpTOM20 and PpPEX3 only protein domains were chosen. In this case, the addition of C or N to the protein name indicated a selection of the protein domain of the C- or N-terminus (fragment selection in table 23). N (nucleus).

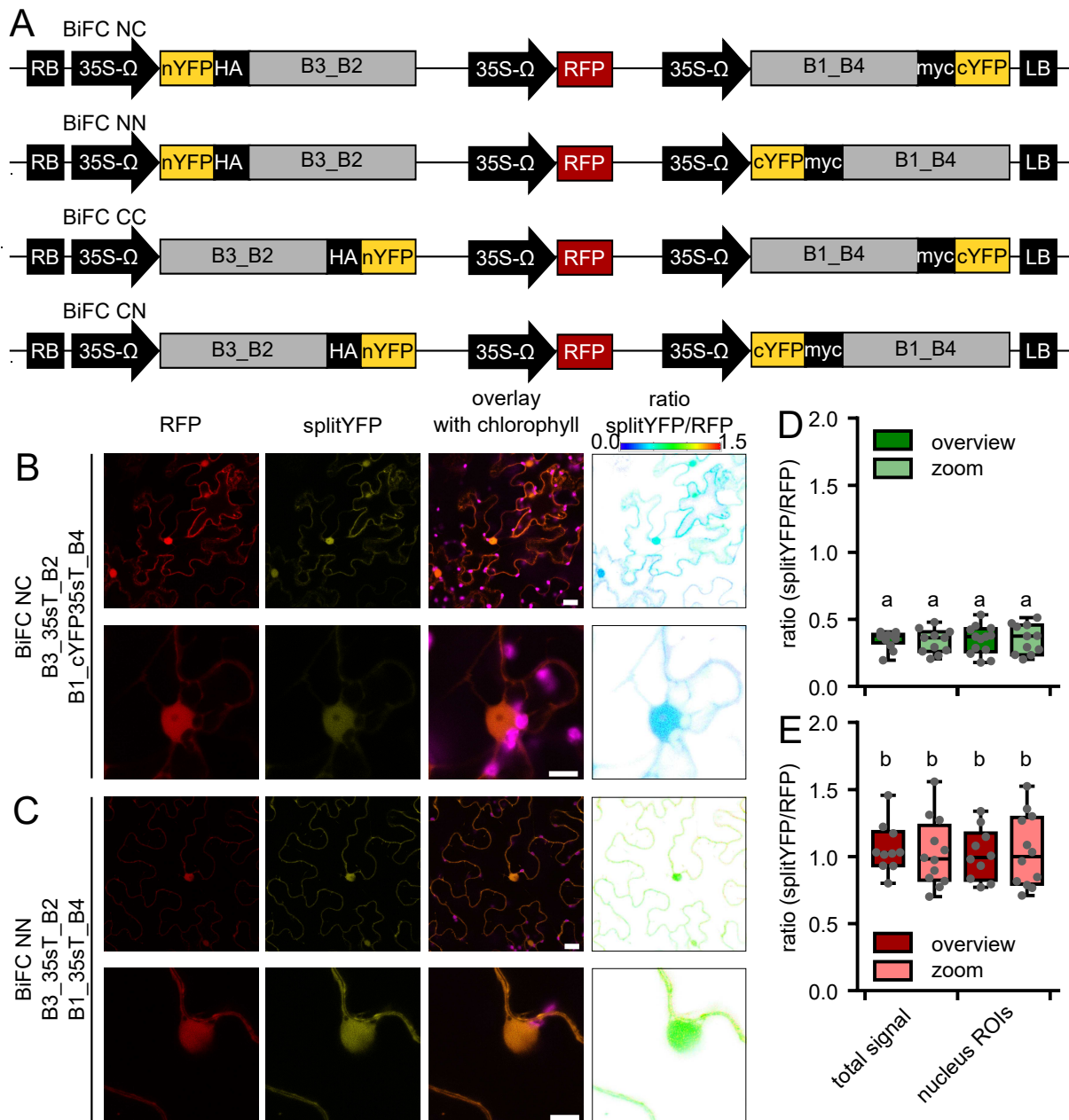


Figure 18: Verification of cytosolic expression control.

A: Gateway-based 2in1 ratiometric BiFC (rBiFC) vector system of Christopher Grefen [160], which was used for the topology assay after Zamyatnin Jr *et al.* 2006 [165]. **B, C:** CLSM images of transient expression in *N. tabacum* for the constructs BiFC NC nYFP:35sT cYFP(Stop):35sT and BiFC NN nYFP:35sT cYFP:35sT, resulting in cytosolic splitYFP signal. **D, E:** Ratiometric analysis of the total fluorescence BiFC normalised by that of cytosolic expression control RFP. Data are shown as box plot with median and Tukey whiskers. **D, E:** Ratiometric analysis of the total fluorescence splitYFP normalised by that of the cytosolic expression control RFP. Two different zooms were used and either the total signal (cytosol + nucleus) or regions of interest (ROIs) in the nucleus served as basis for the analysis. Data are shown as box plot with median and Tukey whiskers. Significant differences were calculated according to 2-way ANOVA with Tukey's multiple comparisons test. Scale bar = 10 μ m.

formation control in the absence of a YFP signal [160].

In a first step, constructs encoding cytosolic expressed splitYFP fragments needed to be established. To do this, two different approaches were tested (figure 18) with the vectors BiFC NC nYFP:35sT cYFP(Stop):35sT and BiFC NN nYFP:35sT cYFP:35sT. The Gateway-cassette B3B2 contained a stop codon plus a 35s terminator (35sT) and the Gateway-cassette B1B4 either a stop codon plus a 35sT or the cYFP fragment including a stop codon plus a 35sT

(figure 18 A). The expectation was that the missing targeting signal automatically led to a cytosolic expression of both splitYFP fragments, where they can mature and emit a cytosolic YFP signal. This could be confirmed for both constructs using CLSM imaging (figure 18 B, C). The average ratio of the splitYFP to the independently expressed RFP differed with 0.35 and 1.0 for the cYFP:35sT and 35sT construct, respectively. A ratio of about 1.0 corresponded to the results published in the original publication of the rBiFC vector system [160]. Thus, for further localisation experiments the cloning cassettes (B3B2/B1B4) including a stop codon plus a 35sT were used.

2.1 Known ER-PM contact site proteins as fusion protein

ER-PM contact sites (EPCS) are the best characterised MCS in plants with already identified MCS proteins in *A. thaliana* as the ER-PM protein pair VAP27-1 and NET3C [58] or the tether protein SYT1 [29, 59]. The idea was to use those MCS-known proteins or mutated/truncated versions of them as control for the proximity reporter system using MCS-specific and interacting proteins. To compare whether the functionality of the proximity reporter systems depends on the properties of the protein fusion partners, meaning whether the fusion partners have to be MCS-specific proteins and whether they have to interact with each other or not.

As control, where proteins are located at MCS and interact, we chose the EPCS protein pair VAP27-1 and NET3C. VAP27-1 (At3g60600) was published to be localised to the ER at the EPCS, where its mutated form VAP27-1(59T/60A) was still localised to the ER but failed to label EPCS [58]. The N-terminus of the ER TM protein VAP27-1 is exposed towards the cytosolic face [58]. Therefore, we created the fusion constructs nYFP:L:VAP27-1 or nYFP:L:VAP27-1(59T/60A) with a cytosolic cYFP (cYFP:35sT). For both constructs, the splitYFP signals co-localise with the co-infiltrated CFP-ER marker (AtWak2(signal peptide):CFP:ER retention signal) [186] (figure 19 B, C). Thus, we were able to confirm the expected ER membrane localisation and the topology.

One interaction partner of VAP27-1 at EPCS is NET3C (At2g47920), which was published to be associated to the cytoskeleton and probably also directly to PM [58, 64]. We created the construct BiFC NN cYFP:L:NET3C nYFP:35sT using the same FP-fusion site than in P. Wang *et al.* for the VAP27-1-NET3C FRET/FLIM interaction assay [58]. No YFP signal could be detected 2 d or 3 d after infiltration. On request to the authors of P. Wang *et al.* [58], they informed us that they were only able to detect NET3C by co-infiltrating a construct, which encodes the protein p19. p19 is a protein of the Tomato bushy stunt virus, which suppresses post-transcriptional gene silencing [226], and therefore is required for NET3C expression. Repeating the infiltration for 5-times and checking after 2 d and 3 d, we did detect any YFP signal for NET3C with and without co-infiltration with a p19 vector construct (figure 20 A).

As second control, where proteins are located at MCS but do not interact, we chose

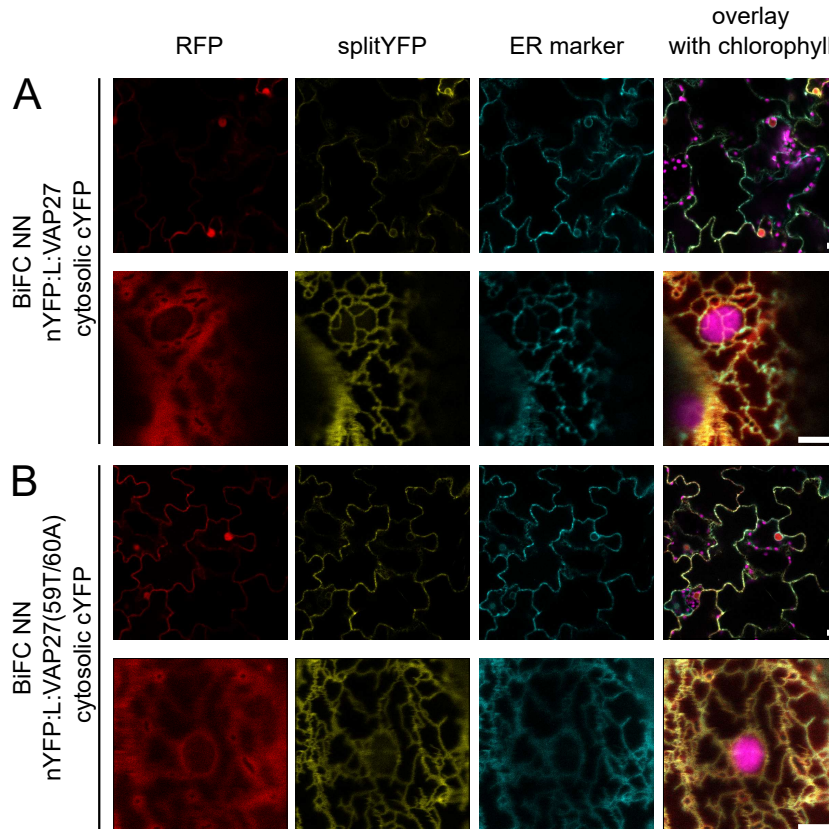


Figure 19: Localisation and topology control of ER membrane protein candidates.

A, B: Topology assay of VAP27-1 (At3g60600) and its mutated form VAP27-1(59T/60A) form confirmed ER membrane localisation. Generated constructs BiFC NN nYFP:VAP27-1 cYFP:35sT and BiFC NN nYFP:VAP27-1(59T/60A) cYFP:35sT were coinfiltrated with a CFP ER marker construct (AtWak2(signal peptide):CFP:ER retention signal) [186]. Split YFP fragments of the fusion proteins are exposed to the cytosolic face of the membrane. Scale bar = 5 μ m.

VAP27-1 and the C-terminal protein domain of SYT1. SYT1 (At2g20990) is a tether protein at EPCS, where two C-terminal calcium-binding domains (C_2A/C_2B) are responsible for PM association [29]. We designed two constructs including these domains of SYT1 (SYT1C, 244-541 aa) fused either N- or C-terminal to the FP-tag to verify SYT1C localisation and topology. Localisation of both constructs revealed no exclusive PM but also cytosolic localisation (figure 20 B, C). For the fusion cYFP:L:SYT1C the YFP signal was enhanced compared to SYT1C:L:cYFP, what is the reason to use the N-terminal fusion site for further experiments.

III. RESULTS

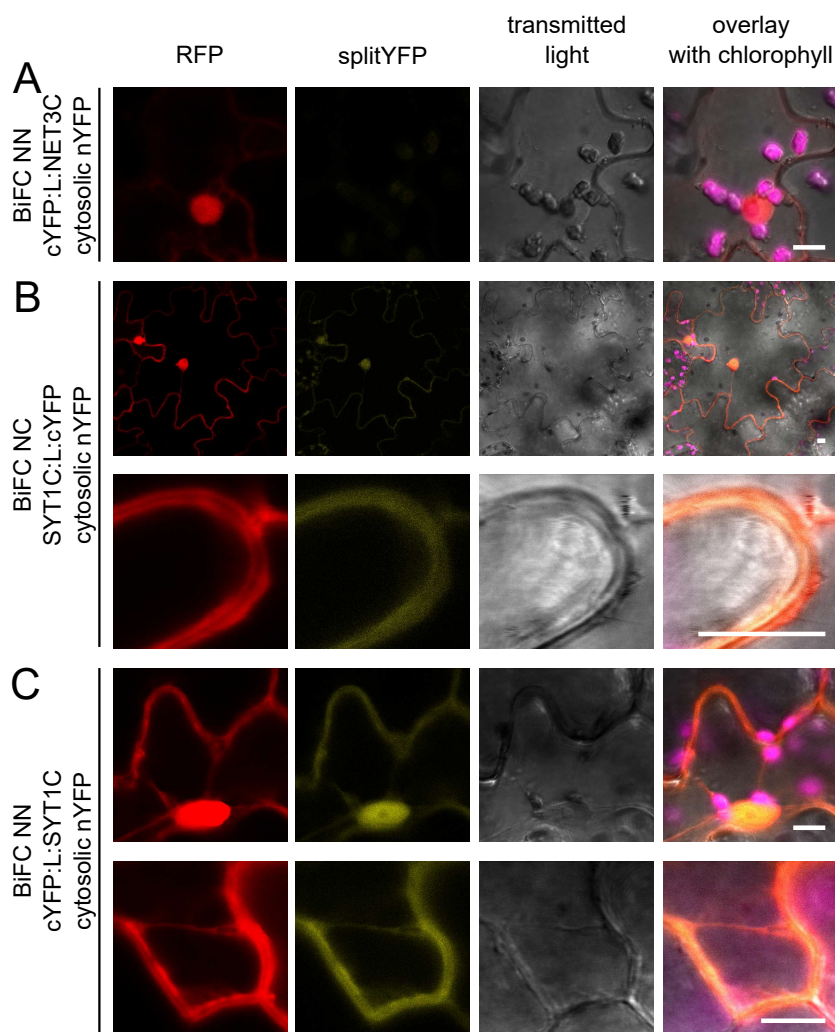


Figure 20: Localisation and topology control of PM protein candidates.

A: Topology assay of NET3C (At2g47920) reveal no splitYFP signal using the construct BiFC NN cYFP:L:NET3C nYFP:35sT. **B, C:** Topology assay of SYT1C (At2g20990, 244-541 aa) do not confirm exclusive PM but also cytosolic localisation for both fusion sites. Generated constructs BiFC NC SYT1C:L:cYFP nYFP:35sT and BiFC NN cYFP:L:SYT1C nYFP:35sT were infiltrated in *N. tabacum* leaves. Split YFP fragments of the fusion proteins are exposed to the cytosolic face of the membrane. Scale bar = 10 μ m.

2.2 MCS-unspecific OE, MOM and PerM protein or protein domains as fusion protein

In this thesis, we were mainly interested in the role of MCS between chloroplasts, peroxisomes and mitochondria. Since no MCS proteins between them have been identified yet, MCS-unspecific and non-interacting proteins or protein domains were used to label the organellar membrane homogeneously.

As OE protein, we chose OEP7 (AT3G52420), which is a common candidate for labelling the OE of chloroplasts. The C-terminal region face towards the cytosol [209] and the topology prediction from UniProt (<https://www.uniprot.org/>). We confirmed the topology of OEP7 with the construct BiFC CN OEP7:nYFP and cytosolic cYFP, as it is shown in figure 21, where the YFP signal surrounds the chlorophyll auto-fluorescence signal.

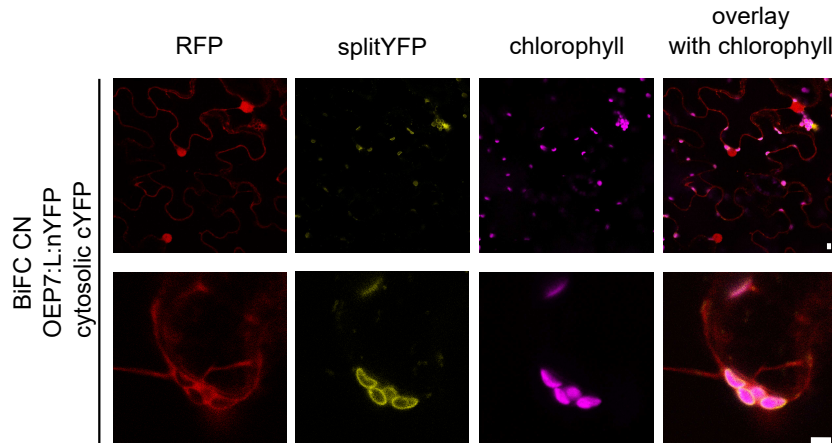


Figure 21: Localisation and topology control of outer envelope (OE) protein candidate of the chloroplast.

Topology assay of OEP7 (AT3G52420) confirms OE localisation. Generated construct BiFC CN OEP7:L:nYFP cYFP:35sT was infiltrated in *N. tabacum* leaves. Split YFP fragments of the fusion proteins are exposed to the cytosolic face of the membrane. Scale bar = 5 μ m.

For labelling the MOM and PerM, truncated protein candidates derived from *P. patens* were tested, since they were designed for the usage in in *P. patens* protoplasts in the first place (pre-work of Stefanie Müller-Schüssele).

Perry *et al.* investigated conserved domains features of translocase of the outer membrane 20 (TOM20) in plants and found the TM domain to be at its C-terminal end with the N-terminal region facing the cytosol, whereas the TM motif in animals is N-terminal [227]. We tested the topology of the C-terminal region of PpTOM20 (PpTOM20C, Pp1s15_226V6.1, 161-204 aa) using the construct BiFC NN nYFP:L:PpTOM20C cYFP:35sT transiently in *N. tabacum* (figure 22 A). As mitochondrial marker MitoTracker orange was vacuum infiltrated and is represented in the same channel as the cytosolic RFP expression control. The splitYFP signal is located to the MOM, but also miss-localised to the OE of the chloroplasts. To test, if a full-length version an *N. tabacum* TOM protein AtTOM20-2 (AT1G27390) show an exclusive localisation to MOM with the rBiFC vector system, we generated the construct BiFC NN nYFP:L:AtTOM20-2 cYFP:35sT. As shown in figure figure 22 B, AtTOM20-2 is localised to the MOM but also to the OE.

Peroxin 3 (PEX3) is a peroxisomal membrane bound receptor for PEX19 and it was reviewed that the TM domain is N-terminal in Arabidopsis. Bioinformatic analysis revealed a TM domain in *P. patens* PEX3 at the N-terminal end (Pp3c24_12050V1.1). Based on this knowledge, a truncated version PEX3N (1-50 aa) was cloned, followed by generation of the constructs BiFC NC nYFP:35sT PpPEX3N(GGSGG)₁₃:L:cYFP including a a flexible, long linker and BiFC NC nYFP:35sT PpPEX3N:L:cYFP. In figure 23, the localisation for both constructs is shown. Co-infiltration with a peroxisomal CFP marker construct (pSS02:CFP-SKL) [221] reveals the YFP signal being located to the PerM surrounding the peroxisomal CFP marker.

III. RESULTS

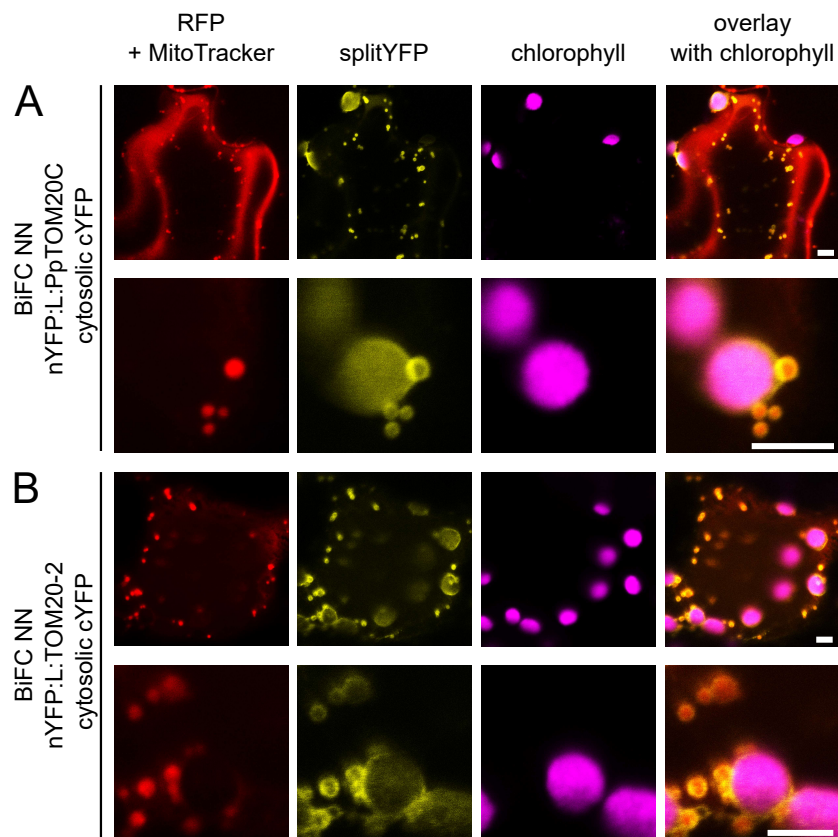


Figure 22: Localisation and topology control of mitochondria outer membrane (MOM) protein candidates.

A, B: Topology assay of PpTOM20C (Pp1s15_226V6.1, 161-204 aa) and AtTOM20-2 (AT1G27390) confirms MOM localisation but also mislocalisation to the outer envelope (OE) of chloroplasts. Generated constructs BiFC NN nYFP:L:PpTOM20C cYFP:35sT and BiFC NN nYFP:L:TOM20-2 cYFP:35sT were infiltrated in *N. tabacum* leaves. Split YFP fragments of the fusion proteins are exposed to the cytosolic face of the membrane. As mitochondrial marker MitoTracker orange was used (in RFP channel). Scale bar = 5 μ m.

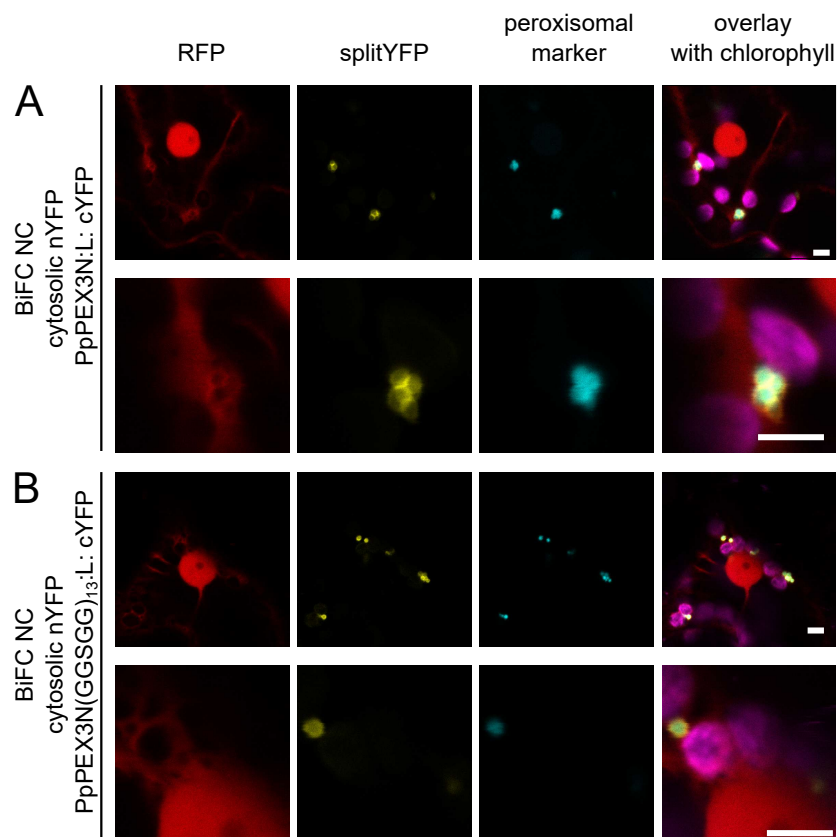


Figure 23: Localisation and topology control of peroxisomal membrane (PerM) protein candidates.

A, B: Topology assay of PpPEX3N (Pp3c24_12050V1.1, 1-50 aa) and PpPEX3N(GGSGG)₁₃ confirms PerM localisation. Generated constructs BiFC NC PpPEX3N:L:cYFP nYFP:35sT and BiFC NC PpPEX3N(GGSGG)₁₃:L:cYFP nYFP:35sT were co-infiltrated with a peroxisomal CFP marker construct (pSS02:CFP-SKL) [221] in *N. tabacum* leaves. Split YFP fragments of the fusion proteins are exposed to the cytosolic face of the membrane. Scale bar = 5 µm.

3 Characterisation of splitFP sensor systems for the visualisation of MCS in plants

SplitFP systems are commonly known to be used for verifying protein-protein interactions. However, since splitFPs convert proximity directly into a fluorescent signal, they can be also used to investigate organellar proximity [6]. SplitFP systems have emerged as one key technique for the visualisation of MCS in mammalian and yeast cells, while plants studies this techniques has been applied less frequently to explore MCS (references see table 2 and table 3).

SplitFPs are composed of two non-fluorescent peptides, which reassemble, when they come in close proximity [161]. Targeted to organellar membranes, emission of a fluorescent signal indicates organellar proximity. The most frequently used BiFC reporter systems investigating MCS are splitYFP or saGFP (references see table 2). In this work, we designed splitYFP-based proximity reporter system for the investigation of MCS between chloroplasts, peroxisomes and mitochondria. The splitYFP is composed of approximately equally sized N- and C-terminal fragments split between 154 aa and 155 aa [159]. As cloning system, we used a published rBiFC 2in1 Gateway vector system [160] containing the mentioned splitYFP reporter, which can be fused to two genes of interest. Those fusion proteins are simultaneously expressed with a cytosolic RFP expression control under the 35sP promoter, which allows the identification of successfully transformed cells in the transient system of tobacco, as well as a ratiometric quantification of the BiFC signal [160].

In order to visualise the proximity of organelles, the fluorescent probes needed to be targeted to the organellar membranes. Therefore, full length or protein domains of membrane proteins were fused to the splitYFP fragments. The fusion partners had to be carefully chosen, as specific targeting and a cytosolic orientation of the FP-tag needed to be ensured [6] (topology verification see results section 2). At the time of starting this thesis, no studies were known that investigated the proximity of organelles using splitFP systems in plants. For that reason, the aim was to test if splitFP systems are generally suitable as proximity sensors in plants with focus on: 1) possible requirements of the organellar fusion proteins, 2) the role of the bridging distance of the sensor and 3) the impact of the characteristics of two different splitFP systems.

3.1 Assessment of BiFC sensor system fused to non-interacting and homogeneously distributed proteins of OE, MOM and PerM

Possible requirements of the organellar fusion proteins are: 1) organellar targeting and homogeneous labelling of the organellar membrane, 2) MCS-specificity and/or 3) protein-protein interaction. The first goal was to verify, if organellar targeting and homogeneous la-

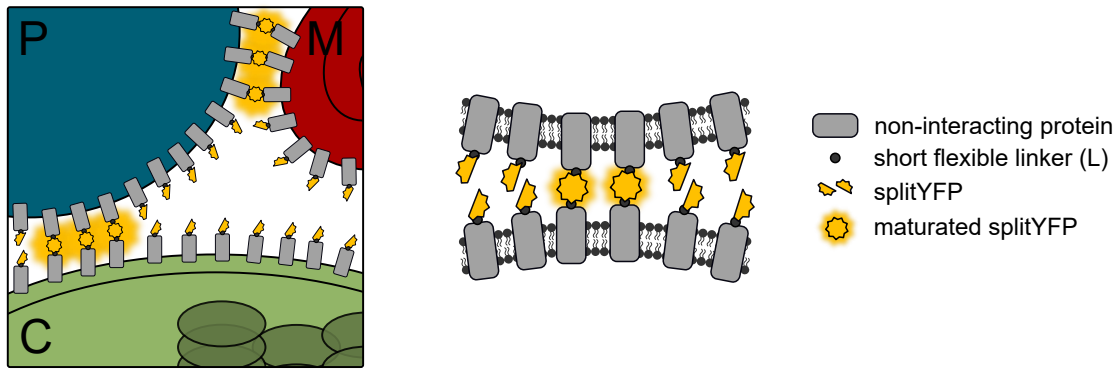


Figure 24: Schematic overview of the proximity BiFC (bimolecular fluorescence complementation) reporter using the example of splitYFP and the expected signal distribution.

The splitYFP fragments are fused to non-interacting and MCS-unspecific proteins (full-length or truncated versions) to target the fluorescent probes to the respective organellar membranes. At MCS between the three organelles chloroplasts (C), peroxisomes (P), mitochondria (M), specific fluorescent signal is expected, since the chromophore is able to mature. Regions with larger distances should not be fluorescently labelled, as the distance for the reassembly of the splitYFP is too wide.

bellings of organellar membranes of the splitYFP are sufficient to function as organellar proximity sensor system. Therefore, MCS-unspecific and non-interacting proteins of chloroplasts, peroxisomes and mitochondria were chosen as fusion partners.

3.1.1 Specificity of fluorescence pattern of splitYFP transiently expressed in *N. tabacum*

Assuming that the splitYFP fragments are targeted to different organellar membranes, in theory, they should mature at the contact sites of those organelles, while regions with larger organelle spacing should not be fluorescently labelled (figure 24). To test this hypothesis on plants, expression clones were generated encoding fusion proteins of full length or truncated versions of respective membrane proteins with either the nYFP or cYFP fragment and expressed transiently in *N. tabacum*. If not depicted otherwise, *N. tabacum* leaves were infiltrated with *A. tumefaciens* containing the respective proximity reporter construct 2 d prior imaging.

The first construct rBiFC NC 2in1 PpPEX3N:cYFP nYFP:PpTOM20C was designed to investigate simultaneously the proximity between chloroplasts-peroxisomes and mitochondria-peroxisomes (figure 25 A). The fragments of the splitYFP reporter were either targeted to the MOM and OE by fusion to PpTOM20C, or to the PerM by fusion to PpPEX3N (topology and localisation see results section 2). In figure 25 B, representative CLSM images of the aforementioned proximity reporter in *N. tabacum* pavement cells are shown, which was co-infiltrated with the peroxisomal marker construct pSS02:CFP-SKL [221]. The peroxisomal marker is depicted in cyan, the splitYFP in yellow, the cytosolic RFP expression control in red and the chlorophyll autofluorescence in magenta (from left to right). In all representative images, the YFP signal surrounded the peroxisomal marker signal, where single peroxisomes or peroxisomal clusters were adjacent to chloroplasts. Additionally, the images with a higher resolution and zoom revealed a YFP signal of the OE of the chloroplasts. To verify how the BiFC signal and the peroxisome-mitochondria interaction were linked to each

III. RESULTS

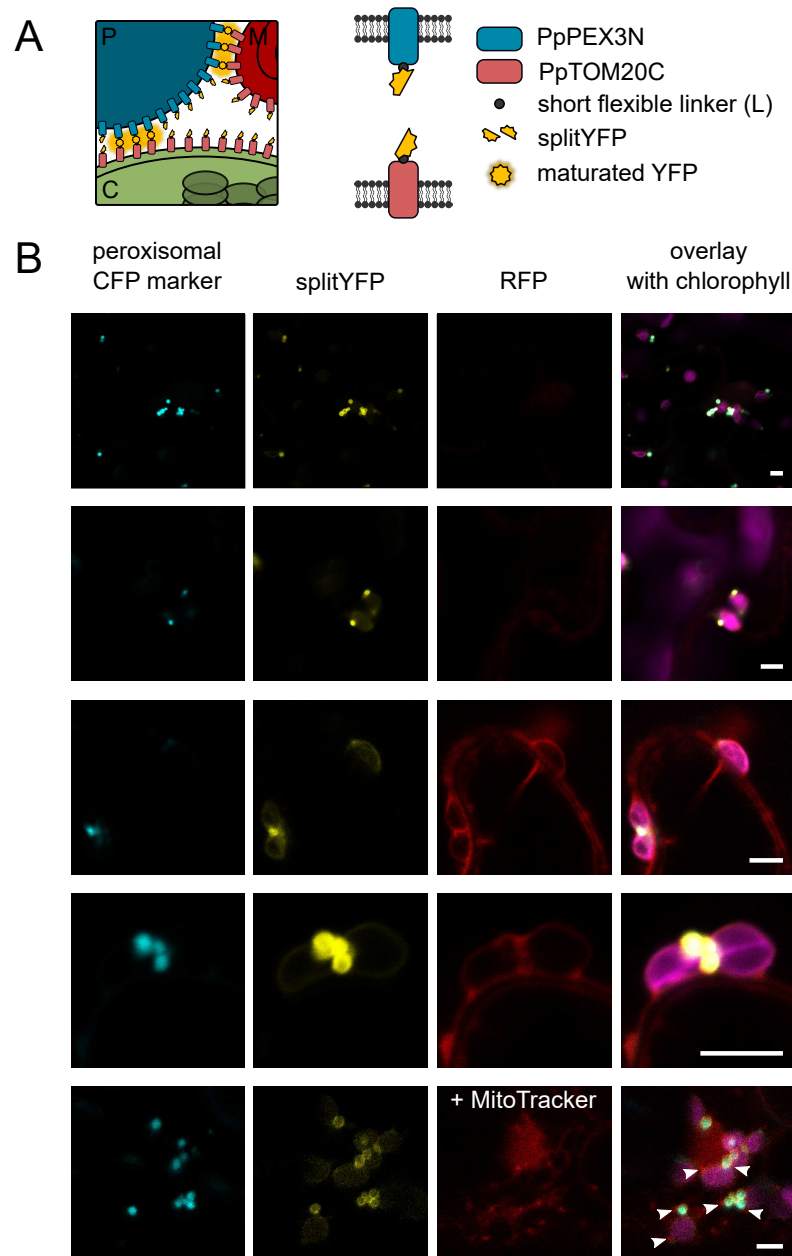


Figure 25: Signal distribution of splitYFP proximity reporter using PpPEX3N and PpTOM20C as fusion partners in the transient system of *N. tabacum*.

A: Design of the splitYFP proximity reporter system. **B:** Representative qualitative CLSM (confocal laser scanning microscopy) images of *N. tabacum* pavement cells co-infiltrated with the construct rBiFC NC 2in1 PpPEX3N:cYFP nYFP:PpTOM20C and pss02:CFP-SKL (peroxisomal CFP marker, [221]). The cytosolic RFP signal was expressed simultaneously with splitYFP fusion proteins and functioned as expression control in this experiment. If labelled, sample was stained with MitoTracker orange (500 nM) by vacuum infiltration for 10-15 min. Arrows mark a mitochondrial signal neighbouring to the YFP signal. Image material with MitoTracker staining was generated in collaboration with Andrea Wübben. Scale bar = 5 μ m.

other, mitochondria were stained with 500 nM MitoTracker orange. The mitochondrial signal is adjacent to the peroxisomal marker signal (marked by arrows), but we did not detect a specific punctual signal at the contact site. Thus, we found a ring-like YFP signal surrounding both peroxisomes and chloroplasts, while neither the peroxisome-mitochondria nor the peroxisome-chloroplast contact sites were specifically labelled with YFP signal.

Although the splitYFP signal was not MCS-specific, the question remained, whether the amount of signal would increase under conditions, where the contact between peroxisomes, mitochondria and chloroplasts is known to be enriched. Oikawa *et al.* tested various photosynthetic conditions and found a higher interaction rate between chloroplasts, peroxisomes and mitochondria under light conditions compared to dark conditions [26]. Therefore, we aimed to test, if the BiFC signal is increased under light conditions compared to dark conditions and to quantify the BiFC signal using the ratiometric BiFC system [160].

For this experiment the same proximity sensor than previously was applied with rBiFC NC 2in1 PpPEX3N:cYFP nYFP:PpTOM20C (figure 26 B). 1 d after the infiltration, *N. tabacum* plants were either transferred to normal light (NL) or dark conditions for 1 d prior to imaging. CLSM images were taken under the same imaging setup for both, light and dark conditions (figure 26 A). The brightness of YFP signal was similar under both conditions, while the RFP signal was brighter in samples of the light treatment than of the dark treatment (figure 26 C). Both observations were confirmed by a signal intensity quantification via python. As readout parameters of the python analysis, the signal area, the total FP fluorescence and the ratio of both (FP fluorescence/area) were chosen (figure 26 D, E). For splitYFP (BiFC), there was no significant difference between light and dark treatment for all three parameters. Regarding the cytosolic RFP signal, the area, the total fluorescence and the ratio were significantly decreased under dark compared to light conditions. This, in turn, had also an impact on the ratiometric analysis (figure 26 E). When the fluorescence per area of BiFC was normalised by that of RFP, the ratio was significantly increased under dark compared to light conditions.

Another question was, whether the overexpression of the splitYFP reporter induce organellar tethering. This was verified in a proximity analysis (results section 1.2 investigating the interaction rate between chloroplasts and peroxisomes (chloroplasts with contact / chloroplasts total (c_c/c_t), peroxisomes with contact / peroxisomes total (p_c/p_t)). We identified that overexpression of the construct BiFC NC PpPEX3N:cYFP nYFP:PpTOM20C (19#2) induced tethering reflected by higher values for c_c/c_t and p_c/p_t compared to WT (figure 14).

The fusion protein PpTOM20C was shown to be localised at MOM and OE (results section 2, figure 22). To be able to exclusively investigate the proximity of one organellar pair and not of two simultaneously, PpTOM20C was replaced by the full length and common OE marker protein OEP7 (figure 27 A, topology see results section 2). The resulting construct rBiFC CC PpPEX3N:cYFP OEP7:nYFP was also co-infiltrated with the peroxisomal marker construct pSS02:CFP-SKL [221]. Representative images depict a clear ring-like YFP signal surrounding the peroxisomes adjacent to the chloroplasts similar to the construct rBiFC NC

III. RESULTS

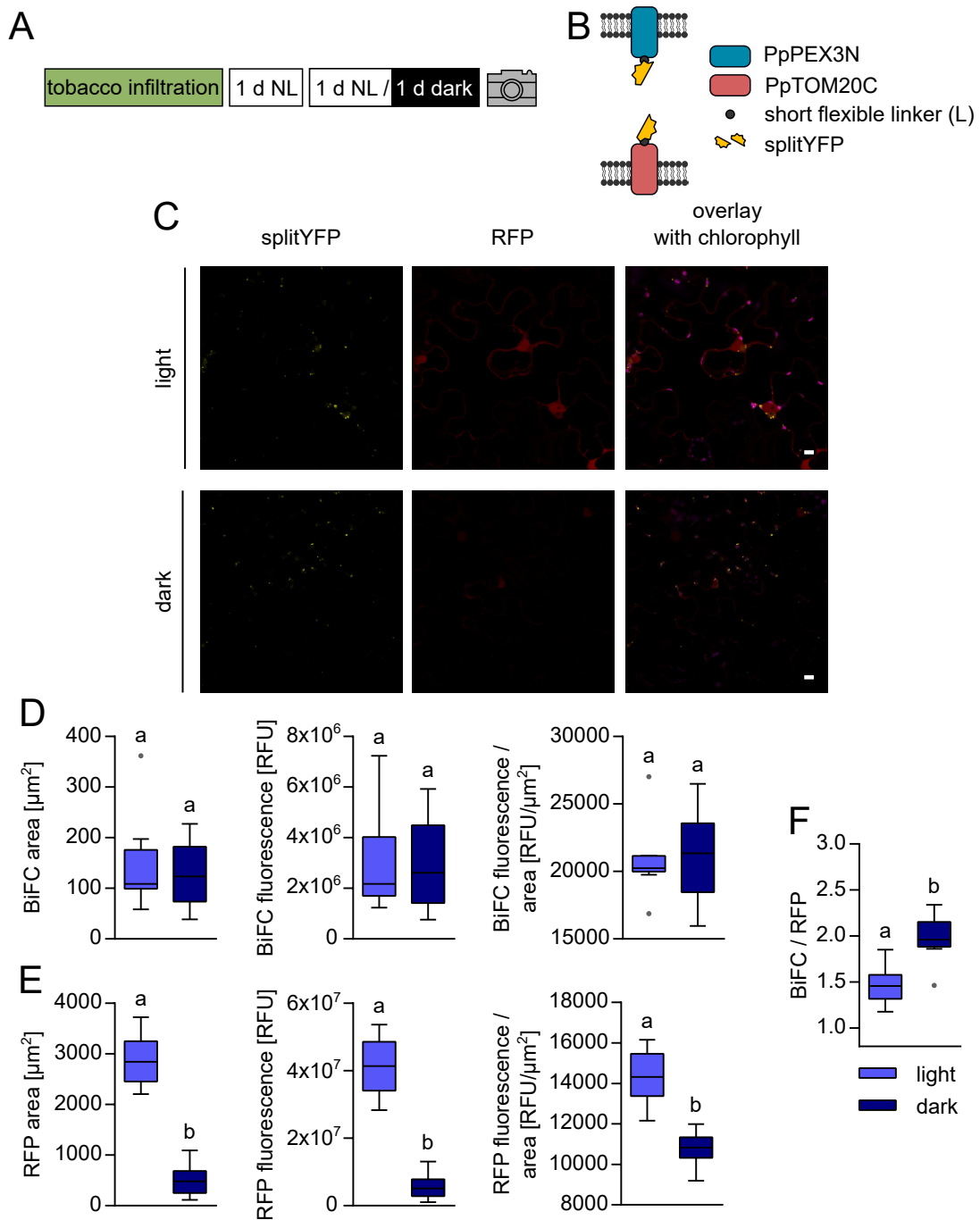


Figure 26: Quantification of BiFC signal under light and dark conditions using PpPEX3N and PpTOM20C as fusion partners in the transient system of *N. tabacum*. **A:** Experimental setup. Normal light (NL, $100\text{--}120 \mu\text{mol photons m}^{-2} \text{s}^{-1}$). **B:** Design of the splitYFP proximity reporter system. **C:** Representative CLSM (confocal laser scanning microscopy) images of light and dark treated plants. Original histogram of CLSM images; 40x objective; 1x zoom; excitation: 488 nm (2,2%) (YFP), 543 nm (8%) (RFP); emission: 535 - 561 nm (YFP), 579 - 615 nm (RFP); gain: 800 (YFP, RFP). Scale bar = 10 μm . **D, E, F:** Quantification of BiFC (splitYFP) (**D**) and RFP (**E**) signal by python. As parameters the area [μm^2], the total fluorescence [RFU] and the ratio of both are shown (**D, E**). Ratiometric analysis of the total fluorescence per area of BiFC normalised by that of RFP (**F**). $n \geq 11$. Data are shown as box plot with median and Tukey whiskers. Significant differences were calculated by an unpaired t-test.

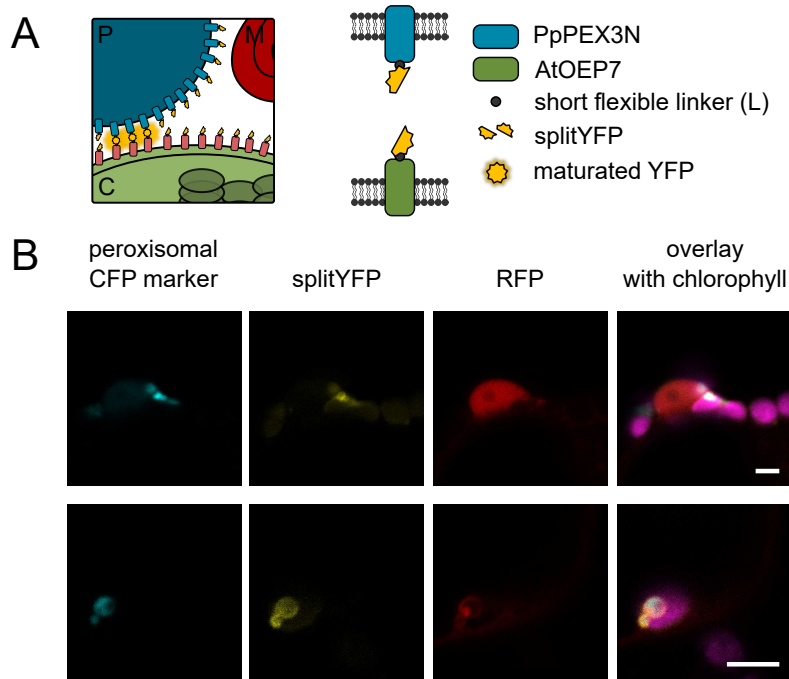


Figure 27: Signal distribution of splitYFP proximity reporter using PpPEX3N and OEP7 as fusion partners in the transient system of *N. tabacum*.

A: Design of the splitYFP proximity reporter system. **B:** Representative qualitative CLSM (confocal laser scanning microscopy) images of *N. tabacum* pavement cells co-infiltrated with the construct rBiFC CC 2in1 PpPEX3N:cYFP OEP7:nYFP and pss02:CFP-SKL (peroxisomal CFP marker, [221]). The cytosolic RFP signal was expressed simultaneously with splitYFP fusion proteins and functioned as expression control in this experiment. Scale bar = 5 μ m.

2in1 PpPEX3N:cYFP nYFP:PpTOM20C, while the OE signal in the splitYFP channel was substantially less pronounced (figure 27 B).

Summarising the previous results, the signal distribution of both proximity reporters (figure 25, 27) was rather similar and not specific at putative contact sites. The only difference was that the YFP signal of the sensor including OEP7 resulted in a relative weaker OE signal than the one including PpTOM20C. For experiments that further test the suitability of splitFP systems as proximity reporters in plants, we continued to work with OEP7 and PpPEX3N as fusion proteins. The reason for this was that this proximity sensor only detects the proximity of exclusively one organelle pair, namely chloroplasts and peroxisomes.

3.1.2 Distance: Influence of linker length to bridge different distances between organel-lar membranes on BiFC signal distribution

Another parameter, which might influence the reassembly of the splitYFP fragments, is the natural distance between the organel-lar membranes at MCS. At MCS, endogenous tethers can occur as bridging complexes as for example SYT1 between ER-PM in plants [228]. These bridging complexes may define the natural distance between the respective organel-lar membranes. Two studies in mammalian cell cultures have demonstrated that the bridging distance of the splitFP reporter is an important parameter to consider. Both investigated ER-MOM contact sites with splitFP reporter of different sizes ranging from approximately 8 nm up to 50 nm [151, 172]. The addition of different linker to their respective reporters

III. RESULTS

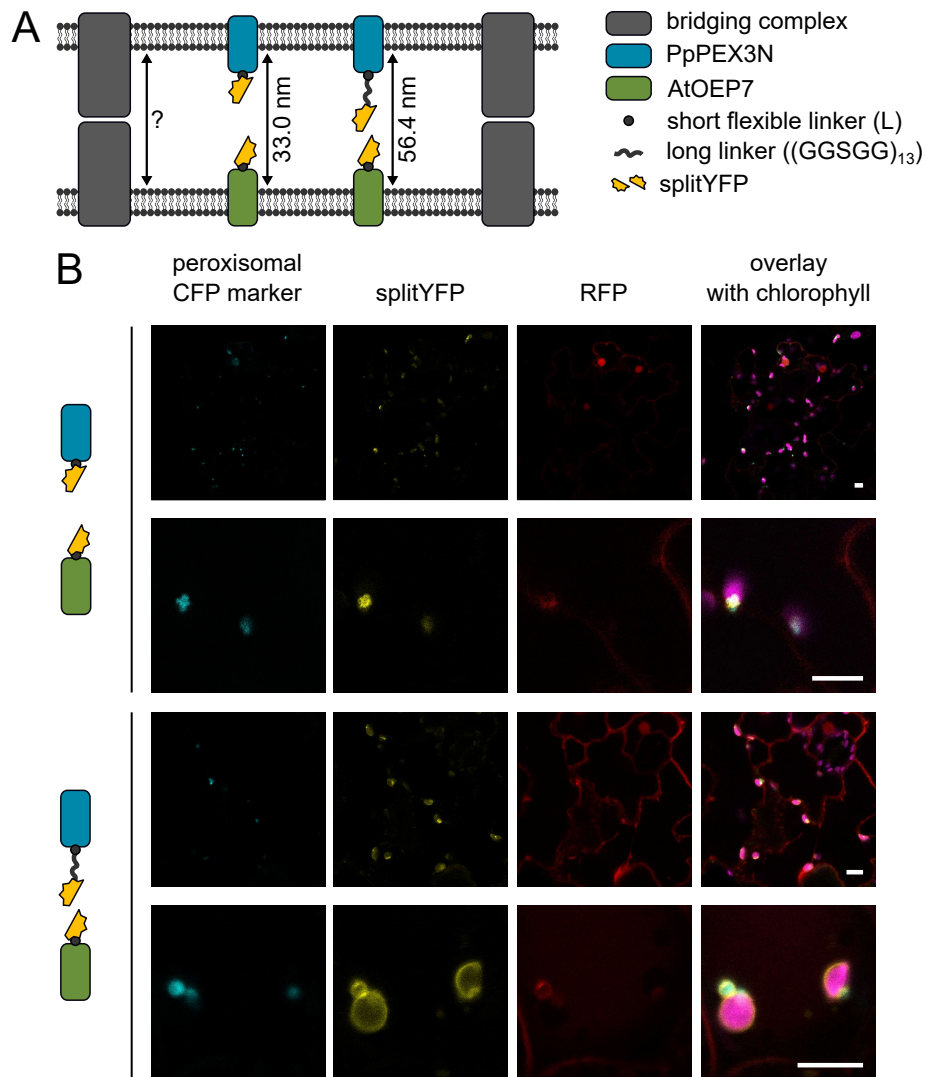


Figure 28: Signal distribution of splitYFP proximity reporter bridging two different distances between the outer envelope (OE) and the peroxisomal membrane (PerM) in the transient system of *N. tabacum*.

A: Schematic scheme of putative organellar contact sites and the different BiFC reporter systems. So far no bridging complexes were identified between OE and PerM leading to an unknown distance to be bridged at membrane contact sites (MCS) of chloroplasts and peroxisomes. Therefore two BiFC reporter systems were designed being able to bridge either 33.0 nm or 56.4 nm between the organellar membranes. **B:** Representative qualitative CLSM (confocal laser scanning microscopy) images of *N. tabacum* pavement cells co-infiltrated with the construct rBiFC CC 2in1 PpPEX3N:cYFP OEP7:nYFP (no additional linker) / rBiFC CC 2in1 PpPEX3N:(GGSGG)₁₃:cYFP OEP7:nYFP (additional long linker) and pss02:CFP-SKL (peroxisomal CFP marker, [221]). The cytosolic RFP signal was expressed simultaneously with splitYFP fusion proteins and functioned as expression control in this experiment. Scale bar = 5 μ m.

altered the pattern of the BiFC signal [151, 172] (for details see table 3). Between chloroplasts and peroxisomes, no bridging complexes have been identified yet, which is why the required distance to be bridged is still unknown. It was therefore of particular interest to use proximity reporters of different sizes in plants in order to test, how and whether the splitYFP pattern changed. The minimal size of the sensor was predefined by rBiFC vector building blocks (HA-tag, Myc-tag, splitYFP, Gateway-linker) [160] and a short flexible linker connecting the FP-tag and the protein fusion partner resulting in a calculated size of 33.0 nm (figure 28 A). For this reason, it was only possible to increase the size of the reporter by adding an additional linker, similar to the two mammalian studies [151, 172]. As additional long linker an flexible and repetitive aa sequence (GGSGG)₁₃ was chosen to increase the distance to be bridged by 23.4 nm to 56.4 nm (figure 28 A). To test, if an addition of a long linker had an impact on the YFP signal distribution, a replica of the proximity sensor including OEP7 was cloned adding a long linker between PpPEX3N and cYFP (BiFC CC PpPEX3N(GGSGG)₁₃:cYFP OEP7:nYFP, figure 28 A).

As previously described, imaging of the construct without the linker (see also figure 27) revealed a clear PerM signal in the splitYFP channel and a weak OE signal (figure 28 B). Adding the (GGSGG)₁₃-linker, the signal distribution was quite similar to those of the construct without the additional long linker, but the OE and PerM signal were substantially brighter and more clear (figure 28 B). In summary, the splitYFP signal increased proportional to the size of the proximity reporter, while the signal distribution itself did not alter towards MCS-specificity.

3.1.3 Comparison of splitFP sensor systems

Besides splitYFP, another BiFC reporter called saGFP has been widely used to study MCS (references see table 2 & 3). While the splitYFP is divided in almost equally sized fragments [159], the saGFP is divided between 214 aa and 215 aa, which resulting in the unequally sized GFP₁₋₁₀ (1-214 aa, β -barrel₁₋₁₀) and GFP₁₁ (215-230 aa, β -barrel₁₁) [166]. Differently to splitYFP, the maturation of the two fragments is not dependent on protein-protein interaction of the fusion proteins but they can self-assemble [159, 166]. In 2020, a combinatorial saGFP reporter system for ER-organellar MCS visualisation in plant cells was published [152]. Investigating the interaction of ER-chloroplasts, the study detected punctual signal in transient systems (*N. benthamiana* pavement cells, *N. tabacum* protoplasts) [152]. Based on this more recent results, we aimed to compare both splitFP systems for our proximity reporter approach regarding their signal distribution.

For a reliable BiFC readout, equal expression levels of both saGFP fragments is crucial [160]. This can only be guaranteed if both fragments are expressed simultaneously and under the same promoter. This principle was used in the rBiFC 2in1 vector systems of Christopher Grefen [160]. However, no vector system was available, which fulfil the mentioned criteria and contained saGFP instead of splitYFP. For that reason, we designed a vector system using a similar approach as the one used by Grefen & Blatt [160] including the Gate-

III. RESULTS

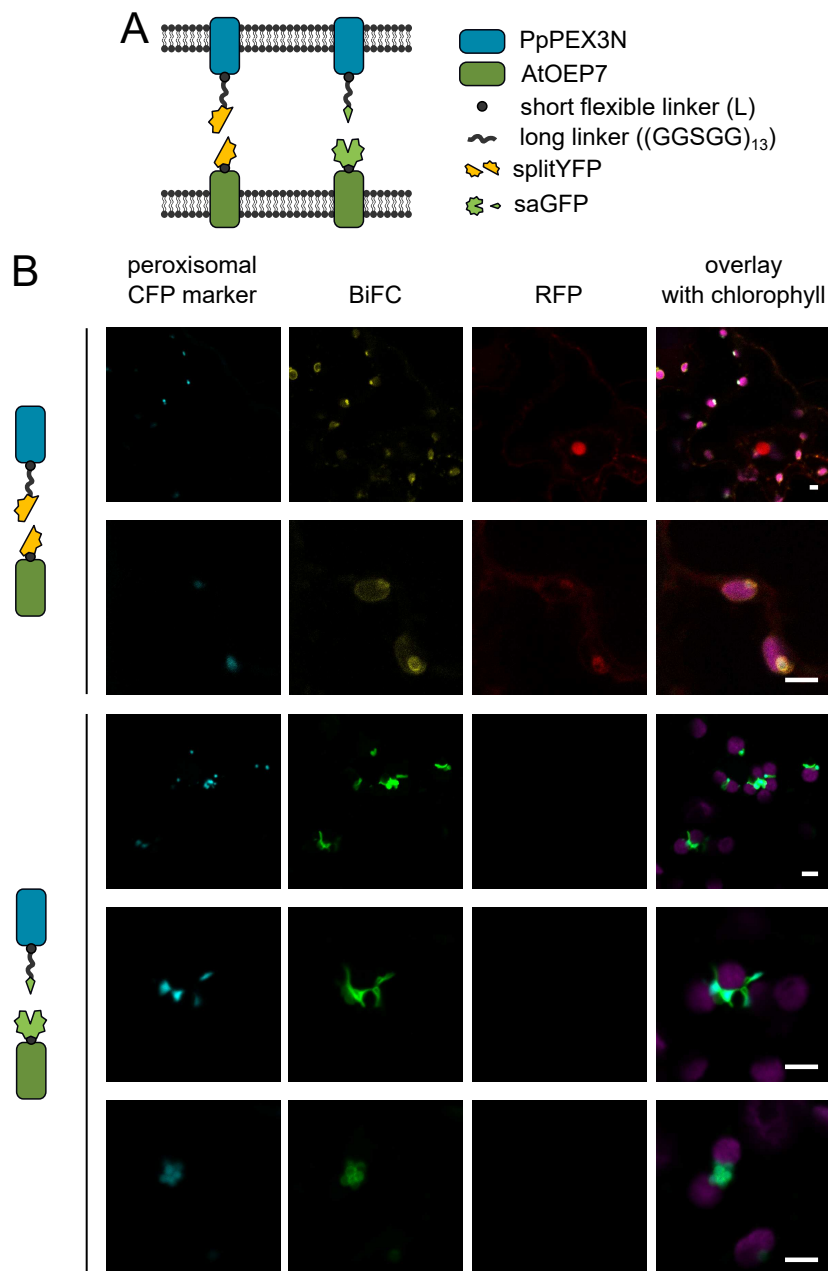


Figure 29: Comparison of splitYFP and saGFP signal using using PpPEX3N:(GGSGG)₁₃ and OEP7 as fusion partners in the transient system of *N. tabacum*.

A: Schematic overview of the proximity BiFC (bimolecular fluorescence complementation) reporter systems using splitYFP and saGFP fused to PpPEX3N:(GGSGG)₁₃ and OEP7. **B:** Representative qualitative CLSM (confocal laser scanning microscopy) images of *N. tabacum* pavement cells co-infiltrated with the construct rBiFC CC 2in1 PpPEX3N:(GGSGG)₁₃:cYFP At:OEP7:nYFP / 2in1 pInd CC PpPEX3N:(GGSGG)₁₃:GFP₁₁ At:OEP7:GFP₁₋₁₀ and pss02:CFP-SKL (peroxisomal CFP marker, [221]). The cytosolic RFP signal was expressed simultaneously with splitYFP fusion proteins and functioned as expression control in for the rBiFC 2in1 system (splitYFP). For the saGFP signal verification the self-cloned 2in1 pInd dexamethasone inducible system was used (further information see results section 4). The induction was performed after 2 d of *N. tabacum* leaf infiltration for additional 1 d with 20 μ M dexamethasone. BiFC signal: splitYFP in yellow, saGFP in green. Scale bar = 5 μ m.

way cloning cassettes, but under an inducible promoter system [207, 229–231]. The reason for implementing an inducible promoter was that it can also be helpful to generate stable *N. tabacum* lines without influencing the organelle interaction by unwanted artificial tethering (cloning procedure and verification see results section 4).

In figure 29 the comparison of the splitYFP and saGFP reporter systems are depicted using PpPEX3N:(GGSGG)₁₃ and At:OEP7 as fusion partners. Both constructs were co-infiltrated with a peroxisomal CFP marker (pSS02:CFP-SKL, [221]) in *N. tabacum* and imaged in pavement cells. The splitYFP construct was expressed constitutively under the 35sP, whereas the saGFP expression was induced by 20 μM dexamethasone for 1 d prior imaging (further information for the dexamethasone inducible system see results section 4). The reason, that both BiFC reporters were not compared under the same promoter system, was simply a time limitation and the priority on the 2in1 pInd saGFP vector.

While splitYFP (BiFC channel, yellow) labelled the OE and the PerM, the saGFP signal was differently distributed (figure 29 B). In some cells, we detected a GFP signal surrounding the peroxisomal matrix similar as the splitYFP and the peroxisomes formed clusters adjacent to chloroplasts (figure 29 B, 5th row). In other cells, the GFP signal was increased at the putative interaction sites between chloroplasts and peroxisomes. The involved peroxisomes appeared to be deformed and to elongate alongside the saGFP signal (figure 29 B, 3rd/4th row). The GFP signal was not only concentrated on the contact site between chloroplasts and peroxisomes but seemed to be partly stretched alongside the chloroplast (figure 29 B, 3rd/4th row).

In general, we were able to generate a saGFP-based proximity reporter system and to compare both sensors side by side. The comparison revealed that, the splitYFP mainly labelled the whole organellar membrane of both chloroplasts and peroxisomes, whereas in some cells the saGFP was also located the whole PerM. In other cells, however, the saGFP signal labelled not the whole PerM but appeared to be more targeted to chloroplasts-peroxisome contact sites.

3.2 Testing the BiFC system using known interacting and non-interacting MCS proteins at EPCS

Another parameter, which might influence the suitability of splitFP systems as proximity reporter, are the properties of their fusion proteins. In the previous section we tested the suitability of splitFP systems as proximity sensors, when the FP fragments homogeneously labelled the organellar membranes. We also wanted to address the question, if the signal distribution of splitFP altered, when either interacting or non-interacting MCS-specific proteins functioned as fusion partners. Especially for splitYFP, which maturation is known to be dependent on protein-protein interaction [159], one open question was, if its maturation can also be caused by the proximity of the organelle or whether a protein-protein interaction

III. RESULTS

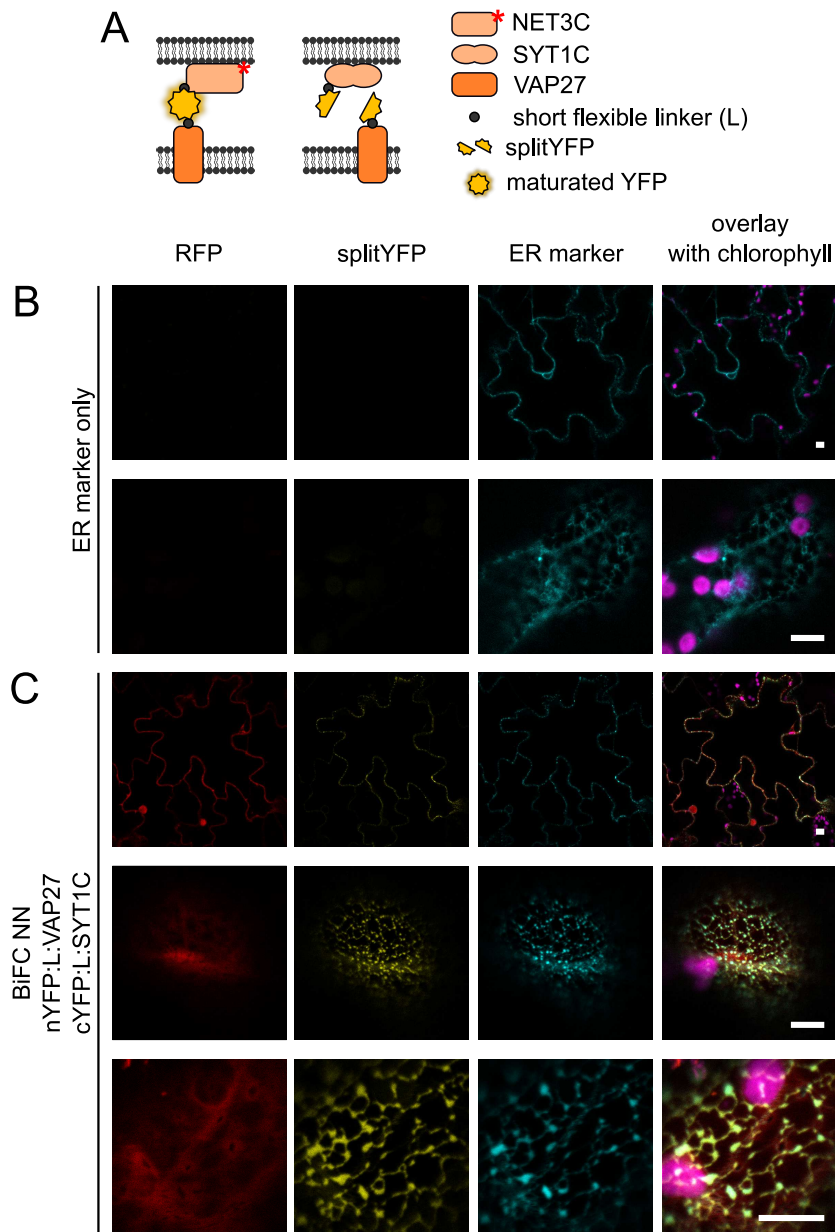


Figure 30: Signal distribution of splitYFP proximity reporter using VAP27-1 and SYT1C as fusion partners in the transient system of *N. tabacum*.

A: Schemata of the design of the splitYFP proximity reporter system. The protein pair VAP27-1 and NET3C serve as control for MCS specific and interacting proteins. NET3C is labelled with a red asterisk, since in our hands protein expression did not emit a YFP signal, as well as in combination with VAP27-1 in the 2in1 rBIFC vector system (data not shown). The protein pair VAP27-1 and C-terminal region of SYT1 (SYT1C) serve as control for MCS specific and non-interacting proteins. **B, C:** Representative qualitative CLSM (confocal laser scanning microscopy) images of *N. tabacum* pavement cells infiltrated with CFP-ER marker construct (AtWak2(signal peptide):CFP:ER retention signal [186]) (**B**) and **C:** CFP-ER marker co-infiltrated with the construct rBIFC NN 2in1 nYFP:L:VAP27-1 cYFP:L:SYT1C. The cytosolic RFP signal was expressed simultaneously with splitYFP fusion proteins and functioned as expression control in this experiment. Scale bar = 10 μm .

is required in this case as well. So far MCS specific proteins have not been identified between the photorespiratory organelles.

To test if the specificity of the splitYFP reassembly demand MCS specific proteins, we chose known EPCS membrane proteins as fusion partners. The idea was to investigate on the one hand MCS specific and interacting fusion partners represent protein-protein interaction. For this purpose the ER membrane located VAP27-1 and PM located NET3C were chosen ([58], figure 30 A). Unfortunately, in our hands the expression of NET3C did not work, neither for the topology assay (figure 20 A) nor in combination with VAP27-1 (data not shown).

On the other hand we chose MCS specific but non-interacting proteins as FP-fusion partners for labelling MCS. Therefore, we combined the ER membrane protein VAP27-1 and C-terminal calcium-binding domains (C₂A/C₂B) of SYT1 (SYT1C), which is an EPCS tether protein [29] (topology see results section 2). In figure 30 C representative CLSM images of the construct rBiFC NN 2in1 nYFP:L:VAP27-1 cYFP:L:SYT1C co-infiltrated with CFP-ER marker (AtWak2(signal peptide):CFP:ER retention signal [186]) are shown. The ER marker signal overlapped with those of the splitYFP-based reporter (figure 30 C). It is worth noting that the structure of the ER in general changed overexpressing the control splitYFP-based sensor compared to WT cells (figure 30 B, C). While the ER marker in the WT background had the expected network structure (B), the ER was additionally accumulated at puncta when co-infiltrated with the splitYFP-based control sensor construct (C).

4 Generation and verification of a 2in1 inducible vector system (pInd) for fluorescent protein (FP) sensor systems

To be able to compare the two BiFC reporter systems splitYFP and saGFP, a new vector system was cloned in this study. Another requirement of this system was to obtain inducible tether constructs for the generation of stable lines. The reason for this was that at that time it was unclear, whether the plants would be viable, when a synthetic tether was constitutively expressed (further results see 6) or splitFP proximity sensor constructs. For the cloning design, several criteria had to be considered: 1) The equal expression level of the splitFP fragments, 2) the suitability for generating stable lines, but being also suitable to be tested in a transient system, 3) the flexibility to change the fusion partners of the splitFP fragments easily and quickly, and 4) a quality check of the vector system in design and functionality.

4.1 Cloning of pInd vectors for split fluorescent proteins (splitFP) and Förster resonance energy transfer (FRET)/ FLIM systems

The first criteria regarding the vector design was, to ensure the same expression level of non-fluorescent splitFP fragments [160]. To meet the criteria, we chose a similar strategy as in the rBiFC 2in1 vector system [160] co-expressing both fusion-proteins under the same promoter and from a single plasmid (design see figure 31 A). For the rBiFC 2in1 vector system, the authors used the viral 35S promoter (35sP) system [160]. Starting this project, it has not been tested, if stable plant lines are viable under a constitutive expression of a splitYFP-based proximity sensor construct. For this reason, we decided to exchange the 35sP by a glucocorticoid-inducible promoter system and, to allow stable transformation, adding the plant selection marker BastaR cassette (figure 31 A, B). The origin of an inducible promoter system was developed by Moore *et al.* [229] and it was further developed to a system, which enables glucocorticoid-dependent transgene expression [230, 231]. It consists of three building blocks: 1) A chimeric promoter pOp, which consists of two ideal lac operators, repeated 6 times and cloned upstream of a minimal CaMV35S promoter (pOp6Cam35Sm), 2) a transcription activator consisting of a high-affinity DNA binding mutant of the lac repressor and the transcription activation domain-II of GAL4 (LhG4) of *Saccharomyces cerevisiae* and 3) the ligand binding domain of a rat glucocorticoid receptor (GR), which is fused N-terminally to LhG4 ([229, 230], figure 31). The principle of the induction using the pOp6/GR-LhG4 system introduced in our vector system is shown in figure 31 B. The fusion protein GR-LhG4 is constitutively expressed under an UBQ10P. If no glucocorticoid, here dexamethasone, is present, the heat shock protein HSP90 interacts with the GR, which in turn leads to an inactivation of the complex. The addition of dexamethasone mediates the dissociation of the GR-LhG4 from the heat shock protein and allows the binding to pOp6, which leads to an activation of

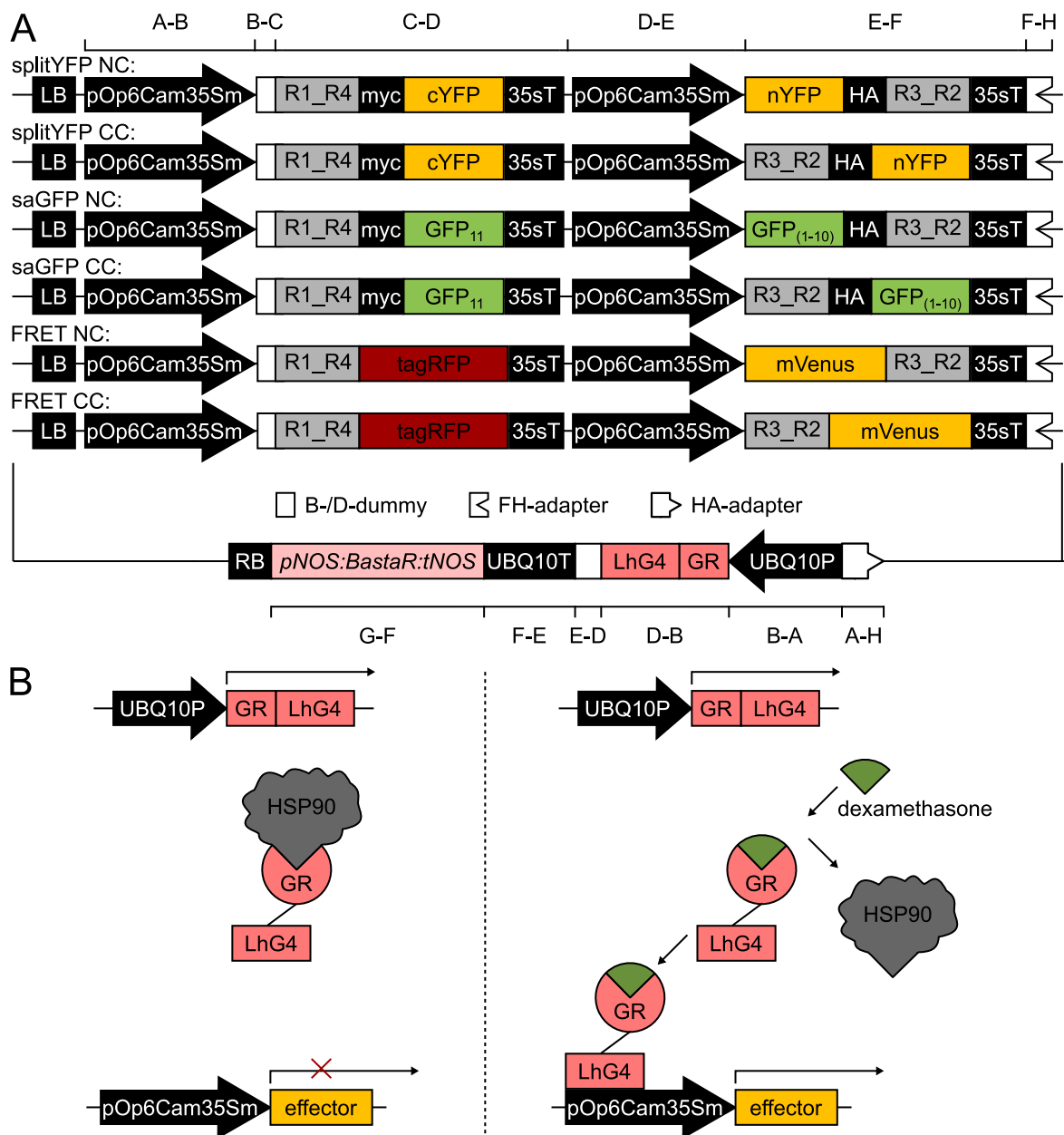


Figure 31: Cloning strategy for dexamethasone inducible 2in1 reporter system.

A: Schematic vector maps of 2in1 pInd destination system. The cloning procedure was performed via Greengate cloning [206], which is based on modular system. The correct assembly of the modules is ensured by different overhangs (A-H) resulting from a digestion with Eco311 (Bsal), with the overhangs of adjacent fragments complementing each other. The vector design was based on a pOp6/GR-LhG4 dexamethasone inducible vector system [207, 229–231], the Grefen 2in1 vector system (splitYFP: [160]; FRET/FLIM: [177]), a plant proven saGFP reporter [208] and available Greengate modules [206]. LB (left border), pOp6Cam35Sm (chimeric promoter pOp consisting of two ideal lac operators, repeated 6 times and cloned upstream of a minimal CaMV35S promoter), B-/D-dummy (default random sequence if no specific N-/C-tag is desired), R2_R3/R1_R4 (recombination Gateway sites), HA (hemagglutinin epitope-tag), myc (myc epitope-tag), 35sT (cauliflower mosaic virus 35T terminator), nYFP/cYFP (N- or C-terminal EYFP fragments (nYFP: 1–155 aa, cYFP: 156–239 aa), GFP_{1–10}/GFP₁₁ (N- or C-terminal of GFP fragments (GFP_{1–10}: 1–215 aa, GFP₁₁: 216–232 aa), UBQ10P (UBIQUITIN10 promoter), GR (ligand binding domain of a rat glucocorticoid receptor), LhG4 (transcription activator consisting of a high-affinity DNA binding mutant of the lac repressor and the transcription activation domain-II of GAL4 of *Saccharomyces cerevisiae*), UBQ10T (UBIQUITIN10 terminator), pNOS:BastaR:tNOS (plant selection marker cassette, Basta resistance), RB (right border).

B: Schematic principle of the 2in1 pInd dexamethasone inducible system (schemata adapted from [207]). The pOp6/GR-LhG4 system consists of following building blocks: A chimeric promoter pOp6Cam35m, a transcription activator LhG4 and the ligand binding domain of a rat glucocorticoid receptor (GR), which is fused N-terminal to LhG4 [229, 230]. The fusion protein GR-LhG4 is constitutively expressed under an UBQ10P. In the absence of a steroid ligand (dexamethasone), the heat shock protein HSP90 interacts with the GR, leading an inactivation of the complex. The presence of dexamethasone to GR mediates dissociation of the fusion protein from the heat shock protein and allow the binding to pOp6 to activate the effector transcription [230, 232, 233].

the effector transcription [230, 232, 233].

As effector, we used the FP expression cassettes similar to that of the rBiFC system [160]. Upstream and downstream of the respective FP or splitFP so called MultiSite Gateway cassettes [234] were attached. The technology based on the bacteriophage λ site-specific recombination system [235, 236]. Grefen & Blatt developed a 2in1 cloning system that enabled the simultaneous and specific cloning of two genes into two independent expression cassettes on the same plasmid [160]. As one recombination cassette they used attR1-attR4 sites flanking a cassette of chloramphenicol acetyltransferase resistance gene (CmR) and gyrase inhibitor gene *ccdB*, which is a positive selection gene [237]. The 2nd recombination cassettes consisted of a lacZ expression cassette, which enabled blue/white selection in *Escherichia coli* flanked by attR3-attR2 sites. Thus, two genes of interest were allowed to be integrated within in one recombination Gateway step [160], which facilitate the flexibility to easily and quickly change the fusion partners of the splitFP fragments. Additional to the splitFP systems splitYFP and saGFP, two similar vectors were designed including mVenus and tagRFP as FP instead of a BiFC reporter. Since tagRFP and mVenus each are capable of fluorescence, these vectors were intended as proof of functionality of the vector system itself and the induction (figure 31 A).

The cloning procedure itself was performed by Greengate cloning [206], which is a module based system. Normally, the Greengate cloning system is based on six different types of entry vectors (plant promoter, N-terminal tag, coding sequence, C-terminal tag, plant terminator and plant selection marker cassette), which are commercially available. The Entry vectors contain two Eco31I (BsaI) recognition sites, leading to specific overhangs of 4 bases (A-G). The correct assembly of the modules with a destination vector was ensured by these respective overhangs (A-H) after a digestion with Eco31I (BsaI), with the overhangs of adjacent fragments complementing each other [206]. In order to be able to assembly more than only six modules, Lampropoulos *et al.* developed intermediate vectors for combining two expression cassettes on one T-DNA [206]. As intermediate step, two expression cassettes with overhangs A-H and H-G were generated by using the intermediate vectors (pGGM000, pGGN000) and Entry vector adapter (FH-/HA-adapter). Both intermediate vectors were combined and assembled with the available destination vector of the Greengate module kit.

In this work, we applied the Greengate method with the intermediate vectors. Instead of using only modules available in the Greengate kit, most modules were cloned individually. Following vectors were chosen as templates for the Entry modules: 1) available Addgene vectors of Schürholz *et al.* [207] for the pOp6/GR-LhG4 dexamethasone inducible vector system, 2) the Grefen 2in1 vector system (splitYFP: [160]; FRET/FLIM: [177]) for the FP expression cassettes, and 3) an in plants applied saGFP reporter [208] as substitute for the splitYFP reporter. As depicted in table 19 the modules were either generated by synthesis or by PCR. The PCR fragments were cloned into the respective empty pEntry vector of the Greengate kit and verified by sequencing. The next step was to generate the intermediate vectors. There-

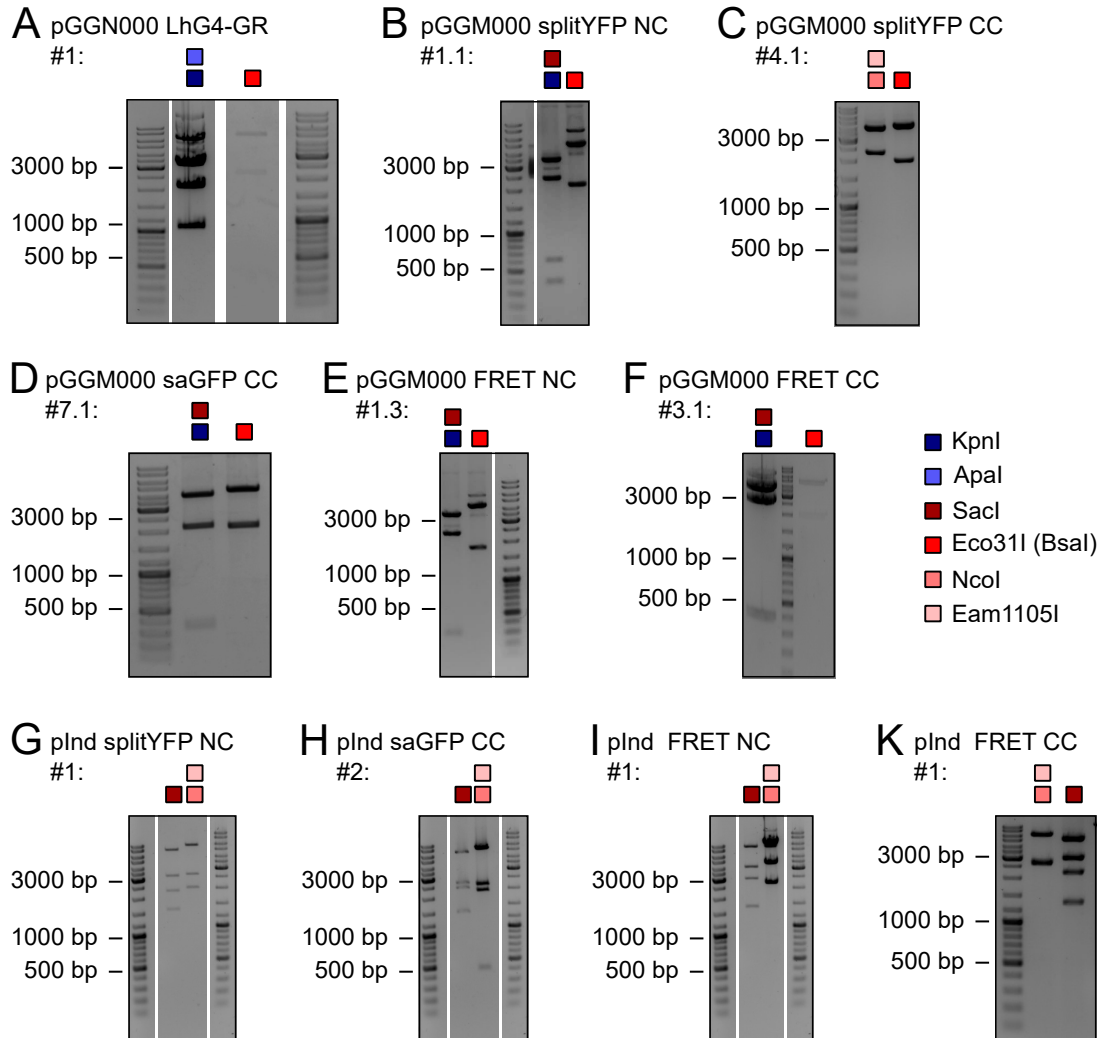


Figure 32: Verification of successfully cloned intermediate and destination vectors of the 2in1 pInd system by usage of restriction enzymes.

A-F: Digest of successfully cloned intermediate (pGGN000 LhGR, pGGM000) plasmids with KpnI, ApaI, SacI and Eco31I (BsaI). The right assembly of the Entry modules were additionally verified by sequencing. pGGM000 saGFP NC was not successfully cloned during this work. **G-K:** Digest of successfully cloned destination (pInd) plasmids with SacI, NcoI and Eam1105I. All shown pInd clones were additionally verified by sequencing regarding the right assembly of the intermediate vectors. The vector pInd splitYFP CC #2 was also successfully cloned, but only verified by sequencing. Expected fragment size: **A:** KpnI + ApaI: 3.490 bp, 2.116 bp, 1.054 bp; Eco31I (BsaI): 4.625 bp, 2035 bp. **B:** KpnI + SacI: 3.260 bp, 2.306 bp, 615 bp, 409 bp; Eco31I (BsaI): 4.555 bp, 2.035 bp. **C:** NcoI + Eam1105I: 4.237 bp, 2.362 bp; Eco31I (BsaI): 4.564 bp, 2.035 bp. **D:** KpnI + SacI: 4.064 bp, 2.102 bp, 409 bp; Eco31I (BsaI): 4.540 bp, 2.035 bp. **E:** KpnI + SacI: 4.175 bp, 2.699 bp, 409 bp; Eco31I (BsaI): 5.248 bp, 2.035 bp. **F:** KpnI + SacI: 4.074 bp, 2.699 bp, 409 bp; Eco31I (BsaI): 5.147 bp, 2.035 bp. **G:** SacI: 5.672 bp, 2.715 bp, 2.090 bp, 1.398 bp; NcoI + Eam1105I: 6.852 bp, 2.894 bp, 2.129 bp. **H:** SacI: 5.622 bp, 2.511 bp, 2.279 bp, 1.398 bp; NcoI + Eam1105I: 6.802 bp, 2.408 bp, 2.158 bp, 442 bp. **I:** SacI: 5.622 bp, 3.108 bp, 2.390 bp, 1.398 bp; NcoI + Eam1105I: 6.802 bp, 3.488 bp, 2.228 bp. **K:** SacI: 5.622 bp, 3.108 bp, 2.289 bp, 1.398 bp; NcoI + Eam1105I: 6.802 bp, 2.860 bp, 2.755 bp. GeneRuler DNA Ladder Mix (Thermo) was used as marker. For vector maps see supplemental figure S2 & S3.

III. RESULTS

fore, additional available Greengate modules [206] were used. The GR-LhG4 under the constitutive ubiquitin promoter (UbiQP) and Basta plant selection marker cassette were cloned in the pGGN000 backbone. In the backbone of pGGM000, all different Gateway-FP expression cassettes as NC and CC combination were planned to be cloned under the pOp6Cam35m promoter (figure 31 A).

After the transformation of the respective Greengate reaction in *E. coli*, single colonies were screened via a colony PCR. Plasmids of the positive colonies were accumulated and purified. The plasmid verification was performed via digestion (figure 32 A-F) and sequencing of the assembly sites, where the Entry modules overlapped. The vectors were digested with BsaI and with an enzyme combination (KpnI + ApaI, KpnI + SacI, NcoI + Eam1105I). For pGGN000 GR-LhG4 #1 (Figure 32 A), the gel of digestion with KpnI and ApaI showed, in addition to the three expected bands, further higher bands at about 4000 bp, 6000 bp and >10000 bp. The bands at 4000 bp and 6000 bp were probably partially digested fragments, as they resulted from the sum of the individual expected fragments. Moreover, additional sequencing of this clone confirmed correct assembly of the entry modules and proved that the clone was correct. The same was true for other intermediate clones whose digestion showed additional bands. Similarly, the size of the fragments was determined by the sum of the individual expected bands and the correct assembly of the input modules was confirmed by sequencing.

In reference to the digestion pattern and sequencing, positive clones were found for pGGN000 GR-LhG4, pGGM000 splitYFP NC, pGGM000 splitYFP CC, pGGM000 saGFP CC, pGGM000 FRET NC and pGGM000 FRET CC (figure 32 A-F), whereas for pGGM000 saGFP NC, no positive clones were identified.

Performing a Greengate reaction with Greengate destination vector pGGZ001 and the generated intermediate vectors (pGGN000 GR-LhG4 vector with respective pGGM000 vector), five different 2in1 pInd destination vectors were generated. Four vectors were verified by digestion with SacI and NcoI + Eam1105I (pInd splitYFP NC #1, pInd split saGFP CC #2, pInd FRET NC #1, pInd FRET CC #1, figure 32 G-K) and sequencing, whereas the correct assembly of pInd splitYFP CC #1 was only verified by sequencing. As the intermediate vector pGGM000 saGFP NC was missing, generating the pInd saGFP NC vector was not possible.

4.2 Verification of the dexamethasone induction of 2in1 pInd vector

The next step was to test, if the dexamethasone induced FP expression of the 2in1 pInd vector system worked in general and if it showed a dose dependency. The pOp6/GR-LhG4 promoter system was investigated in detail in stable *A. thaliana* [230] and *N. tabacum* [231] lines. In both organisms, they tested the dose-dependency as well as the time course of the induction using a GUS reporter. The induction of the GUS gene expression or activity was shown to increase over time and to be dose-dependent in both species [230, 231].

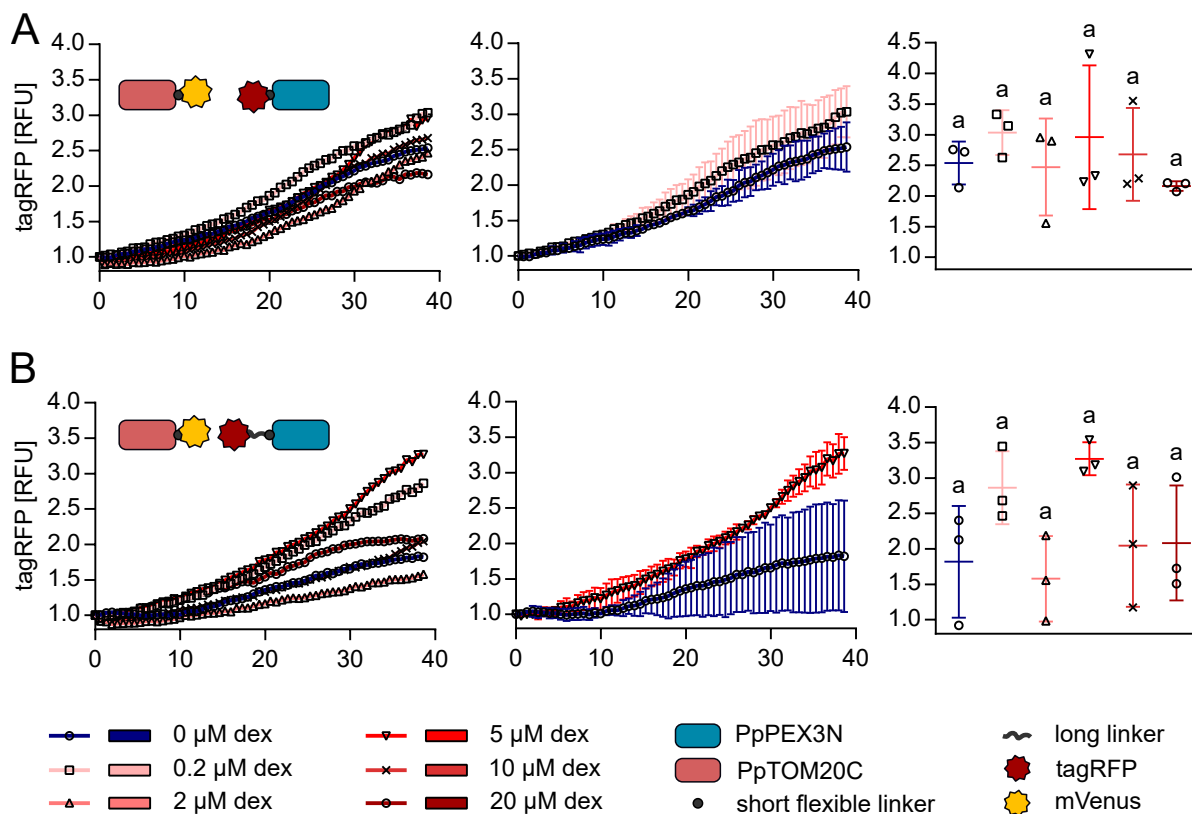


Figure 33: *In vivo* monitoring of dexamethasone induction of pInd FRET vector system verified by the respective sensor fluorescence in the transient system of *N. tabacum*.

N. tabacum leaves were infiltrated with FRET (A, B) sensor constructs. *N. tabacum* leaf discs were submerged in wells of a 96-well plate prefilled with assay medium. After about 1 h of dark incubation, assay medium was exchanged by fresh medium with different concentrations of dexamethasone (t_0). The relative fluorescence unit (RFU) of the respective fluorescent sensor was detected over time by the plate reader. The graphs represent the relative fluorescence unit (RFU) normalised over the respective t_0 value of each replicate. While the left graphs show the RFU over time of all concentrations without standard deviations, the middle graph represents the results of the control and the data set the largest deviation to the control including the standard deviations. The right panel represents the RFU at the end of the monitoring (t_E). $n = 3$ (of one infiltrated leaf) (A, B). Data are represented as mean, mean + standard deviation (SD) and box plot with Tukey whiskers (from left to right). Significant differences were calculated according to One-way ANOVA with Tukey's multiple comparisons test. Excitation: 540-20 nm; emission: 580-20 nm.

As we used the same inducible promoter system as Craft *et al.* [230] and Samalova *et al.* [231], we aimed to test the time- and dose-dependency of the transcript gene expression with a similar experimental setup. Since the 2in1 pInd vector system includes FP expression cassettes, we quantified the relative fluorescence intensity instead of the GUS transcript level or activity. We developed an plate reader assay using a similar concentration range than in Craft *et al.* [230] and Samalova *et al.* [231] to be able to monitor the dexamethasone induction simultaneously at different concentration and over time. The assay was performed using transiently infiltrated *N. tabacum* leaves 2 d to 5 d after infiltration with the respective 2in1 pInd sensor construct. *N. tabacum* leaf discs were submerged in wells of a 96-well plate prefilled with assay medium. To minimise autofluorescence signal triggered by the cutting process, the leaf discs were incubated for 1 h in the dark. Afterwards, the assay medium was exchanged with fresh medium including different concentrations of dexamethasone (t_0) and the FP fluorescence was monitored over time.

Since the 2in1 pInd splitFP vector system did not implement a expression control, the FP

III. RESULTS

expression was first tested in one of the generated 2in1 pInd FRET vectors. Therefore, Pp-TOM20C and PpPEX3N or PpPEX3N(GGSGG)₁₃ were cloned into the destination vector 2in1 pInd FRET NC via Gateway recombination. The induction assay was performed 5 d after the *N. tabacum* infiltration. In figure 33 the tagRFP fluorescence normalised over the respective t_0 fluorescence of both pInd FRET NC constructs is shown. In the left column, the means of all induction curves are depicted (0 μ M, 0.2 μ M, 2 μ M, 5 μ M, 10 μ M, 20 μ M dexamethasone). The tagRFP fluorescence was neither dose-dependent nor consistent between the two constructs (figure 33, left column). Within the replicates the standard deviation was quite high, which is depicted in figure 33 (the middle column) showing the curve of the negative control of 0 μ M dexamethasone and the curve with the highest mean plus the respective standard deviation.

However, for both constructs a time dependent increase of the relative tagRFP fluorescence was detected independent on the dexamethasone application (figure 33, left column). Comparing the raw tagRFP fluorescence values at the beginning of the experiment (t_0) with that at the end of the monitoring (t_E), there were no significant differences within one time point of the different concentrations, but a significant increase from t_0 to t_E (supplemental figure S4 D, E). This increase was also reflected in the relative increase at the end point of the experiment (38.6 h, figure 33, right column), which average was also for the negative control higher than 1. The average normalised fluorescence ranged between 1.81 and 3.2 and were not significantly different between the different dexamethasone concentrations and the control treatment. Thus, a time dependent increase of RUF was identified but the dose-dependency of the gene expression could not be detected by the plate reader assay using the 2in1 pInd FRET NC vector backbone.

In addition, the 2in1 pInd splitFP destination vectors needed to be test. Therefore, OEP7 and PpPEX3N or PpPEX3N(GGSGG)₁₃ were selected as protein partners. *N. tabacum* leaves were infiltrated with *A. tumefaciens* containing the respective 2in1 pInd splitYFP or saGFP constructs. The procedure and analysis of the plate reader experiment was performed similar as previously described using the pInd FRET vector system. The only difference in the experimental setup was that the leaves for the constructs without the long linker (figure 34 A, C; pInd saGFP/splitYFP CC OEP7 PpPEX3N) were infiltrated 2 d instead of 5 d prior starting with the dexamethasone application. In figure 34 the BiFC (saGFP/splitYFP) fluorescence normalised over the respective t_0 fluorescence is shown. For all shown constructs, the fluorescence monitoring revealed a time dependent increase of the saGFP or splitYFP fluorescence (figure 34, left column). The constructs without the additional long linker showed an relative increase ranging between 1.3 and 1.7-fold after 20.2 h or 24.2 h (figure 34 A, C, right column), while the relative increase for the construct with the additional long linker ranged between 1.5 and 3.8-fold after 38.6 h (figure 34 B, right column). That the BiFC signal became significantly brighter over time was also proven for two of the three constructs, namely pInd saGFP / splitYFP OEP7 PpPEX3N (supplemental figure S4 A, C). Despite the fluorescence in-

crease over time, no consistent dose-dependent trend of the for the dexamethasone induction was revealed (figure 34 A, B, C, left column). For the constructs pInd saGFP / splitYFP OEP7 PpPEX3N, the normalised induction curves were quite similar for all dexamethasone concentrations and the negative control (0 μ M dexamethasone) (figure 34 A, C). As shown in the box-plots in figure 34 A, C, the relative increase of the leaf discs treated with dexamethasone was not significantly higher compared to that of the negative control at the end of the experiment (20.2 h and 24.2 h for the saGFP and splitYFP construct, respectively). Only for the construct pInd saGFP CC OEP7 PpPEX3N(GGSGG)₁₃, there seemed to be a more distinct trend that the samples treated with dexamethasone had a brighter saGFP signal than in the control treatment (figure 34 B, left column). However, the replicates showed a high standard deviation (figure 34 B, middle column) and replicate number was only n = 3, which is why the dexamethasone induction was not significantly proven.

Summarising the results of a transient induction assay, samples treated with 0 μ M dexamethasone, showed a similar trend of the induction curve than the samples treated with various concentrations of dexamethasone. Thus, no dose-dependency was confirmed for the pInd vector system using leaf discs in a liquid solution but an increase of the respective fluorescence signal over time for all treatments was revealed.

Another opportunity for the dexamethasone application was to brush adult leaves with a dexamethasone solution containing 0.02 % (v/v) Silwet. This technique was already performed both in stable *N. tabacum* [231] and *A. thaliana* lines [230]. We aimed to test if this technique is also functional in a transient system by brushing the leaves 2 d or 5 d after the infiltration with the respective construct with a 20 μ M dexamethasone solution and imaged them after 24 h (experimental setup see figure 35 A).

For this approach, we chose the construct pInd saGFP CC OEP7 PpPEX3N(GGSGG)₁₃. In figure 35 representative CLSM images of *N. tabacum* pavement cells are shown, which were brushed with the dexamethasone (experimental setup see figure 35 A). In leaves, which were brushed with the control treatment (0.02 % (v/v) Silwet) 2 d after the infiltration, mainly no saGFP signal was detected (figure 35 B). Only few cells were found to have a weak saGFP signal as indicated by arrows in figure 35 B. In contrast, the application of 20 μ M dexamethasone lead to a bright saGFP signal of transformed cells. The visualisation of leaves, which were brushed 5 d after the infiltration, revealed a saGFP signal (figure 35 C). The saGFP signal was also present in the control treatment, but in the samples with the dexamethasone application the saGFP signal was substantially brighter.

In conclusion, the expectation of an dose-dependent fluorescence induction was not confirmed in a transient induction assay. The visualisation of the induction using the example of pInd saGFP CC OEP7 PpPEX3N(GGSGG)₁₃ revealed, that in a transient system the pOp6/Gr-LhG4 2in1 promoter system was slightly leaky, but an application with dexamethasone led to a distinct increase in the fluorescence signal.

III. RESULTS

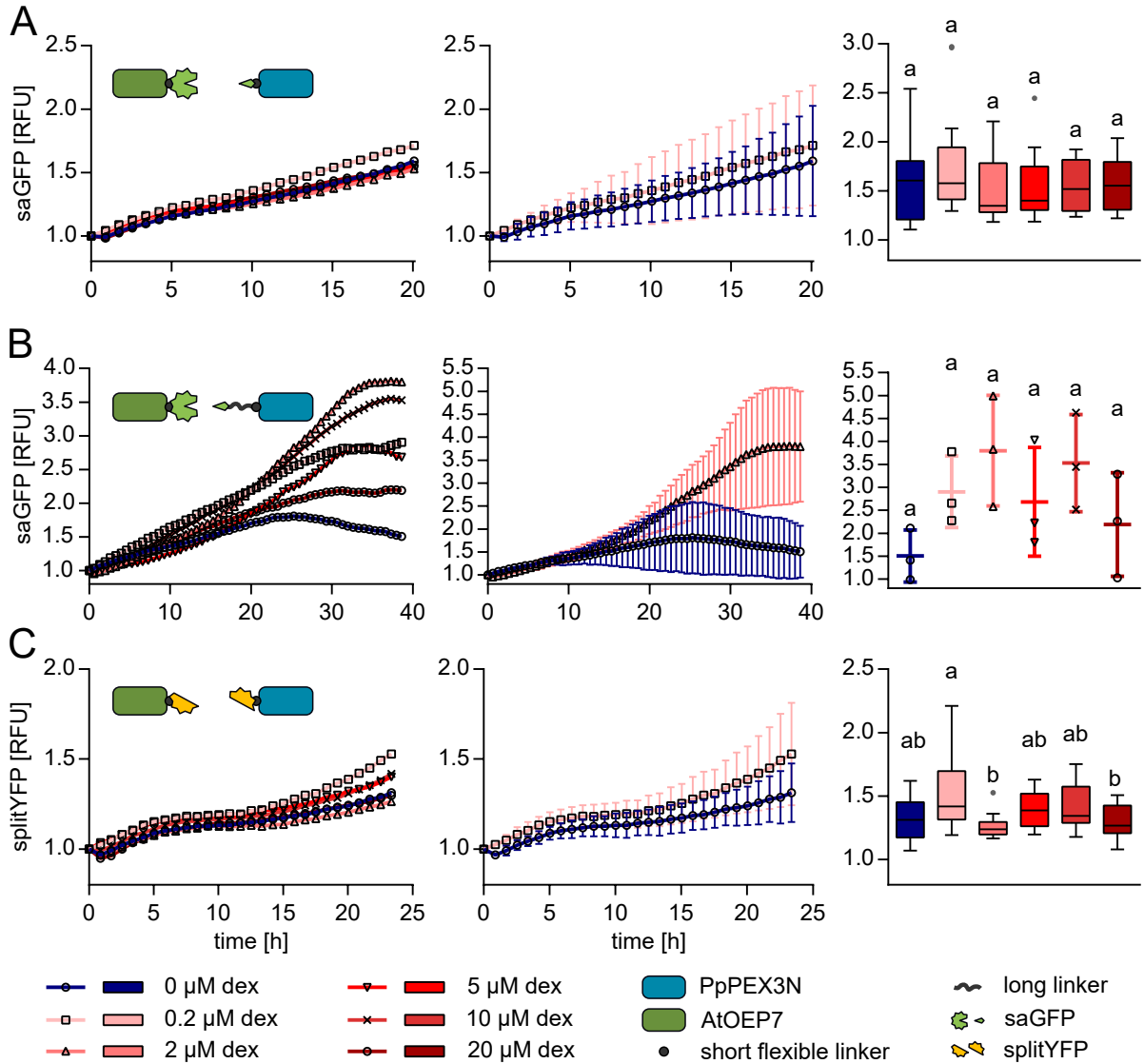


Figure 34: *In vivo* monitoring of dexamethasone induction of pInd BiFC vector system verified by the respective sensor fluorescence in the transient system of *N. tabacum*.

N. tabacum leaves were infiltrated with saGFP (A, B) and splitYFP (C) sensor constructs. *N. tabacum* leaf discs were submerged in wells of a 96-well plate prefilled with assay medium. After about 1 h of dark incubation, assay medium was exchanged by fresh medium with different concentrations of dexamethasone (t_0). The relative fluorescence unit (RFU) of the respective fluorescent sensor was detected over time by the plate reader. The graphs represent the relative fluorescence unit (RFU) normalised over the respective t_0 value of each replicate. While the left graphs show the RFU over time of all concentrations without standard deviations, the middle graph represents the results of the control and the data set the largest deviation to the control including the standard deviations. The right panel represents the RFU at the end of the monitoring (t_E). $n = 12$ (of three infiltrated leaves, 4 discs per leaf) (A, C); $n = 3$ (of one infiltrated leaf) (B). Data are represented as mean, mean + standard deviation (SD) and box plot with Tukey whiskers (from left to right). Significant differences were calculated according to One-way ANOVA with Tukey's multiple comparisons test. Excitation: 482 nm (saGFP, splitYFP); emission: 530-20 nm (saGFP), 540-20 nm (splitYFP).

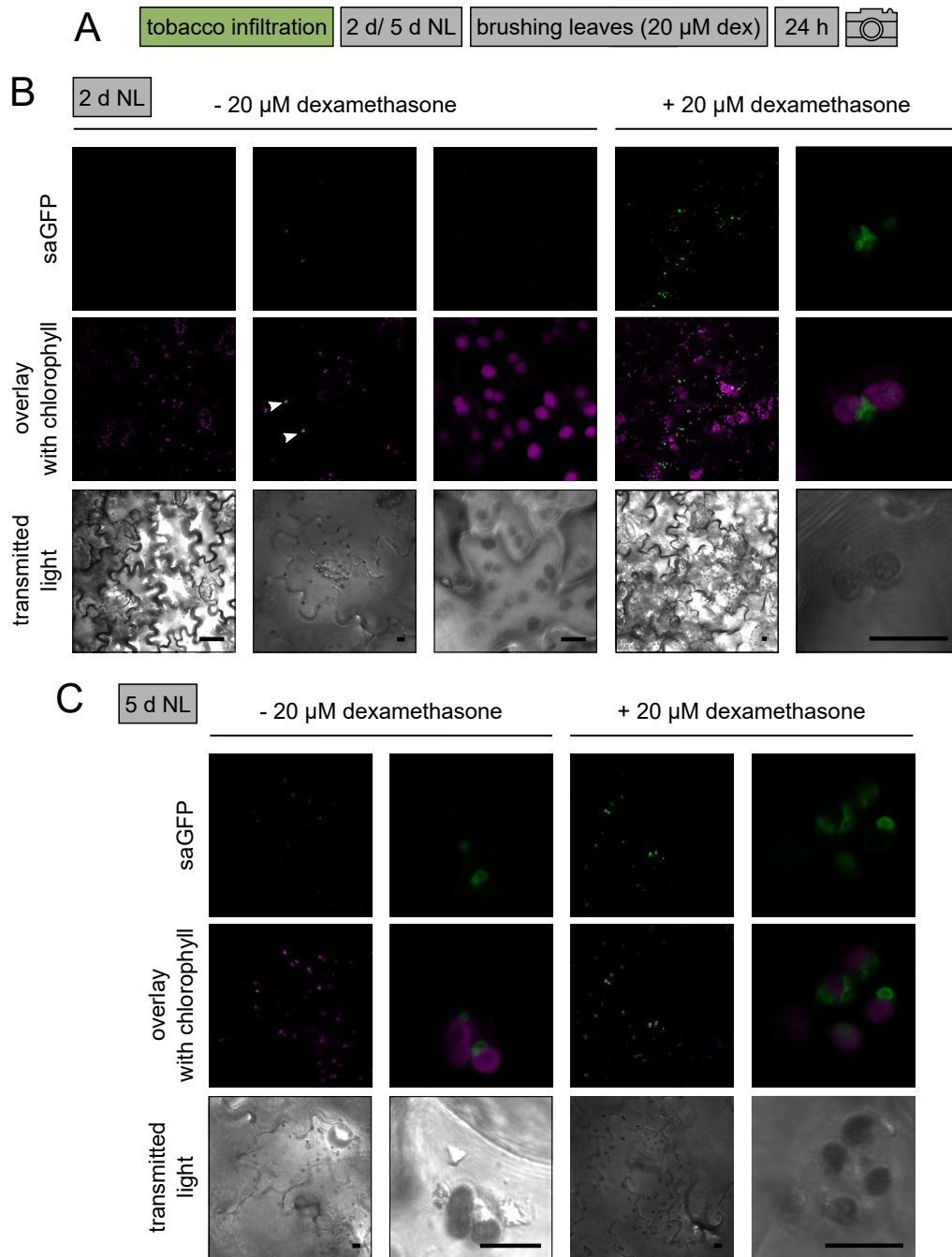


Figure 35: Visualisation of induced saGFP fluorescence using the OEP7 and PpPEX3N(GGSGG)₁₃ as fusion partners and transient in *N. tabacum*.

A: Schemata of the experimental setup. *N. tabacum* leaves were infiltrated with *A. tumefaciens* containing the construct pInd saGFP CC OEP7 PpPEX3N(GGSGG)₁₃. **B, C:** Representative CLSM images of *N. tabacum* pavement cells treated with control treatment (0.02 % Silwet) or 20 μ M dexamethasone (supplemented with 0.02 % Silwet) 2 d (**B**) or 5 d (**C**) after the infiltration. Scale = 10 μ m.

5 FRET/FLIM as a putative tool to visualise the dynamics of MCS

In contrast to the previously described BiFC, the usage of a FRET sensor system allows to monitor transient interactions dynamically without inducing artificial tethering. FRET is an energy transfer from an acceptor to a donor FP. The donor FP in its excited state transfers its excitation energy to a neighbouring acceptor FP, which in turn emits a fluorescent signal ([174, 175], figure 4 E). The efficiency of the energy transfer is affected by the distance of donor to acceptor and the Förster radius of the chosen FRET pair (see references in [174, 176]). In our case, the FRET pair is composed of mVenus as donor and tagRFP as acceptor with a Förster radius of 5.9 nm [177].

There are two common methods to detect and quantify the energy transfer. FRET can be detected by either observing the ratio between acceptor and donor fluorescence intensity, when only the donor gets excited, or the decrease in the fluorescence lifetime of the donor using Fluorescence Lifetime Imaging (FLIM) (see references in [150]). In this work, we chose FLIM as detection method, since it is unaffected by donor and acceptor concentrations, spectral bleedthrough and photobleaching [150, 178]. However, it is important to consider that in our experimental setup FLIM requires a detection time of several seconds per image, which might lead to short contacts being missed [6].

5.1 Determination of FLIM measurement range

Prior to dynamic imaging of putative MCS, we aimed to define the FLIM measurement criteria. Therefore, two sensor controls were designed (figure 36 A). One FRET/FLIM control should represent the unquenched donor lifetime with the donor mVenus unable to be in close proximity to the acceptor tagRFP. For this purpose, mVenus was fused to protein domains or full-length versions of the two *P. patens* MOM proteins PpTOM20C or PpTOM5 (localisation see results section 2), while the tagRFP was fused to a signal peptide (PpAP1sp [238]) targeting tagRFP to the ER lumen (hereafter termed negative control). The other FRET/FLIM control should imitate a permanent close proximity of donor and acceptor leading to a decrease in the fluorescence lifetime of the donor. For this purpose, synthetic tether constructs were designed composed of the fusion proteins or protein domains PpTOM20C or PpTOM5 (MOM) and PpPEX3N (PerM). These proteins flank the FRET pair mVenus and tagRFP, which in turn are linked by a flexible linker (schemata see figure 36 A and 41 A, hereafter positive control).

Representative images of the controls are shown in figure 36 B. For the negative control using PpTOM20C as fusion partner, the mVenus signal was localised to the OE of the chloroplasts and was not adjacent to the tagRFP signal. In contrast, the mVenus and tagRFP

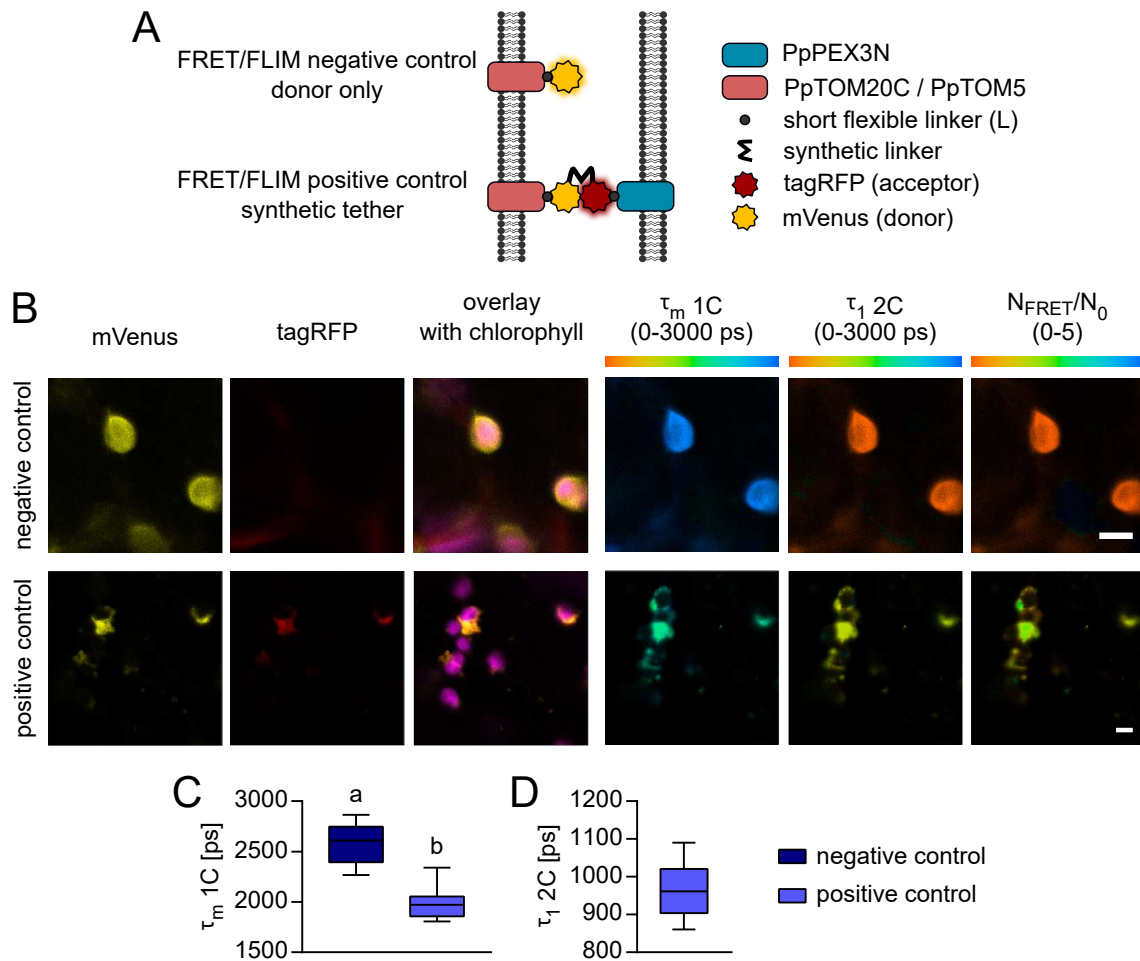


Figure 36: Determination of FLIM detection range in *Nicotiana benthamiana* pavement cells.

A: Sensor design of the FRET/FLIM (Förster resonance energy transfer/fluorescence lifetime imaging) controls. The negative control consists of the donor mVenus fused to truncated or full-length versions of two *Physcomitrella patens* (Pp) mitochondrial outer membrane (MOM) proteins PpTOM20C or PpTOM5. PpTOM20C is composed of the C-terminus of PpTOM20, and localised to the MOM and the outer envelope (OE) of chloroplasts (see results section 3). The RFP was fused to a signal peptide (PpAP1sp [238]) targeting tagRFP to the ER lumen (data not shown). The positive control is based on a synthetic tether construct composed of PpTOM20C/PpTOM5 and PpPEX3N as flanking proteins mimicking 100%. PpPEX3N is a truncated version of PpPEX3 and localised to the peroxisomal membrane (PerM). In the centre of the fusion protein the FRET pair mVenus and tagRFP are located connected by a synthetic linker (PpPEX3N:tagRFP:mVenus:PpTOM20C; PpPEX3N:tagRFP:mVenus:PpTOM5). **B:** Representative images *N. benthamiana* cells overexpressing the negative (PpAP1sp:tagRFP:mVenus:PpTOM20C) and positive (PpPEX3N:tagRFP:mVenus:PpTOM20C) controls. FRET is an energy transfer from an acceptor (mVenus) to a donor (tagRFP). The efficiency of the FRET is dependent on the Förster radius (here-5.9 nm [177]). As readout FLIM was used with the medium fluorescence lifetime τ_m of a 1 component analysis of exponential decay (1C), and (τ_1) and N_{FRET}/N_0 of a 2 component analysis of exponential decay (2C). N_{FRET}/N_0 visualise the ratio of the number of interacting (=quenched) donor (τ_1) to non-interacting (=unquenched) donor molecules (τ_2). Scale = 5 μ m. **C, D:** Quantification of the FRET/FLIM negative and positive controls regarding τ_m 1C (**C**) and τ_1 2C (**D**). $n \geq 15$ (C) or $n = 6$ (D); box plot with median and Tukey's multiple comparisons test. Significant differences were calculated according to One-way ANOVA with Tukey's multiple comparisons test.

signals of the positive control co-localised and were adjacent to the chlorophyll autofluorescence. The medium fluorescence lifetime τ_m of a 1 component analysis of exponential decay (1C) revealed that τ_m 1C was decreased for the quenched donor of the positive control (green colour) compared to the unquenched donor of the negative control (blue colour). This was also confirmed by a quantification (figure 36 C) with the unquenched donor lifetime determined as $\tau_m = 2575.67 \text{ ps} \pm 191,75 \text{ ps}$ and the lifetime of the quenched donor as $\tau_m = 1975.8 \text{ ps} \pm 134.5$ using the negative and positive control, respectively. Using a double exponential decay analysis of the donor lifetime, the decay amplitudes of the number of in-

interacting (=quenched) donor (τ_1) and of non-interacting (=unquenched) donor molecules (τ_2) can be determined and depicted as ratio N_{FRET}/N_0 . For the 2C analysis, τ_2 was set to 2575.67 ps, which is the unquenched donor lifetime τ_m of the negative control. When FRET was not present, the ratio N_{FRET}/N_0 was <1 with τ_1 (negative control, red colour). When FRET was present, τ_1 (quenched donor lifetime) was determined as $965 \text{ ps} \pm 77.77 \text{ ps}$ (figure 36 B, D) and N_{FRET}/N_0 reached values between of 2-5 (figure 36 B, yellow to blue).

Based on this results, we defined the following criteria for FLIM analysis: 1) a co-localisation of the mVenus and tagRFP signal, 2) a decrease in τ_m compared to the negative control, 3) $\tau_1 \approx 965 \text{ ps} \pm 77.77 \text{ ps}$ and 4) N_{FRET}/N_0 value higher than that for the negative control (>1).

5.2 Suitability verification of FRET/FLIM sensor system to monitor dynamic MCS

After defining the dynamic range for the FLIM analysis, we aimed to test whether the membrane proximity of organelles could be visualised by the decrease in the fluorescence lifetime of mVenus.

For this purpose, FLIM measurements were performed transiently in *N. tabacum* leaves expressing mVenus:TOM20C and PpPEX3N:tagRFP (schemata see figure 37 A). Two representative images of the FLIM analysis in mesophyll cells are shown in figure 37 B. In mesophyll cells, the mVenus signal was localised to the OE, whereas the tagRFP signal was found in the PerM (see also results section 2). ROIs of putative interaction sites were marked, where the tagRFP signal was adjacent to the mVenus donor signal (dotted circles). The local donor lifetime τ_m within the ROIs did not differ to that of the remaining areas and the false-colouring was similar to that of the unquenched, negative control (blue, figure 36 B). This was also underlined by the 2C analysis, which revealed no distinct differences of τ_1 and N_{FRET}/N_0 values comparing the ROIs and remaining areas.

FLIM measurements are based on photon collection over time and the readout gets more robust the more photons are collected. The FLIM detection time for this analysis was set to 30 s - 35 s to reach a count of approximately 50.000 photons. The dynamics of putative chloroplast-peroxisome MCS are not known yet. For this reason, interactions below the detection time of 30 s could be overlooked with this experimental setup. Therefore, FLIM detection time was decreased to 10 s for the same cell in order to test, if the photon count was high enough to guarantee a robust readout and if transient MCS were overlooked using a long detection time. The false-colouring of the representative τ_m time series was similar to that after 30 s - 35 s detection time. However, the amount of photons that was collected after 10 s was low. To guarantee a robust analysis, a high photon count was beneficial for the calculation of the donor decay, while in our case a low photon count led to high scattering of the measurement values and a more error-prone analysis (data not shown).

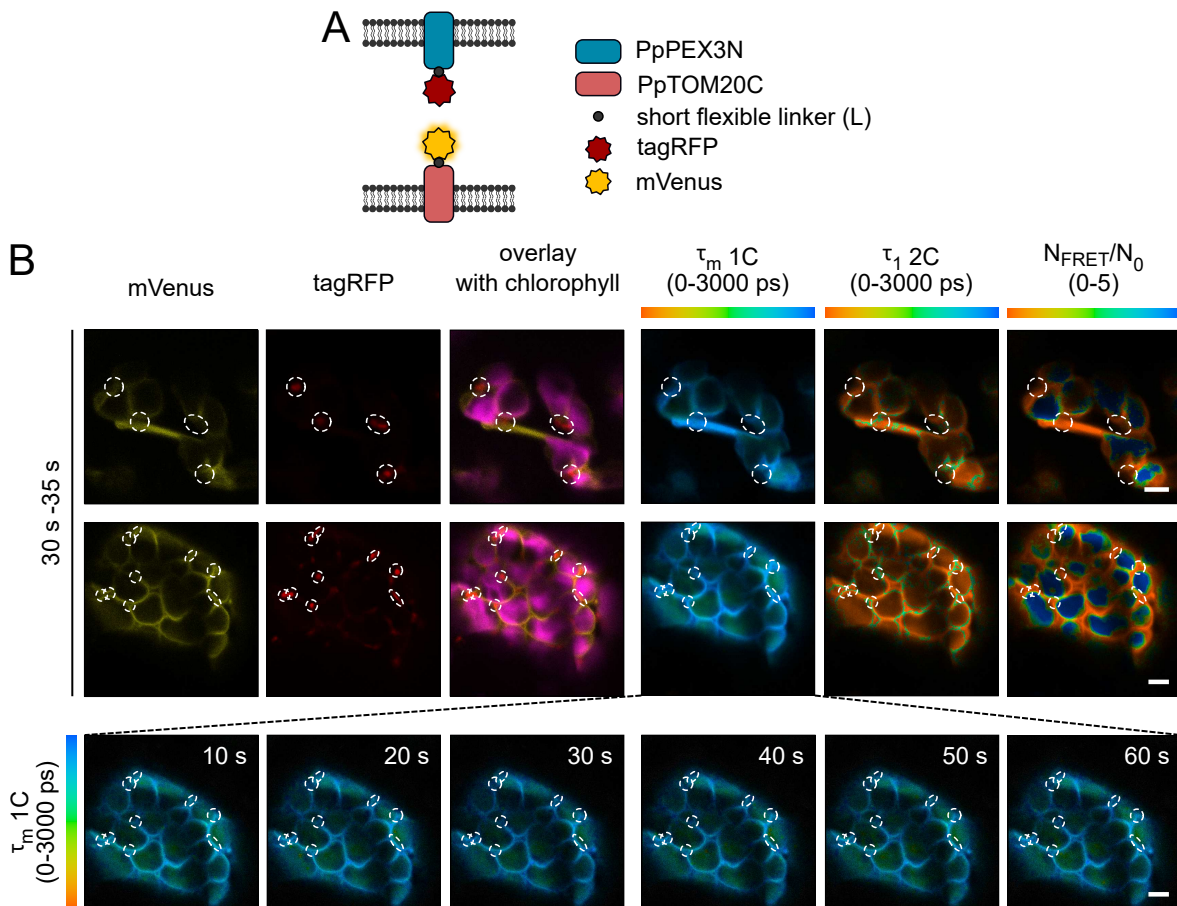


Figure 37: Imaging setup adaption for dynamic FRET-FLIM measurements in *N. tabacum* leaf cells.

A: Scheme showing the general design of the FRET-FLIM sensor. mVenus is fused C-terminal to PpTOM20C and localised to outer envelope (OE) and mitochondrial outer membrane (MOM), whereas the acceptor tagRFP is fused C-terminal to a truncated version of PpPEX3 and localised to peroxisomal membrane (PerM). The Förster radius of mVenus and tagRFP is 5.9 nm [177]. **C:** Representative images of FRET-FLIM measurements of transiently transformed *N. tabacum* cells overexpressing the construct PpPEX3N:tagRFP mVenus:PpTOM20C. Putative regions of interactions (overlap of tagRFP and mVenus signals) are marked with dotted circles. As readout for FRET a local decrease in τ_m 1C and the appearance of quenched donor lifetime values (τ_1 2C) are expected. N_{FRET}/N_0 visualise the ratio of quenched donor (τ_1) to unquenched donor (τ_2). Two different approaches regarding the detection time were performed with 30 s - 35 s and a time series with 10 s collecting photons (τ_m 1C). Scale = 5 μ m.

Based on these results, a longer detection time was used for further FLIM experiments. However, the question remained whether the frequency and duration of MCS formation is too fast or too transient for visualisation of organellar proximity with our FLIM imaging settings. An alternative to reducing the detection time was to stabilise the putative MCS. The organelle positioning was shown to be regulated by actin cytoskeleton [217–220]. In order to stabilise putative MCS between peroxisomes and chloroplasts, the actin depolymerising drug cytD (20 μ M) was used in order to reduce the active movement of the organelles (supplemental figure S1).

Additionally, the natural distance, which need to be bridged between the chloroplasts and peroxisomes at the putative MCS, is unknown. Therefore, an additional larger sensor was designed including a long linker (figure 38 B). OEP7 and PpPEX3N were used as fusion proteins for mVenus and tagRFP, respectively. OEP7 was shown to be localised to the OE transiently in *N. tabacum* pavement cells (results section 2). The construct without the

III. RESULTS

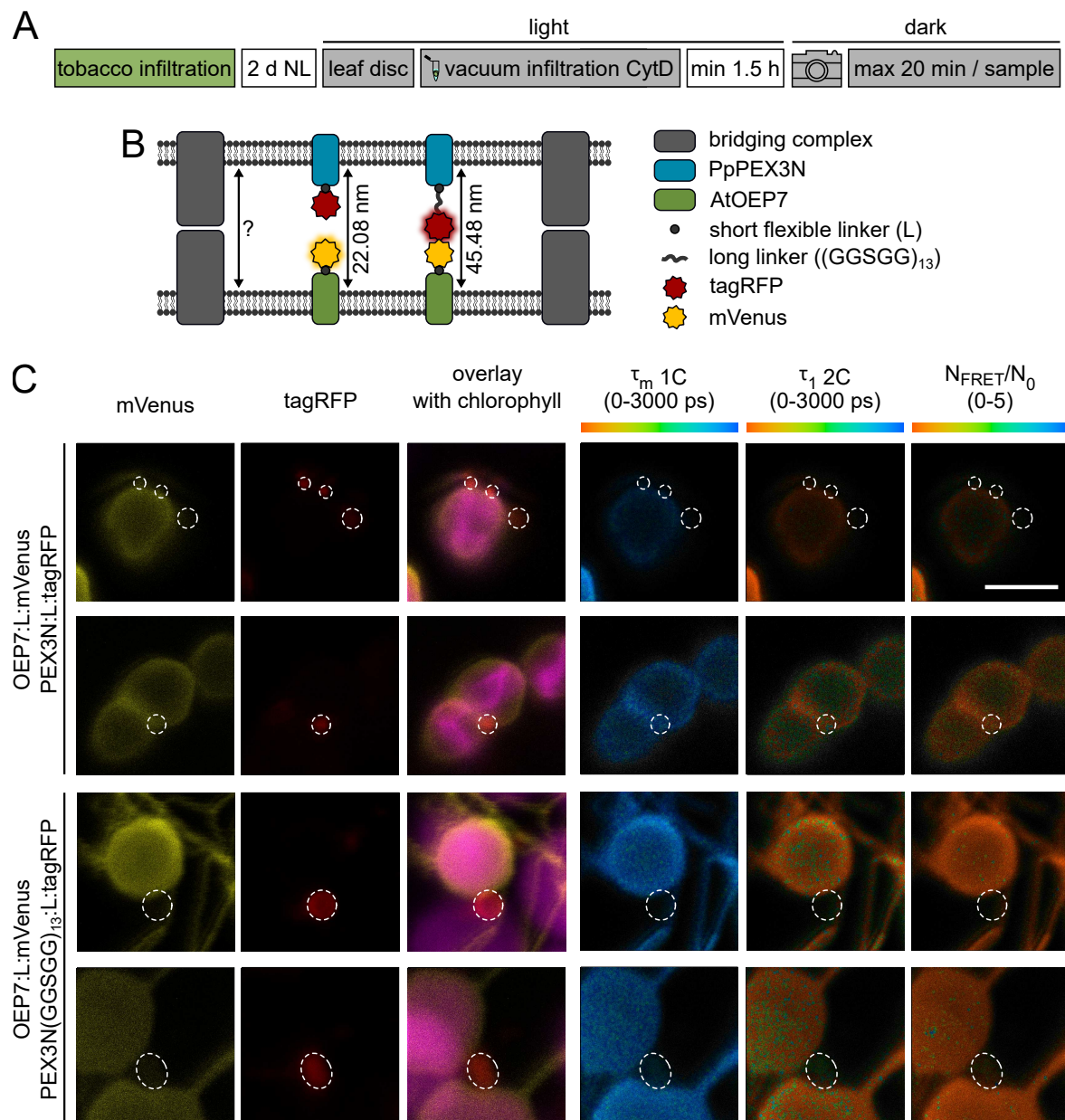


Figure 38: FRET-FLIM-based proximity sensor between outer envelope (OE) and peroxisomal membrane (PerM) with short and long linker under light conditions and cytochalasin D (CytD) treatment transient in *N. tabacum*.

A: Experimental setup of sample preparation and imaging procedure. Leaves of *N. tabacum* were infiltrated with the respective *Agrobacterium* strain. Two d after infiltration, leaf discs were vacuum infiltrated in CytD (20 μ M) and imaged after 1.5 h incubation at 20 μ mol $m^{-2} s^{-1}$. Maximum time of imaging per sample was 20 min. **B:** Scheme showing the general approach of the design of the FRET-FLIM based sensor system. Membrane contact sites conditions, protein composition and distance between OE and PerM are still unknown. Therefore two sensor pairs with short or short + long linker were designed to bridge different distances. mVenus is fused C-terminal to OEP7 and localised to OE, whereas the acceptor tagRFP is fused C-terminal to a truncated version of PpPEX3 and localised to PerM. The bridging distance of this constructs between both membranes are ≤ 22.08 nm or ≤ 45.48 nm + the Förster radius (≈ 5.9 nm [177]). **C:** Representative images of FRET-FLIM measurements of *N. tabacum* mesophyll cells. As readout for FRET a local decrease in τ_m and the appearance of quenched donor lifetime values (τ_1) are expected. N_{FRET}/N_0 visualise the ratio of quenched donor (τ_1) to unquenched donor (τ_2). Scale = 2.5 μ m.

long linker bridged 22.08 nm plus the Förster radius of 5.9 nm [177] between OE and PerM (OEP7:mVenus, PpPEX3N:tagRFP) (figure 38 B). The ROIs labelling the putative interaction sites showed a blue false-colouring for τ_m similar to the negative control. Also the false-colouring for τ_1 and N_{FRET}/N_0 of the 2C analysis did not differ from that of the negative control and the remaining areas (figure 38 C, supplemental figure S5; controls see figure 36

B).

Adding the long and flexible linker ((GGSGG)₁₃) between PpPEX3N and tagRFP increased the bridging distance to 45.48 nm plus the Förster radius of -5.9 nm [177] (figure 38 B). The false-colouring of τ_m , τ_1 and N_{FRET}/N_0 did not differ to those of the construct without the additional linker and of the negative control (figure 38 C, supplemental figure S6; controls see figure 36 B). Summarising the results of the experiments in *N. tabacum*, the donor lifetime was not reduced, independently of the protein fusion partners, detection time, pharmaceutical treatment or bridging distance.

The proximity and interaction rate of chloroplasts and peroxisomes has been described to be increased under light conditions [26]. In *N. tabacum*, the Agrobacterium-mediated transformation was mostly efficient in pavement leaf cells, whereas infection of photosynthetic active mesophyll tissue was rare. We wanted to collect more data in photosynthetic active tissue and under light conditions to verify, whether the proximity of chloroplasts and peroxisomes could be detected by using FRET/FLIM. Thus, stable *A. thaliana* lines of the constructs with and without long linker were generated (FRET CC OEP7:mVenus PpPEX3N / PpPEX3N(GGSGG)₁₃:tagRFP). The FLIM detection was performed in mesophyll cells of T2 plants either under light conditions (figure 39, supplemental figure S7, S9, S10, S11) or under light conditions with additional cytD treatment (figure 40, supplemental figure S8, S12, S13, S14). Under light conditions for both FLIM sensors with and without the long linker, the τ_m , τ_1 and N_{FRET}/N_0 false-colouring did not differ from that of the negative control (figure 36 B) or the dynamic data in *N. tabacum* (figure 37, 38). Also an addition of cytD to inhibit the active organellar movement did not lead to a decrease in the donor lifetime, since all FLIM parameters were similar to that of the negative control (τ_m blue, τ_1 and N_{FRET}/N_0 red).

In summary, we did not observe any decrease in the fluorescence lifetime of mVenus at putative chloroplast-peroxisome interaction sites regardless of the species, the bridging distance of the sensor construct and the experimental conditions.

III. RESULTS

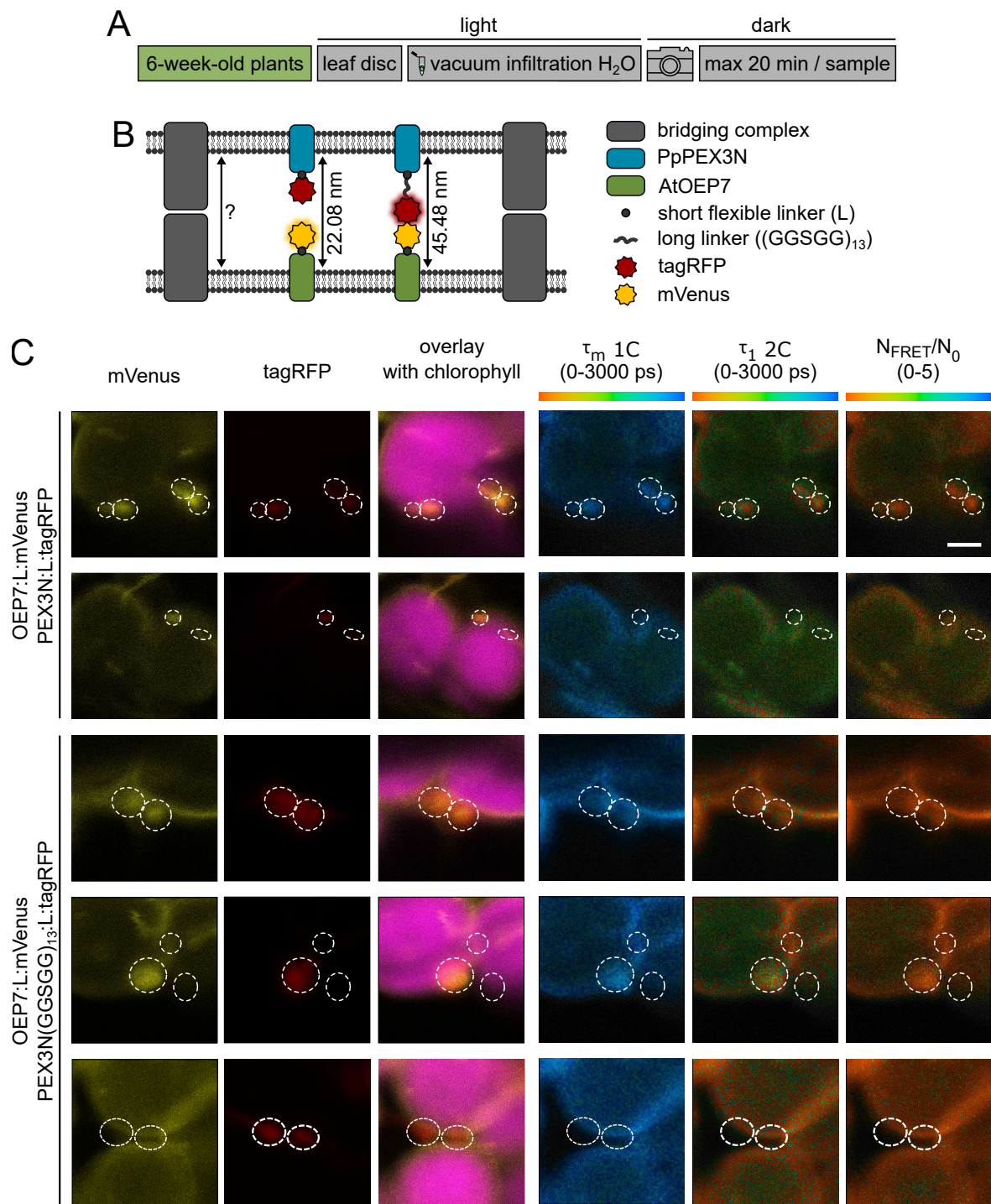


Figure 39: FRET-FLIM-based proximity sensor between outer envelope (OE) and peroxisomal membrane (PerM) with short and long linker under light conditions in stable *A. thaliana* lines.

A: Experimental setup of sample preparation and imaging procedure. Leaf discs were vacuum infiltrated in water and directly imaged or incubated at $20 \mu\text{mol m}^{-2} \text{s}^{-1}$. Maximum time of imaging per sample was 20 min. **B:** Scheme showing the general approach of the design of the FRET-FLIM based sensor system. Membrane contact sites conditions, protein composition and distance between OE and PerM are still unknown. Therefore two sensor pairs with short or short + long linker were designed to bridge different distances. mVenus is fused C-terminal to OEP7 and localised to OE, whereas the acceptor tagRFP is fused C-terminal to a truncated version of PpPEX3 and localised to PerM. The bridging distance of this constructs between both membranes are $\leq 22.08 \text{ nm}$ or $\leq 45.48 \text{ nm} + \text{the F\u00f6rster radius } (5.9 \text{ nm [177])}$. **C:** Representative images of FRET-FLIM measurements of independent stable *A. thaliana* lines (px-ck 48#1 #21, Col-0 84#2 #12, Col-0 84#2 #15, px-ck 84#2 #35). As readout for FRET a local decrease in τ_m and the appearance of quenched donor lifetime values (τ_1) are expected. N_{FRET}/N_0 visualise the ratio of quenched donor (τ_1) to unquenched donor (τ_2). Scale = $2.5 \mu\text{m}$.

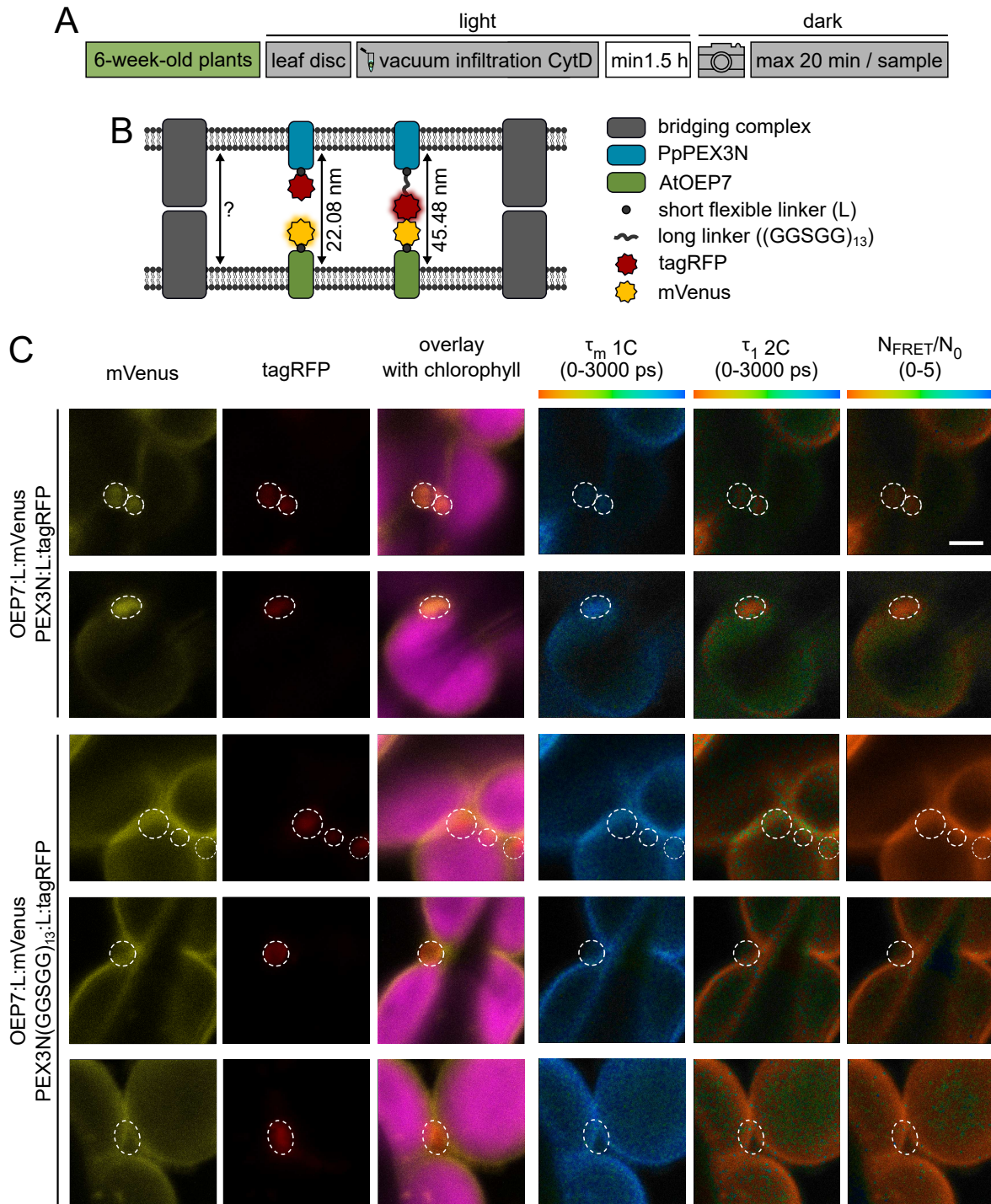


Figure 40: FRET-FLIM-based proximity sensor between outer envelope (OE) and peroxisomal membrane (PerM) with short and long linker under light conditions and cytochalasin D (CytD) treatment in stable *A. thaliana* lines.

A: Experimental setup of sample preparation and imaging procedure. Leaf discs were vacuum infiltrated in CytD (20 μM) and imaged after 1.5 h incubation at $20 \mu\text{mol m}^{-2} \text{s}^{-1}$. Maximum time of imaging per sample was 20 min. **B:** Scheme showing the general approach of the design of the FRET-FLIM based sensor system. Membrane contact sites conditions, protein composition and distance between OE and PerM are still unknown. Therefore two sensor pairs with short or short + long linker were designed to bridge different distances. mVenus is fused C-terminal to OEP7 and localised to OE, whereas the acceptor tagRFP is fused C-terminal to a truncated version of PpPEX3 and localised to PerM. The bridging distance of this constructs between both membranes are $\leq 22.08 \text{ nm}$ or $\leq 45.48 \text{ nm}$ + the Förster radius ($\approx 5.9 \text{ nm}$ [177]). **C:** Representative images of FRET-FLIM measurements of independent stable *A. thaliana* lines (px-ck 48#1 #21, Col-0 84#2 #12, Col-0 84#2 #15, px-ck 84#2 #35). As readout for FRET a local decrease in τ_m and the appearance of quenched donor lifetime values (τ_1) are expected. N_{FRET}/N_0 visualise the ratio of quenched donor (τ_1) to unquenched donor (τ_2). Scale = 2.5 μm .

6 Perturbing organelle interactions

In addition to the visualisation of MCS, the interactions between organelles could be also investigated by perturbing and manipulating them. Therefore, we designed a synthetic tether construct, which contains targeting signals to two different membranes being linked by a FRET/FLIM pair (figure 41 A). In this work, the focus was in particular on the organelles chloroplasts, peroxisomes and mitochondria. Photorespiration takes place between these organelles, exchanging metabolites to detoxify 2-phosphoglycolate being generated by the oxygenase activity of RubisCo [1].

6.1 Effects of synthetic tethering on cellular organisation in plant cells

To perturb the natural interaction between the photorespiratory organelles, a synthetic tether construct was designed using truncated versions of *P. patens* TOM20 (PpTOM20) and PEX3 (PpPEX3) for the organellar targeting. In *N. tabacum*, the localisation control of the C-terminus of the MOM protein PpTOM20 (PpTOM20C) was shown to be localised to MOM, but also miss-localised to OE of chloroplasts (figure 22). As peroxisomal anchor, the N-terminus PpPEX3 (PpPEX3N) was used, which was localised to PerM in *N. benthamiana* (figure 23). The synthetic tether construct 24#5 PpPEX3N:tagRFP:mVenus:PpTOM20C (table 24) was expressed constitutively under a CaMV35S promoter. In this section, we aimed to test, what impact the overexpression of the fusion protein PpPEX3N:tagRFP:mVenus:PpTOM20C had on the cellular organisation and structure with a special focus on peroxisomes, mitochondria and chloroplasts (figure 41 A).

6.1.1 Peroxisomal cluster formation in *N. benthamiana* and *N. tabacum* cells overexpressing the synthetic tether construct

To test the localisation and the intactness of the synthetic tether construct, it was first investigated transiently in *N. benthamiana* and *N. tabacum* co-infiltrated with peroxisomal CFP marker construct (pSS02:CFP-SKL [221], figure 41 B). The representative images of transiently transformed *N. benthamiana* pavement cells show a co-localisation of the mVenus and tagRFP signal indicating an intactness of the synthetic tether fusion protein. The signals surrounded the peroxisomes, which were mostly either directly adjacent to chloroplasts (see chlorophyll autofluorescence signal) or part of a group of peroxisomes adjacent to a chloroplast (figure 41 B). Mitochondrial staining was not performed in *N. benthamiana*, which in turn does not allow any conclusion on the tether effect between peroxisomes and mitochondria.

To test if the overexpression of the synthetic tether construct influences the peroxisome-chloroplast proximity, a manual and an automated proximity analysis were performed in *N. tabacum* pavement cells (results section 1.2). The results of both analyses were that neither the ratio chloroplast with contact to peroxisomes per total chloroplasts (c_c/c_t [%]) or

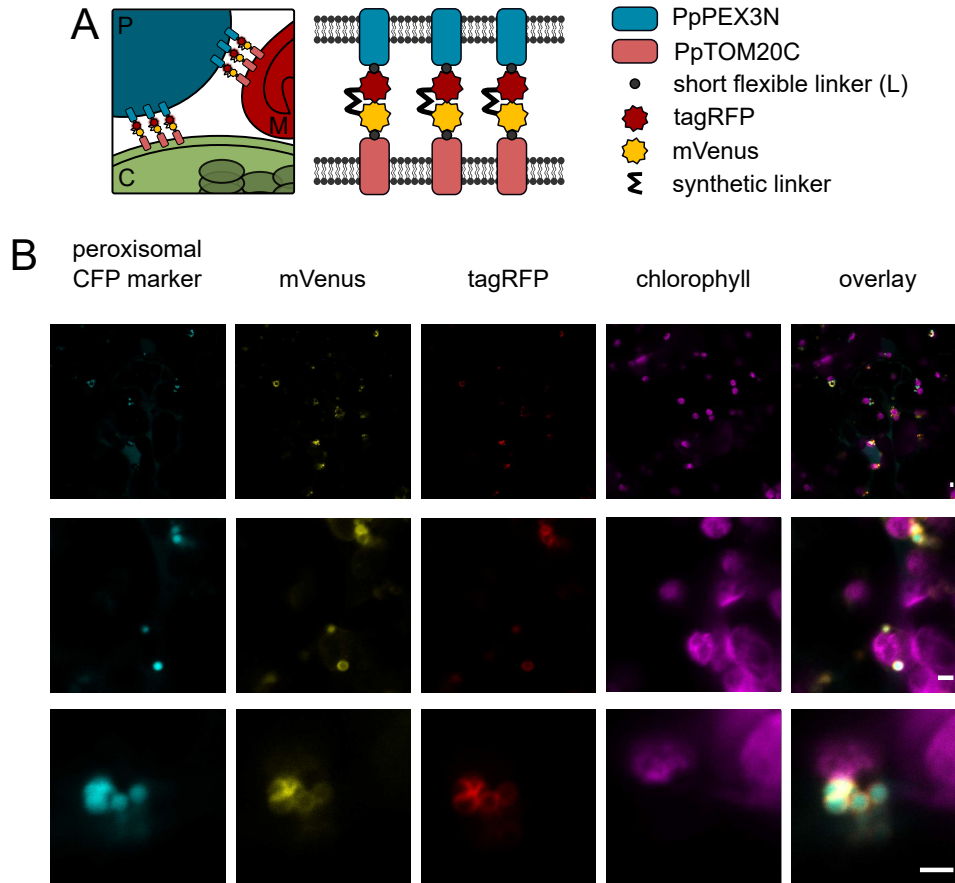


Figure 41: Perturbing organellar interaction by transient expression of the synthetic tether construct 24#5 (PpPEX3N:tagRFP:mVenus:PpTOM20C) in *N. benthamiana*.

A: Schemata of the design of tether construct. PpPEX3N and PpTOM20C are truncated versions of respective proteins consisting of their transmembrane domain. The localisation controls of PpPEX3N was localised to the PerM (peroxisomal membrane) and that of PpTOM20C both to MOM (mitochondrial outer membrane) and OE (outer envelope of the chloroplast) (results section 3). Thus the expectation is that the fusion protein PpPEX3N:tagRFP:mVenus:PpTOM20C tether either PerM-MOM as PerM-OE. **B:** Representative CLSM images of transient expression in *N. benthamiana* under the constitutive promoter CaMV35S. The peroxisomal CFP marker (CFP-SKL) was also constitutively expressed, leading to a side affected enrichment of CFP signal in the cytosol. Scale bar = 2 μ m

peroxisomes with contact to chloroplasts per total peroxisomes per cell (p_c/p_t [%]) were significantly different for cells overexpressing the synthetic tether construct to those of WT cells (figure 14).

6.1.2 Cluster formation of peroxisomes and elongated mitochondria in synthetic tether lines

In order to investigate the effect of overexpressing the synthetic tether construct not only in a transient system, transgenic *A. thaliana* overexpression lines were generated. The aim was to study these lines at the cellular level regarding the effects on the spatial organellar organisation, as well as to investigate them at phenotypic level. Two different WT background lines were transformed with the synthetic tether construct PpPEX3N:tagRFP:mVenus:PpTOM20C (24#5). Besides Col-0, the commercial available px-ck line was chosen, which is a Col-0 ecotype with a peroxisomal CFP marker (CFP-SKL, [186], further information see methods section 2.1). The Basta selection marker of the synthetic tether construct 24#5 allowed screening

III. RESULTS

either on soil or on plates.

All individual T₁ lines, which survived the Basta selection on soil, were screened for a bright fluorescence signals for both tagRFP and mVenus (supplemental figure S15). For all T₁ lines, the tether signals of mVenus and tagRFP overlapped, indicating an intact tether construct. Lines with the Col-0 background had punctual and bright signals for both FP. Since these lines do not have a peroxisomal marker, the tether signal could not be clearly assigned to distinct organelles. Nevertheless, the distribution, shape and size of the signal strongly suggested that the synthetic tether construct was localised to the PerM. The punctual signal was mostly co-localised or adjacent to the chlorophyll autofluorescence (supplemental figure S15).

To verify the localisation of the synthetic tether construct, transgenic *A. thaliana* lines in the px-ck background [186] were generated. As already suggested in Col-0, the peroxisomal localisation of the tether signal of mVenus and tagRFP could be confirmed in the *A. thaliana* px-ck lines (supplemental figure S15). Similar to *N. benthamiana*, in *A. thaliana* the signal of tagRFP and mVenus was not only localised at peroxisomes allocated to the chloroplasts, but was additionally localised to spherical clusters of peroxisomes, which were mainly found in pavement cells. However, these clusters were mostly not in the immediate proximity of chloroplasts.

For all individual T₁ lines, which survived the Basta selection on soil and had a bright fluorescence signal (supplemental figure S15), the segregation pattern of the T₂ generation was tested (table 27 and 8). Examining the segregation pattern in T₂ revealed, how many independent insertion events per line took place in the actual transformation step. For one insertion event, 50% heterozygous, 25% homozygous and 25% WT plants would be expected in T₂. The expected segregation pattern 3:1 (survivor:dead) on Basta selection plates was tested using a χ^2 -test.

Table 27 shows the segregation pattern of the lines selected for phenotyping. The two independent lines Col-0 24#5 #11 and px-ck 24#5 #31 showed the expected segregation pattern 3:1 in the T₂ generation. Due to its bright signal and the lack of a third line with the expected segregation pattern at this time point, the line px-ck 24#5 #12 was also propagated further to the third generation (T₃), albeit its χ^2 -value indicated more than one T-DNA insertion event.

Table 27: Segregation on plates with Basta selection of independent *A. thaliana* T₂ synthetic tether lines expressing the synthetic tether construct 24#5 (PpPEX3N:tagRFP:mVenus:PpTOM20C) under the constitutive promoter CaMV35S.

For one T-DNA insertion event in the second generation (T₂) a segregation pattern of 3:1 (survivor:dead, 75% survivors) is expected, which was used as expected ratio for the Chi-square value (χ^2 -value). The segregation pattern is mathematically defined as survivor divided by total amount of seedlings. As degree of freedom DF = 1 was used, since two different phenotypic observations (survivor, dead) were investigated.

<i>A. thaliana</i> line	Survivor	Dead	Segregation pattern [%]	χ^2 -value
Col-0 24#5 #11	37	11	77.08	0.12
px-ck 24#5 #12	44	1	97.78	107.45
px-ck 24#5 #31	32	14	69.57	0.64

Table 28: Segregation on plates with Basta selection of *A. thaliana* synthetic tether lines expressing the synthetic tether construct 24#5 (PpPEX3N:tagRFP:mVenus:PpTOM20C) in the third generation (T₃).
 In order to verify a homozygous T₃ seed batch, the segregation pattern of the independent lines must 1:0 (survivor:dead; 100% survivors). The segregation pattern is mathematically defined as survivor divided by total amount of seedlings.

<i>A. thaliana</i> line	Survivor	Dead	Segregation pattern [%]
px-ck 24#5 #12B	28	0	100
px-ck 24#5 #12G	27	0	100
px-ck 24#5 #31F	30	0	100
Col-0 24#5 #11C	28	0	100

In the T₃ generation, selected lines were screened for homozygous plants (table 28 and 9). For the following phenotyping experiments, one homozygous T₃ plant was chosen, respectively, for both lines with one T-DNA insertion event (Col-0 24#5 #11C and px-ck 24#5 #31F), whereas for the line px-ck 24#5 #12 with more than one T-DNA insertion event, two T₃ plants were chosen (#12B/G).

Prior to the phenotyping, the effect of overexpressing the synthetic tether construct was investigated further on cellular level in the transgenic *A. thaliana* lines (T₂ and T₃ generation). Similar to the transient system (figure 41), the tether signal of mVenus and tagRFP co-localised and surrounded partly the peroxisomal CFP marker in the *A. thaliana* synthetic tether lines (figure 42 A). In the WT px-ck, the peroxisomes were equally distributed, while the overexpression of the synthetic tether construct resulted in clustering of peroxisomes (indicated by arrows in overlay channel). The peroxisomal clusters were spherical, with the peroxisomes surrounding the sphere rather than forming it, whereas the tether signal was shown to be located at the inward-facing side of the peroxisomal cluster. Those clusters were mainly found in pavement cells, but smaller ones could also be detected in mesophyll leaf tissue (figure 43). Different than in *N. tabacum*, these clusters were not adjacent to chloroplasts (figure 42 A).

The questions raised by these results were, which additional components these clusters had been composed of and why they had a spherical shape in pavement cells. One possibility was that the spherical shape of the peroxisomal clusters was caused by the accumulation around the nucleus. To verify this, CLSM images of the cluster and the bright field channel for detecting the nucleus were compared for a co-localisation. Three representative images of transgenic T₃ lines shown that the clusters (Cl) did not surround the nucleus (N) (figure 42 B). The synthetic tether construct was also designed for mitochondria-peroxisomes tethering, which was why we tested if mitochondria are localised within those spherical clusters (figure 42 C). Mitochondria had accumulated within the spherical cluster and were partially adjacent to with the tether signal (mVenus, tagRFP).

Although the proximity analysis (see results section 1.2) of chloroplasts and peroxisomes did not reveal significant differences in tether T₂ plants to px-ck, the impact of overexpressing the synthetic tether construct on organellar morphology was investigated in two rep-

III. RESULTS

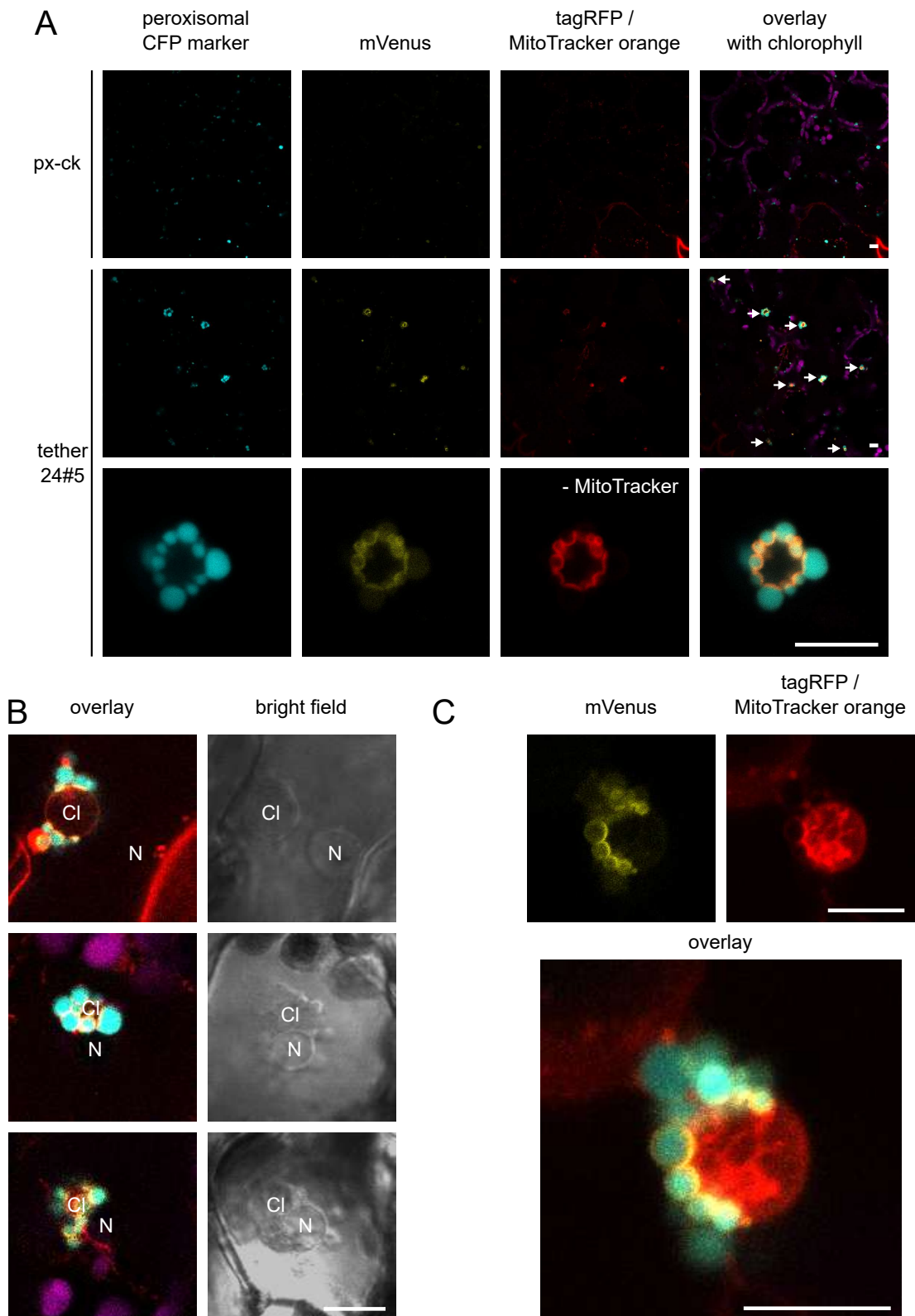


Figure 42: Overexpression of tether construct PpPEX3N:tagRFP:mVenus:PpTOM20C (24#5) lead to peroxisomal cluster formation in leaf cells of transgenic *A. thaliana* lines (T_3 generation).

A: Representative CLSM images giving an overview of the distribution of the peroxisomal and tether signal in *A. thaliana* leaf tissue of px-ck (Col-0 with peroxisomal CFP marker (CFP-SKL), [186]) and a px-ck tether line (24#5, PpPEX3N:tagRFP:mVenus:PpTOM20C). Peroxisomal clusters are indicated by arrows in the overlay channel, whereas a representative close up image shows structure of these clusters.

B: Representative CLSM images showing the peroxisomal clusters (CI) and the nucleus (N) of the same cell. **C:** Representative image of tether induced cluster coloured with MitoTracker orange (red). Scale bar 10 μ m.

representative T₃ transgenic lines (px-ck 24#5 #12B, px-ck 24#5 #31F). The morphology was studied by performing a 3-D modulation of CLSM z-stacks via the software Imaris. Figure 44 visualises the MIP of the CLSM signals and the Imaris surface modulation of representative z-stacks showing chloroplasts in magenta, peroxisomes in cyan and mitochondria (MitoTracker orange) in red. For the individual organelles, the original CLSM signals (red) matched with the objects of the Imaris surface modulation (transparent green).

In addition to those spherical clusters described above, the tether signal in *A. thaliana* mesophyll cells was mainly found at smaller groups or individual peroxisomes, both adjacent to the chloroplasts (figure 43 A, marked by arrows). To verify the impact of the tether overexpression in non-photosynthetic tissue and in seedling age, the root elongation zone of 5-7 d old seedlings were imaged. In figure 43 B a MIP and 3D surface modulation by Imaris are shown of the px-ck and two representative transgenic synthetic tether lines (px-ck 24#5 #12B, px-ck 24#5 #31F). Comparing px-ck and the transgenic synthetic tether lines, the distribution of peroxisomes and mitochondria in the root elongation tissue was mostly similar with additional peroxisomal and mitochondrial clusters for the synthetic tether lines (marked by arrows).

Similar than in *N. tabacum*, we aimed to test if the overexpression of the synthetic tether construct affected the proximity ratio between chloroplasts and peroxisomes (results section 1.2). The results of the analysis revealed no differences in the ratio chloroplast with contact to peroxisomes per total chloroplasts (c_c/c_t [%]) or peroxisomes with contact to chloroplasts per total peroxisomes per cell (p_c/p_t [%]) for two representative the overexpression lines (T₂, px-ck 24#5 #12, px-ck 24#5 #31) to px-ck (figure 15).

Both, chloroplasts and peroxisomes showed no changes in their morphology, which was also reflected in a similar percentage volume per cell compared to WT px-ck (figure 44 B, C). However, mitochondria seemed to be more elongated in both synthetic tether lines compared to the WT (figure 44 A). The mitochondrial volume normalised per cell volume was increased compared to the WT plants, albeit only significantly different for px-ck 24#5 #31F. This might also correlate with a trend towards an increase in mitochondria number per total cell volume in both transgenic lines (figure 44 E). As third parameter, the sphericity of mitochondria was examined. The sphericity value describes how perfectly spherical a structure is. By the definition of the Imaris manual, the sphericity Ψ of an object is the ratio of surface area of a sphere with the same volume as the compared particle to the surface area of the particle. Thus a perfect sphere has a sphericity $\Psi = 1$, whereas objects less spherical have values $\Psi < 1$. The mitochondrial sphericity of px-ck and the synthetic tether lines were in an equal range, but that of synthetic tether lines were significantly decreased (figure 44 F, px-ck: $\Psi = 0.86 \pm 0.11$, px-ck 24#5 #12B $\Psi = 0.78 \pm 0.14$, px-ck 24#5 #31F $\Psi = 0.80 \pm 0.14$).

III. RESULTS

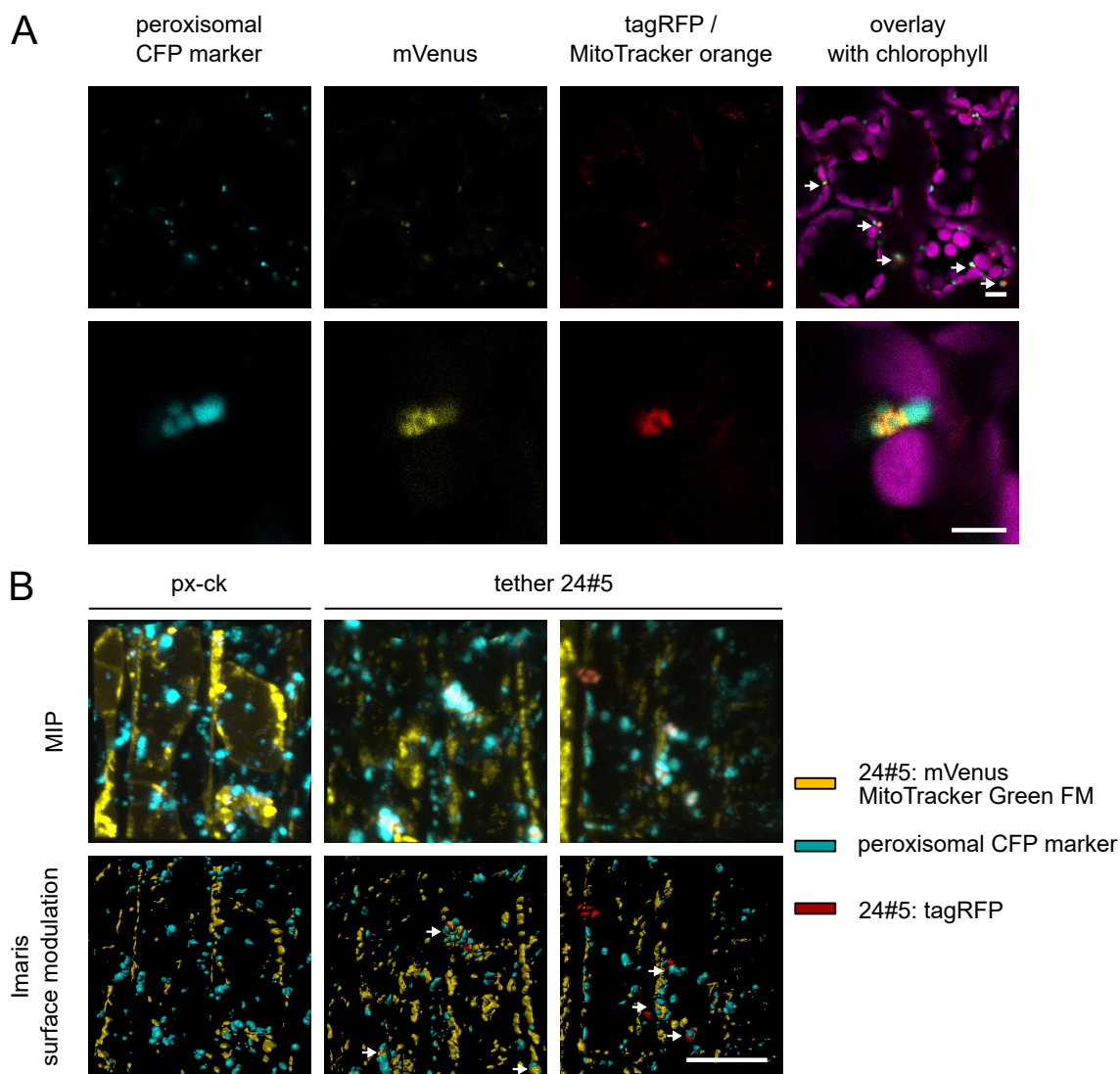


Figure 43: Signal distribution of the synthetic tether construct PpPEX3N:tagRFP:mVenus:PpTOM20C (24#5) in transgenic T_3 *A. thaliana* lines in leaf and root tissue.

A: Representative overview and close up image of mesophyll leaf tissue of transgenic *A. thaliana* synthetic tether lines (T_3). Co-localisation of peroxisomes and tether signal are marked by arrows in the overlay channel. **B:** 3D-reconstruction of elongation zone of *A. thaliana* wild type (px-ck) and T_3 synthetic tether lines. Representative images of cells of 5-day-old background line (px-ck) and two independent synthetic tether lines (#12B, #31) grown on plates. Mito Tracker Green FM is shown in yellow in the maximum intensity projection (MIP) and Imaris segmentation, the peroxisomal CFP marker in cyan and the signal of tether construct in red. Co-localisation of peroxisomes and tether signal are marked by arrows in Imaris surface modulation channel. 3D segmentation and surface modulation was performed using Imaris x 64 (version 9.2.1, surface module). Imaris software was provided by Prof. Dr. Nicole Frankenberg-Dinkel and Dr. David Scheuring of TU Kaiserslautern. Scale bar 10 μ m.

In summary, the microscopic analyses in *N. benthamiana*, *N. tabacum* and *A. thaliana*, revealed that the overexpression of the synthetic tether construct led to a spherical cluster formation of peroxisomes. In *A. thaliana*, a qualitative evaluation of the CLSM image material suggested that these clusters or single peroxisomes were adjacent to the chloroplasts, although a quantification did not reveal any difference in the interaction rates of those two organelles between synthetic tether lines and WT. However, we were able to identify that mitochondria were located within the peroxisomal clusters and that they were more elongated transgenic synthetic tether lines than in WT.

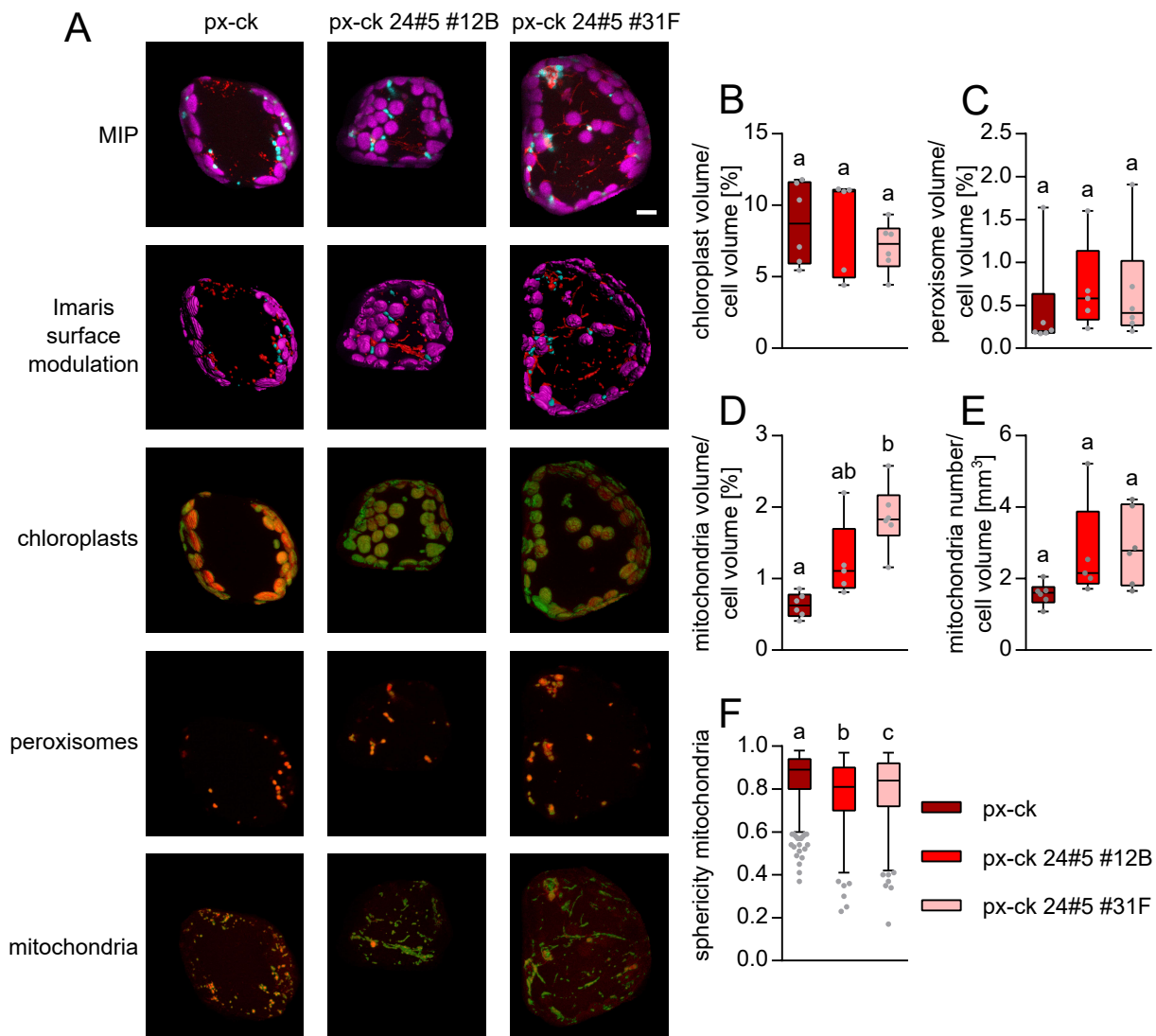


Figure 44: Organelle morphology of *A. thaliana* wild type (px-ck) and T₃ synthetic tether lines (PpPEX3N:tagRFP:mVenus:PpTOM20C; 24#5) in mesophyll cells.

A: Representative 3D images of cells of 6-week-old background line (px-ck) and two independent transgenic lines (#12B, #31) grown under standard conditions. Organelles were detected via chlorophyll autofluorescence (magenta), a peroxisomal CFP marker (cyan) and Mito Tracker orange (red) and shown as maximum intensity projection (MIP). For 3D surface modelling via Imaris the same colour scheme were used for the respective organelles. **B, C, D, E:** Quantification of percentage of organellar volume and number per cell volume. $n \geq 5$. box plot with Min to Max showing all data points. Significant differences were calculated according to One-way ANOVA with Tukey's multiple comparisons test. **E:** Sphericity of mitochondria. $n \geq 487$ mitochondria of 5 – 6 mesophyll cells; box plot with median and Tukey whiskers. Significant differences were calculated according to One-way ANOVA with Tukey's multiple comparisons test. Organelle parameters were analysed using Imaris (version 9.2.1, surface module). Imaris software was provided by Prof. Dr. Nicole Frankenberg-Dinkel and Dr. David Scheuring of TU Kaiserslautern. Plants were grown under standard conditions on soil.

6.2 Synthetic tethers – influence on the plant performance tested in transgenic *A. thaliana* T₃ plants

This section aimed to investigate the influence of the tether overexpression on the plant performance performing various phenotyping experiments in transgenic T₃ lines, Col-0 and px-ck. To get a comprehensive impression of the impact overexpressing the synthetic tether construct, the plant phenotype of transgenic *A. thaliana* lines were analysed in different tissues and ages.

6.2.1 No distinct trend in terms of germination and root growth of seedlings

In the previous section (6.1), it was shown that overexpression of the synthetic tether construct led to a formation of peroxisomal, spherical clusters (figure 42). In addition, various mitochondria were adjacent to the peroxisomes within those spherical clusters (figure 42). The β -oxidation is known to be required for the termination of dormancy and initiation of germination in *A. thaliana* seeds [239, 240]. Nietzel *et al.* described a redox-mediated kick start of the mitochondrial energy metabolism to be essential for an efficient seed germination [90]. They suggested that citrate functions as main respiratory substrate during the seed imbibition [90], which was in turn shown to be exported from peroxisomes [87].

Therefore, we wanted to test if and how the peroxisomal clustering and the mitochondrial localisation within this clusters might affect the germination of the transgenic synthetic tether lines. WT lines (Col-0, px-ck) and synthetic tether lines were studied regarding their germination efficiency. As a control line *trx-o1*, a thioredoxine knock-out mutant, was used, which was shown to have an impaired germination in a recent study [90]. Synchronised seed material, except for *trx-o1*, was observed over 4 d after sowing to track the testa rupture as well as the radicle penetration, which was termed as germination. Seeds were sown on ½ MS media with or without 1% sucrose, which served as an external carbon source.

First testa rupture and germination were detected after 48 h (figure 45). In the first 48 h control line *trx-o1* had a higher germination rate than both WT lines, but after 96 h showed a significant decrease in its germination rate (figure 45 C, F, I, L). For the tether and WT lines and independently under both conditions, a fast increase in testa rupture was detected from 24 h to 48 h. After 72 h most of the seeds had a break in the seed coat, with a percentage of about 94%, which slowly increased to a maximum between 96-99% (figure 45 A, B, G, H). Whereas the synthetic tether lines in the background of px-ck showed significantly faster testa rupture than the WT px-ck (figure 45 B, H), Col-0 24#5 #11C was significantly delayed compared to its background line Col-0 (figure 45 A, G).

+ sucrose

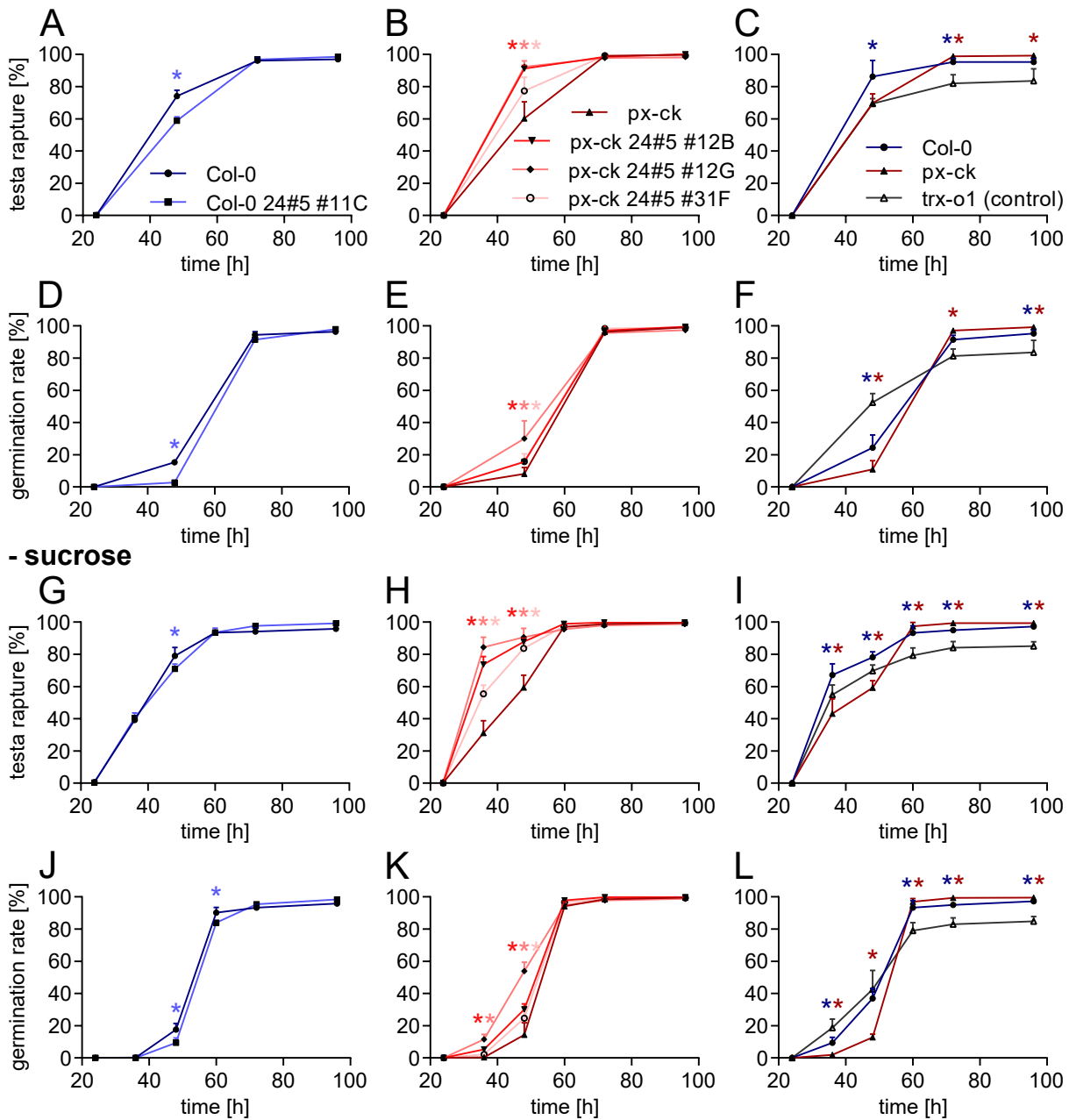


Figure 45: Germination rate of *A. thaliana* wild type background lines (Col-0, px-ck) and T_3 synthetic tether lines (PxPEX3N:tagRFP:mVenus:PpTOM20C; 24#5) under standard growth conditions on plates.

Synchronised *A. thaliana* seeds (except for *trx-o1*) were sown on plates (1/2 MS, 10 mM MES, pH 5.8 with KOH, 0.8% (w/v) phytigel) with 1% (w/v) sucrose (A-F) and without sucrose (G-L). The average emergence of testa rapture (A-C, G-I) and the complete germination with radicle penetration of the testa and endosperm (D-E, J-L) within the first 4 d after sowing is shown (n=300 - 500; average \pm SD). *trx-o1* was used as a control line, since it is published to have a decreased germination rate [90]. Significant differences were calculated according to 2-way ANOVA with Tukey's multiple comparisons test. Significant differences compared to the wild type background lines were indicated with * in respective colour.

As expected, radicle emergence was delayed compared to testa rupture. A strong increase in germination rate took place between 48 h and 60 h or 72 h. As for testa rupture all px-ck synthetic tether lines showed a significantly faster germination rate than their WT, whereas Col-0 tether line was significantly slower in germination (figure 45 D, E, J, K). Thus, there is not a consistent trend in germination efficiency. Only two independent lines (px-ck 24#5

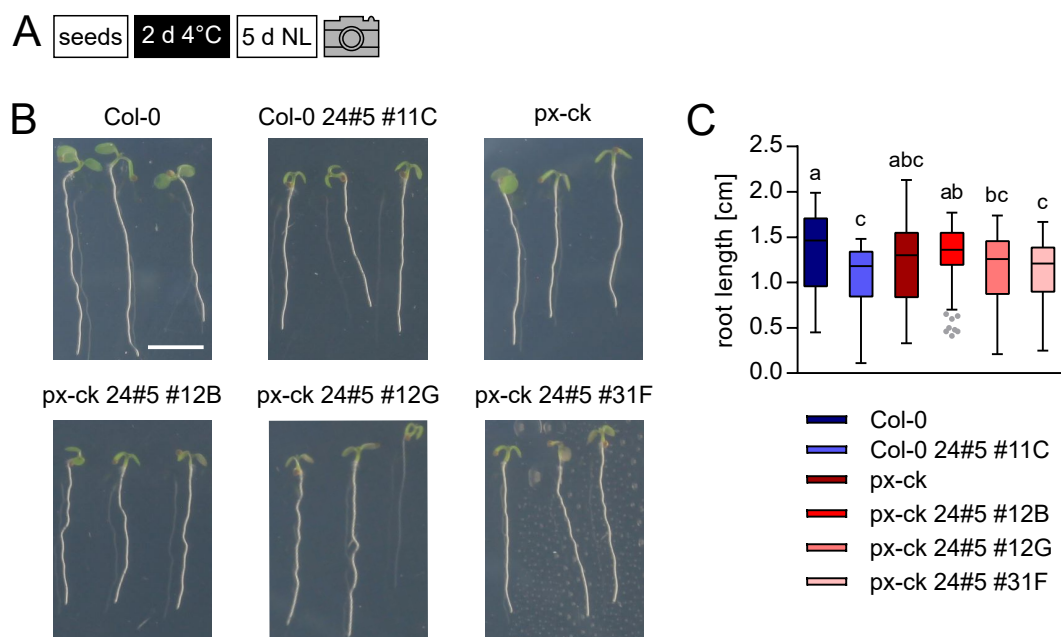


Figure 46: Root development of *A. thaliana* wild type background lines (Col-0, px-ck) and T₃ synthetic tether lines (PpPEX3N:tagRFP:mVenus:PpTOM20C; 24#5) under standard growth conditions.

A: Experimental setup of root development experiment under standard growth conditions ($100\text{--}200\ \mu\text{mol photons m}^{-2}\ \text{s}^{-1}$) on plates. Seeds on plates were stratified for 2 d at 4°C. **B:** Representative images of 5-day-old background lines (Col-0, px-ck) and three independent transgenic lines (#11C, #12B/#12G, #31F). **C:** Quantification of primary root growth after 5 d. $n \geq 92$; box plot with median and Tukey whiskers. Significant differences were calculated according to One-way ANOVA with Tukey's multiple comparisons test. Root growth was analysed with RootNav [185].

#12B/G /#31F) were significantly faster in germination, whereas one independent line (Col-0 24#5 #11C) was significantly delayed.

To verify if the root and seedling growth of the synthetic tether lines are affected, seeds were sown on $\frac{1}{2}$ MS media with 0.1% sucrose, stratified for 2 d at 4°C and transferred to standard growth conditions. The primary root length was detected after 5 d via photo and analysed with RootNav [185] (figure 46 A). One tether line Col-0 24#5 #11C showed a significantly impaired root growth of 20% compared its background WT Col-0. This was not confirmed by the other transgenic lines in the px-ck background (#12B/G, #31F), which were not significantly different to px-ck WT in root growth (figure 46 C). This was in line with the previously mentioned results where the line Col-0 24#5 #11C, the only line with shorter roots, was also the only one delayed in germination.

6.2.2 Rolled leaf and early senescence phenotype in synthetic tether lines

To investigate the impact of the organellar tethering in adults plants, their development on soil was studied in terms of leaf morphology, analysis of the rosette leaf area, fresh weight, and inflorescence development (figure 47).

Notably, all adult synthetic tether lines exhibited a curly leaf phenotype represented in figure 47 A. Compared to both WT lines, they had smaller leaves with a more yellow colouring (figure 47 C). This was also confirmed by studying the rosette leaf area (figure 47 B). After 3 weeks, synthetic tether lines were not significantly different compared to WT lines, but

from week 4 on, all transgenic lines had a significantly smaller leaf area compared to WT. The reduction of the leaf area ranged from 25% to 54% in week 4 and after 5 weeks even from 40% to 62%. This was also reflected in the fresh weight of 6-week-old plants (figure 47 E), which was clearly decreased in the overexpression lines compared to WT plants (reduction of 37%, 33%, 56% and 49% for Col-0 24#5 #11C, px-ck 24#5 #12B, #12G and #31F, respectively). Independently of rosette leaf area and the fresh weight, the induction of inflorescence was not significantly delayed for transgenic lines compared to both WT (figure 47 F), whereas the inflorescence height of 8-week-old plants was significantly decreased in all synthetic tether lines with a reduction of 41% to 67% compared to WT plants (figure 47 G).

To check if the curly leaf phenotype is also reflected at leaf morphology, leaf cross sections and quantification of the cell size were performed for the two representative synthetic tether lines px-ck 24#5 #12B and px-ck 24#5 #31F (figure 48). Leaf cross sections revealed that the tether leaves were creased and inconsistently thick, which was not true for that of px-ck WT plants (figure 48 A). The general cell structure of the synthetic tether lines was poorly organised and no clear border between palisade and sponge mesophyll tissue was identified. Additionally, the chloroplasts of both mutants seemed to be green-yellowish, whereas the chloroplasts of px-ck showed a saturated green colour.

To determine whether the curly phenotype was also reflected in a different cell size between synthetic tether lines and WT, z-stacks of mesophyll cells of 6-week old plants were analysed by Imaris to quantify the volume of represented lines. In figure 48 B the 3D-modulation of representative cells are shown, with chloroplasts in magenta, mitochondria in red, peroxisomes in blue and the 3D reconstruction of the cell in a transparent grey. Representative cells of both synthetic tether lines were distinctly smaller than that of WT px-ck (red frame in figure 48 C). Quantification of the cell size (volume) confirmed this results (figure 48 D). Whereas the average cell size of px-ck was $69.69 \cdot 10^3 \mu\text{m}^3$, px-ck 24#5 #12B and px-ck 24#5 #31F showed a significantly decrease in cell size with $39.08 \cdot 10^3 \mu\text{m}^3$ and $39.47 \cdot 10^3 \mu\text{m}^3$, respectively.

As already shown under normal growth conditions, adult plants showed an early senescence phenotype compared to WT plants (figure 47 A, C). To verify this phenotype, the 3rd and 4th leaf of individual WT and tether plants were covered with aluminium foil for 5 d (figure 49 A; method adapted from F. Li *et al.* [193]). Images were taken and the greenness was quantified using the ratio of green to red intensities per pixel. As shown in figure 49 B the 3rd (left) and 4th (right) leaves of the tether plants were more yellowish as WT leaves, which was also confirmed by a quantification of the greenness of those leaves (figure 47 B, C). The overexpression lines showed a trend (px-ck 24#5 #31F) or even a significantly decrease (Col-0 24#5 #11C, px-ck 24#5 #12B/G) in their leaf greenness compared to their respective WT background line. Thus, these results underline the early senescence phenotype, which was found under control growth conditions (figure 47 A, C).

III. RESULTS

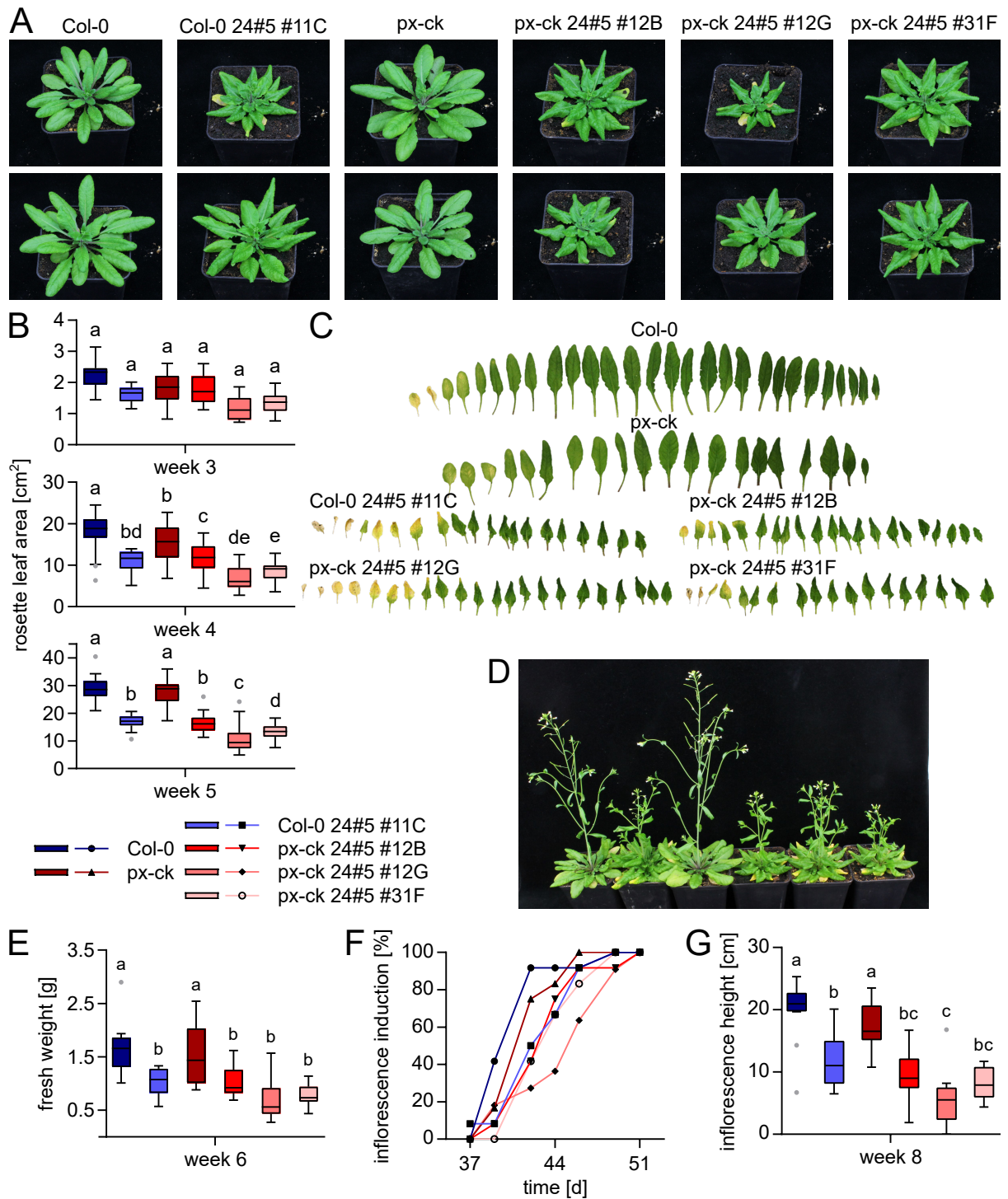


Figure 47: Comparison of *A. thaliana* wild type background lines (Col-0, px-ck) and T₃ synthetic tether lines (PpPEX3N:tagRFP:mVenus:PpTOM20C; 24#5) under standard growth conditions on soil.

A: Representative images of 6-week-old background lines (Col-0, px-ck) and three independent synthetic tether lines (#11C, #12B/#12G, #31F) grown under standard conditions. **B:** Rosette leaf area after three, four and five weeks. n = 24; box plot with median and Tukey whiskers. Significant differences were calculated according to One-way ANOVA with Tukey's multiple comparisons test. **C:** Representative images of leaves of 7-week-old plants. **D:** Representative images of 8-week-old plants (from left to right: Col-0, Col-0 24#5 #11C, px-ck, px-ck 24#5 #31F, px-ck 24#5 #12B, px-ck 24#5 #12G). **E:** Fresh weight of 6-week-old plants. n = 12; box plot with median and Tukey whiskers. Significant differences were calculated according to One-way ANOVA with Tukey's multiple comparisons test. **F:** Analysis from vegetative to generative growth of plants. Induction was counted when inflorescence was 1 cm or higher. n = 12 except for px-ck 24#5 #12G (n = 11). Significant differences were calculated according to 2-way ANOVA with Tukey's multiple comparisons test. No significant differences in inflorescence induction were detectable. **G:** Inflorescence height of 8-week-old plants. n = 12; box plot with median and Tukey whiskers. Significant differences were calculated according to One-way ANOVA with Tukey's multiple comparisons test.

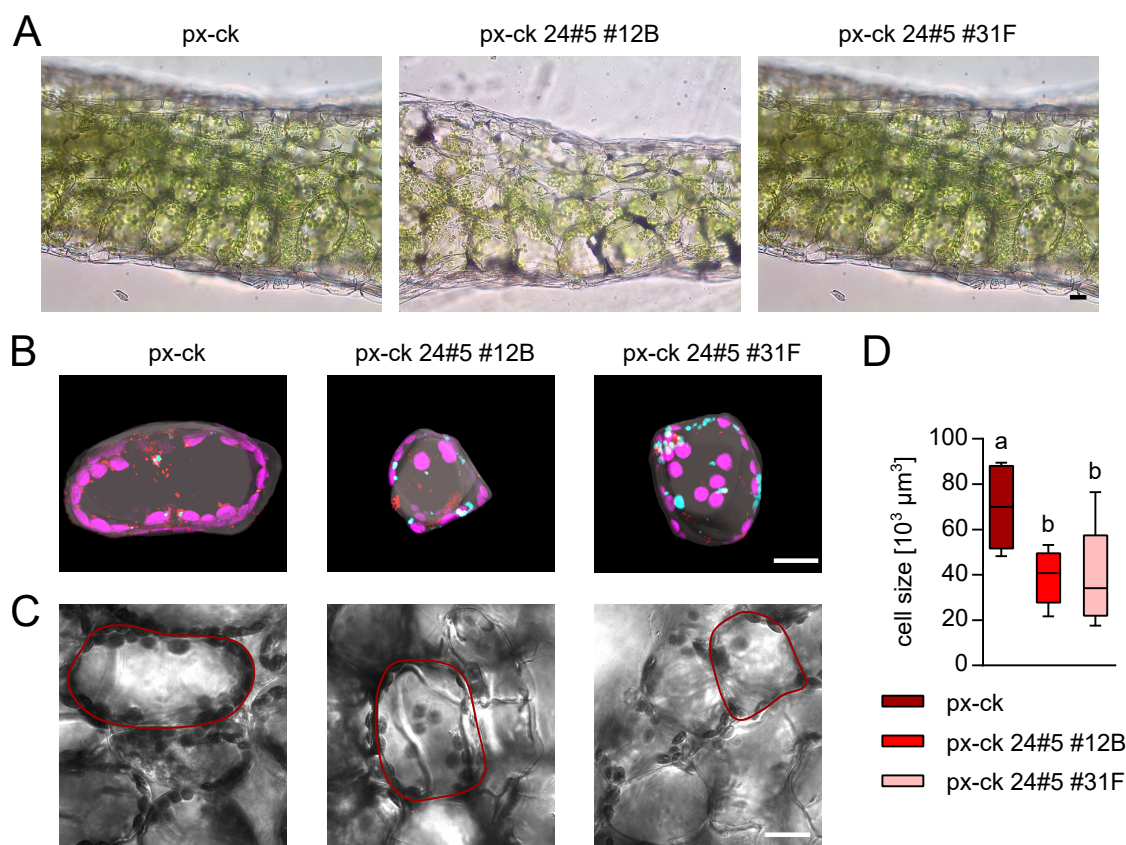


Figure 48: Leaf morphology and mesophyll cell size of *A. thaliana* wild type px-ck and T₃ synthetic tether lines (PpPEX3N:tagRFP:mVenus:PpTOM20C; 24#5).

A: Representative images of leaf cross sections of 5-week-old *A. thaliana* WT px-ck and two representative synthetic tether lines (px-ck 24#5 #12B, px-ck 24#5 #31F). **B, C:** Representative images of cells of 6-week-old background line (px-ck) and two independent synthetic tether lines (#12B, #31) grown under standard conditions. 3D representation of representative cell with chloroplasts (magenta), peroxisomes (cyan) and mitochondria (red) (**B**) and respective bright field image. (**C**). **D:** Quantification of cell size [μm³]. $n \geq 5$. box plot with median and Tukey whiskers. Significant differences were calculated according to One-way ANOVA with Tukey's multiple comparisons test. Cell volume was analysed using Imaris x 64 (version 9.2.1, surface module). Imaris software was provided by Prof. Dr. Nicole Frankenberg-Dinkel and Dr. David Scheuring of TU Kaiserslautern. Plants were grown under standard conditions on soil. Scale bar 20 μm.

6.2.3 Inconsistently altered reproductive development in synthetic tether lines

Besides the curly leaves, overexpression of the construct 24#5 led to a decrease in inflorescence height. Although inflorescence induction was not impaired, the difference in its height raised the question of whether this is due to poorer plant growth in general or whether the mutants are also impaired in their reproductive development.

Therefore, the morphology of the primary inflorescence and the flowers were studied. As represented in figure 50 A, the inflorescence with the siliques and flowers of WT and mutants were quite similar, while the siliques seem to be slightly smaller for the synthetic tether lines. Shorter siliques might indicate difficulties in the reproductive development. Thus, different criteria regarding plant reproductions were analysed. At the first glance, the flower morphology of the synthetic tether lines (figure 50 B) was similar to that of WT. The morphology of the stem as the morphology and number of the stamen (6 stamen, indicated with red arrows) of all synthetic tether lines did not differ to WT plants in the shown resolution.

III. RESULTS

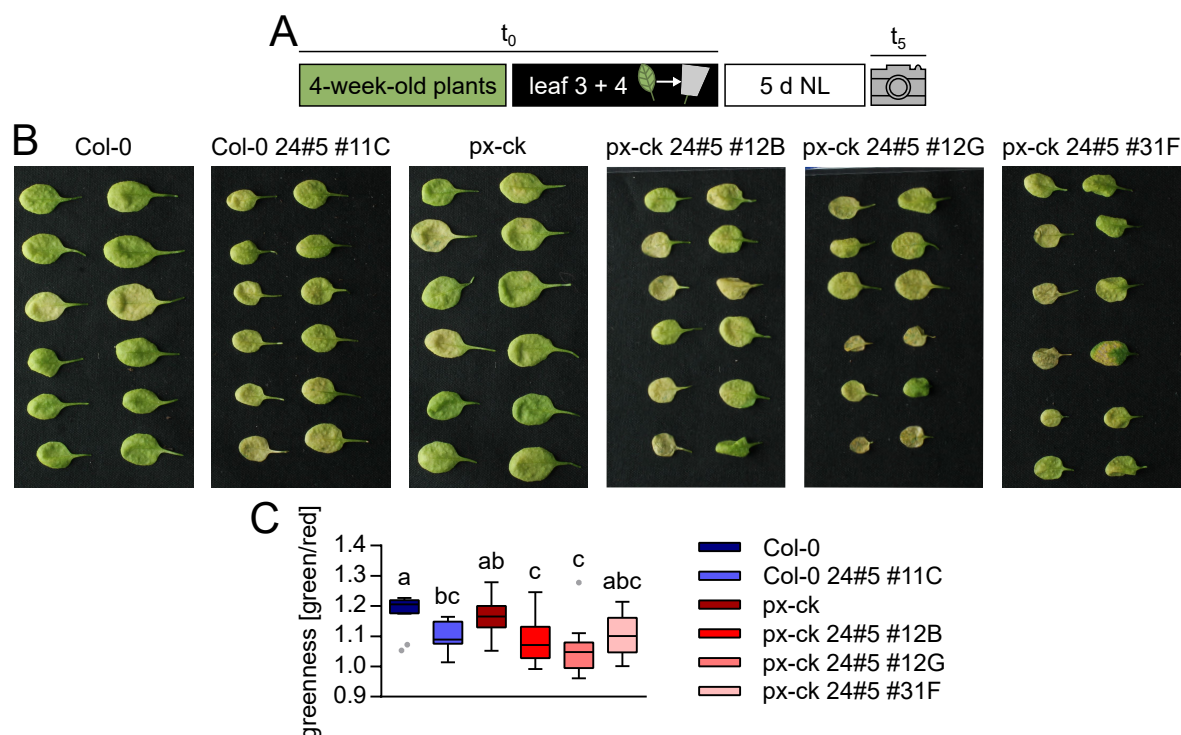


Figure 49: Dark-induced senescence of 4-week-old *A. thaliana* wild type background lines (Col-0, px-ck) and T₃ synthetic tether lines (PpPEX3N:tagRFP:mVenus:PpTOM20C; 24#5).

A: Experimental setup of dark induce senescence experiment. Third and fourth rosette leaves of 4-week-old *A. thaliana* background lines and synthetic tether lines were individually darkened with aluminium foil for 5 d, whereas the plant itself is grown under control conditions. **B:** Representative images of individually darkened leaves of 4-week-old background lines (Col-0, px-ck) and three independent synthetic tether lines (24#5: #11C, #12B/#12G, #31F). **C:** Quantification of the progression of dark-induced senescence in leaves shown in (B) by analysis of leaf greenness (green pixel intensity divided by red pixel intensity from RGB encoded image). n = 12 (6 different plants). box plot with median and Tukey whiskers. Significant differences were calculated according to ordinary One-way ANOVA with Tukey’s multiple comparisons test.

Nevertheless, quantification of the silique length revealed a trend of shorter siliques for all synthetic tether lines with a reduction of 44% (Col-0 24#5 #11C), 9% (px-ck 24#5 #31F) and 3% (px-ck 24#5 #12B) compared to respective WT siliques (figure 51 B). Col-0 24#5 #11C showed a much more severe decrease in silique length than both lines in px-ck background.

Studying the seed development, the next logical step was to test if the strong decrease in silique length for Col-0 24#5 #11C was reflected in the ability to generate viable seeds. In figure 51 A representative images of a silique dissection are shown. While both WT lines had fully developed siliques, a lot of empty spaces were found in Col-0 24#5 #11C. In the higher resolution, little rudiments of a putative seed were visible instead of the fully developed seeds. The other two synthetic tether lines did not have empty spaces, but the line px-ck 24#5 #12B showed in average 19.5% transparent seeds (figure 51 A, quantification not shown). A quantification of the amount of seeds per silique confirmed the results described above. Whereas the plants of WT px-ck 24#5 #12B and px-ck 24#5 #31F did not differ in their seed production, Col-0 24#5 #11C produced significantly less seeds per silique.

Thus, two of the three synthetic tether lines showed different but still distinct limitations in silique and seed development. To further examine where these limitations came from, we

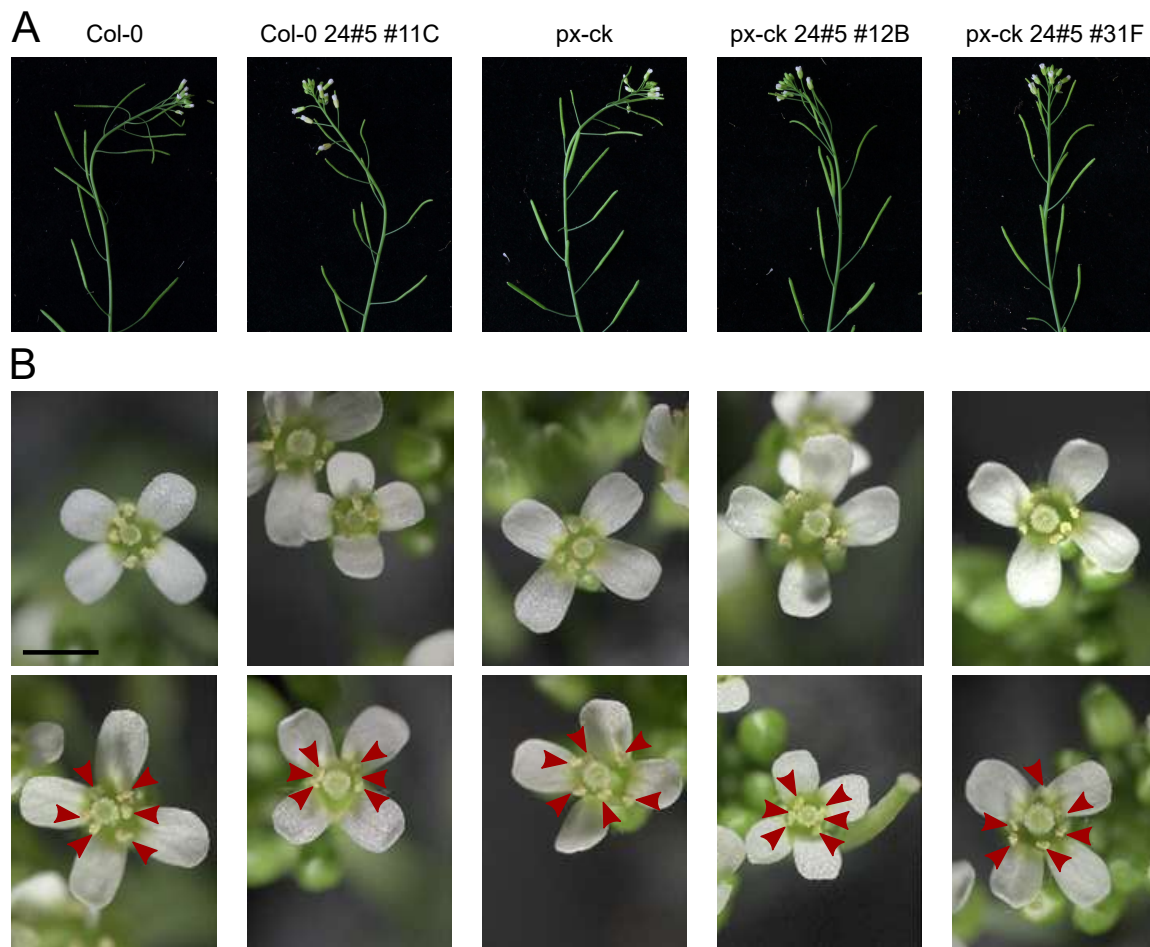


Figure 50: Inflorescence and flower morphology of *A. thaliana* wild type background lines (Col-0, px-ck) and T₃ synthetic tether lines (PpPEX3N:tagRFP:mVenus:PpTOM20C; 24#5) under standard growth conditions.

A, B: Representative images of inflorescence with flower and siliques (A) and flowers (B) of 8-week-old background lines (Col-0, px-ck) and three independent synthetic tether lines (#11C, #12B/#12G, #31). Red arrows marked 6 stamens of representative flower. Scale bar = 1 mm.

studied the pollen viability of all synthetic tether lines with an Alexander staining approach. For intact pollen grains, the cytosol is coloured in magenta-red surrounded by the greenish cell wall. Dead pollen grains lost their cytoplasm and therefore look smaller and have only the green envelope. In figure 52 A representative images of all lines are shown, with all lines having a similar stamen morphology and mostly viable and alive pollen. One exception was the synthetic tether line Col-0 24#5 #11C with a high number of dead pollen grains (figure 52 A). This was also confirmed quantifying the ratio of dead pollen as shown in figure 52 B. The overexpression lines px-ck 24#5 #12B and #31F did not have a significantly different ratio of dead pollen compared to WT lines, where Col-0 24#5 #11C showed a severe and significant increase of the dead pollen ratio. Also the total number of pollen grain per replicate (n = 5; for #11C: n = 6) differed. For WT lines and synthetic tether lines px-ck 24#5 #12B and px-ck 24#5 #31F, the average number of pollen counted per replicate ranged from 975 to 1169 (alive: 944 – 1088, dead: 21 - 83); for #11C, the average number was lowest at 879 pollen per replicate (alive: 634, dead: 245) (supplemental table S2).

As shown beforehand, all synthetic tether lines had partially and consistent disturbed

III. RESULTS

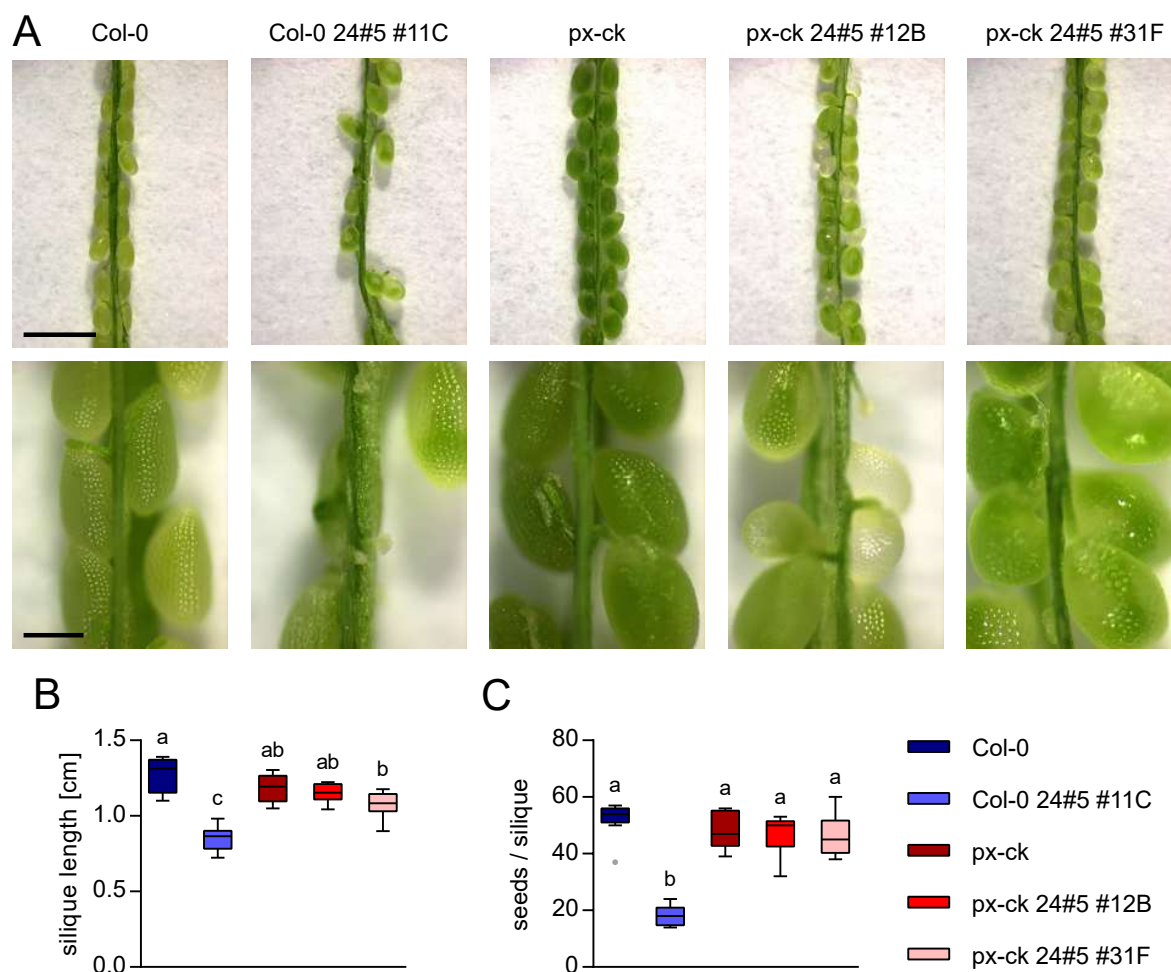


Figure 51: Silique morphology and seed development of *A. thaliana* wild type background lines (Col-0, px-ck) and T₃ synthetic tether lines (PpPEX3N:tagRFP:mVenus:PpTOM20C; 24#5) under standard growth conditions.

A: Representative images of silique dissection of 8-week-old background lines (Col-0, px-ck) and three independent synthetic tether lines (#11C, #12B, #31). Scale bar 1 mm (upper row) and 200 μm (lower row). **B, C:** Quantification of silique length (**B**) and total number of seeds per silique (**C**). n = 6. box plot with median and Tukey whiskers. Significant differences were calculated according to One-way ANOVA with Tukey's multiple comparisons test. Images were generated by Dr. José Manuel Ugalde.

growth phenotype regarding curly leaves, smaller rosette leaf area, less fresh weight and smaller primary inflorescence, whereas the inflorescence induction and flower morphology was similar to that of WT background plants. The root growth, the germination rate, and the reproductive development were not equally altered in all lines compared to WT. The tether line Col-0 24#5 #11C showed a severe but unique disturbance in pollen death resulting in less seeds production and significantly smaller siliques. Additionally, also the germination efficiency was significantly delayed compared to WT Col-0, which might also go hand in hand with a significantly decrease in root length. In contrast, all synthetic tether lines in the background of px-ck showed a significantly faster germination and no significant differences in root length, rate of dead pollen and seeds per silique compared to the WT px-ck. Additionally, the line px-ck 24#5 #12B produced 19% transparent seeds.

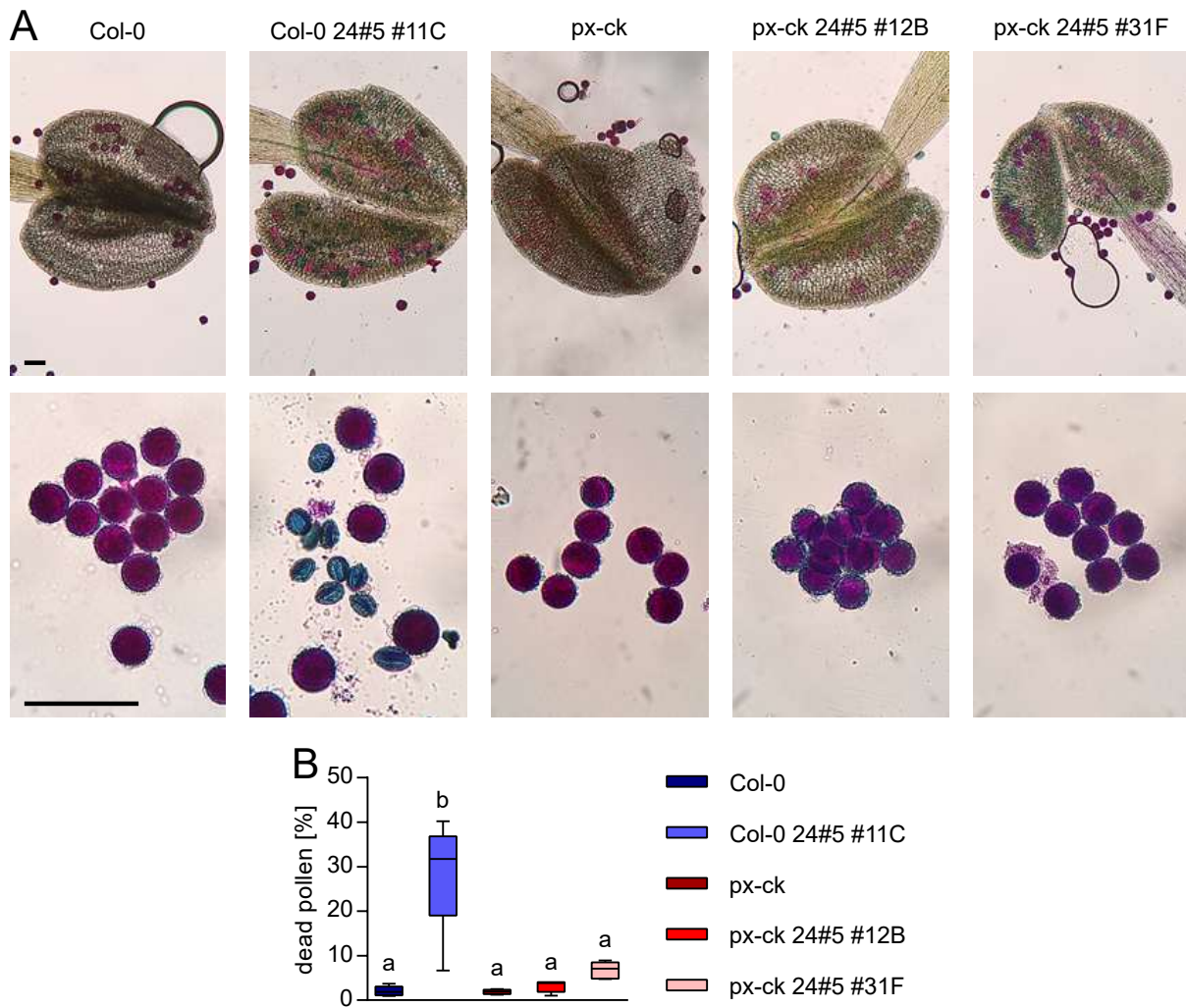


Figure 52: Pollen grains and stamena development of *A. thaliana* wild type background lines (Col-0, px-ck) and T₃ synthetic tether lines (PpPEX3N:tagRFP:mVenus:PpTOM20C; 24#5) under standard growth conditions.

A: Representative images of stamens and pollen of 8-week-old background lines (Col-0, px-ck) and three independent synthetic tether lines (#11C, #12B, #31) with Alexander staining. Scale bar 50 μ m. **B:** Quantification of dead pollen [%]. n = 5; box plot with median and Tukey whiskers. Significant differences were calculated according to One-way ANOVA with Tukey's multiple comparisons test. Images and data analysis were performed in collaboration with Dr. José Manuel Ugalde.

6.3 Photosynthetic performance and respiration of synthetic tether plants

The photorespiratory organelles chloroplasts, peroxisomes and mitochondria are known to have an increased proximity in light compared to dark conditions [26]. Since the CLSM data revealed that mitochondrial morphology and the distribution of peroxisomes and mitochondria were altered in the synthetic tether lines compared to WT plants (results section 6.1), the question raised if overexpression of the tether has any impact photosynthetic activity or the mitochondrial respiration.

To study the photosynthetic activity, a JUNIOR-PAM (Heinz Walz GmbH) was used and following parameters were investigated: 1) The photochemical quantum yield of photosystem II (PSII) ($Y(II)$), 2) the maximum quantum yield of photochemistry of PSII ($F_V/F_M = (F_M - F_0)/F_M$) and 3) non-photochemical fluorescence quenching (NPQ) (figure 53). The $Y(II)$ and

III. RESULTS

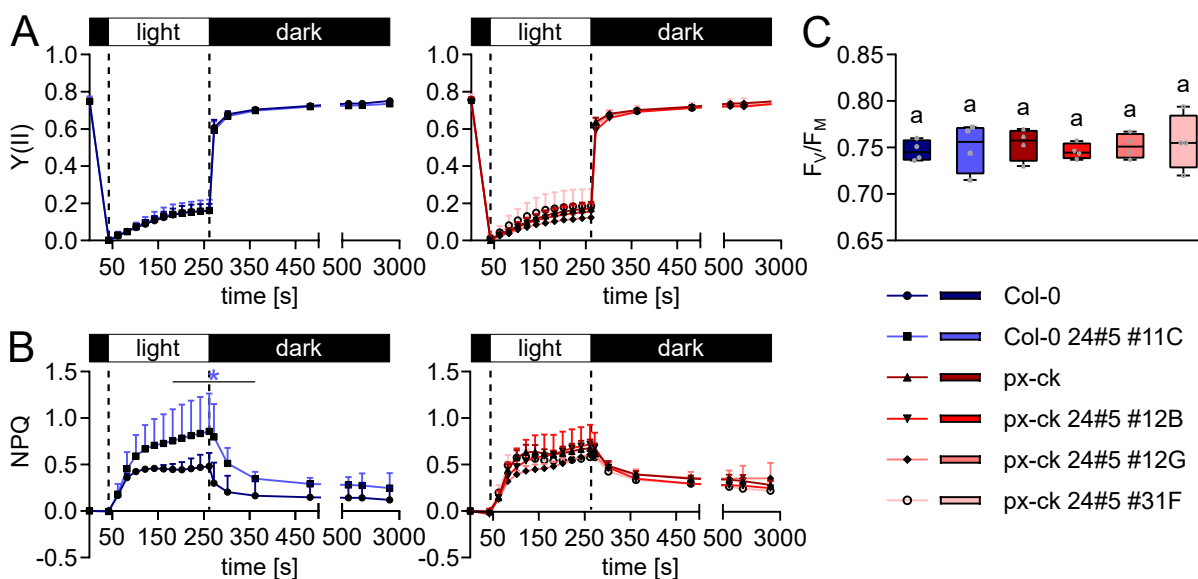


Figure 53: Pulse Amplitude Modulation (PAM) fluorometry analysis of 9-week-old *A. thaliana* wild type background lines (Col-0, px-ck) and T₃ synthetic tether lines (PpPEX3N:tagRFP:mVenus:PpTOM20C; 24#5) under standard conditions on soil.

A, B, C: Analysis of photosynthetic activity of 9-week-old background lines (Col-0, px-ck) and three independent synthetic tether lines (24#5: #11C, #12B/#12G, #31F) grown under standard growth conditions. Plants were dark adapted for at least 45 min prior measuring the photosynthetic activity by using a JUNIOR-PAM (Heinz Walz GmbH). The predefined program “induction curve + recovery” (IC + Recov) was performed under high light (HL) conditions with an actinic light intensity of $250 \mu\text{mol photons m}^{-2} \text{s}^{-1}$ (Act. Int. 6) (yellow background) for 200 s followed by a recovery phase of 45 min 50 s in the dark. As readout the photochemical quantum yield of photosystem II (PSII) ($Y(II)$) (A), non-photochemical fluorescence quenching (NPQ) (B) and the maximum quantum yield of photochemistry of PSII (F_V/F_M) (C) are shown. $n = 4$; A, B: Mean + SD. Significant differences were calculated according to 2way ANOVA with Tukey’s multiple comparisons test. C: box plot with median and Tukey whiskers. No significant differences were calculated according to ordinary One-way ANOVA with Tukey’s multiple comparisons test. Significant differences compared to the wild type background lines were indicated with * in respective colour.

F_V/F_M are calculated on the basic fluorescence yield (F_0), when all reaction centres of PSII are open, and the maximum chlorophyll fluorescence yield (F_M), when PSII reaction centres are closed after excited with a strong light pulse. NPQ summarises all other modification of fluorescence yield, which are based on heat dissipation [197].

Prior to the measurements, plants needed to be incubated for at least 45 min in the dark to relax all reaction centres of PSII. As shown in figure 53 A, the photosynthetic yield $Y(II)$ was detected over time with a short dark period of 50 s, followed by a photosynthetic induction with light ($250 \mu\text{mol photons m}^{-2} \text{s}^{-1}$) of 200 s and a recovery phase of about 45 min. All overexpression lines behaved similar to WT background lines. This was also true for the maximum photosynthetic yield at time point 0 s, which is individually shown in figure 53 C as F_V/F_M . all synthetic tether lines in the background of px-ck did not exhibit a different NPQ over time, whereas Col-0 24#5 #11C showed a higher NPQ in the late phase of light induction and also in the beginning of the recovery phase (see figure 53 B).

In the synthetic tether lines, mitochondria were shown to be altered in shape compared to WT (figure 44) and some also to be localised within peroxisomal clusters (figure 42). Mitochondria are the place for the respiration. Similar to the synthetic tether lines, a complex I mutant *ndufs4* has curly rosette leaves and its inflorescence is also smaller compared to the WT. This mutant was detected to have a higher oxygen consumption than the WT [198].

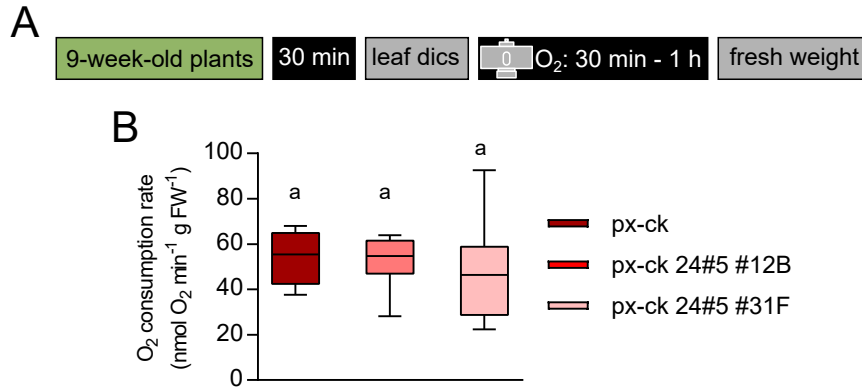


Figure 54: Analysis of respiration of *A. thaliana* wild type px-ck and T₃ synthetic tether lines (PpPEX3N:tagRFP:mVenus:PpTOM20C; 24#5) under standard growth conditions on soil.

A: Experimental setup of procedure for respiration detection. 9-week-old plants were at least dark adapted for 30 min before leaf discs of 7 mm diameter were cut out and measured in 1 mL H₂O_{dd} for 30 min to 1 h in the dark. **B:** Oxygen (O₂) consumption normalised over the fresh weight (FW). $n \geq 5$. box plot with median and Tukey whiskers. No significant differences were calculated according to One-way ANOVA with Tukey's multiple comparisons test.

Due to the similarity of our synthetic tether lines and the complex I mutant, we hypothesise an altered or higher respiration than in WT plants. This hypothesis was verified using WT px-ck and two synthetic tether lines px-ck 24#5 #12B / #31F. The oxygen consumption was detected by using a Clark type oxygen electrode Oxytherm (Hansatech).

In order to guarantee a stop in photosynthetic activity in the leaf tissue, plants must be incubated for at least 30 min in the dark prior the experiment, which also needs to be performed under dark conditions. The measured oxygen consumption was normalised via fresh weight of the leaf discs. For both synthetic tether lines, the oxygen consumption was not significantly different to that of px-ck.

Summarising the results of both, photosynthetic activity and the oxygen consumption, the synthetic tether lines behaved similar to WT plants except for NPQ, where one line Col-0 24#5 #11C exhibits a significantly increase.

6.4 Synthetic tethers – influence on the plant performance under stress conditions

Adult plants showed already under normal growth conditions a clearly altered phenotype compared to WT plants. The growing conditions termed as normal do not reflect realistic conditions in a natural environment, but optimal and constant conditions. In a natural environment, the plants would have to cope with changing environmental conditions as well as pathogens. Both, abiotic or biotic stresses in general induce cellular oxidative stress, which in turn activate a ROS scavenging system [40, 241–243].

6.4.1 Increased resilience to heat in seedling in roots

In the synthetic tether plants, mitochondria and peroxisomes were shown to be altered in shape and localisation in the cell, respectively, compared to WT (figure 44). Both organelles

III. RESULTS

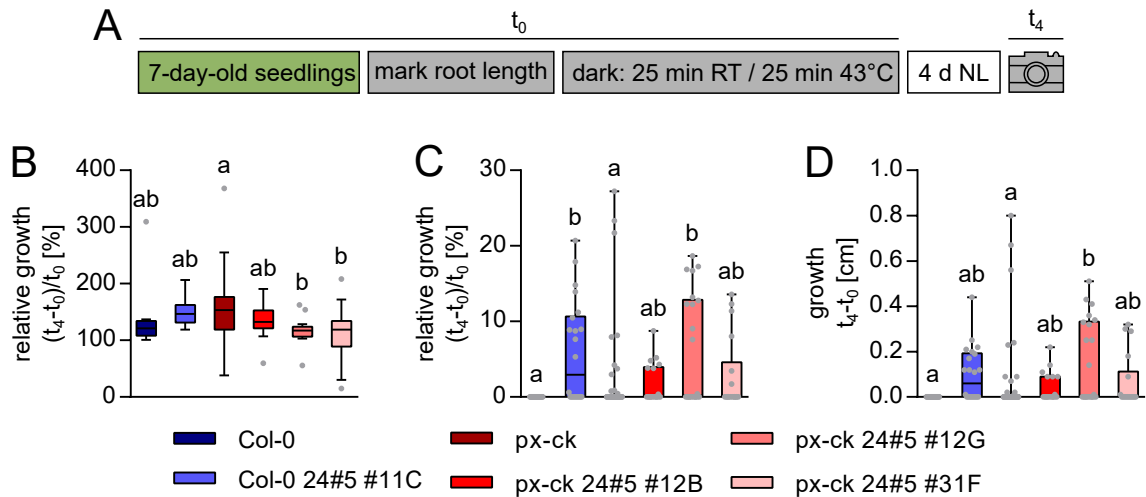


Figure 55: Root development of *A. thaliana* wild type background lines (Col-0, px-ck) and T₃ synthetic tether lines (PpPEX3N:tagRFP:mVenus:PpTOM20C; 24#5) after heat stress on plates.

A: Experimental setup: Root length of 7-week-old seedlings on plates were marked. Half of the plates were stressed at 43°C for 25 min in a water bath, whereas the control plates were incubated at room temperature (RT) in the. After treatment plates were grown for 4 d under standard growth conditions before taking images. **B, C:** Quantification of relative root growth of background lines (Col-0, px-ck) and three independent synthetic tether lines (#11C, #12B/#12G, #31) 4 d after control condition (B) and heat stress of (C). The growth [%] is calculated as (primary root growth ($t_4 - t_0$)/primary root growth (t_0)) *100. $n \geq 15$. **D:** Absolute root growth of heat stressed plants after 4 d. $n \geq 16$. Data are shown as box plot with median and Tukey whiskers (B) and box plot with Min to Max showing all points (C,D). Significant differences were calculated according to One-way ANOVA with Tukey's multiple comparisons test. Root growth was analysed with RootNav [185].

play also a role in plant stress response and in the ROS scavenging machinery (see reviews [244] (mitochondria), [245] (peroxisomes)). Therefore, we performed different stress treatments in different tissues and ages to study, if the response to stress is altered in the synthetic tether lines.

Mitochondria have been shown to be important for stress scavenging, including heat [246]. Therefore, the question raised, if the change in mitochondrial sphericity and proximity to peroxisomes in prior mentioned clusters (figure 42) impact their heat stress tolerance. This was tested on seedlings, by marking the root length of 7-day-old seedlings on plates (t_0) and transferring half of the plates to a water bath at 43°C for 25 min, while incubating the control plates for 25 min at RT under dark conditions (figure 55 A). After 4 d (t_4) photos were taken and the absolute and relative root growth after the treatment was calculated (figure 55 B, C, D). Under control conditions, the transgenic plants exhibited a similar or a small but significantly decrease in the relative root growth (figure 55 B). However, after heat stress a trend of an increase in the relative root growth was identified (figure 55 C). This trend was based on the absolute root growth (figure 55 D) but also especially on the higher survival rate of the synthetic tether lines compared to the WT after heat treatment (Col-0: 0.0%, px-ck: 19.6%, Col-0 24#5 #11C: 54.5%, px-ck 24#5 #12B: 38.9%, px-ck 24#5 #12G: 50.0%, px-ck 24#5 #31F: 33.3%).

6.4.2 Higher susceptibility to high light stress in adult plants than in young plants

High light (HL) was described to increase peroxule-mitochondria interactions in *A. thaliana* leaves [20]. Since the two organelles seemed to be mostly affected by overexpressing the

synthetic tether construct (see results section 6.1), it would be interesting to investigate, how the tether plants can cope with HL stress situations.

The experimental setup was adapted from Garcia-Molina *et al.* [247], performing either a HL or a control treatment (normal light (NL)), followed by 4 d of recovery under NL. The production of anthocyanins is known to be up-regulated under HL and serve as a protection mechanism against the UV light [247, 248]. Thus, fresh weight, anthocyanin concentration and, to quantify the damage to the photosystems, the maximum photosynthetic yield of PSII (F_V/F_M) were chosen as readout parameters (figure 56 A and 57 A). Since the synthetic tether lines already showed an age-dependent phenotype with more severe differences in higher ages under normal growth conditions, HL treatments were performed in seedlings and adult plants.

To verify the impact in an early growth state, 2-week-old plants of the WT px-ck and two representative synthetic tether lines px-ck 24#5 #12B and px-ck 24#5 #31F were investigated. As shown in figure 56 B, leaves of all investigated seedlings were bent downwards as light avoidance response to the HL treatment (t_4). After additional 4 d of recovery (t_8) no differences between the genotypes but also between NL and HL treatment were identified by eye.

Quantification of the FW after 4 d (t_4) revealed that only one of the overexpression lines (px-ck 24#5 #31F) was significantly lighter than the WT px-ck, but independent on HL or NL treatment (figure 56 C, D). After additional 4 d (t_8) under NL, the control plants showed the same trend as after 4 d (t_4). However, HL treated tether plants seemed to have difficulties in the recovery phase, as the FW was significantly reduced by 20% and even 51% after additional 4 d under NL for px-ck 24#5 #12B and px-ck 24#5 #31F, respectively, compared to the WT (figure 56 F).

As a second parameter the relative anthocyanin content was quantified directly after the HL treatment (t_4). Albeit WT and tether plants looked similar after the HL treatment to NL treated plants (figure 56 B), a quantification of the relative anthocyanin content revealed that HL treated plants had a relative higher amount of anthocyanin than plants under NL treatment (t_4) (figure 56 G, H). Within the same treatment the genotypes had a similar relative anthocyanin content except for the tether line px-ck 24#5 #31F under NL conditions. This line, which showed also under NL conditions a reduction in FW (figure 56 C), had significantly higher anthocyanin content compared to WT (figure 56 G).

The same experimental setup was applied to 5-week-old plants as shown in figure 57. Different to the 2-week-old seedlings, all synthetic tether lines performed differently to WT plants, both directly after the HL treatment (t_4) and after additional 4 d of recovery (t_8) (figure 57 B). On the one hand they differed in their size, namely synthetic tether lines were smaller than WT plants, albeit independently on the light treatment. The size difference was also confirmed by a significantly decrease in FW of all synthetic tether lines compared to WT (figure 57 G, H), which was even more severe in plants grown under HL conditions. On the other hand, the colouring of the leaves differed between WT and synthetic tether lines.

III. RESULTS

Directly after the HL treatment WT leaves were reddish coloured, whereas the leaves of all synthetic tether lines were yellowish (t_4). These yellowish leaves died instead of recovering, as WT leaves did after additional 4 d under NL (t_8). The reddish colour of the HL treated WT plants indicated an increase in anthocyanin content. This was confirmed qualitatively by the colouring of the isolation liquid, whose reddish colour was proportional to the anthocyanin content. The observation, that the WT lines produced more anthocyanin than the synthetic tether lines after HL treatment, was also confirmed by an absorbance quantification normalised over FW (figure 57 I, K). While under control conditions all lines had a similar anthocyanin content (figure 57 I), after HL treatment and recovery adult tether plants exhibited a significantly decrease in their relative anthocyanin content (figure 57 K). The relative anthocyanin content ranged only between 22% and 32% of that of WT plants. Thus, adult tether plants produced much less anthocyanin than WT plants. In order to verify how the low amount of anthocyanin affect the protection mechanism of the photosynthetic machinery, F_V/F_M was quantified at t_0 , t_4 and t_8 as an additional parameter. Prior to treatment t_0 all lines showed a similar maximum photosynthetic yield F_V/F_M , whereas after 4 d of HL treatment all synthetic tether lines had a significant reduction in F_V/F_M compared WT plants indicating a damage of the photosystems. Also, after a recovery phase of 4 d under NL, they showed the same reduction in F_V/F_M as directly after the HL treatment.

In summary, the synthetic tether lines exhibited varying responses to different types of stress and also dependent on their growth stages. Whereas 2-week-old plants seemed to be less affected by HL stress, adult plants showed a more severe reaction.

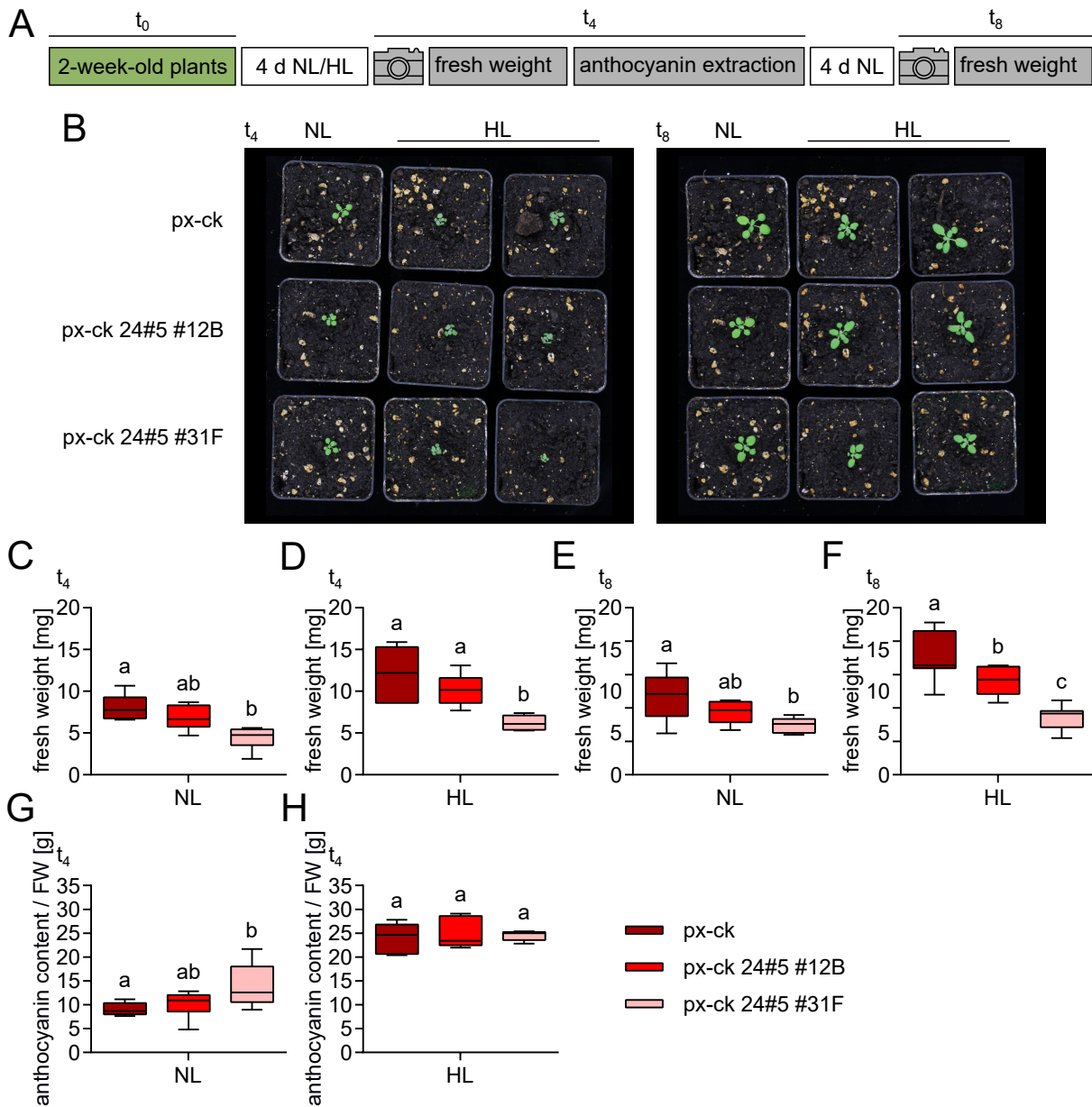


Figure 56: Comparison of 2-week-old *A. thaliana* wild type px-ck and two T₃ synthetic tether lines (#12B, #31F) containing the synthetic tether construct PpPEX3N:tagRFP:mVenus:PpTOM20C (24#5) under high light stress conditions on soil.

A: Experimental setup of high light (HL, 350 $\mu\text{mol photons m}^{-2} \text{s}^{-1}$) experiment with normal light (NL 100–120 $\mu\text{mol photons m}^{-2} \text{s}^{-1}$) as control conditions. **B:** Representative images of 2-week-old background line px-ck and two independent synthetic tether lines (24#5: #12B, #31F) grown under standard conditions (NL) or HL conditions at day 4 (left image) and 8 (right image). **C, D, E, F:** Fresh weight of plants after NL or HL treatment (t_4) (**C, D**) and after recovery of 4 d (t_8) under NL (**E, F**). $n \geq 6$; box plot with median and Tukey whiskers. Significant differences were calculated according to One-way ANOVA with Tukey's multiple comparisons test. **G, H:** Quantification of anthocyanin content (t_4) after NL (**G**) and HL treatment (**H**). Relative anthocyanin content is calculated according to following equation: $A535 - 0.25 \cdot A650 / \text{FW} [\text{g}]$ [194]. $n = 6$; box plot with median and Tukey whiskers. Significant differences were calculated according to One-way ANOVA with Tukey's multiple comparisons test.

III. RESULTS

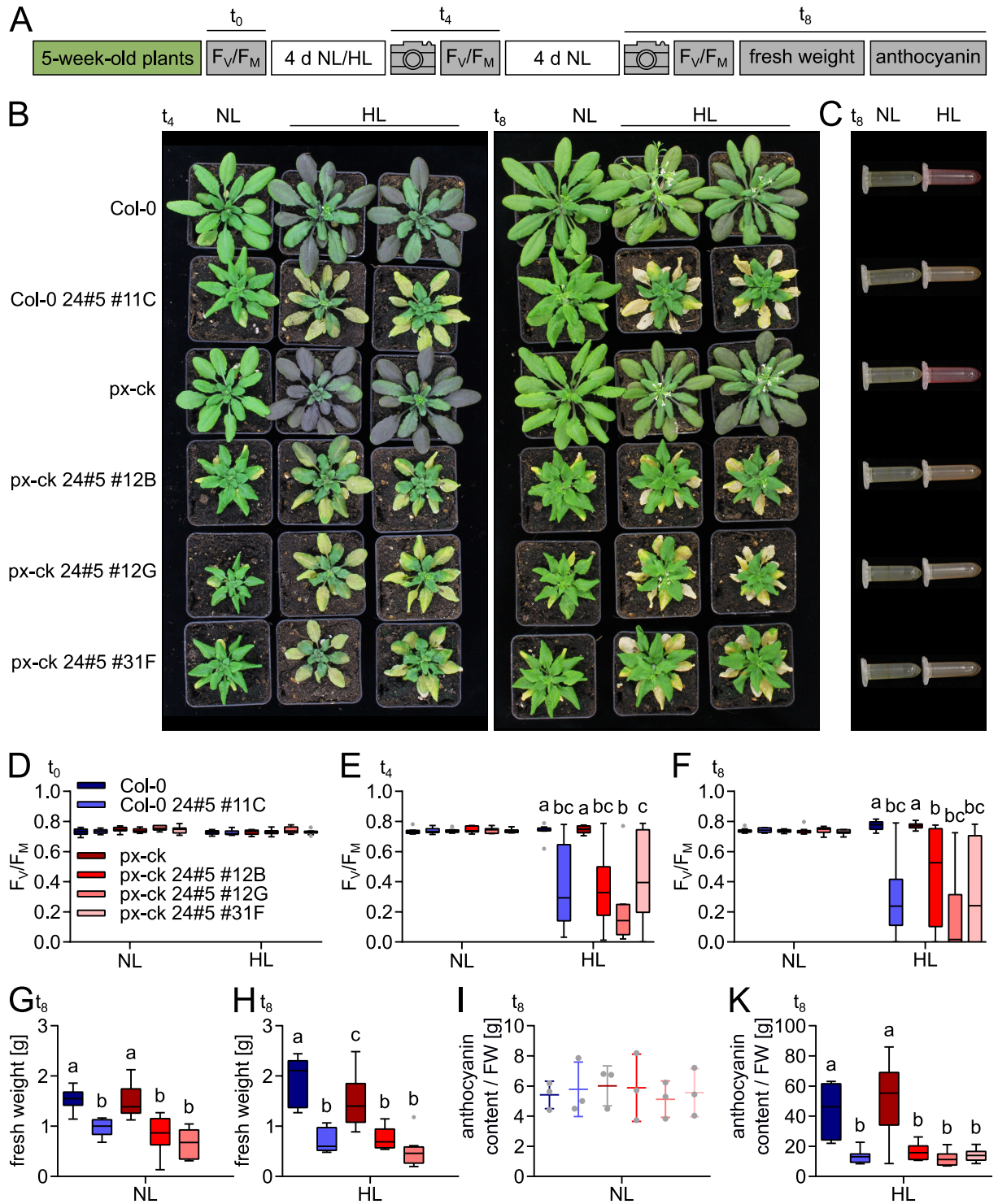


Figure 57: Comparison of 5-week-old *A. thaliana* wild type background lines (Col-0, px-ck) and T₃ synthetic tether lines (PpPEX3N:tagRFP:mVenus:PpTOM20C; 24#5) under high light stress conditions on soil.

A: Experimental setup of high light (HL, 350 $\mu\text{mol photons m}^{-2} \text{s}^{-1}$) experiment with normal light (NL 100–120 $\mu\text{mol photons m}^{-2} \text{s}^{-1}$) as control conditions. F_V/F_M represents the photosynthetic activity measured by usage of a JUNIOR-PAM (Heinz Walz GmbH). **B:** Representative images of 5-week-old background lines (Col-0, px-ck) and three independent synthetic tether lines (24#5: #11C, #12B/#12G, #31F) grown under standard conditions (NL) or HL conditions at day t₄ (left image) and t₈ (right image) **C:** Representative anthocyanin extraction colour at t₈. **D, E, F:** Analysis of photosynthetic activity represented by F_V/F_M measurements under NL and HL conditions at t₀ (**D**), t₄ (**E**) and t₈ (**F**). $n \geq 10$; box plot with median and Tukey whiskers. Significant differences were calculated according to 2-way ANOVA with Tukey's multiple comparisons test. **G, H:** Fresh weight of plants after recovery of 4 d (t₈) under NL (**G**) and HL (**H**) conditions. $n = 10$; box plot with median and Tukey whiskers. Significant differences were calculated according to One-way ANOVA with Tukey's multiple comparisons test. **I, K:** Quantification of anthocyanin content shown in **B** (t₈) and **C**. $n = 3$ (**I**), $n = 8$ (**K**); Data are shown as mean with standard deviation (**I**) and as box plot with median and Tukey whiskers (**K**). Significant differences were calculated according to 2-way ANOVA with Tukey's multiple comparisons test.



IV Discussion

1 Inconclusive trend of the chloroplast-peroxisome proximity

Photorespiration is a light-dependent reaction [129]. Therefore, we had to consider that light might be crucial for the proximity between chloroplasts, peroxisomes and mitochondria. This was pointed out by Oikawa *et al.* 2015 who studied the impact of different photosynthetic conditions to the adhesion, morphology and interaction rate of photorespiratory organelles in *A. thaliana* mesophyll tissue [26]. As we wanted to detect proximity, we chose the same light conditions that were reported by Oikawa *et al.* 2015 [26]. However, we were not able to replicate their findings. In the following sections, the advantages and limitations of the Python-based proximity analysis pipeline will be emphasised and possible reasons, why the results of this study differ from those in the literature, will be discussed.

1.1 The Python-based proximity analysis pipeline enabled a high-throughput analysis

In Oikawa *et al.* 2015, the interaction rate is defined as ratio of the number of three-organelle complexes to the number of total chloroplasts, peroxisomes or mitochondria [26]. However, clearly defined criteria regarding the arrangement and the maximal distance of the photorespiratory organelles to be counted as three-organelle complex are missing in this study. To our knowledge, it was not indicated how they performed the quantification. The information, what kind of image material was used as basis for their analysis, was missing, but we assumed that it was based most likely on 2 dimensional (2D) images.

Starting this project, we decided to quantify the organellar proximity between chloroplasts and peroxisomes based on z-stacks as raw image material. The reason for this was, that in 2D images the spatial information is missing, whether an organellar contact is present in the z-plane. Using confocal z-stacks as raw image material for the analysis allowed us to expand the scope of information spatially and thus to obtain more comprehensive results. To enable a high-throughput analysis of the 3D image material, we established a Python-based analysis pipeline, which is able to calculate the minimal surface-to-surface distance of different organelles.

To additionally expand the information content of the analysis compared to the already published data by Oikawa *et al.* 2015, we investigated three species, namely *A. thaliana*, *N. tabacum* and *P. patens*. Since chloroplasts and peroxisomes differ in shape and size, both

among themselves and generally between species (figure 10), two individually adaptable filters were implemented in the analysis process (figure 11). Those filters allow an easy adaptation for different organelle shapes, which is represented in figure 12. Adjusting the filter settings allowed a very accurate segmentation of peroxisomes and chloroplasts in all three species being investigated. To verify the general functionality of the Python-based analysis pipeline, a comparison was performed between the automatically generated results and a manual quantification (figure 14). Although we observed differences in the percentage ratio between peroxisomes or chloroplasts with contact to the total number of the respective organelle (p_c/p_t ; c_c/c_t), we found a similar trend for both analysis methods.

One main difference between the analysis of Oikawa *et al.* 2015 and our study is the definition of their interaction rate and our proximity ratio. In our study, we excluded the mitochondria and focused on the chloroplast-peroxisome proximity ratios (p_c/p_t ; c_c/c_t). On the one hand, this gave us the opportunity to simplify the Python-based analysis pipeline. On the other hand, the exclusion of mitochondria in the analysis process could carry the risk of deviating results compared to already published studies [25, 26]. We did not consider this risk to be particularly high, since physical interactions of peroxisomes and chloroplasts were described before and were found to be increased under light compared to dark conditions [25, 26]. However, we could not exclude that the analysis process might lose information by excluding the mitochondria and that investigating the proximity of all photorespiratory organelles would improve the analysis. We already took this into account when developing the analysis process. For that reason, the Python-based analysis pipeline is modular structured, which allows mitochondria to be incorporated into the script as an additional organelle.

A recent study supported the suggestion that excluding the mitochondria in the analysis process is not disadvantageous [249]. Oikawa *et al.* 2022 revealed peroxisome-chloroplast interactions to be increased in dependence to light with a high-throughput analysis method for the quantification [249]. Their analysis approach is remarkably similar to ours in terms of the raw image material and the quantification method. The authors of Oikawa *et al.* 2022 used z-stacks as image material. They performed a 3D reconstruction via the software Imaris, which was also used to calculate the shortest surface-to-surface distances of peroxisomes and chloroplasts. Differently to our analysis approach, they did not calculate the proximity ratio (peroxisomes or chloroplasts with contact/ total number of respective organelle). Instead, they used the frequency as readout defined as number of interactions in a distance range $\leq 0.5 \mu\text{m}$ divided by the total number of interactions within a distance of $1 \mu\text{m}$ [249]. To be able to test, if such readout would result in similar results compared to those of Oikawa *et al.* 2022, the calculation of frequency should be included in the Python script.

In summary, we are convinced of the functionality of our self-developed and cost-free analysis pipeline. It allows a transparent, high-throughput and automatically performed quantification of the chloroplast-peroxisome proximity. In addition, the modular structure allows further adaptations such as incorporating mitochondria as additional organelle in the

analysis process and implementing the frequency as readout.

1.2 Minor but probably critical changes in the experimental setup lead to results different to already published data

The authors of Oikawa *et al.* 2015 found the peroxisome-chloroplasts interaction to be increased under light compared to dark conditions. The images shown in their publication (figure 5B) clearly exhibited that the mitochondria and peroxisomes are tightly clustered around the chloroplasts during the light treatment [26]. Although our experimental setup was adapted from Oikawa *et al.* 2015, we were not able to replicate these results (results section 1). In contrast, the MIPs of our study revealed no obvious differences in the peroxisome-chloroplast proximity among all treatments in the three species (figure 10). This impression was also confirmed by our quantitative analysis (figure 16). Possible reasons for the lack of reproducibility of the published data could be that our treatments were not effective, minor changes in the experimental setup or that the proximity of chloroplasts and peroxisomes was not induced by light, contrary to what is described in the literature.

All differences to Oikawa *et al.* 2015 in the experimental setup are listed in table 29. To our knowledge, the authors did not clearly indicate whether they applied a light intensity of $20 \mu\text{mol m}^{-2} \text{s}^{-1}$ or $100 \mu\text{mol m}^{-2} \text{s}^{-1}$ for their interaction assay. For our experimental setup, we chose to test the lower light intensity of $20 \mu\text{mol m}^{-2} \text{s}^{-1}$. This light intensity was substantially lower than $100\text{-}120 \mu\text{mol m}^{-2} \text{s}^{-1}$ which was used for normal growth of higher plants. In the retrospect, this raises the question if this low light intensity was sufficient to induce an increase in the proximity between chloroplasts and peroxisomes.

A recently published study by the same authors brings more clarity to this question [249]. Similar to our analysis, they investigated peroxisome-chloroplasts interactions with a high-throughput analysis method [249]. Oikawa *et al.* 2022 treated *A. thaliana* mesophyll cells with $200 \mu\text{mol m}^{-2} \text{s}^{-1}$ as normal light (NL) and found a higher frequency of short interaction distances in the light compared to dark conditions. Based on this new information, it is likely that the results of the interaction assay in Oikawa *et al.* 2015 are based on cells treated with $100 \mu\text{mol m}^{-2} \text{s}^{-1}$ instead of $20 \mu\text{mol m}^{-2} \text{s}^{-1}$. Thus, it is reasonable to assume that we were not able to detect differences in *N. tabacum* and *A. thaliana* comparing light and dark conditions due to the fact that with $20 \mu\text{mol m}^{-2} \text{s}^{-1}$ the light intensity was too low.

However, in *P. patens* protonema, the ratio of chloroplasts with peroxisomal contact to all chloroplasts (c_c/c_t) of dark treated cells was significantly decreased compared to that of light treated cells. The normal light intensity for *P. patens* with $70 \mu\text{mol m}^{-2} \text{s}^{-1}$ [222] is lower than that for higher plants. Based on our results, we suggest that a light intensity of $20 \mu\text{mol m}^{-2} \text{s}^{-1}$ in *P. patens* is sufficient to induce an increased proximity, while this is not the case in higher plants.

Although we found only few differences in the proximity ratios within one species, there

Table 29: Comparison of the experimental settings for the proximity analysis between Oikawa *et al.* 2015 [26] and our work.

PTS1: peroxisome targeting signal; Mt-GFP: ATPase delta presequence-GFP [250]; SKL: serine-lysine-leucine ^{*1}: Imaging time was limited to maximal 20 min, since it is described that the effect of light is lost within 30 minutes [26]. ^{*2}: Dark adaptation was set to at least 30 min, since such time was described to be sufficient for other light sensitive experiments as PAM and oxygen consumption measurements after JUNIOR-PAM Teaching Chlorophyll Fluorometer Manual [197] and Kühn *et al.* [198], respectively.

Terms	Oikawa <i>et al.</i> 2015	This thesis
Species	<i>A. thaliana</i> (mesophyll)	<i>N. tabacum</i> (pavement) <i>A. thaliana</i> (mesophyll) <i>P. patens</i> (protonema)
Cytoskeleton treatment	latB	cytD (higher plants) Oryzalin (<i>P. patens</i>)
Pharmaceutical application	1) Vacuum infiltration 2) 30 min dark adaptation 3) Pharmaceutical treatment 1.5-3 h light 4) Imaging	1) Vacuum infiltration with pharmaceutical treatment 2) 30 min dark adaptation 3) 1.5-3 h $20 \mu\text{mol m}^{-2} \text{s}^{-1}$ 4) Maximal imaging time 20 min ^{*1}
Dark treatment	1) 30 min dark adaptation 2) Dark 2 h 3) Imaging	1) Minimum 30 min dark ^{*2} 2) Maximal imaging time 20 min ^{*1}
Light treatment	1) 30 min dark adaptation 2) 1.5-3 h light: Not clearly indicated if: - $20 \mu\text{mol m}^{-2} \text{s}^{-1}$ - $100 \mu\text{mol m}^{-2} \text{s}^{-1}$ 3) Imaging	1) 30 min dark adaptation 2) 1.5-3 h $20 \mu\text{mol m}^{-2} \text{s}^{-1}$ 3) Maximal imaging time 20 min ^{*1}
Temperature	23 °C	25 °C (higher plants)
Organelles	Chloroplasts (transmitted light) Peroxisomes (RFP-PTS1) Mitochondria (Mt-GFP)	Chloroplasts (chlorophyll auto-fluorescence) Peroxisomes (CFP-SKL)

was still variance among the three species. In contrast to *A. thaliana* and *P. patens*, the analysis in *N. tabacum* was performed in photosynthetic inactive pavement cells. The reason for this was, that too few mesophyll cells were transformed to serve as a basis for a high throughput analysis, whereas the transient transformation was effective in pavement cells. As the experiment was designed to investigate if the peroxisome-chloroplast proximity is light-dependent and driven by photosynthetic reactions in the first place, a less pronounced or even entirely changed trend in *N. tabacum* was not unlikely compared to those of Oikawa *et al.* 2015. However, as previously emphasised, even in *A. thaliana* mesophyll and *P. patens* protonema cells, both photosynthetic active tissues, we did not identify any clear light-dependent trend (figure 16).

Interestingly, in *P. patens* the lowest average of the ratio between chloroplasts with peroxisomal contact to the total number of chloroplasts was substantially higher with $c_c/c_t = 70.3\%$

than the maximum averages of *A. thaliana* and *N. tabacum* with $c_c/c_t = 55.7\%$ and 41.9% , respectively. A similar trend could be identified for the ratio between peroxisomes with chloroplastidic contact to the total number of peroxisomes. While the lowest average of p_c/p_t in *P. patens* was 89.1% , the average values of p_c/p_t in *A. thaliana* and *N. tabacum* reached only 59.9% and 40.3% , respectively (figure 16 E). One possible reason for these pronounced differences between the species might be their different organellar morphology. The chloroplast morphology between all three species did not differ (figure 12 C) and also a quantification of the area revealed no significant differences between *A. thaliana* and *P. patens* with $74.3\mu\text{m}^2 \pm 14.0\mu\text{m}^2$ and $50.1\mu\text{m}^2 \pm 15.6\mu\text{m}^2$, respectively (data not shown). However, a striking difference between the species was that the peroxisomes in *P. patens* are more elongated and less spherical than in *A. thaliana* and *N. tabacum* independent of the treatment. This elongated peroxisomal shape might be responsible for the higher proximity ratios, as it resulted in a larger surface area being able to be in close proximity to the chloroplasts (figure 12 C).

In summary, we were not able to identify a consistent trend towards a light-dependency of the peroxisome-chloroplast proximity. The most likely reason for this is that the chosen light intensity was too low. Based on recent findings in the literature, our experimental conditions need to be revised for future studies with respect to a higher light intensity and also to resolve the other differences to Oikawa *et al.* 2015 as listed in table 29.

2 Fluorescent probes for the visualisation of MCS: challenges and possibilities

While photorespiration is well understood on a metabolic level, the potential role of MCS between chloroplasts, peroxisomes and mitochondria is still missing. In the recent years, CLSM using FP has become a preferred choice investigating organellar interaction including FRAP studies at EPCS [16], cell 3D remodelling of ER-peroxisome MCS [63] and time series on organelle dynamics between the photorespiratory organelles [26]. Nevertheless, there is still a lack of an efficient and reliable system in plant cells to visualise MCS between those organelles. The reason for that is the resolution limit of CLSM with ~ 250 nm and $500\text{-}700$ nm in xy and z level, respectively [5]. Since the distance between organelles range typically within 10 nm to 30 nm at MCS [5, 6], the proximity in CLSM imaging data is no evidence for a specific and functional MCS. One possibility to overcome the diffraction barrier and allow imaging of biological structures in greater detail is using other microscopy methods such as EM and super resolution techniques [37]. These are powerful imaging techniques but sample fixation is mostly required, which implies losing the possibility for dynamic visualisation of MCS (see review [6]).

To allow live cell imaging and simultaneously be able to detect proximity in a nanometer

scale, we tried to develop proximity sensors for use in CLSM to potentially detect MCS. We designed those sensors using two different genetically encoded FP-based reporter systems, namely BiFC and FRET/FLIM. Both sensor systems convert proximity directly into a fluorescent signal, which make them a potential tool to explore MCS. Since we wanted to contribute to the understanding of MCS regarding photorespiration, we targeted the FP-tags to chloroplasts, peroxisomes and mitochondria. As no MCS specific proteins was proven to be related to photorespiration have been identified yet, the targeting to organellar membranes of the fluorescent probes was performed using MCS unspecific proteins or protein domains of OE, PerM or MOM, which do not interact (results section 2). The scientific question was, if it is possible to detect proximity with these sensor systems when they are homogeneously distributed at the outer organellar membranes. In this section, we will emphasise the individual experience with each FP-based proximity reporter system separately, followed by a consideration regarding common possibilities and challenges for both proximity sensor systems.

2.1 Suitability of splitFP as proximity reporter system needs further investigation

Since the start of this project, BiFC-based reporter systems have been successfully applied for MCS visualisation in eukaryotic cells detecting a specific signal at the interaction sites (references see table 2). Although they are very sensitive tools, there is a risk of spontaneous reassembly of the BiFC probes. This can cause false-positive artefacts and non-specific signals with an accumulation at pre-existing contact sites or even generating artificial ones [6, 59, 152, 155]. In this section, we discuss two different BiFC reporter systems in plants in terms of their suitability as proximity sensors.

YFP signal distribution is not specifically located at putative MCS using BiFC-based proximity sensors. To detect putative MCS between chloroplasts, peroxisomes and mitochondria two different proximity sensors have been generated using the rBiFC vector system of Christopher Grefen [160]. Applying the construct nYFP:L:PpTOM20C and PpPEX3N:L:cYFP transiently in *N. tabacum*, we aimed to investigate chloroplast-peroxisome and peroxisome-mitochondrion interaction sites simultaneously taking advantage of the miss-targeting of PpTOM20C to MOM and OE (figure 22). We did not visualise a YFP signal specifically located at the putative contact sites. The expression of the BiFC construct nYFP:L:PpTOM20C and PpPEX3N:L:cYFP resulted in a bright PerM and a weaker OE signal, while the MOM of neighbouring mitochondria was not labelled (figure 25 B). An additional quantification of the BiFC signal did also not indicate any differences between light ($100 - 120 \mu\text{mol m}^{-2} \text{s}^{-1}$) and dark treated plants (figure 26 C, D), while under light conditions an increased proximity was reported in literature [26, 249]. Using the rBiFC vector system, the RFP signal can be used as a reference fluorescence in order to normalise the BiFC signal. However, as shown in

IV. DISCUSSION

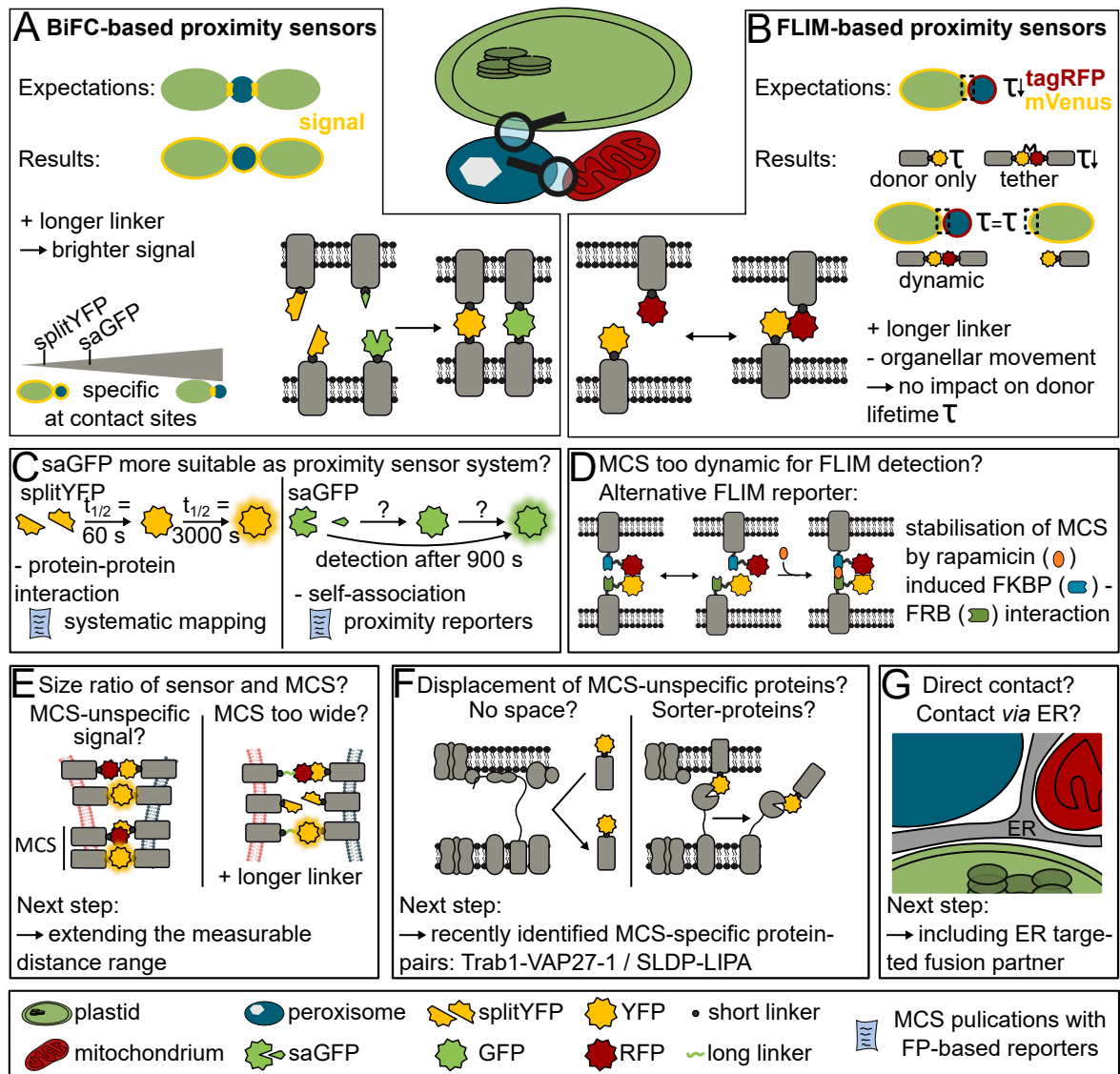


Figure 58: Main findings of this study investigating contact sites with FP-based sensors, putative underlying reasons and ways to improve FP-based proximity sensors.

A, B: Overview of main results investigating MCS between chloroplasts, peroxisomes and mitochondria by BiFC-based (**A**) and FLIM-based proximity sensors (**B**). **A:** While the expectation using BiFC was a specific signal at contact areas between the areas, we monitored whole organellar membrane signals. Increasing the reporter size by adding a long linker led only to brighter but not more specific signal. The comparison between splitYFP and saGFP as proximity reporter system revealed that both sensors label the PerM but the saGFP signal was slightly increased at the putative contact sites to chloroplasts. **B:** The expectation was to detect a decrease fluorescence lifetime (τ_m) at organellar contact sites. We established a positive (tether, quenched donor) and a negative control (donor only, unquenched donor, decreased τ). Using dynamic FLIM-based reporters, no decrease in τ was detected, neither by adding a longer linker or decreasing the organellar movement by cytD. **C:** Evidences, why saGFP-based proximity sensors might be better suited as proximity reporter (information from [159, 166]). **D:** Alternative FLIM reporter system, which allows transient stabilisation of MCS (used in [4, 156, 157]), might be a compromise between imaging dynamics and being able to detect FLIM. **E-G:** Putative possibilities, which might explain, why we were not able to visualise neither specific signal by BiFC or a decrease lifetime at putative MCS (further information in the text).

figure 26, the RFP signal was so unevenly bright between the different treatments. Therefore, we assume that the calculation of the BiFC/RFP ratio cannot be considered as representative in terms of the level of interaction (figure 26 E, F).

In the first place, we anticipated that the dual targeting of PpTOM20C may offer the possibility to investigate the proximity of all three photorespiratory organelles at once. However, to rule out that the non-specific YFP signal was caused by the non-specific targeting of Pp-

TOM20C, we exchanged this fusion partner with OEP7, which is exclusively targeted to the OE (figure 21). Applying this proximity sensor in *N. tabacum*, we received an almost imperceptible spitYFP signal in the OE, which was substantially weaker than for PpTOM20C as fusion partner, while the PerM signal was similar (figure 27 B). Using both splitYFP-based proximity sensors, we were not able to monitor a specific YFP signal reflecting putative organellar contact sites.

One possible explanation for the YFP signal labelling the whole organellar membrane of peroxisomes and chloroplasts may be that the splitYFP reassembly partly takes place prior to PpTOM20C, OEP7 and / or PpPEX3N integration to their organellar membranes. Both splitYFP fusion proteins were expressed under the strong, constitutive 35S promoter [160, 251]. The high expression potentially led to an overload of those fragments in the cytosol, where they possibly act similar to the cytosolic expressed splitYFP fragment in the BiFC topology assay [165] (figure 5). The assumption only applies, if the BiFC reassembly is truly irreversible. This has been proven for most splitFP sensors [161, 166], and some were even shown to be suitable working as artificial tether between organellar membranes [59, 155]. Nevertheless, a review about BiFC reported some studies, which claimed BiFC to be partly reversible [164, 252–254]. What all of these studies have in common, is that their claims are founded largely on observations that the splitYFP or saGFP signals decreased in response to aggressive pharmaceutical treatments [151, 152, 164, 252–254]. However, we still suggest BiFC to be irreversible. First, most publications of either splitYFP, splitGFP and saGFP characterised the sensor systems to be irreversible [150, 159, 161, 162, 164, 166]. And secondly, we were able to underline this prevailing opinion, since we were able to quantify that the BiFC-based proximity sensor induced organellar tethering (figure 14).

Comparison of splitYFP and saGFP: Different reassembly characteristics may influence their applicability as proximity sensor. By using the available rBiFC vector system [160], we automatically used splitYFP as reporter system. However, splitYFP reporters were more frequently used for protein-protein interaction at MCS or systematic mapping of potential MCS protein candidates. Since the start of this study, most of the publications, which used BiFC as proximity sensor, chose saGFP as reporter system (references see table 2). This goes also along with the individual reassembly characteristics of both reporter systems (figure 58 C). While splitYFP or similar splitFP were mainly reported to rely on a protein-protein interaction [159, 161, 162], saGFP was engineered to perform self-association and is therefore independent on protein-protein interaction [166]. A faster maturation and self-association potentially make saGFP the better choice when it comes to proximity reporters. A recent study in plants revealed that saGFP reporter in combination with MCS-unspecific fusion proteins in plants in general work as proximity sensors. The authors investigated ER-organellar contact sites and generated therefore a combinatorial saGFP-based reporter set [152].

Since no plant compatible 2in1 system including saGFP as reporter was available, when

this project started, we designed vector system as indicated in figure 31. As an additive, we added a plant selection marker cassette to allow stable transformations and the constitutive promoter was exchanged by an inducible promoter system. The idea of using an inducible system was that we were able to control the beginning of the expression of the reporter and therefore inductively modify organelle positioning. Applied transiently in *N. tabacum*, the generated vector constructs seemed to be leaky (figure 33 & 34 & 35 B, C). This deviates from the results of the original publications of the pOp6/Gr-LhG4 promoter [230, 231]. However, differently to our approach, these studies were performed in stable *A. thaliana* and *N. tabacum* lines [207, 230, 231]. We can only speculate, why the system is leaky in a transient approach. One possible explanation might be linked to the fact that leaf infiltration goes along with a bacterial infection. For the inducible system, HSP90 inactivates the GR-LhG4 complex leading to no effector expression (figure 31 B). HSP90 is a chaperone for folding and regulation and was shown to be involved in defence responses [233, 255]. Hypothetically, if HSP90 would be redirected to the antibacterial defence due to infiltration with *A. tumefaciens*, the expression of the effector would be less suppressed. During this work, *A. thaliana* were transformed with the same construct and T₁ seeds of dipped plants are available. Propagating this plant material further to the T₃ generation and repeating the experiment, as we performed in *N. tabacum*, might answer this question. In addition, *A. thaliana* transgenic lines would allow to test inducible chloroplast-peroxisome tethering.

Craft *et al.* revealed that the positioning of LhG4 and GR is crucial for the induction. While GR-LhG4 provided the best expression characteristics, LhG4-GR was leaky in *A. thaliana* [230]. As Greengate pEntry we used a commercial vector pSW610-GR-LhG4_BD (Addgene plasmid #115992 [207]). Double checking the sequence using blast (<https://blast.ncbi.nlm.nih.gov/Blast.cgi>) confirmed the N-terminal fusion of GR to LhG4 (GR-LhG4).

To verify the splitYFP and saGFP signal distribution, we compare both using the same fusion partners, namely OEP7 and PpPEX3N(GGSGG)₁₃. The YFP signal labelled both OE and PerM, while the saGFP signal surrounded the PerM but partly being increased at putative MCS between chloroplasts and peroxisomes. The saGFP signal seemed to be stretched at those interaction site with the peroxisomes appeared to be elongated alongside the FP signal (figure 29). Although the saGFP signal was not exclusively located at chloroplast-peroxisome interaction sites, the signal distribution of this sensor system seemed to be more promising than that of splitYFP.

Based on our results, we can assume that saGFP is better suited than splitYFP as a proximity sensor system. However, the question remains, if adjustments to the reporter system enable the detection of a specific MCS signal similar than in T. Li *et al.* [152] (see also discussion section 2.3).

2.2 Unaltered lifetime of FRET/FLIM-based proximity sensors at putative MCS

Worth mentioning, both splitFP systems are irreversible, which is a limitation for monitoring the dynamics of MCS under changing environmental conditions. Sensors, which fulfil both a dynamic and high resolution visualisation are splitFast and FRET/FLIM reporters. The splitFast is a reversible split fluorescent reporter, which was designed for real-time imaging of protein interactions [173]. Using this reporter in combination with organellar targeting would enable a dynamic visualisation of MCS formation and dissociation. Since this system was not published before 2019, we used a FRET/FLIM reporter as a dynamic proximity sensor. FRET/FLIM sensors are sensitive tools and have already been shown to be suitable to investigate MCS dynamics [4, 58, 91, 156, 157].

Similar for the BiFC proximity systems, the fluorophores of the FRET pair were targeted to OE, PerM or MOM with the FP-tag facing towards the cytosol. As readout, we chose FLIM instead of FRET, since this method is independent on the donor-acceptor ratio and can be quantified. We were able to establish controls mimicking 100 % and no organellar interaction. Based on that, the measurement range for medium fluorescence lifetime τ_m of a 1 component analysis of exponential decay (1C) could be set from 1978 ps to 2575 ps (figure 36). Applying $20 \mu\text{mol m}^{-2} \text{s}^{-1}$ light, we did not detect any differences in τ_m using dynamic FRET/FLIM-based proximity reporters both in *A. thaliana* and transiently in *N. tabacum* (figures 37, 39; supplemental figures S7, S9, S10, S11).

One possible explanation could be related to the frequency of MCS formation and dissociation [6], which has not been studied yet for chloroplast-peroxisome and peroxisome-mitochondrion MCS in plants. In our experimental setup, the FLIM measurement took between 30 - 35 s per image (figure 37). Such long detection time carries the risk to overlook transient contacts. Neither reducing the detection time to 10 s (figure 37) nor the stabilisation of MCS by reducing the organellar movement (figure 38, 40, supplemental figures S13, S12, S14, S5, S6 & S8) affected the donor lifetime.

As discussed before (discussion section 1.2), a recent publication found an increased interaction between chloroplasts and peroxisomes using $200 \mu\text{mol m}^{-2} \text{s}^{-1}$ [249]. For the FRET/FLIM experiment, we imaged the plants directly after the vacuum infiltration or after an incubation of minimum 1.5 h at $20 \mu\text{mol m}^{-2} \text{s}^{-1}$. Thus, we can not exclude the possibility that the FRET/FLIM-based proximity reporters did not detect MCS, since MCS were not induced under the applied imaging conditions. As a proof, future studies could repeat the experiment with a light intensity of $200 \mu\text{mol m}^{-2} \text{s}^{-1}$.

Based on our results, we cannot conclude, whether we did not detect a decrease in the donor lifetime because of the experimental setup or whether the applied sensor itself is not suitable for organellar proximity visualisation. Various studies in animal cells, which chose MCS-unspecific and non-interacting proteins/protein domains for organellar membrane

targeting, used an alternative FRET/FLIM-based reporter system [4, 156, 157, 182] (principle see figure 58 D). This FRET/FLIM-based proximity sensor is less dynamic compared to our approach but allow stabilisation of transient contacts. It includes the FKBP domain of HsFKBP12 and the FKBP rapamycin-binding domain (FRB) of mTOR, whose dimerisation is induced by rapamycin [256, 257]. Using the rapamycin-dependent FRET/FLIM-based proximity sensor system, the application of rapamycin lead to dimerisation of the sensor and therefore stabilise the MCS [4]. Stabilisation by the ramamycin-dependent FRET/FLIM reporter may facilitate monitoring short contacts. However, the experimental setup must be carefully chosen using those sensor systems, since a longer incubation with rapamycin lead to expansion of the FRET interface [4]. All publications, which investigated MCS with the rapamycin-dependent FRET/FLIM reporter, were conducted in animal cells. Nonetheless, the FRB-FKBP dimerisation tool has been applied in plants as well [258–260]. Thus, the rapamycin-dependent FRET/FLIM-based reporter may be a promising tool to investigate MCS in plants and be a compromise between imaging dynamics and artificial tethering.

In summary, based on our results we cannot conclude whether the unaltered lifetime is due to the lack of existence of MCS between chloroplasts and peroxisomes or due to the experimental/imaging design.

2.3 Limitations of FP-based proximity sensors used for MCS visualisation

Establishing proximity sensor systems for MCS between chloroplasts, peroxisomes and mitochondria is clearly challenging. Possible limiting factors that need to be considered when using FP-based proximity sensors are discussed in this section.

Interdependency of FP-based sensor size and the organellar membrane distance at MCS.

One possible explanation of our results might be related to the interdependency of the FP-sensor size and the organellar distance at MCS. Tether proteins or bridging complexes, which are located at MCS, may also function as spacer and therefore may define the distance between the organellar membranes at MCS [6]. The natural organellar distance might impact, whether the applied sensors are able to detect the organellar proximity. On the one hand, if the range of the proximity sensors is lower than the natural organellar distance, existing MCS might not be detected. On the other hand, if the natural organellar distance is smaller than the range of the proximity sensors, existing MCS might not exclusively be labelled but also adjacent areas (figure 58 E). Therefore, it is crucial to ensure that the proximity sensor's size is compatible with the distance between organelles.

So far, no tether proteins or bridging complexes have been identified at the MCS between the photorespiratory organelles. Thus, the distance, which need to be bridged by the proximity sensors, is unknown. This made the development of FP-based sensors with the right size a particular challenging task. We could only go by what we knew, which was that MCS are

usually between 10-30 nm [5, 6], although much larger bridging complexes have been identified with 325 nm ([17], yeast). The minimal size of both sensors systems is composed of the predefined FRET/rBiFC vector building blocks (only rBiFC: HA-tag, Myc-tag, splitYFP; only FRET: mVenus, tagRFP; both: Gateway-linker) [160, 177], and a short flexible linker connecting the FP-tag (22 nm: FRET/FLIM / 33 nm: BiFC) (table 25). To extend the size range of the reporters, we integrated an additional flexible linker to add 23.3 nm. Thus, our FRET/FLIM- and BiFC-based proximity reporters can reach membranes within a distance of approximately 22 nm to 57 nm (figure 38 B & 28 A).

When applying FRET/FLIM-based proximity sensors with or without the longer linker, we did not detect any changes in the fluorescence lifetime (figure 38, 39, 40, supplemental figure S7, S9, S10, S11). Our FRET/FLIM-based sensors could bridge 22 nm and 45.5 nm, while sensors applied in published studies ranged in their size from 5 nm to 15 nm [4, 157, 182]. Using splitYFP-based proximity sensors, we detected an unspecific organellar membrane labelling, which was even slightly increased adding a longer linker to the same reporter (figure 28). Our splitYFP-based sensors could bridge approximately 33 nm and 57 nm, while in literature applied BiFC-based sensors range from 4.2 nm to 50 nm (references see table 3). The question of different distances at MCS has been more intensively addressed using BiFC-based sensors. Most of the saGFP- or splitYFP-based proximity reporter systems have a maximal bridging distance less than 30 nm (table 3). Nonetheless, investigating various and also larger distance between organelles have already been shown to be informative in mammalian cell culture (table 3). A proportional correlation of increasing linker length and BiFC signal has been already identified in human [151]. This observation has been confirmed in a recent plant study [152]. The authors of the plant study were able to detect punctual FP signals at ER-chloroplast interaction sites using a saGFP-based reporters. The unspecific signal was increasing proportional to the reporter size until at approximately 24.5 nm ([152], calculation self derived: table 30) the whole organellar membrane was labelled. Since their largest sensor is still smaller than the smallest in our measuring range with 33 nm, it is not unlikely that we missed the required sensor size. We therefore recommend as a next step to increase the detection range in the direction of smaller distances, for both FP-based proximity reporters.

Suitability of MCS-unspecific proteins as fusion partners for FP-tags Independent on changing conditions or extending the distance range by including an additional linker, we were not able to distinctly visualise MCS. In the previous sections (discussion section 2.1, 2.2 & 2.3) we discussed the suitability of FP-based sensors for monitoring MCS, focusing on the FP-tags. In this section we will concentrate on the potential role of the other important component of the proximity sensors, namely the fusion partners. It needs to be discussed, is, if non-interacting and MCS-unspecific proteins or protein domains are suitable as fusion partners for the FP-tag.

IV. DISCUSSION

Table 30: Comparison of linker length to investigate MCS via Bimolecular fluorescence complementation (BiFC) from Cieri *et al.* [151], T. Li *et al.* [152] and our study.

The design of the SPLICS sensor system served as template for introducing an additional linker in our BiFC system. Endoplasmic reticulum (ER), mitochondrial outer membrane (MOM), outer envelope (OE), plasma membrane (PM), peroxisomal membrane (PerM).

Ref.	Organism	Organellar mem-branes	Sensor method + linker/ spatial information	Distance readout
[151]	Human (cell culture)	ER-MOM	<p><u>saGFP:</u> split-GFP-based contact site sensor (SPLICS_{S/L}): MOM:GFP₁₋₁₀ ER:S/L:GFP₁₁ (S: short linker; L: long linker)</p> <p>1) SPLICS_S: 8 - 10 nm 2) SPLICS_L: 40 - 50 nm</p>	Signal proportional to linker length. FP signal differs for SPLICS _{S/L} .
[152]	<i>Nicotiana benthamiana</i> , <i>A. thaliana</i> (transient)	ER-MOM ER-OE ER-PM	<p><u>saGFP:</u> saGFP-based MCS reporter: GFP₁₋₁₀:ER OE:GFP₁₁ MOM:GFP₁₁ PM: GFP₁₁</p> <p>1) increasing length via multiple GFP₁₁ (1/2/4x) (6.12 nm/GFP₁₁) 2) GS-linker (3nm)</p> <p>4.2 -24.48 nm</p>	Signal increases with length of protein, either due to GS-linker or multiple GFP ₁₁ .
This study	<i>N. tabacum</i> (transient)	OE-PerM	<p><u>splitYFP/saGFP:</u> Proximity labelling of OE, PerM: PerM:L(+/-long linker):cYFP/GFP₁₁ OE:L:nYFP/GFP₁₋₁₀</p> <p>1) short linker (L) ~1.8 nm 2) long linker ~23.4 nm</p> <p>33.0 - 56.4 nm</p>	YFP signal label whole PerM and OE. Signal increases proportional to bridging distance.

MCS are highly specialised micro-environments differing in their lipid and protein composition compared to the surrounding membrane regions [5]. Therefore, one question is if MCS-unspecific proteins are able to enter those micro-environments (figure 58 F). One possibility is that contact sites are already filled with MCS specific lipids and proteins, so there is simply no room for non-specific proteins (figure 58 F, left). Another possibility is that "sorter-/recruitment proteins" might sort out MCS-unspecific proteins including the FP-based proximity sensors (figure 58 F, right). What argues against this assumption is that a combinatorial saGFP-based reporter using organellar targeting have been recently established to investigate ER-organellar contacts in plants [152].

Two plant studies were able to detect a decrease of the donor lifetime at EPCS or LD-PM contact sites using a similar FRET/FLIM sensor than we did [58, 91]. However, they investigated protein-protein interaction of MCS-specific protein pairs, namely NET3C-VAP27-1 or SLDP-LIPA [58, 91] and did not use MCS-unspecific fusion partners. Therefore, we planned to test the dependency of the FP-based proximity sensors on MCS localisation and protein-protein interaction of their fusion partners. For that, we included two different controls using already identified EPCS proteins: 1) VAP27-1 with SYT1C (C-terminus of SYT1) as non-interacting MCS specific proteins or protein domains [29, 58] or 2) VAP27-1 with NET3C interacting MCS specific proteins [58]. Unfortunately, neither of the controls could be performed as planned. On the one hand, SYT1C was reported to be located exclusively at PM [29], while we found it additionally localised in the cytosol in transient overexpression in *N. tabacum* (figure 20). On the other hand, we were not able to detect any fluorescent signal for NET3C independent of several optimisation variants as coinfiltration of p19. The reason is probably that NET3C is affected by post-transcriptional silencing (personal communication with authors of P. Wang *et al.* [58]).

For future studies, recently identified MCS protein pairs could be considered as alternatives for SYT1 and NET3C. VAP27-1 have been identified to be not only part of EPCS but also of ER-mitochondria contact sites (EMCS). Together with the MOM protein TRAB1 it is part of a novel plant EMCS complex [82]. Another MCS-specific and interacting protein pair was identified at PM-LD (lipid droplet) contact sites. SEED LD PROTEIN 1/2 (SLDP1/2) and LD-PM ADAPTOR (LIPA) are part of an LD-PM tethering complex in plants, which is essential for anchoring LD to the PM during early seedling growth in *A. thaliana* [91]. One of those MCS protein pairs could replace NET3C-VAP27-1, while combining VAP27-1 with LIPA would address the question of MCS-specific but non-interacting fusion partners.

Is there direct contact between the photorespiratory organelles or does the ER play a mediating role? Experimental evidences support contact between the photorespiratory organelles [20, 25, 26]. However, it remains unclear whether direct contact between chloroplasts to peroxisomes and peroxisomes to mitochondria exists based on the current state of knowledge. An alternative hypothesis is that their contact is mediated via the ER resulting in an indirect connectivity [25] (figure 58 G). ER tubules can partly be very narrow with approximately 40 nm [261] and therefore, might easily be overlooked and miss-interpreted as direct contact between other organelles.

The possibility of an indirect contact was already discussed by the authors of Gao *et al.* [25]. They tested the chloroplast-peroxisome connectivity via optical tweezers and found chloroplast to be connected to peroxisomes. They argued, if the ER mediate the chloroplast-peroxisome connectivity, the ER must be tightly anchored around the chloroplasts. This hypothesis have not been tested yet. However, there is also evidence that the chloroplasts are completely or mostly embedded within the ER ([262], figure 19), which would decrease the

probability of chloroplasts to have a direct contact to other organelles than the ER. Additional evidences for a ER-chloroplast connectivity were found performing an *in vitro* optical trapping experiments and analysing plastid-associated membranes from pea protoplasts regarding ER protein and lipid contaminants [30]. The ER have also been shown to be associated or co-localised with mitochondria and peroxisomes [9, 49–51, 63].

As soon as the first MCS protein of the photorespiratory organelles has been identified, the identification of interaction partners of this protein may elucidate, if the contact is directly or mediated over the ER. However, from the current state of knowledge we can neither exclude nor confirm that the ER serves as mediator at MCS between the photorespiratory organelles.

3 Perturbing the proximity of photorespiratory organelles lead to sever phenotypic and physiological alterations

Perturbing the natural movement and the cellular positioning may enable us to answer the question of the biological relevance of spatial organelle organisation in the context of photorespiration and other physiological functions of those organelles. Tethering of organelles has already shown to be a suitable tool altering the movement and the dynamics of ER-PM and ER-MVBs [59, 155]. However, since those studies were performed under transient expression in *N. tabacum*, they did not investigate the impact of the tethering on the phenotypic level. We generated stable *A. thaliana* lines overexpressing the synthetic tether PpPEX3N:tagRFP:mVenus:PpTOM20C (24#5), which was expected to cross-link chloroplast-peroxisome and peroxisome-mitochondrion. The stable transformation allowed us to study the effect of perturbing the spatial organisation of the photorespiratory organelles at both the cellular and phenotypic levels.

On a cellular level (figure 59 A), we found visual evidence that chloroplast-peroxisome and peroxisome-mitochondria complexes might be tethered in the stable *A. thaliana* tether lines (figure 42, 43). Contradictory to that, this impression was not underlined by the quantification of the proximity ratio between peroxisomes and chloroplasts neither in *N. tabacum* nor in transgenic *A. thaliana* lines (figure 14 & 15). In the transgenic *A. thaliana* lines, we visualised striking abnormalities in the peroxisomal localisation and mitochondrial morphology, while the chloroplasts seemed to be unaffected (figure 42, 43 & 44). In photosynthetic active tissue, small peroxisomal clusters were found adjacent to chloroplasts and mitochondria. In addition, we found prove that the mitochondrial morphology and number was changed in mesophyll cells. The overexpression of the synthetic tether construct resulted in more elongated mitochondria compared to WT ones (figure 44 F). In pavement cells, we identified spherical peroxisomal clusters, in which mitochondria accumulated and were partly adjacent to the synthetic tether signal (figure 42).

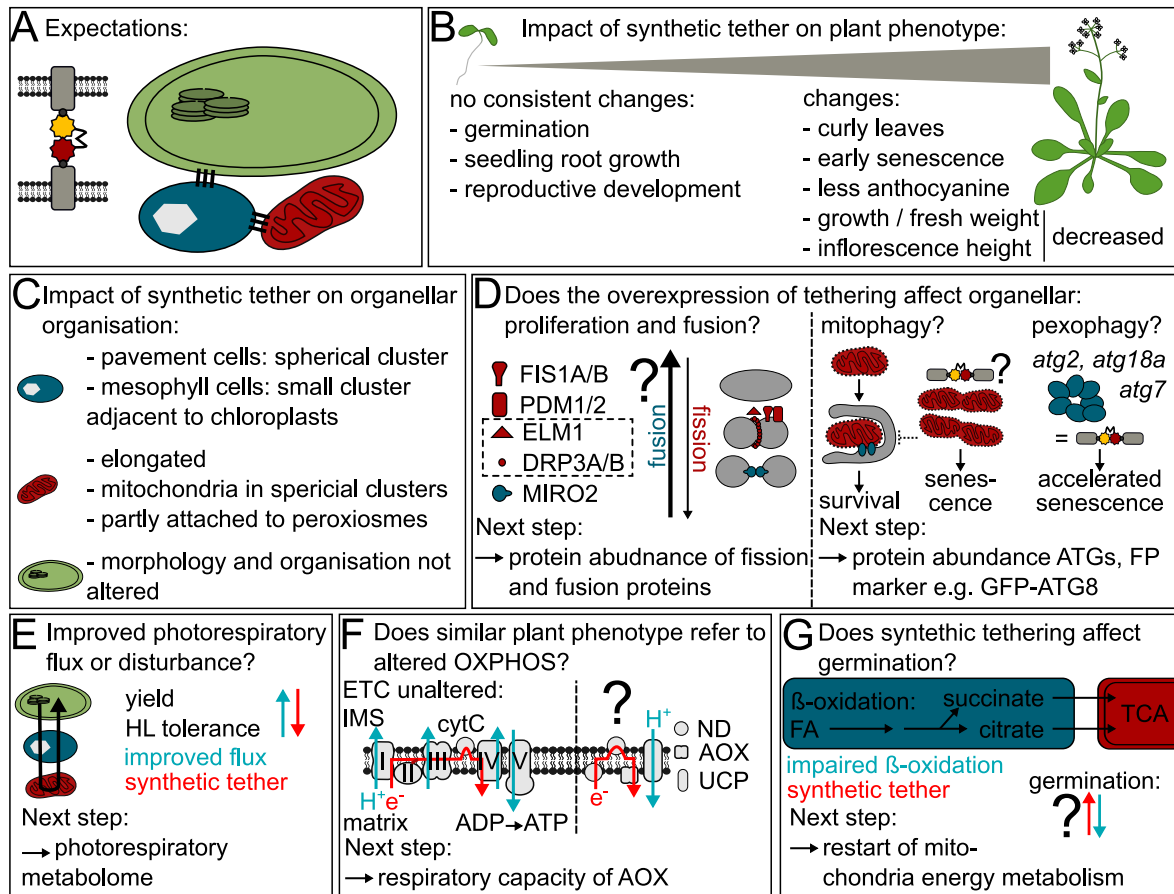


Figure 59: Main findings and putative underlying mechanisms investigating perturbation of the spatial organisation by introducing a synthetic tether.

A: The synthetic tether construct PpPEX3N:tagRFP:mVenus:PpTOM20C (24#5) was expected to cross-link chloroplast-peroxisome and peroxisome-mitochondrion. **B, C:** Main results perturbing MCS between chloroplasts, peroxisomes and mitochondria by the synthetic tether on plant (A) and cellular (B) level. **D-H:** Possibilities, how perturbing the natural spatial organisation of chloroplasts, peroxisomes and mitochondria might affect cellular and plant phenotype. **D left:** Organellar tethering might interfere with the shared mitochondrial and peroxisomal fission machinery or/and might shift the fission-fusion rate towards fusion [9, 38, 263]. Knockout mutants of the proteins marked by the grey box are the most similar to the phenotype of the synthetic tether lines. **D, right:** Defects in mitophagy or pexophagy lead to an accelerated senescence similar to tether lines. Small mitochondria can be easily recycled in mitophagy, whereas larger and accumulations of mitochondria may be more resistant [264, 265]. Pexophagy mutants have peroxisomal cluster similar in shape than tether lines [266]. **E:** Improvement of photorespiration by a higher flux [267–271] or lower the energetic costs during photorespiration [271] result in a higher yield and partly in increased high light (HL) tolerance (blue arrow). In contrast, tether lines were smaller than WT plants and had a decreased tolerance towards HL (red arrow). **F:** Synthetic tether lines had a similar growth and leaf phenotype than electron transport chain (ETC) mutants [198, 272, 273] but an unaltered oxygen consumption in leaves indicating the ETC to be unaffected. However, there are evidences that the ETC bypass composed of NAD(P)H-Dehydrogenases (ND), Alternative Oxidases (AOX) and Uncoupling Proteins (UCP) might be altered in tether lines. **G:** Fatty acids (FA) are converted to Acetyl-CoA during β -oxidation and further to citrate and succinate, which serves as energy source for the mitochondrial tricarboxylic acid (TCA) cycle [87]. The germination of mutants impaired in storage lipid degradation has been reported to be dependent on external sucrose [54, 86, 274] (blue arrow). Two independent synthetic tether overexpression lines showed a faster germination (red arrow), while one independent line was delayed.

On the plant level (figure 59 B), we observed an age-dependent phenotype in plants overexpressing the synthetic tether construct. While germination, seedling growth and reproductive development were not consistently altered in the transgenic lines (figure 45, 46, 50, 51 & 52), adult plants showed consistently curled leaves, an early leaf senescence, as well as a decrease in the rosette leaf area, fresh weight and inflorescence height (figure 47).

In the following section, we will discuss and estimate potential dependencies between organellar cross-linking and the relevance of organellar organisation for proliferation, shared or individual physiological functions and stress resistance mechanisms.

3.1 Tether overexpression potentially interfere with organellar proliferation, fusion and autophagy

As described before, the synthetic tether lines showed peroxisomal clustering, changes in the mitochondria morphology and number, and an impaired growth phenotype. Some studies, which investigated mutants in the mitochondrial and peroxisomal proliferation, reported similar alterations [275–280]. Both organelles share proteins involved in proliferation including the peroxisomal and mitochondrial division (PMD) proteins and the fission machinery consisting of dynamin-related proteins (DRP3A, DRP3B) and the membrane anchors FISSION 1A (FIS1A) and FIS1B [275–278, 281–286]. Mitochondria additionally have an adaptor protein Elongated mitochondria 1 (ELM1) localising DRP3A to the mitochondria fission sites [279, 287].

Knockout mutants of DRP3A, DRP3B and ELM1 are most similar to the synthetic tether lines in terms the organellar morphology and the plant phenotype. *drp3A* and *drp3b* show clustering of peroxisomes similar to the synthetic tether lines, but partly also tubular extensions [276, 278]. Mitochondria in *drp3A* and also in *elm1-6* [279] are elongated, which was also true for the synthetic tether lines, although less pronounced (figure 44). The *elm1* mutant do not match with the plant phenotype of the synthetic tether lines, since they are only slightly impaired in plant growth, but do not show to any extent a curled leaf or early senescence phenotype [279]. Double knockout mutants *drp3a/drp3b-1* and several non-sense mutants of DRP3A have a dwarf phenotype with a decreased inflorescence height [275, 276, 278] similar to the synthetic tether lines. In one publication a distorted leaf phenotype in the double knockout mutant was also reported [275], which was quite similar to the curly leaf phenotype of the synthetic tether lines (figure 47 A, C). However, differently to the synthetic tether lines (figure 46), seedling growth and pollen viability is affected in the DRP3A and DRP3B mutants [276, 278].

Mitochondrial size and number is not only regulated by fission but by a controlled rate of fusion and fission events [288]. Instead of the fission machinery, proteins involved in the fusion process has been mainly unknown. A recent publication in tobacco pavement cells identified the first fusion component, namely the GTPase MIRO2. This protein tethers the mitochondria to the ER to promote mitochondrial fusion [9]. It is possible that overexpression of the synthetic tether 24#5 disturbs the ER-mitochondria connectivity leading to putative interference in the fusion process. Therefore, one possible explanation for the elongated mitochondria in the synthetic tether lines might not be based on the perturbation of the fission machinery but on a shift of the fusion-fission rate towards fusion (figure 59 D). In future, this can be tested by examining the position of mitochondria and ER applying respective fluorescent markers in the synthetic tether lines. However, based on our results, we cannot conclude, if and how the peroxisomal fission and mitochondrial fission and fusion is altered in the synthetic tether lines.

Accumulation of peroxisomes and changes in the mitochondrial morphology may also indicate problems in the mechanism of organelle recycling, termed autophagy. Normally, autophagy enables redistribution of nutrients and removes damaged organelles to ensure the survival of the cell [264]. Similar than the synthetic tether lines, most of the *A. thaliana* autophagy mutants show an accelerated senescence and slower growth [193, 264, 266, 289–295]. This mutants include knockout or knockdown mutants of autophagy-related proteins (ATG) being involved in mitophagy and/or pexophagy.

The synthetic tether lines exhibited elongated mitochondria, which partly accumulated within the peroxisomal clusters (figure 42 & 44). Regarding the mitophagy mutants, the reports mainly focused on the plant phenotypes, whereas imaging data about the mitochondrial morphology was missing or different compared to those of the synthetic tether lines [193, 266]. The authors of a mitophagy review, however, suggested that the mitochondrial size affects the mitophagy [264]. While individual mitochondria may be easily recycled, the degradation of mitochondrial accumulations may be more difficult [264, 265, 296]. It has been also reported that mitochondria accumulation is a early sign for cell death [265]. In the synthetic tether lines, we found elongated mitochondria, which partly accumulated (figure 42 & 44). One possible assumption is that the synthetic tether construct led to an accumulation of mitochondria, which in turn disturb the mitophagy and lead to cell death and senescence (figure 59 D, right).

Peroxisomes in knockout mutants of ATG2, ATG18a and ATG7 aggregate to clusters [266] similar to those in the synthetic tether lines. The authors of the same study claimed that H₂O₂ induces the peroxisomal aggregation, since they found *cat2* mutants and plants treated with external H₂O₂ to show similar clusters of peroxisomes [266]. Thus, two further possible explanation for the peroxisomal clustering in the synthetic tether lines may be either accumulation via enhanced ROS levels or an interference with the pexophagy mechanism itself. The use of autophagy markers such as GFP-ATG8 or monodansylcadaverine staining [297] could provide information as autophagy may be disturbed in the synthetic tether lines. In order to possibly distinguish if mitophagy, pexophagy or both mechanism are affected in the synthetic tether lines, an analysis of the respective ATG protein abundance and their phosphorylation state may provide further insights (ATGs: mitophagy model [264], pexophagy [266, 294]).

3.2 The biological relevance of MCS regarding photorespiration needs further investigation

While the metabolic flux of photorespiration is well understood [1, 109], only little is known about the potential role of inter-organellar contacts. Overexpressing the synthetic tether construct led to changes in the spatial organisation of peroxisomes and the mitochondria morphology, while chloroplasts seemed to be unaffected. In this section, we want to dis-

cuss, if and how the changes in the organellar morphology and the plant phenotype of the synthetic tether lines might be linked to photorespiration.

Photorespiration has been considered to be an energy-losing process. Therefore, it is a prime target for crop improvement. One approach to enhance plant productivity is to lower the energetic costs during photorespiration [271]. On the one hand, this can be achieved by reducing the oxygenase activity of RuBisCO by either genetic modifications or by concentrating CO₂ (reviewed in [298]). On the other hand, introducing non-native synthetic bypasses for photorespiration were shown in several studies to improve plant growth under laboratory and field conditions [113–115, 271, 299–303].

An alternative approach to reduce the photorespiration-caused yield losses is to improve the flux of photorespiration, preventing the accumulation of the toxic intermediate 2PG [271]. Overexpression of components of the mitochondrial glycine decarboxylase complex (GDC) results in enhanced plant growth and photosynthesis, which is assumed to be caused by an increased flux through the photorespiratory pathway [267–270]. López-Calcagno *et al.* 2019 additionally showed that overexpression of some of the GDC components under high photorespiratory conditions (low CO₂ and continuous light) lead to less damage of PSII. One question during this thesis was if a permanent proximity between the organelles would also lead to an improved flux and thus to a similar plant phenotype as the overexpression lines of the GDC components. Differently to GDC overexpression lines, the synthetic tether lines showed an impaired growth phenotype and no enhanced tolerance towards high light conditions (figure 46, 47 & 57). Based on these observations, we can only suggest that the photorespiration rate is not increased in the synthetic tether lines, although direct evidence is lacking. In addition, we must also consider that synthetic tether overexpression might have the opposite effect and altered organellar positioning might interfere with the photorespiratory metabolism instead of improving its flow. Timm & Bauwe classified the photorespiratory phenotypes according to the degree of symptom severity: Class I mutations are lethal under ambient and high CO₂. Class II mutants show lethality under ambient CO₂, but survival can be restored under elevated CO₂. One prominent example belonging to class II is the *dct* mutant, which is deficient in the plastidic glutamate/malate translocator DiT2 [305]. Class III mutants are still viable under ambient CO₂, but show impaired growth or leaf chlorosis [304]. Phenotypes can be completely compensate under elevated CO₂. The mutant *plgg1-1* lacking the IE Plastidic glycolate glycerate translocator 1 (PLGG1) can be normally grown under elevated CO₂, while shift to ambient air lead to yellow and bleached lesions [306]. When *plgg1-1* grow under ambient CO₂ the entire time, it exhibit an impaired growth phenotype [307], which is much stronger pronounced than in the synthetic tether lines (figure 47). Class IV mutants are also phenotypically not affected in normal air, which is why a second redundant enzyme fully compensates the deletion [304].

According to this classification, the synthetic tether phenotype would best fit into class III. Nonetheless, future studies would need to test, if the growth phenotype of the synthetic

tether lines could be rescued by an elevated CO₂ concentration. The question, of whether photorespiration is impaired in the synthetic tether lines, can only be conclusively clarified by a photorespiratory metabolome analysis of the synthetic tether lines.

Based on our results, we cannot report with certainty that the photorespiratory metabolism is affected by the overexpression of the synthetic tether construct. We cannot exclude that also other metabolic or developmental processes relying on the exchange of chloroplasts, peroxisomes and mitochondria are affected by perturbing their natural spatial organisation. For future studies, a broad metabolome analysis would provide insights, into which metabolic processes are altered in the synthetic tether lines. From this, conclusions could be drawn about the relevance of organelle organisation and/or MCS in these processes.

3.3 Impact of synthetic tethering on germination

Overexpression of the synthetic tether construct led to peroxisomal cluster formation, in which mitochondria partly accumulated (figure 42). Peroxisomes are widely known to play an important role in the plant reproduction, seed-development and germination [308]. They host various physiological functions including β -oxidation of fatty acids, phytohormone biosynthesis, nitrogen metabolism and photorespiration [308, 309].

We screened the literature for mutants that are affected in the peroxisomal physiology and exhibit a similar peroxisomal phenotype than the synthetic tether lines. The mutants *mfp2-1*, *mfp2-7*, *ped1* and *sdp1* are impaired in β -oxidation or upstream processes and show a similar distribution of peroxisomes to the synthetic tether lines [54, 310]. Sugar-dependent 1 (SDP1) hydrolyses storage lipids producing fatty acids [274], which are transferred to peroxisomes and processed during β -oxidation [87–90]. Multifunctional protein 2 (MFP2) catalyses the second and third step of fatty acid β -oxidation [310], while PED1 (also termed KAT2) catalyses the last step of this metabolic pathway [311, 312]. The germination of mutants impaired in storage lipid degradation has been reported to be sucrose-dependent [54, 86, 274] (figure 59 G), which is why we tested the germination efficiency of the synthetic tether lines on medium with and without sucrose (figure 45). Assuming that β -oxidation is altered in the synthetic tether lines, the germination phenotype should be also sucrose-dependent.

Testing the germination, we simultaneously wanted to answer a contradictory question, namely, if the potential mitochondrion-peroxisome cross-linkages in the synthetic tether lines support germination. In oil seeds including those of *A. thaliana*, the breakdown of long-chain fatty acids during β -oxidation and downstream processes has been shown to be essential providing substrates for the mitochondrial respiration [87–90]. Assuming that the constant proximity of the two organelles makes the substrate exchange more effective between peroxisomes and mitochondria, synthetic tethering may result into faster germination.

The germination rate of two of the independent transgenic lines px-ck 24#5 #31E, px-

ck 24#5 #12B/G was faster compared to px-ck on medium with and without sucrose (figure 45). However, one independent line Col-0 24#5 #11C was slower in germination than the WT but also the seedling establishment (figure 46) and the reproductive development were impaired in this specific line (figure 52 & 51). Nevertheless, as only one of three lines showed those results, we can assume that the T-DNA insertion led to disruption of one or several genes specifically in this line, which probably caused the unique behaviour. To draw further conclusions, the line Col-0 24#5 #11C should be excluded for future studies and experiments should be repeated with another independent transgenic line.

In summary, the germination was faster in two of three independent lines. Based on these results, we can not clearly state if the synthetic tether construct is beneficial for the substrate transfer from peroxisomes towards mitochondria. Comparing the restart of the mitochondrial respiratory energy metabolism in seeds of synthetic tether lines to WT (after Nietzel *et al.* [90]) may be helpful to contribute further insights.

3.4 Assessment of possible correlations between the synthetic tether phenotype and altered oxidative phosphorylation

Besides photorespiration, mitochondria are involved in various cellular functions including respiration. Cellular respiration consists of the glycolysis, the oxidative decarboxylation of pyruvate, the tricarboxylic acid (TCA) cycle and the oxidative phosphorylation (OXPHOS), with the latter two taking place in the mitochondria. While the first three pathways generate reduced co-factors as NAD(P)H [198], they are converted to ATP during OXPHOS involving the mitochondrial electron transport chain (ETC) (complex I-V, figure 59 F).

Interestingly, adult mutants of of complex I and complex IV are visually rather alike to the synthetic tether lines with impaired growth and a curly leaf phenotype [198, 272, 273] (figure 47). Conversely, those mutants are delayed in their development including germination, which is not the case in the synthetic tether lines (figure 45 & 46). The phenotype manifestation of the OXPHOS mutants depends on the remaining activity of complex I and complex IV. The two mutants *rpoTmp-1*, *rpoTmp-2* have 80% or more reduction in the activity complex I and complex IV [272, 273]). They most closely resemble the synthetic tether lines in terms of leaf and a growth phenotype and have only a slightly delayed germination [272, 273]. Although some of the phenotypical characteristics of mentioned OXPHOS and tether lines do not match in early developmental stages, the adult phenotype is strikingly alike.

To get evidences, if those similarities are accidentally or is based on altered OXPHOS, we checked the leaf O₂ consumption in two independent synthetic tether lines (figure 54). While leaf respiration of all complex I mutants is slightly higher than in WT plants [198, 272, 273], we can report no differences in the leaf respiration rate comparing WT and the synthetic tether lines. This indicate no alterations in the respiratory flux and ETC. Nonetheless, OXPHOS mutants have been described to show an increased capacity of AOX activated by oxid-

ative stress [198]. As an additional proof, future studies should measure the AOX-dependent respiration and perform a western blot to verify the AOX level in the synthetic tether lines.

3.5 Synthetic tethering potentially causes alterations in signalling cascades

Both chloroplasts and mitochondria are important cellular sensors for fluctuating environmental conditions [313]. To respond appropriately to such fluctuating environmental conditions, rapid and delicate adaptations must take place at metabolic, post-translational and transcriptional levels. Therefore, retrograde signalling pathways from chloroplasts and mitochondria to the nucleus are required, aiming to coordinate the nuclear gene expression [194]. Four major types of signalling molecules have been identified, namely RNA, proteins including transcription factors (TF), ROS and metabolites. These signalling molecules can originate not only from the endosymbiotic organelles but also from peroxisomes [313].

Whether and to what extent physical associations between organelles and a dynamic, spatial organisation in a cell are relevant for retrograde signalling is mostly unexplored. It has been reported that a direct transfer of H₂O₂ from chloroplasts to nucleus can occur via physical association between those two [19, 41]. Suzuki *et al.* already suggested that changes in the spatial organellar arrangement hypothetically influence retrograde signalling cascades [314]. Assuming that this is the case, perturbing the dynamic and the spatial organisation of mitochondria, peroxisomes and eventually chloroplasts by introducing the synthetic tether construct has the potential to disturb signalling cascades.

We screened the literature for mutants with disrupted retrograde signalling pathways involving mitochondria, peroxisomes or chloroplasts and with a similar growth phenotype than the synthetic tether lines. One potential candidate was the knockout mutant *rcd1*. Similar to the synthetic tether lines, *rcd1* shows impaired growth and curly leaves [315] (figure 47). Radical-Induced Cell Death1 (RCD1) is suggested to be a regulatory protein of chloroplast and mitochondria retrograde ROS signalling pathways. Chloroplastidic ROS likely affect the redox state of RCD1 and its ability to function as suppressor in a signalling cascade controlling the expression of mitochondrial dysfunction stimulon (MDS) genes including AOX1 [315].

To test, if this ROS dependent signalling cascade is affected in the here generated synthetic tether lines, the protein abundance of RCD1 and the downstream targets of the signalling cascade could be investigated by performing a Western Blot. In addition, the respiration capacity of AOX1 or the tolerance against methyl viologen being enhanced in *rcd1* could be also tested in the synthetic tether lines.

3.6 Potential interdependency of anthocyanin biosynthesis and synthetic tethering

When we investigated the synthetic tether lines, we unexpectedly found that adult plants had significantly decreased anthocyanin levels compared to WT plants in response to HL (figure 57). The synthetic tether lines showed yellowing of leaves in response to HL similar to mutants, which are impaired in the flavonoid/anthocyanin biosynthesis (FAB) such as *chi* and *ans* [316]. The regulation of FAB is very complex including positively and negatively regulatory proteins, post-translational modifications, a set of TF and chloroplast-derived retrograde signalling cascades [248, 317–319]. There is still an ongoing discussion about the exact signal and downstream factors involved in HL-induced FAB. On the one hand, FAB was reported to be regulated by ROS- and/or phytohormone as signalling molecules with ANAC032 as TF [320, 321]. This TF simultaneously induces chlorophyll degradation genes and other senescence-associated genes, promoting leaf senescence [320, 321]. On the other hand, a FAB signalling cascade including PAP1 and SNF1-RELATED PROTEIN KINASE (SnRK1) has been described to be sugar-dependent [322, 323]. Zirngibl *et al.* recently proposed this sugar-dependent pathway to be essential for rapid HL-induction of anthocyanin biosynthesis, while ROS and phytohormones play only a minor role [248].

Based on our results, we can only make assumptions of how and whether a disturbance of the natural cellular organelle organisation leads to a disturbance in the FAB signalling cascades. It is not clear, which FAB signalling cascade is affected in the synthetic tether lines. To be able to make a precise conclusion, the synthetic tether lines should be investigated regarding their relative expression levels of genes and TFs involved in FAB [194].



V Conclusion and outlook

This thesis investigated the role of organellar proximity in plants using the photorespiratory organelles as a model. One aim was to quantify the proximity between chloroplasts and peroxisomes under different photosynthetic conditions and to develop an automated, high-throughput analysis process. On the one hand, we were able to develop a Python-based analysis pipeline and to verify its functionality by comparing the automatically generated results to a manual quantification and finding a similar trend for both analysis methods. On the other hand, in our experimental system we were not able to increase organellar proximity in *A. thaliana*, *N. tabacum* and *P. patens* by light. Thus, we suggest that the experimental setup requires optimisation to increase MCS between chloroplasts and peroxisomes. We conclude that we developed a robust and automated high-throughput analysis pipeline for confocal z-stacks of cells with fluorescently labelled organelles. Future studies could incorporate new data sets of different light and dark treatments.

A second aim was to establish novel *in vivo* FP-based proximity sensor systems in plants. We successfully created homogenous targeting of reporter constructs to the cytosolic face of the (outer) membrane of chloroplasts, peroxisomes and mitochondria. For splitYFP- and saGFP(self-assembly GFP)-based proximity sensors tested by transient expression in *N. tabacum*, we can report an unspecific labelling of the whole organellar membranes. Comparing splitYFP- and saGFP-based reporters, the saGFP signal was potentially increased at the putative interaction sites between peroxisomes and chloroplasts. Overexpression of the splitYFP-based proximity sensors induced tethering of peroxisomes and chloroplasts. To provide a system for stable transgenic *A. thaliana* lines with an inducible expression of the proximity reporters or synthetic organelle tethers, we generated a dexamethasone-inducible 2in1 gateway vector system (pInd). Transiently transfected *N. tabacum* plants showed reporter expression without induction, an effect which is not expected for stable *A. thaliana* and *N. tabacum* plants [230, 231]. During this work, we were able to transform *A. thaliana* plants with an inducible saGFP-based proximity sensor construct for chloroplasts and peroxisomes and to generate T₁ seeds. Future studies will be able to test inducible chloroplast-peroxisome tethering as well as the induction behaviour of the new vector system.

Using FRET/FLIM-based proximity sensors, we were not able to detect any decrease in the donor lifetime at putative MCS under the tested conditions both in *A. thaliana* and transiently in *N. tabacum*. As mentioned before, we suggest that an increased proximity of chloroplasts and peroxisomes requires a higher light intensity than we applied. Therefore, we recommend as a next step to extend the previous experiment by a light treatment with a higher intensity. It is also possible that the lack of change in the fluorescence lifetime was

due to the dynamic nature of MCS, which may have been too rapid for FLIM detection that lasted approximately 30 s per image. However, based on our results, we cannot conclude whether the unaltered lifetime is due to the experimental/imaging design or due to the lack of existence of MCS between chloroplasts and peroxisomes.

Finally, we were able to gain first evidence of the importance of dynamic MCS formation and dissociation in plants by disrupting the natural spatial organisation within a cell. Introducing a synthetic tether construct in *A. thaliana* plants led to formation of spherical peroxisomal clusters and elongated mitochondria. Stable lines constitutively expressing this synthetic tether showed curly leaves, an accelerated senescence, impaired growth and a reduced high light tolerance including decreased anthocyanin accumulation. Future research will need to address the exact causes of the observed phenotypic and physiological alterations. Expression of the used synthetic tether potentially influences for instance mitophagy, local generation of ROS or sugar-dependent retrograde signalling cascades.

In conclusion, this study provides a solid foundation for further studies that aim to clarify the importance of MCS between chloroplasts, peroxisomes and mitochondria in plants.

Bibliography

1. Bauwe, H., Hagemann, M. & Fernie, A. R. Photorespiration: Players, Partners and Origin. *Trends in Plant Science* **15**, 330–336 (2010).
2. Wu, H., Carvalho, P. & Voeltz, G. K. Here, There, and Everywhere: The Importance of ER Membrane Contact Sites. *Science* **361**, eaan5835 (2018).
3. Michaud, M. & Jouhet, J. Lipid Trafficking at Membrane Contact Sites During Plant Development and Stress Response. *Frontiers in Plant Science* **10** (2019).
4. Csordás, G. *et al.* Imaging Interorganelle Contacts and Local Calcium Dynamics at the ER-mitochondrial Interface. *Molecular cell* **39**, 121–132. pmid: 20603080 (2010).
5. Scorrano, L. *et al.* Coming Together to Define Membrane Contact Sites. *Nature Communications* **10**, 1287 (1 2019).
6. Baillie, A. L., Falz, A.-L., Müller-Schüssele, S. J. & Sparkes, I. It Started With a Kiss: Monitoring Organelle Interactions and Identifying Membrane Contact Site Components in Plants. *Frontiers in Plant Science* **11**, 517 (2020).
7. Phillips, M. J. & Voeltz, G. K. Structure and Function of ER Membrane Contact Sites with Other Organelles. *Nature Reviews Molecular Cell Biology* **17**, 69–82 (2 2016).
8. Müller-Schüssele, S. J. & Michaud, M. in *Plastids: Methods and Protocols* (ed Maréchal, E.) 87–109 (Springer US, New York, NY, 2018).
9. White, R. R. *et al.* Miro2 Tethers the ER to Mitochondria to Promote Mitochondrial Fusion in Tobacco Leaf Epidermal Cells. *Communications Biology* **3**, 1–8 (1 2020).
10. Liu, X., Weaver, D., Shirihai, O. & Hajnóczky, G. Mitochondrial 'Kiss-and-Run': Interplay between Mitochondrial Motility and Fusion-Fission Dynamics. *The EMBO Journal* **28**, 3074–3089 (2009).
11. Bernhard, W. & Rouiller, C. Close Topographical Relationship between Mitochondria and Ergastoplasm of Liver Cells in a Definite Phase of Cellular Activity. *The Journal of Biophysical and Biochemical Cytology* **2**, 73–78. pmid: 13357525 (4 Suppl 1956).
12. Copeland, D. E. & Dalton, A. J. An Association between Mitochondria and the Endoplasmic Reticulum in Cells of the Pseudobranch Gland of a Teleost. *The Journal of Biophysical and Biochemical Cytology* **5**, 393–396. pmid: 13664679 (1959).
13. Tolbert, N. & Essner, E. Microbodies: Peroxisomes and Glyoxysomes. *The Journal of cell biology* (1981).

-
14. Rizzuto, R. *et al.* Close Contacts with the Endoplasmic Reticulum as Determinants of Mitochondrial Ca²⁺ Responses. *Science* **280**, 1763–1766 (1998).
 15. Vance, J. E. Phospholipid Synthesis in a Membrane Fraction Associated with Mitochondria. *Journal of Biological Chemistry* **265**, 7248–7256 (1990).
 16. Siao, W., Wang, P., Voigt, B., Hussey, P. J. & Baluska, F. Arabidopsis SYT1 Maintains Stability of Cortical Endoplasmic Reticulum Networks and VAP27-1-enriched Endoplasmic Reticulum–Plasma Membrane Contact Sites. *Journal of Experimental Botany* **67**, 6161–6171 (2016).
 17. Klecker, T., Scholz, D., Förtsch, J. & Westermann, B. The Yeast Cell Cortical Protein Num1 Integrates Mitochondrial Dynamics into Cellular Architecture. *Journal of Cell Science* **126**, 2924–2930 (2013).
 18. Feng, Q. & Kornmann, B. Mechanical Forces on Cellular Organelles. *Journal of Cell Science* **131**, jcs218479 (2018).
 19. Caplan, J. L. *et al.* Chloroplast Stromules Function during Innate Immunity. *Developmental cell* **34**, 45–57. pmid: 26120031 (2015).
 20. Jaipargas, E.-A., Mathur, N., Bou Daher, F., Wasteneys, G. O. & Mathur, J. High Light Intensity Leads to Increased Peroxisome-Mitochondria Interactions in Plants. *Frontiers in Cell and Developmental Biology* **4**, 6 (2016).
 21. Lee, E. *et al.* Ionic Stress Enhances ER-PM Connectivity via Phosphoinositide-Associated SYT1 Contact Site Expansion in Arabidopsis. *Proceedings of the National Academy of Sciences of the United States of America* **116**, 1420–1429. pmid: 30610176 (2019).
 22. McFarlane, H. E. *et al.* Multiscale Structural Analysis of Plant ER–PM Contact Sites. *Plant and Cell Physiology* **58**, 478–484 (2017).
 23. Sparkes, I. Using Optical Tweezers to Characterize Physical Tethers at Membrane Contact Sites: Grab It, Pull It, Set It Free? *Frontiers in Cell and Developmental Biology* **4** (2016).
 24. Sparkes, I. A. Lessons from Optical Tweezers: Quantifying Organelle Interactions, Dynamics and Modelling Subcellular Events. *Current Opinion in Plant Biology* **46**, 55–61 (2018).
 25. Gao, H. *et al.* In Vivo Quantification of Peroxisome Tethering to Chloroplasts in Tobacco Epidermal Cells Using Optical Tweezers. *Plant Physiology* **170**, 263–272. pmid: 26518344 (2016).
 26. Oikawa, K. *et al.* Physical Interaction between Peroxisomes and Chloroplasts Elucidated by in Situ Laser Analysis. *Nature Plants* **1**, 15035 (2015).

BIBLIOGRAPHY

27. Jouhet, J. *et al.* Phosphate Deprivation Induces Transfer of DGDG Galactolipid from Chloroplast to Mitochondria. *Journal of Cell Biology* **167**, 863–874 (2004).
28. Mehrshahi, P. *et al.* Transorganellar Complementation Redefines the Biochemical Continuity of Endoplasmic Reticulum and Chloroplasts. *Proceedings of the National Academy of Sciences* **110**, 12126–12131 (2013).
29. Pérez-Sancho, J. *et al.* The Arabidopsis Synaptotagmin1 Is Enriched in Endoplasmic Reticulum-Plasma Membrane Contact Sites and Confers Cellular Resistance to Mechanical Stresses. *Plant Physiology* **168**, 132–143. pmid: 25792253 (2015).
30. Andersson, M. X., Goksör, M. & Sandelius, A. S. Optical Manipulation Reveals Strong Attracting Forces at Membrane Contact Sites between Endoplasmic Reticulum and Chloroplasts. *The Journal of Biological Chemistry* **282**, 1170–1174. pmid: 17077082 (2007).
31. Helle, S. C. J. *et al.* Organization and Function of Membrane Contact Sites. *Biochimica Et Biophysica Acta* **1833**, 2526–2541. pmid: 23380708 (2013).
32. Fernández-Busnadiego, R., Saheki, Y. & De Camilli, P. Three-Dimensional Architecture of Extended Synaptotagmin-Mediated Endoplasmic Reticulum–Plasma Membrane Contact Sites. *Proceedings of the National Academy of Sciences* **112**, E2004–E2013 (2015).
33. Prinz, W. A., Toulmay, A. & Balla, T. The Functional Universe of Membrane Contact Sites. *Nature Reviews Molecular Cell Biology* **21**, 7–24 (1 2020).
34. Michaud, M. *et al.* AtMic60 Is Involved in Plant Mitochondria Lipid Trafficking and Is Part of a Large Complex. *Current Biology* **26**, 627–639. pmid: 26898467 (2016).
35. Michaud, M., Prinz, W. A. & Jouhet, J. Glycerolipid Synthesis and Lipid Trafficking in Plant Mitochondria. *The FEBS Journal* **284**, 376–390 (2017).
36. Hönscher, C. *et al.* Cellular Metabolism Regulates Contact Sites between Vacuoles and Mitochondria. *Developmental Cell* **30**, 86–94. pmid: 25026035 (2014).
37. Falz, A.-L. & Müller-Schüssele, S. J. Spezifische Membrankontaktstellen bei Pflanzen: wer mit wem, warum und wie. *BIOspektrum* **27**, 693–696 (2021).
38. Fuchs, P. *et al.* Single Organelle Function and Organization as Estimated from Arabidopsis Mitochondrial Proteomics. *The Plant Journal* **101**, 420–441 (2020).
39. Müller-Schüssele, S. J. *et al.* Plasticity in Plastid Redox Networks: Evolution of Glutathione-Dependent Redox Cascades and Glutathionylation Sites. *BMC Plant Biology* **21**, 322 (2021).
40. Ugalde, J. M. *et al.* Chloroplast-Derived Photo-Oxidative Stress Causes Changes in H₂O₂ and EGSH in Other Subcellular Compartments. *Plant Physiology* **186**, 125–141 (2021).

-
41. Exposito-Rodriguez, M., Laissue, P. P., Yvon-Durocher, G., Smirnoff, N. & Mullineaux, P. M. Photosynthesis-Dependent H₂O₂ Transfer from Chloroplasts to Nuclei Provides a High-Light Signalling Mechanism. *Nature Communications* **8**, 49 (1 2017).
 42. Kornmann, B. *et al.* An ER-Mitochondria Tethering Complex Revealed by a Synthetic Biology Screen. *Science* **325**, 477–481 (2009).
 43. Raturi, A. & Simmen, T. Where the Endoplasmic Reticulum and the Mitochondrion Tie the Knot: The Mitochondria-Associated Membrane (MAM). *Biochimica et Biophysica Acta (BBA) - Molecular Cell Research. Including Special Section: Mitochondrial Dynamics and Physiology* **1833**, 213–224 (2013).
 44. Higa, T., Suetsugu, N., Kong, S.-G. & Wada, M. Actin-Dependent Plastid Movement Is Required for Motive Force Generation in Directional Nuclear Movement in Plants. *Proceedings of the National Academy of Sciences* **111**, 4327–4331. pmid: 24591587 (2014).
 45. Suetsugu, N. & Wada, M. in *The Chloroplast: Interactions with the Environment* (eds Sandelius, A. S. & Aronsson, H.) 235–266 (Springer, Berlin, Heidelberg, 2009).
 46. Iwabuchi, K., Minamino, R. & Takagi, S. Actin Reorganization Underlies Phototropin-Dependent Positioning of Nuclei in Arabidopsis Leaf Cells. *Plant Physiology* **152**, 1309–1319. pmid: 20107027 (2010).
 47. Oikawa, K. *et al.* CHLOROPLAST UNUSUAL POSITIONING1 Is Essential for Proper Chloroplast Positioning. *The Plant Cell* **15**, 2805–2815. pmid: 14615600 (2003).
 48. Jung, H.-S. & Chory, J. Signaling between Chloroplasts and the Nucleus: Can a Systems Biology Approach Bring Clarity to a Complex and Highly Regulated Pathway? *Plant Physiology* **152**, 453–459. pmid: 19933385 (2010).
 49. Sinclair, A. M., Trobacher, C. P., Mathur, N., Greenwood, J. S. & Mathur, J. Peroxule Extension over ER-defined Paths Constitutes a Rapid Subcellular Response to Hydroxyl Stress. *The Plant journal* **59**, 231–242. pmid: 19292761 (2009).
 50. Müller, S. J. & Reski, R. Mitochondrial Dynamics and the ER: The Plant Perspective. *Frontiers in Cell and Developmental Biology* **3**, 78 (2015).
 51. Jaipargas, E.-A., Barton, K. A., Mathur, N. & Mathur, J. Mitochondrial Pleomorphy in Plant Cells Is Driven by Contiguous ER Dynamics. *Frontiers in Plant Science* **6**, 783. pmid: 26442089 (2015).
 52. Friedman, J. R. *et al.* ER Tubules Mark Sites of Mitochondrial Division. *Science (New York, N.y.)* **334**, 358–362. pmid: 21885730 (2011).
 53. Falz, A.-L. & Müller-Schüssele, S. J. Physcomitrella as a Model System for Plant Cell Biology and Organelle–Organelle Communication. *Current Opinion in Plant Biology* **52**, 7–13 (2019).

BIBLIOGRAPHY

54. Cui, S. *et al.* Sucrose Production Mediated by Lipid Metabolism Suppresses the Physical Interaction of Peroxisomes and Oil Bodies during Germination of Arabidopsis Thaliana. *The Journal of Biological Chemistry* **291**, 19734–19745. pmid: 27466365 (2016).
55. Friedman, J. R. & Voeltz, G. K. The ER in 3D: A Multifunctional Dynamic Membrane Network. *Trends in Cell Biology* **21**, 709–717 (2011).
56. Schwarz, D. S. & Blower, M. D. The Endoplasmic Reticulum: Structure, Function and Response to Cellular Signaling. *Cellular and Molecular Life Sciences* **73**, 79–94. pmid: 26433683 (2016).
57. Prinz, W. A. Bridging the Gap: Membrane Contact Sites in Signaling, Metabolism, and Organelle Dynamics. *The Journal of Cell Biology* **205**, 759–769. pmid: 24958771 (2014).
58. Wang, P. *et al.* The Plant Cytoskeleton, NET3C, and VAP27 Mediate the Link between the Plasma Membrane and Endoplasmic Reticulum. *Current Biology* **24**, 1397–1405 (2014).
59. Tao, K., Waletich, J. R., Arredondo, F. & Tyler, B. M. Manipulating Endoplasmic Reticulum-Plasma Membrane Tethering in Plants Through Fluorescent Protein Complementation. *Frontiers in Plant Science* **10**, 635 (2019).
60. Pérez-Sancho, J. *et al.* Stitching Organelles: Organization and Function of Specialized Membrane Contact Sites in Plants. *Trends in Cell Biology* **26**, 705–717 (2016).
61. Osterrieder, A. *et al.* Stacks off Tracks: A Role for the Golgin AtCASP in Plant Endoplasmic Reticulum-Golgi Apparatus Tethering. *Journal of Experimental Botany* **68**, 3339–3350. pmid: 28605454 (2017).
62. Sparkes, I. A., Ketelaar, T., De Ruijter, N. C. & Hawes, C. Grab a Golgi: Laser Trapping of Golgi Bodies Reveals in Vivo Interactions with the Endoplasmic Reticulum. *Traffic* **10**, 567–571 (2009).
63. Barton, K., Mathur, N. & Mathur, J. Simultaneous Live-Imaging of Peroxisomes and the ER in Plant Cells Suggests Contiguity but No Luminal Continuity between the Two Organelles. *Frontiers in Physiology* **4**, 196. pmid: 23898304 (2013).
64. Wang, P. *et al.* Plant VAP27 Proteins: Domain Characterization, Intracellular Localization and Role in Plant Development. *The New Phytologist* **210**, 1311–1326. pmid: 27159525 (2016).
65. Laurent, F., Labesse, G. & de Wit, P. Molecular Cloning and Partial Characterization of a Plant VAP33 Homologue with a Major Sperm Protein Domain. *Biochemical and Biophysical Research Communications* **270**, 286–292 (2000).
66. Stefan, C. J. *et al.* Osh Proteins Regulate Phosphoinositide Metabolism at ER-plasma Membrane Contact Sites. *Cell* **144**, 389–401. pmid: 21295699 (2011).

-
67. Loewen, C. J., Young, B. P., Tavassoli, S. & Levine, T. P. Inheritance of Cortical ER in Yeast Is Required for Normal Septin Organization. *The Journal of Cell Biology* **179**, 467–483. pmid: 17984322 (2007).
 68. Deeks, M. J. *et al.* A Superfamily of Actin-Binding Proteins at the Actin-Membrane Nexus of Higher Plants. *Current biology: CB* **22**, 1595–1600. pmid: 22840520 (2012).
 69. Craxton, M. Synaptotagmin Gene Content of the Sequenced Genomes. *BMC Genomics* **5**, 43 (2004).
 70. Yamazaki, T., Kawamura, Y., Minami, A. & Uemura, M. Calcium-Dependent Freezing Tolerance in Arabidopsis Involves Membrane Resealing via Synaptotagmin SYT1. *The Plant Cell* **20**, 3389–3404 (2008).
 71. Craxton, M. Evolutionary Genomics of Plant Genes Encoding N-terminal-TM-C2 Domain Proteins and the Similar FAM62 Genes and Synaptotagmin Genes of Metazoans. *BMC Genomics* **8**, 259 (2007).
 72. Manford, A. G., Stefan, C. J., Yuan, H. L., MacGurn, J. A. & Emr, S. D. ER-to-Plasma Membrane Tethering Proteins Regulate Cell Signaling and ER Morphology. *Developmental Cell* **23**, 1129–1140 (2012).
 73. Jiménez, J. L. & Davletov, B. β -Strand Recombination in Tricalbin Evolution and the Origin of Synaptotagmin-like C2 Domains. *Proteins: Structure, Function, and Bioinformatics* **68**, 770–778 (2007).
 74. Schapire, A. L. *et al.* Arabidopsis Synaptotagmin 1 Is Required for the Maintenance of Plasma Membrane Integrity and Cell Viability. *The Plant Cell* **20**, 3374–3388. pmid: 19088329 (2008).
 75. Levy, A., Zheng, J. Y. & Lazarowitz, S. G. Synaptotagmin SYTA Forms ER-Plasma Membrane Junctions That Are Recruited to Plasmodesmata for Plant Virus Movement. *Current Biology* **25**, 2018–2025 (2015).
 76. Bayer, E. M., Mongrand, S. & Tilsner, J. Specialized Membrane Domains of Plasmodesmata, Plant Intercellular Nanopores. *Frontiers in Plant Science* **5** (2014).
 77. Brunkard, J. O., Runkel, A. M. & Zambryski, P. C. The Cytosol Must Flow: Intercellular Transport through Plasmodesmata. *Current Opinion in Cell Biology. Cell Organelles* **35**, 13–20 (2015).
 78. Otero, S., Helariutta, Y. & Benitez-Alfonso, Y. Symplastic Communication in Organ Formation and Tissue Patterning. *Current Opinion in Plant Biology. Growth and Development* **29**, 21–28 (2016).
 79. Wang, P., Liang, Z. & Kang, B.-H. Electron Tomography of Plant Organelles and the Outlook for Correlative Microscopic Approaches. *The New Phytologist* **223**, 1756–1761. pmid: 31058325 (2019).

BIBLIOGRAPHY

80. Stefano, G. *et al.* Plant Endocytosis Requires the ER Membrane-Anchored Proteins VAP27-1 and VAP27-3. *Cell Reports* **23**, 2299–2307 (2018).
81. Greer, M. S. *et al.* SEIPIN Isoforms Interact with the Membrane-Tethering Protein VAP27-1 for Lipid Droplet Formation. *The Plant Cell* **32**, 2932–2950. pmid: 32690719 (2020).
82. Li, C. *et al.* TraB Is a Novel Component of the ER-Mitochondria Contact Site (EMCS) with Dual Roles in ER-Mitochondrial Tethering and Mitophagy, 2022.02.25.481886 (2022).
83. Hamasaki, M. *et al.* Autophagosomes Form at ER–Mitochondria Contact Sites. *Nature* **495**, 389–393 (7441 2013).
84. López-Crisosto, C. *et al.* ER-to-mitochondria Miscommunication and Metabolic Diseases. *Biochimica et Biophysica Acta (BBA) - Molecular Basis of Disease* **1852**, 2096–2105 (10, Part A 2015).
85. Noda, N. N., Ohsumi, Y. & Inagaki, F. Atg8-Family Interacting Motif Crucial for Selective Autophagy. *FEBS letters* **584**, 1379–1385. pmid: 20083108 (2010).
86. Hayashi, M., Toriyama, K., Kondo, M. & Nishimura, M. 2,4-Dichlorophenoxybutyric Acid-Resistant Mutants of Arabidopsis Have Defects in Glyoxysomal Fatty Acid Beta-Oxidation. *The Plant Cell* **10**, 183–195. pmid: 9490742 (1998).
87. Pracharoenwattana, I., Cornah, J. E. & Smith, S. M. Arabidopsis Peroxisomal Citrate Synthase Is Required for Fatty Acid Respiration and Seed Germination. *The Plant Cell* **17**, 2037–2048. pmid: 15923350 (2005).
88. Eastmond, P. J. & Graham, I. A. Re-Examining the Role of the Glyoxylate Cycle in Oilseeds. *Trends in Plant Science* **6**, 72–78. pmid: 11173291 (2001).
89. Raymond, R., Spiteri, A., Dieuaide, M., Gerhardt, B. & Pradet, A. Peroxisomal Beta - Oxidation of Fatty Acids and Citrate Formation by a Particulate Fraction from Early Germinating Sunflower Seeds. *Plant Physiology and Biochemistry (France)* (1992).
90. Nietzel, T. *et al.* Redox-Mediated Kick-Start of Mitochondrial Energy Metabolism Drives Resource-Efficient Seed Germination. *Proceedings of the National Academy of Sciences* **117**, 741–751. pmid: 31871212 (2020).
91. Krawczyk, H. E. *et al.* SEED LIPID DROPLET PROTEIN1, SEED LIPID DROPLET PROTEIN2, and LIPID DROPLET PLASMA MEMBRANE ADAPTOR Mediate Lipid Droplet–Plasma Membrane Tethering. *The Plant Cell*, koac095 (2022).
92. Li-Beisson, Y. *et al.* Acyl-Lipid Metabolism. *The Arabidopsis Book / American Society of Plant Biologists* **11**, e0161. pmid: 23505340 (2013).

-
93. Härtel, H., Dörmann, P. & Benning, C. DGD1-independent Biosynthesis of Extraplasmatic Galactolipids after Phosphate Deprivation in Arabidopsis. *Proceedings of the National Academy of Sciences* **97**, 10649–10654 (2000).
 94. Andersson, M. X., Larsson, K. E., Tjellström, H., Liljenberg, C. & Sandelius, A. S. Phosphate-Limited Oat: The Plasma Membrane and the Tonoplast as Major Targets for Phospholipid-to-Glycolipid Replacement and Stimulation of Phospholipases in the Plasma Membrane. *Journal of Biological Chemistry* **280**, 27578–27586. pmid: 15927962 (2005).
 95. Xu, C., Moellering, E. R., Muthan, B., Fan, J. & Benning, C. Lipid Transport Mediated by Arabidopsis TGD Proteins Is Unidirectional from the Endoplasmic Reticulum to the Plastid. *Plant and Cell Physiology* **51**, 1019–1028 (2010).
 96. Alboresi, A., Storti, M. & Morosinotto, T. Balancing Protection and Efficiency in the Regulation of Photosynthetic Electron Transport across Plant Evolution. *New Phytologist* **221**, 105–109 (2019).
 97. Li, Z., Wakao, S., Fischer, B. B. & Niyogi, K. K. Sensing and Responding to Excess Light. *Annual Review of Plant Biology* **60**, 239–260. pmid: 19575582 (2009).
 98. Eberhard, S., Finazzi, G. & Wollman, F.-A. The Dynamics of Photosynthesis. *Annual Review of Genetics* **42**, 463–515. pmid: 18983262 (2008).
 99. Roach, T. & Krieger-Liszkay, A. K. Regulation of Photosynthetic Electron Transport and Photoinhibition. *Current Protein & Peptide Science* **15**, 351–362. pmid: 24678670 (2014).
 100. Zaffagnini, M. *et al.* Redox Homeostasis in Photosynthetic Organisms: Novel and Established Thiol-Based Molecular Mechanisms. *Antioxidants & Redox Signaling* **31**, 155–210 (2019).
 101. Wang, W.-H. *et al.* The Reduced State of the Plastoquinone Pool Is Required for Chloroplast-Mediated Stomatal Closure in Response to Calcium Stimulation. *The Plant Journal* **86**, 132–144 (2016).
 102. Waszczak, C., Carmody, M. & Kangasjärvi, J. Reactive Oxygen Species in Plant Signaling. *Annual Review of Plant Biology* **69**, 209–236. pmid: 29489394 (2018).
 103. Kasahara, M. *et al.* Chloroplast Avoidance Movement Reduces Photodamage in Plants. *Nature* **420**, 829–832 (6917 2002).
 104. Müller, P., Li, X.-P. & Niyogi, K. K. Non-Photochemical Quenching. A Response to Excess Light Energy¹. *Plant Physiology* **125**, 1558–1566 (2001).
 105. Elsässer, M. *et al.* *Photosynthetic Activity Triggers pH and NAD Redox Signatures across Different Plant Cell Compartments* preprint (Plant Biology, 2020).

BIBLIOGRAPHY

106. Yokochi, Y. *et al.* Redox Regulation of NADP-malate Dehydrogenase Is Vital for Land Plants under Fluctuating Light Environment. *Proceedings of the National Academy of Sciences* **118**, e2016903118 (2021).
107. Selinski, J. & Scheibe, R. Malate Valves: Old Shuttles with New Perspectives. *Plant Biology* **21**, 21–30 (2019).
108. Taniguchi, M. & Miyake, H. Redox-Shuttling between Chloroplast and Cytosol: Integration of Intra-Chloroplast and Extra-Chloroplast Metabolism. *Current Opinion in Plant Biology* **15**, 252–260. pmid: 22336038 (2012).
109. Bauwe, H., Hagemann, M., Kern, R. & Timm, S. Photorespiration Has a Dual Origin and Manifold Links to Central Metabolism. *Current Opinion in Plant Biology* **15**, 269–275 (2012).
110. Voss, I., Sunil, B., Scheibe, R. & Raghavendra, A. S. Emerging Concept for the Role of Photorespiration as an Important Part of Abiotic Stress Response. *Plant Biology* **15**, 713–722 (2013).
111. Heldt, H. W. & Piechulla, B. *Pflanzenbiochemie* (Springer Berlin Heidelberg, Berlin, Heidelberg, 2015).
112. Anderson, L. E. Chloroplast and Cytoplasmic Enzymes II. Pea Leaf Triose Phosphate Isomerases. *Biochimica et Biophysica Acta (BBA) - Enzymology* **235**, 237–244 (1971).
113. Kebeish, R. *et al.* Chloroplastic Photorespiratory Bypass Increases Photosynthesis and Biomass Production in Arabidopsis Thaliana. *Nature Biotechnology* **25**, 593–599 (5 2007).
114. Peterhansel, C., Niessen, M. & Kebeish, R. M. Metabolic Engineering towards the Enhancement of Photosynthesis. *Photochemistry and Photobiology* **84**, 1317–1323. pmid: 18764897 (2008).
115. Betti, M. *et al.* Manipulating Photorespiration to Increase Plant Productivity: Recent Advances and Perspectives for Crop Improvement. *Journal of Experimental Botany* **67**, 2977–2988. pmid: 26951371 (2016).
116. Hodges, M. *et al.* Perspectives for a Better Understanding of the Metabolic Integration of Photorespiration within a Complex Plant Primary Metabolism Network. *Journal of Experimental Botany* **67**, 3015–3026 (2016).
117. Rachmilevitch, S., Cousins, A. B. & Bloom, A. J. Nitrate Assimilation in Plant Shoots Depends on Photorespiration. *Proceedings of the National Academy of Sciences of the United States of America* **101**, 11506–11510. pmid: 15272076 (2004).
118. Bloom, A. J. Photorespiration and Nitrate Assimilation: A Major Intersection between Plant Carbon and Nitrogen. *Photosynthesis Research* **123**, 117–128. pmid: 25366830 (2015).

-
119. Tcherkez, G. *et al.* Respiratory Metabolism of Illuminated Leaves Depends on CO₂ and O₂ Conditions. *Proceedings of the National Academy of Sciences* **105**, 797–802 (2008).
 120. Kelly, G. J. & Latzko, E. Inhibition of Spinach-Leaf Phosphofructokinase by 2-Phosphoglycollate. *FEBS letters* **68**, 55–58. pmid: 134908 (1976).
 121. Bobik, K. & Burch-Smith, T. M. Chloroplast Signaling within, between and beyond Cells. *Frontiers in Plant Science* **6** (2015).
 122. Schumann, U. *et al.* Requirement of the C3HC4 Zinc RING Finger of the Arabidopsis PEX10 for Photorespiration and Leaf Peroxisome Contact with Chloroplasts. *Proceedings of the National Academy of Sciences of the United States of America* **104**, 1069–1074. pmid: 17215364 (2007).
 123. Kriechbaumer, V. *et al.* Reticulomics: Protein-Protein Interaction Studies with Two Plasmodesmata-Localized Reticulon Family Proteins Identify Binding Partners Enriched at Plasmodesmata, Endoplasmic Reticulum, and the Plasma Membrane. *Plant Physiology* **169**, 1933–1945. pmid: 26353761 (2015).
 124. Kim, D. I. *et al.* Probing Nuclear Pore Complex Architecture with Proximity-Dependent Biotinylation. *Proceedings of the National Academy of Sciences of the United States of America* **111**, E2453–2461. pmid: 24927568 (2014).
 125. Arora, D. *et al.* Establishment of Proximity-Dependent Biotinylation Approaches in Different Plant Model Systems. *The Plant Cell* **32**, 3388–3407 (2020).
 126. Müller, S. J., Hoernstein, S. N. W. & Reski, R. Approaches to Characterize Organelle, Compartment, or Structure Purity. *Methods in Molecular Biology (Clifton, N.J.)* **1511**, 13–28. pmid: 27730599 (2017).
 127. Senkler, J. *et al.* The Mitochondrial Complexome of Arabidopsis Thaliana. *The Plant Journal: For Cell and Molecular Biology* **89**, 1079–1092. pmid: 27943495 (2017).
 128. Rugen, N. *et al.* Protein Interaction Patterns in Arabidopsis Thaliana Leaf Mitochondria Change in Dependence to Light. *Biochimica et Biophysica Acta (BBA) - Bioenergetics* **1862**, 148443 (2021).
 129. Peterhansel, C. *et al.* Photorespiration. *The Arabidopsis Book / American Society of Plant Biologists* **8**, e0130. pmid: 22303256 (2010).
 130. Roux, K. J., Kim, D. I., Raida, M. & Burke, B. A Promiscuous Biotin Ligase Fusion Protein Identifies Proximal and Interacting Proteins in Mammalian Cells. *Journal of Cell Biology* **196**, 801–810 (2012).
 131. Choi-Rhee, E., Schulman, H. & Cronan, J. E. Promiscuous Protein Biotinylation by Escherichia Coli Biotin Protein Ligase. *Protein Science: A Publication of the Protein Society* **13**, 3043–3050. pmid: 15459338 (2004).

BIBLIOGRAPHY

132. Rhee, H.-W. *et al.* Proteomic Mapping of Mitochondria in Living Cells via Spatially Restricted Enzymatic Tagging. *Science (New York, N.Y.)* **339**, 1328–1331. pmid: 23371551 (2013).
133. Lam, S. S. *et al.* Directed Evolution of APEX2 for Electron Microscopy and Proximity Labeling. *Nature Methods* **12**, 51–54 (1 2015).
134. Jing, J. *et al.* Proteomic Mapping of ER-PM Junctions Identifies STIMATE as Regulator of Ca²⁺ Influx. *Nature cell biology* **17**, 1339–1347. pmid: 26322679 (2015).
135. Van Vliet, A. R. *et al.* The ER Stress Sensor PERK Coordinates ER-Plasma Membrane Contact Site Formation through Interaction with Filamin-A and F-Actin Remodeling. *Molecular Cell* **65**, 885–899.e6. pmid: 28238652 (2017).
136. Han, Y. *et al.* Directed Evolution of Split APEX2 Peroxidase. *ACS Chemical Biology* **14**, 619–635 (2019).
137. De Munter, S. *et al.* Split-BioID: A Proximity Biotinylation Assay for Dimerization-Dependent Protein Interactions. *FEBS letters* **591**, 415–424. pmid: 28032891 (2017).
138. Lin, Q. *et al.* Screening of Proximal and Interacting Proteins in Rice Protoplasts by Proximity-Dependent Biotinylation. *Frontiers in Plant Science* **8**, 749. pmid: 28553299 (2017).
139. Khan, M., Youn, J.-Y., Gingras, A.-C., Subramaniam, R. & Desveaux, D. In Planta Proximity Dependent Biotin Identification (BioID). *Scientific Reports* **8**, 9212 (1 2018).
140. Kim, D. I. *et al.* An Improved Smaller Biotin Ligase for BioID Proximity Labeling. *Molecular Biology of the Cell* **27**, 1188–1196. pmid: 26912792 (2016).
141. Branon, T. C. *et al.* Efficient Proximity Labeling in Living Cells and Organisms with TurboID. *Nature Biotechnology* **36**, 880–887. pmid: 30125270 (2018).
142. Kim, T.-W. *et al.* Application of TurboID-mediated Proximity Labeling for Mapping a GSK3 Kinase Signaling Network in Arabidopsis, 636324 (2019).
143. Mair, A., Xu, S.-L., Branon, T. C., Ting, A. Y. & Bergmann, D. C. Proximity Labeling of Protein Complexes and Cell-Type-Specific Organellar Proteomes in Arabidopsis Enabled by TurboID. *eLife* **8** (eds Menke, F. L. & Hardtke, C. S.) e47864 (2019).
144. Zhang, Y. *et al.* TurboID-Based Proximity Labeling for In Planta Identification of Protein-Protein Interaction Networks. *Journal of Visualized Experiments: JoVE*. pmid: 32478742 (2020).
145. Valm, A. M. *et al.* Applying Systems-Level Spectral Imaging and Analysis to Reveal the Organelle Interactome. *Nature* **546**, 162–167 (7656 2017).
146. Chang, C.-L. *et al.* Feedback Regulation of Receptor-Induced Ca²⁺ Signaling Mediated by E-Syt1 and Nir2 at Endoplasmic Reticulum-Plasma Membrane Junctions. *Cell Reports* **5**, 813–825. pmid: 24183667 (2013).

-
147. Sigal, Y. M., Zhou, R. & Zhuang, X. Visualizing and Discovering Cellular Structures with Super-Resolution Microscopy. *Science* **361**, 880–887 (2018).
 148. Knox, K. *et al.* Putting the Squeeze on Plasmodesmata: A Role for Reticulons in Primary Plasmodesmata Formation. *Plant Physiology* **168**, 1563–1572 (2015).
 149. Modi, S. *et al.* Miro Clusters Regulate ER-mitochondria Contact Sites and Link Cristae Organization to the Mitochondrial Transport Machinery. *Nature Communications* **10**, 4399 (1 2019).
 150. Xing, S., Wallmeroth, N., Berendzen, K. W. & Grefen, C. Techniques for the Analysis of Protein-Protein Interactions in Vivo. *Plant Physiology* **171**, 727–758 (2016).
 151. Cieri, D. *et al.* SPLICS: A Split Green Fluorescent Protein-Based Contact Site Sensor for Narrow and Wide Heterotypic Organelle Juxtaposition. *Cell Death & Differentiation* **25**, 1131–1145 (6 2018).
 152. Li, T. *et al.* A Combinatorial Reporter Set to Visualize the Membrane Contact Sites Between Endoplasmic Reticulum and Other Organelles in Plant Cell. *Frontiers in Plant Science* **11**, 1280. pmid: 32973839 (2020).
 153. Harmon, M., Larkman, P., Hardingham, G., Jackson, M. & Skehel, P. A Bi-fluorescence Complementation System to Detect Associations between the Endoplasmic Reticulum and Mitochondria. *Scientific Reports* **7**, 17467. pmid: 29234100 (2017).
 154. Shai, N. *et al.* Systematic Mapping of Contact Sites Reveals Tethers and a Function for the Peroxisome-Mitochondria Contact. *Nature Communications* **9**, 1761 (1 2018).
 155. Tao, K., Waletich, J. R., Wise, H., Arredondo, F. & Tyler, B. M. Tethering of Multi-Vesicular Bodies and the Tonoplast to the Plasma Membrane in Plants. *Frontiers in Plant Science* **10**, 636 (2019).
 156. Naon, D. *et al.* Critical Reappraisal Confirms That Mitofusin 2 Is an Endoplasmic Reticulum-Mitochondria Tether. *Proceedings of the National Academy of Sciences* **113**, 11249–11254. pmid: 27647893 (2016).
 157. Venditti, R. *et al.* Molecular Determinants of ER–Golgi Contacts Identified through a New FRET–FLIM System. *Journal of Cell Biology* **218**, 1055–1065 (2019).
 158. Kerppola, T. K. Complementary Methods for Studies of Protein Interactions in Living Cells. *Nature methods* **3**, 969–971. pmid: 17117150 (2006).
 159. Hu, C.-D., Chinenov, Y. & Kerppola, T. K. Visualization of Interactions among bZIP and Rel Family Proteins in Living Cells Using Bimolecular Fluorescence Complementation. *Molecular Cell* **9**, 789–798 (2002).
 160. Grefen, C. & Blatt, M. R. A 2in1 Cloning System Enables Ratiometric Bimolecular Fluorescence Complementation (rBiFC). *BioTechniques* **53**, 311–314 (2012).

BIBLIOGRAPHY

161. Magliery, T. J. *et al.* Detecting Protein - Protein Interactions with a Green Fluorescent Protein Fragment Reassembly Trap: Scope and Mechanism. *Journal of the American Chemical Society* **127**, 146–157 (2005).
162. Ghosh, I., Hamilton, A. D. & Regan, L. Antiparallel Leucine Zipper-Directed Protein Reassembly: Application to the Green Fluorescent Protein. *Journal of the American Chemical Society* **122**, 5658–5659 (2000).
163. Landschulz, W. H., Johnson, P. F. & McKnight, S. L. The Leucine Zipper: A Hypothetical Structure Common to a New Class of DNA Binding Proteins. *Science* **240**, 1759–1764 (1988).
164. Kodama, Y. & Hu, C.-D. Bimolecular Fluorescence Complementation (BiFC): A 5-Year Update and Future Perspectives. *BioTechniques* **53**, 285–298 (2012).
165. Zamyatnin Jr, A. A. *et al.* Assessment of the Integral Membrane Protein Topology in Living Cells. *The Plant Journal* **46**, 145–154 (2006).
166. Cabantous, S., Terwilliger, T. C. & Waldo, G. S. Protein Tagging and Detection with Engineered Self-Assembling Fragments of Green Fluorescent Protein. *Nature Biotechnology* **23**, 102–107 (2005).
167. Miyawaki, A., Griesbeck, O., Heim, R. & Tsien, R. Y. Dynamic and Quantitative Ca²⁺ Measurements Using Improved Cameleons. *Proceedings of the National Academy of Sciences of the United States of America* **96**, 2135–2140. pmid: 10051607 (1999).
168. Campbell, R. E. *et al.* A Monomeric Red Fluorescent Protein. *Proceedings of the National Academy of Sciences of the United States of America* **99**, 7877–7882. pmid: 12060735 (2002).
169. Kakimoto, Y. *et al.* Visualizing Multiple Inter-Organelle Contact Sites Using the Organelle-Targeted Split-GFP System. *Scientific Reports* **8**, 6175 (1 2018).
170. Böckler, S. & Westermann, B. Mitochondrial ER Contacts Are Crucial for Mitophagy in Yeast. *Developmental Cell* **28**, 450–458 (2014).
171. Zhang, Y. *et al.* Nanoscale Subcellular Architecture Revealed by Multicolor Three-Dimensional Salvaged Fluorescence Imaging. *Nature Methods* **17**, 225–231 (2 2020).
172. Yang, Z., Zhao, X., Xu, J., Shang, W. & Tong, C. A Novel Fluorescent Reporter Detects Plastic Remodeling of Mitochondria–ER Contact Sites. *Journal of Cell Science* **131** (2018).
173. Tebo, A. G. & Gautier, A. A Split Fluorescent Reporter with Rapid and Reversible Complementation. *Nature Communications* **10**, 2822 (1 2019).
174. Bajar, B. T., Wang, E. S., Zhang, S., Lin, M. Z. & Chu, J. A Guide to Fluorescent Protein FRET Pairs. *Sensors* **16**, 1488 (9 2016).

-
175. Forster, Th. Energiewanderung und Fluoreszenz. *Naturwissenschaften* **33**, 166–175 (1946).
176. Algar, W. R., Hildebrandt, N., Vogel, S. S. & Medintz, I. L. FRET as a Biomolecular Research Tool — Understanding Its Potential While Avoiding Pitfalls. *Nature Methods* **16**, 815–829 (9 2019).
177. Hecker, A. *et al.* Binary 2in1 Vectors Improve in Planta (Co)Localization and Dynamic Protein Interaction Studies. *Plant Physiology* **168**, 776–787 (2015).
178. Bücherl, C. A., Bader, A., Westphal, A. H., Laptенок, S. P. & Borst, J. W. FRET-FLIM Applications in Plant Systems. *Protoplasma* **251**, 383–394 (2014).
179. Becker, W. *The Bh TCSPC Handbook* (Becker & Hickl GmbH, 2014).
180. Osterrieder, A. *et al.* Fluorescence Lifetime Imaging of Interactions between Golgi Tethering Factors and Small GTPases in Plants. *Traffic* **10**, 1034–1046 (2009).
181. Naon, D. *et al.* Critical Reappraisal Confirms That Mitofusin 2 Is an Endoplasmic Reticulum–Mitochondria Tether. *Proceedings of the National Academy of Sciences* **113**, 11249–11254 (2016).
182. Várnai, P., Tóth, B., Tóth, D. J., Hunyady, L. & Balla, T. Visualization and Manipulation of Plasma Membrane-Endoplasmic Reticulum Contact Sites Indicates the Presence of Additional Molecular Components within the STIM1-Orai1 Complex. *Journal of Biological Chemistry* (2007).
183. Alford, S. C., Ding, Y., Simmen, T. & Campbell, R. E. Dimerization-Dependent Green and Yellow Fluorescent Proteins. *ACS synthetic biology* **1**, 569–575. pmid: 23656278 (2012).
184. De Chaumont, F. *et al.* Icy: An Open Bioimage Informatics Platform for Extended Reproducible Research. *Nature Methods* **9**, 690–696 (7 2012).
185. Pound, M. P. *et al.* RootNav: Navigating Images of Complex Root Architectures. *Plant Physiology* **162**, 1802–1814 (2013).
186. Nelson, B. K., Cai, X. & Nebenführ, A. A Multicolored Set of in Vivo Organelle Markers for Co-Localization Studies in Arabidopsis and Other Plants. *The Plant Journal* **51**, 1126–1136 (2007).
187. Murashige, T. & Skoog, F. A Revised Medium for Rapid Growth and Bioassays with Tobacco Tissue Cultures. *Physiol. Plant.*, 473–97 (1962).
188. Clough, S. J. & Bent, A. F. Floral Dip: A Simplified Method for Agrobacterium -Mediated Transformation of Arabidopsis Thaliana. *The Plant Journal* **16**, 735–743 (1998).
189. Nietzel, T. *Mitochondrial Regulation through Thiol-Switching in Plants (Thesis)*, Universitäts-und Landesbibliothek Bonn, 2017.

BIBLIOGRAPHY

190. Schindelin, J. *et al.* Fiji: An Open-Source Platform for Biological-Image Analysis. *Nature Methods* **9**, 676–682 (7 2012).
191. Rueden, C. T. *et al.* ImageJ2: ImageJ for the next Generation of Scientific Image Data. *BMC Bioinformatics* **18**, 529 (2017).
192. Wagner, S. *et al.* The EF-Hand Ca²⁺ Binding Protein MICU Choreographs Mitochondrial Ca²⁺ Dynamics in Arabidopsis[OPEN]. *The Plant Cell* **27**, 3190–3212. pmid: 26530087 (2015).
193. Li, F., Chung, T. & Vierstra, R. D. AUTOPHAGY-RELATED11 Plays a Critical Role in General Autophagy- and Senescence-Induced Mitophagy in Arabidopsis. *The Plant Cell* **26**, 788–807. pmid: 24563201 (2014).
194. Richter, A. S., Tohge, T., Fernie, A. R. & Grimm, B. The Genomes Uncoupled-Dependent Signalling Pathway Coordinates Plastid Biogenesis with the Synthesis of Anthocyanins. *Philosophical Transactions of the Royal Society B: Biological Sciences* **375**, 20190403 (2020).
195. Lohmann, A. *et al.* Deficiency in Phylloquinone (Vitamin K1) Methylation Affects Prenyl Quinone Distribution, Photosystem I Abundance, and Anthocyanin Accumulation in the Arabidopsis AtmenG Mutant. *Journal of Biological Chemistry* **281**, 40461–40472. pmid: 17082184 (2006).
196. Lotkowska, M. E. *et al.* The Arabidopsis Transcription Factor MYB112 Promotes Anthocyanin Formation during Salinity and under High Light Stress1[OPEN]. *Plant Physiology* **169**, 1862–1880. pmid: 26378103 (2015).
197. GmbH, H. W. *JUNIOR-PAM, Teaching Chlorophyll Fluorometer, Manual* 2nd ed. (Heinz Walz GmbH, 2020).
198. Kühn, K. *et al.* Complete Mitochondrial Complex I Deficiency Induces an Up-Regulation of Respiratory Fluxes That Is Abolished by Traces of Functional Complex I. *Plant Physiology* **168**, 1537–1549. pmid: 26134164 (2015).
199. Sew, Y. S. *et al.* Multiplex Micro-Respiratory Measurements of Arabidopsis Tissues. *New Phytologist* **200**, 922–932 (2013).
200. Ugalde, J.-M. *et al.* Phosphatidylinositol 4-Phosphate 5-Kinases 1 and 2 Are Involved in the Regulation of Vacuole Morphology during Arabidopsis Thaliana Pollen Development. *Plant Science: An International Journal of Experimental Plant Biology* **250**, 10–19. pmid: 27457979 (2016).
201. Peterson, R., Slovin, J. P. & Chen, C. A Simplified Method for Differential Staining of Aborted and Non-Aborted Pollen Grains. *International Journal of Plant Biology* **1**, e13–e13 (2 2010).

-
202. Lazo, G. R., Stein, P. A. & Ludwig, R. A. A DNA Transformation–Competent Arabidopsis Genomic Library in Agrobacterium. *Bio/Technology* **9**, 963–967 (10 1991).
 203. Bertani, G. STUDIES ON LYSOGENESIS I: The Mode of Phage Liberation by Lysogenic Escherichia Coli. *Journal of Bacteriology* **62**, 293–300 (1951).
 204. Edwards, K., Johnstone, C. & Thompson, C. A Simple and Rapid Method for the Preparation of Plant Genomic DNA for PCR Analysis. *Nucleic Acids Research* **19**, 1349. pmid: 2030957 (1991).
 205. Hu, W. & Lagarias, J. C. A One-Tube Method for Rapid and Reliable Plant Genomic DNA Isolation for PCR Analysis, 2020.02.13.948455 (2020).
 206. Lampropoulos, A. *et al.* GreenGate - A Novel, Versatile, and Efficient Cloning System for Plant Transgenesis. *PLOS ONE* **8**, e83043 (2013).
 207. Schürholz, A.-K. *et al.* A Comprehensive Toolkit for Inducible, Cell Type-Specific Gene Expression in Arabidopsis. *Plant Physiology* **178**, 40–53 (2018).
 208. Xie, W., Nielsen, M. E., Pedersen, C. & Thordal-Christensen, H. A Split-GFP Gateway Cloning System for Topology Analyses of Membrane Proteins in Plants. *PLOS ONE* **12**, e0170118 (2017).
 209. Lee, Y. J., Kim, D. H., Kim, Y. W. & Hwang, I. Identification of a Signal That Distinguishes between the Chloroplast Outer Envelope Membrane and the Endomembrane System in Vivo. *The Plant Cell* **13**, 2175–2190. pmid: 11595795 (2001).
 210. Duncan, O. *et al.* Multiple Lines of Evidence Localize Signaling, Morphology, and Lipid Biosynthesis Machinery to the Mitochondrial Outer Membrane of Arabidopsis. *Plant Physiology* **157**, 1093–1113 (2011).
 211. Marty, N. J. *et al.* New Insights into the Targeting of a Subset of Tail-Anchored Proteins to the Outer Mitochondrial Membrane. *Frontiers in Plant Science* **5**, 426. pmid: 25237314 (2014).
 212. Orth, T. *et al.* The PEROXIN11 Protein Family Controls Peroxisome Proliferation in Arabidopsis. *The Plant Cell* **19**, 333–350. pmid: 17220199 (2007).
 213. Prestele, J. *et al.* Different Functions of the C3HC4 Zinc RING Finger Peroxins PEX10, PEX2, and PEX12 in Peroxisome Formation and Matrix Protein Import. *Proceedings of the National Academy of Sciences of the United States of America* **107**, 14915–14920. pmid: 20679226 (2010).
 214. Oikawa, K. *et al.* Chloroplast Outer Envelope Protein CHUP1 Is Essential for Chloroplast Anchorage to the Plasma Membrane and Chloroplast Movement. *Plant Physiology* **148**, 829–842. pmid: 18715957 (2008).

BIBLIOGRAPHY

215. Gutensohn, M., Schulz, B., Nicolay, P. & Flügge, U.-I. Functional Analysis of the Two Arabidopsis Homologues of Toc34, a Component of the Chloroplast Protein Import Apparatus†. *The Plant Journal* **23**, 771–783 (2000).
216. Yamaoka, S. & Leaver, C. J. EMB2473/MIRO1, an Arabidopsis Miro GTPase, Is Required for Embryogenesis and Influences Mitochondrial Morphology in Pollen. *The Plant Cell* **20**, 589–601 (2008).
217. Mano, S. *et al.* Distribution and Characterization of Peroxisomes in Arabidopsis by Visualization with GFP: Dynamic Morphology and Actin-Dependent Movement. *Plant and Cell Physiology* **43**, 331–341 (2002).
218. Mathur, J., Mathur, N. & Hülskamp, M. Simultaneous Visualization of Peroxisomes and Cytoskeletal Elements Reveals Actin and Not Microtubule-Based Peroxisome Motility in Plants. *Plant Physiology* **128**, 1031–1045. pmid: 11891258 (2002).
219. Wada, M. & Suetsugu, N. Plant Organelle Positioning. *Current Opinion in Plant Biology* **7**, 626–631 (2004).
220. Higaki, T., Sano, T. & Hasezawa, S. Actin Microfilament Dynamics and Actin Side-Binding Proteins in Plants. *Current Opinion in Plant Biology. Cell Biology* **10**, 549–556 (2007).
221. Yang, W. *et al.* 2-Hydroxy-phytanoyl-CoA Lyase (AtHPCL) Is Involved in Phytol Metabolism in Arabidopsis. *The Plant Journal* **109**, 1290–1304 (2022).
222. Müller, S. J. *et al.* Quantitative Analysis of the Mitochondrial and Plastid Proteomes of the Moss *Physcomitrella Patens* Reveals Protein Macrocompartmentation and Microcompartmentation. *Plant Physiology* **164**, 2081–2095 (2014).
223. Wübben, A. *Suitability of Bimolecular Fluorescence Complementation (BiFC) for Monitoring Membrane Contact Sites (MCS) in Plants* (University Bonn (master thesis), 2021).
224. Roerdink, J. & Meijster, A. The Watershed Transform: Definitions, Algorithms and Parallelization Strategies. *FUNDINF: Fundamenta Informatica* **41** (2000).
225. Wu, S.-Z., Yamada, M., Mallett, D. R. & Bezanilla, M. Cytoskeletal Discoveries in the Plant Lineage Using the Moss *Physcomitrella Patens*. *Biophysical Reviews* **10**, 1683–1693 (2018).
226. Qiu, W., Park, J.-W. & Scholthof, H. B. Tombusvirus P19-mediated Suppression of Virus-Induced Gene Silencing Is Controlled by Genetic and Dosage Features That Influence Pathogenicity. *Molecular plant-microbe interactions: MPMI* **15**, 269–280. pmid: 11952130 (2002).
227. Perry, A. J., Hulett, J. M., Likić, V. A., Lithgow, T. & Gooley, P. R. Convergent Evolution of Receptors for Protein Import into Mitochondria. *Current Biology* **16**, 221–229 (2006).

-
228. Pérez-Sancho, J. *et al.* The Arabidopsis Synaptotagmin1 Is Enriched in Endoplasmic Reticulum-Plasma Membrane Contact Sites and Confers Cellular Resistance to Mechanical Stresses. *Plant Physiology* **168**, 132–143 (2015).
229. Moore, I., Gälweiler, L., Grosskopf, D., Schell, J. & Palme, K. A Transcription Activation System for Regulated Gene Expression in Transgenic Plants. *Proceedings of the National Academy of Sciences of the United States of America* **95**, 376–381. pmid: 9419383 (1998).
230. Craft, J. *et al.* New pOp/LhG4 Vectors for Stringent Glucocorticoid-Dependent Transgene Expression in Arabidopsis. *The Plant Journal* **41**, 899–918 (2005).
231. Samalova, M., Brzobohaty, B. & Moore, I. pOp6/LhGR: A Stringently Regulated and Highly Responsive Dexamethasone-Inducible Gene Expression System for Tobacco. *The Plant Journal* **41**, 919–935 (2005).
232. Picard, D. Steroid-Binding Domains for Regulating the Functions of Heterologous Proteins in Cis. *Trends in Cell Biology* **3**, 278–280 (1993).
233. Picard, D. Heat-Shock Protein 90, a Chaperone for Folding and Regulation. *Cellular and Molecular Life Sciences* **59**, 1640–1648 (2002).
234. Sasaki, Y. *et al.* Evidence for High Specificity and Efficiency of Multiple Recombination Signals in Mixed DNA Cloning by the Multisite Gateway System. *Journal of Biotechnology* **107**, 233–243 (2004).
235. Landy, A. Dynamic, Structural, and Regulatory Aspects of λ Site-Specific Recombination. *Annual Review of Biochemistry* **58**, 913–941. pmid: 2528323 (1989).
236. Hartley, J. L., Temple, G. F. & Brasch, M. A. DNA Cloning Using In Vitro Site-Specific Recombination. *Genome Research* **10**, 1788–1795. pmid: 11076863 (2000).
237. Bernard, P. Positive Selection of Recombinant DNA by CcdB. *BioTechniques* **21**, 320–323 (1996).
238. Schaaf, A., Reski, R. & Decker, E. L. A Novel Aspartic Proteinase Is Targeted to the Secretory Pathway and to the Vacuole in the Moss *Physcomitrella Patens*. *European Journal of Cell Biology* **83**, 145–152 (2004).
239. Graham, I. A. Seed Storage Oil Mobilization. *Annual Review of Plant Biology* **59**, 115–142. pmid: 18444898 (2008).
240. Penfield, S., Pinfield-Wells, H. & Graham, I. A. in *Annual Plant Reviews Volume 27: Seed Development, Dormancy and Germination* 133–152 (John Wiley & Sons, Ltd, 2007).
241. Schwarzländer, M., Fricker, M. D. & Sweetlove, L. J. Monitoring the in Vivo Redox State of Plant Mitochondria: Effect of Respiratory Inhibitors, Abiotic Stress and Assessment of Recovery from Oxidative Challenge. *Biochimica et Biophysica Acta (BBA) - Bioenergetics. Mitochondrial Physiology and Pathology* **1787**, 468–475 (2009).

BIBLIOGRAPHY

242. Qi, Y. C. *et al.* Overexpression of Glutathione S-transferase Gene Increases Salt Tolerance of Arabidopsis. *Russian Journal of Plant Physiology* **57**, 233–240 (2010).
243. Sharma, P., Jha, A. B., Dubey, R. S. & Pessarakli, M. Reactive Oxygen Species, Oxidative Damage, and Antioxidative Defense Mechanism in Plants under Stressful Conditions. *Journal of Botany* **2012**, 1–26 (2012).
244. Dourmap, C. *et al.* Stress Signalling Dynamics of the Mitochondrial Electron Transport Chain and Oxidative Phosphorylation System in Higher Plants. *Annals of Botany* **125**, 721–736 (2020).
245. Su, T., Li, W., Wang, P. & Ma, C. Dynamics of Peroxisome Homeostasis and Its Role in Stress Response and Signaling in Plants. *Frontiers in Plant Science* **10**, 705 (2019).
246. Kim, M. *et al.* mTERF18 and ATAD3 Are Required for Mitochondrial Nucleoid Structure and Their Disruption Confers Heat Tolerance in Arabidopsis Thaliana. *New Phytologist* **232**, 2026–2042 (2021).
247. Garcia-Molina, A. *et al.* Translational Components Contribute to Acclimation Responses to High Light, Heat, and Cold in Arabidopsis. *iScience* **23**. pmid: 32679545 (2020).
248. Zirngibl, M.-E. *et al.* Triosephosphate Export from Chloroplasts and Cellular Sugar Content Regulate Anthocyanin Biosynthesis during High Light Acclimation. *Plant Communications*, 100423 (2022).
249. Oikawa, K., Midorikawa, K., Kodama, Y. & Numata, K. A High-Throughput Quantitative Method to Evaluate Peroxisome-Chloroplast Interactions in Arabidopsis Thaliana. *Frontiers in Plant Science* **13** (2022).
250. Arimura, S.-i., Yamamoto, J., Aida, G. P., Nakazono, M. & Tsutsumi, N. Frequent Fusion and Fission of Plant Mitochondria with Unequal Nucleoid Distribution. *Proceedings of the National Academy of Sciences* **101**, 7805–7808 (2004).
251. Amack, S. C. & Antunes, M. S. CaMV35S Promoter – A Plant Biology and Biotechnology Workhorse in the Era of Synthetic Biology. *Current Plant Biology* **24**, 100179 (2020).
252. Schmidt, C. *et al.* Mechanisms of Proinflammatory Cytokine-Induced Biphasic NF- κ B Activation. *Molecular Cell* **12**, 1287–1300 (2003).
253. Guo, Y., Rebecchi, M. & Scarlata, S. Phospholipase C β 2 Binds to and Inhibits Phospholipase C δ 1*. *Journal of Biological Chemistry* **280**, 1438–1447. pmid: 15509571 (2005).
254. Anderie, I. & Schmid, A. In Vivo Visualization of Actin Dynamics and Actin Interactions by BiFC. *Cell Biology International* **31**, 1131–1135 (2007).
255. Bao, F. *et al.* Arabidopsis HSP90 Protein Modulates RPP4-mediated Temperature-Dependent Cell Death and Defense Responses. *New Phytologist* **202**, 1320–1334 (2014).

-
256. Choi, J., Chen, J., Schreiber, S. L. & Clardy, J. Structure of the FKBP12-Rapamycin Complex Interacting with Binding Domain of Human FRAP. *Science* **273**, 239–242 (1996).
257. Inoue, T., Heo, W. D., Grimley, J. S., Wandless, T. J. & Meyer, T. An Inducible Translocation Strategy to Rapidly Activate and Inhibit Small GTPase Signaling Pathways. *Nature methods* **2**, 415–418. pmid: 15908919 (2005).
258. Rosenfeldt, G., Viana, R. M., Mootz, H. D., von Arnim, A. G. & Batschauer, A. Chemically Induced and Light-Independent Cryptochrome Photoreceptor Activation. *Molecular Plant* **1**, 4–14 (2008).
259. Li, J.-F., Bush, J., Xiong, Y., Li, L. & McCormack, M. Large-Scale Protein-Protein Interaction Analysis in Arabidopsis Mesophyll Protoplasts by Split Firefly Luciferase Complementation. *PLOS ONE* **6**, e27364 (2011).
260. Winkler, J. *et al.* Visualizing Protein-Protein Interactions in Plants by Rapamycin-Dependent Delocalization. *The Plant cell* **33**, 1101–1117. pmid: 33793859 (2021).
261. Pain, C., Kriechbaumer, V., Kittelmann, M., Hawes, C. & Fricker, M. Quantitative Analysis of Plant ER Architecture and Dynamics. *Nature Communications* **10**, 984 (1 2019).
262. Schattat, M., Barton, K., Baudisch, B., Klösgen, R. B. & Mathur, J. Plastid Stroma Branching Coincides with Contiguous Endoplasmic Reticulum Dynamics. *Plant Physiology* **155**, 1667–1677 (2011).
263. Pan, R., Liu, J., Wang, S. & Hu, J. Peroxisomes: Versatile Organelles with Diverse Roles in Plants. *New Phytologist* **225**, 1410–1427 (2020).
264. Broda, M., Millar, A. H. & Van Aken, O. Mitophagy: A Mechanism for Plant Growth and Survival. *Trends in Plant Science* **23**, 434–450 (2018).
265. Scott, I. & Logan, D. C. Mitochondrial Morphology Transition Is an Early Indicator of Subsequent Cell Death in Arabidopsis. *New Phytologist* **177**, 90–101 (2008).
266. Shibata, M. *et al.* Highly Oxidized Peroxisomes Are Selectively Degraded via Autophagy in Arabidopsis. *The Plant Cell* **25**, 4967–4983 (2013).
267. Timm, S. *et al.* Glycine Decarboxylase Controls Photosynthesis and Plant Growth. *FEBS Letters* **586**, 3692–3697 (2012).
268. Timm, S. *et al.* Mitochondrial Dihydrolipoyl Dehydrogenase Activity Shapes Photosynthesis and Photorespiration of Arabidopsis Thaliana. *The Plant Cell* **27**, 1968–1984 (2015).
269. Simkin, A. J. *et al.* Simultaneous Stimulation of Sedoheptulose 1,7-bisphosphatase, Fructose 1,6-bisphosphate Aldolase and the Photorespiratory Glycine decarboxylase-H Protein Increases CO₂ Assimilation, Vegetative Biomass and Seed Yield in Arabidopsis. *Plant Biotechnology Journal* **15**, 805–816. pmid: 27936496 (2017).

BIBLIOGRAPHY

270. López-Calcano, P. E. *et al.* Overexpressing the H-protein of the Glycine Cleavage System Increases Biomass Yield in Glasshouse and Field-grown Transgenic Tobacco Plants. *Plant Biotechnology Journal* **17**, 141–151. pmid: 29851213 (2019).
271. South, P. F., Cavanagh, A. P., Lopez-Calcano, P. E., Raines, C. A. & Ort, D. R. Optimizing Photorespiration for Improved Crop Productivity. *Journal of Integrative Plant Biology* **60**, 1217–1230 (2018).
272. Kühn, K. *et al.* Phage-Type RNA Polymerase RPOTmp Performs Gene-Specific Transcription in Mitochondria of Arabidopsis Thaliana. *The Plant Cell* **21**, 2762–2779. pmid: 19783760 (2009).
273. Kühn, K. *et al.* Decreasing Electron Flux through the Cytochrome and/or Alternative Respiratory Pathways Triggers Common and Distinct Cellular Responses Dependent on Growth Conditions. *Plant physiology* **167** (2014).
274. Eastmond, P. J. SUGAR-DEPENDENT1 Encodes a Patatin Domain Triacylglycerol Lipase That Initiates Storage Oil Breakdown in Germinating Arabidopsis Seeds. *The Plant Cell* **18**, 665–675. pmid: 16473965 (2006).
275. Fujimoto, M. *et al.* Arabidopsis Dynamin-Related Proteins DRP3A and DRP3B Are Functionally Redundant in Mitochondrial Fission, but Have Distinct Roles in Peroxisomal Fission. *The Plant Journal: For Cell and Molecular Biology* **58**, 388–400. pmid: 19144001 (2009).
276. Mano, S., Nakamori, C., Kondo, M., Hayashi, M. & Nishimura, M. An Arabidopsis Dynamin-Related Protein, DRP3A, Controls Both Peroxisomal and Mitochondrial Division. *The Plant Journal: For Cell and Molecular Biology* **38**, 487–498. pmid: 15086806 (2004).
277. Zhang, X.-C. & Hu, J.-P. FISSION1A and FISSION1B Proteins Mediate the Fission of Peroxisomes and Mitochondria in Arabidopsis. *Molecular Plant* **1**, 1036–1047 (2008).
278. Zhang, X. & Hu, J. Two Small Protein Families, DYNAMIN-RELATED PROTEIN3 and FISSION1, Are Required for Peroxisome Fission in Arabidopsis. *The Plant Journal* **57**, 146–159 (2009).
279. Arimura, S.-i. *et al.* Arabidopsis ELONGATED MITOCHONDRIA1 Is Required for Localization of DYNAMIN-RELATED PROTEIN3A to Mitochondrial Fission Sites. *The Plant Cell* **20**, 1555–1566 (2008).
280. Zhang, X. & Hu, J. The Arabidopsis Chloroplast Division Protein DYNAMIN-RELATED PROTEIN5B Also Mediates Peroxisome Division. *The Plant Cell* **22**, 431–442 (2010).
281. Arimura, S.-i., Aida, G. P., Fujimoto, M., Nakazono, M. & Tsutsumi, N. Arabidopsis Dynamin-like Protein 2a (ADL2a), like ADL2b, Is Involved in Plant Mitochondrial Division. *Plant & Cell Physiology* **45**, 236–242. pmid: 14988495 (2004).

-
282. Arimura, S.-i. & Tsutsumi, N. A Dynamin-like Protein (ADL2b), Rather than FtsZ, Is Involved in Arabidopsis Mitochondrial Division. *Proceedings of the National Academy of Sciences of the United States of America* **99**, 5727–5731. pmid: 11960028 (2002).
283. Logan, D. C., Scott, I. & Tobin, A. K. ADL2a, like ADL2b, Is Involved in the Control of Higher Plant Mitochondrial Morphology. *Journal of Experimental Botany* **55**, 783–785. pmid: 14754924 (2004).
284. Scott, I., Tobin, A. K. & Logan, D. C. BIGYIN, an Orthologue of Human and Yeast FIS1 Genes Functions in the Control of Mitochondrial Size and Number in Arabidopsis Thaliana. *Journal of Experimental Botany* **57**, 1275–1280. pmid: 16510519 (2006).
285. Aung, K. & Hu, J. The Arabidopsis Tail-Anchored Protein PEROXISOMAL AND MITOCHONDRIAL DIVISION FACTOR1 Is Involved in the Morphogenesis and Proliferation of Peroxisomes and Mitochondria. *The Plant Cell* **23**, 4446–4461 (2011).
286. Pan, R. & Hu, J. The Conserved Fission Complex on Peroxisomes and Mitochondria. *Plant Signaling & Behavior* **6**, 870–872. pmid: 21617372 (2011).
287. Arimura, S.-i., Kurisu, R., Sugaya, H., Kadoya, N. & Tsutsumi, N. Cold Treatment Induces Transient Mitochondrial Fragmentation in Arabidopsis Thaliana in a Way That Requires DRP3A but Not ELM1 or an ELM1-Like Homologue, ELM2. *International Journal of Molecular Sciences* **18**, 2161 (10 2017).
288. Arimura, S.-i. Fission and Fusion of Plant Mitochondria, and Genome Maintenance. *Plant Physiology* **176**, 152–161 (2018).
289. Liu, Y. & Bassham, D. C. Autophagy: Pathways for Self-Eating in Plant Cells. *Annual Review of Plant Biology* **63**, 215–237. pmid: 22242963 (2012).
290. Avila-Ospina, L., Moison, M., Yoshimoto, K. & Masclaux-Daubresse, C. Autophagy, Plant Senescence, and Nutrient Recycling. *Journal of Experimental Botany* **65**, 3799–3811 (2014).
291. Wada, S. *et al.* Autophagy Plays a Role in Chloroplast Degradation during Senescence in Individually Darkened Leaves. *Plant Physiology* **149**, 885–893 (2009).
292. Sakuraba, Y. *et al.* Delayed Degradation of Chlorophylls and Photosynthetic Proteins in Arabidopsis Autophagy Mutants during Stress-Induced Leaf Yellowing. *Journal of Experimental Botany* **65**, 3915–3925 (2014).
293. Yoshimoto, K. *et al.* Organ-Specific Quality Control of Plant Peroxisomes Is Mediated by Autophagy. *Journal of Cell Science* **127**, 1161–1168 (2014).
294. Xiong, Y., Contento, A. L. & Bassham, D. C. AtATG18a Is Required for the Formation of Autophagosomes during Nutrient Stress and Senescence in Arabidopsis Thaliana. *The Plant Journal* **42**, 535–546 (2005).

BIBLIOGRAPHY

295. Olmedilla, A. & Sandalio, L. M. Selective Autophagy of Peroxisomes in Plants: From Housekeeping to Development and Stress Responses. *Frontiers in Plant Science* **10** (2019).
296. Catanzaro, M., Kobayashi, S., Gerdes, M. & Liang, Q. Mitochondrial Fragmentation and Mitophagy Contribute to Doxorubicin-induced Cardiomyocyte Death. *The FASEB Journal* **29**, 1036.12 (2015).
297. Contento, A. L., Xiong, Y. & Bassham, D. C. Visualization of Autophagy in Arabidopsis Using the Fluorescent Dye Monodansylcadaverine and a GFP-AtATG8e Fusion Protein. *The Plant Journal* **42**, 598–608 (2005).
298. Raines, C. A. Transgenic Approaches to Manipulate the Environmental Responses of the C3 Carbon Fixation Cycle. *Plant, Cell & Environment* **29**, 331–339 (2006).
299. Maurino, V. G. Using Energy-Efficient Synthetic Biochemical Pathways to Bypass Photorespiration. *Biochemical Society Transactions* **47**, 1805–1813 (2019).
300. Maier, A. *et al.* Transgenic Introduction of a Glycolate Oxidative Cycle into A. Thaliana Chloroplasts Leads to Growth Improvement. *Frontiers in Plant Science* **3** (2012).
301. South, P. F., Cavanagh, A. P., Liu, H. W. & Ort, D. R. Synthetic Glycolate Metabolism Pathways Stimulate Crop Growth and Productivity in the Field. *Science* **363**, eaat9077 (2019).
302. Dalal, J. *et al.* A Photorespiratory Bypass Increases Plant Growth and Seed Yield in Biofuel Crop Camelina Sativa. *Biotechnology for Biofuels* **8**, 175 (2015).
303. Shen, B.-R. *et al.* Engineering a New Chloroplastic Photorespiratory Bypass to Increase Photosynthetic Efficiency and Productivity in Rice. *Molecular Plant* **12**, 199–214 (2019).
304. Timm, S. & Bauwe, H. The Variety of Photorespiratory Phenotypes – Employing the Current Status for Future Research Directions on Photorespiration. *Plant Biology* **15**, 737–747 (2013).
305. Renné, P. *et al.* The Arabidopsis Mutant Dct Is Deficient in the Plastidic Glutamate/Malate Translocator DiT2. *The Plant Journal: For Cell and Molecular Biology* **35**, 316–331. pmid: 12887583 (2003).
306. Pick, T. R. *et al.* PLGG1, a Plastidic Glycolate Glycerate Transporter, Is Required for Photorespiration and Defines a Unique Class of Metabolite Transporters. *Proceedings of the National Academy of Sciences of the United States of America* **110**, 3185–3190. pmid: 23382251 (2013).
307. South, P. F. *et al.* Bile Acid Sodium Symporter BASS6 Can Transport Glycolate and Is Involved in Photorespiratory Metabolism in *Arabidopsis Thaliana*. *The Plant Cell* **29**, 808–823 (2017).

-
308. Pan, R., Liu, J. & Hu, J. Peroxisomes in Plant Reproduction and Seed-Related Development. *Journal of Integrative Plant Biology* **61**, 784–802 (2019).
309. Hu, J. *et al.* Plant Peroxisomes: Biogenesis and Function. *The Plant Cell* **24**, 2279–2303. pmid: 22669882 (2012).
310. Rinaldi, M. A. *et al.* The Roles of β -Oxidation and Cofactor Homeostasis in Peroxisome Distribution and Function in Arabidopsis Thaliana. *Genetics* **204**, 1089–1115 (2016).
311. Kato, A., Hayashi, M., Takeuchi, Y. & Nishimura, M. cDNA Cloning and Expression of a Gene for 3-Ketoacyl-CoA Thiolase in Pumpkin Cotyledons. *Plant Molecular Biology* **31**, 843–852. pmid: 8806414 (1996).
312. Germain, V. *et al.* Requirement for 3-Ketoacyl-CoA Thiolase-2 in Peroxisome Development, Fatty Acid β -Oxidation and Breakdown of Triacylglycerol in Lipid Bodies of Arabidopsis Seedlings. *The Plant Journal* **28**, 1–12 (2001).
313. Mielecki, J., Gawroński, P. & Karpiński, S. Retrograde Signaling: Understanding the Communication between Organelles. *International Journal of Molecular Sciences* **21**, 6173. pmid: 32859110 (2020).
314. Suzuki, N., Koussevitzky, S., Mittler, R. & Miller, G. ROS and Redox Signalling in the Response of Plants to Abiotic Stress. *Plant, Cell & Environment* **35**, 259–270 (2012).
315. Shapiguzov, A. *et al.* Arabidopsis RCD1 Coordinates Chloroplast and Mitochondrial Functions through Interaction with ANAC Transcription Factors. *eLife* **8** (eds Hardtke, C. S. & Dietz, K.-J.) e43284 (2019).
316. Zheng, X.-T. *et al.* The Major Photoprotective Role of Anthocyanins in Leaves of Arabidopsis Thaliana under Long-Term High Light Treatment: Antioxidant or Light Attenuator? *Photosynthesis Research* **149**, 25–40 (2021).
317. Maier, A. *et al.* Light and the E3 Ubiquitin Ligase COP1/SPA Control the Protein Stability of the MYB Transcription Factors PAP1 and PAP2 Involved in Anthocyanin Accumulation in Arabidopsis. *The Plant Journal* **74**, 638–651 (2013).
318. Zhang, X., Abraham, C., Colquhoun, T. A. & Liu, C.-J. A Proteolytic Regulator Controlling Chalcone Synthase Stability and Flavonoid Biosynthesis in Arabidopsis. *The Plant Cell* **29**, 1157–1174 (2017).
319. Shi, M.-Z. & Xie, D.-Y. Biosynthesis and Metabolic Engineering of Anthocyanins in Arabidopsis Thaliana. *Recent Patents on Biotechnology* **8**, 47–60 (2014).
320. Mahmood, K., Xu, Z., El-Kereamy, A., Casaretto, J. A. & Rothstein, S. J. The Arabidopsis Transcription Factor ANAC032 Represses Anthocyanin Biosynthesis in Response to High Sucrose and Oxidative and Abiotic Stresses. *Frontiers in Plant Science* **7**, 1548. pmid: 27790239 (2016).

BIBLIOGRAPHY

321. Mahmood, K., El-Kereamy, A., Kim, S.-H., Nambara, E. & Rothstein, S. J. ANAC032 Positively Regulates Age-Dependent and Stress-Induced Senescence in *Arabidopsis Thaliana*. *Plant and Cell Physiology* **57**, 2029–2046 (2016).
322. Baena-González, E., Rolland, F., Thevelein, J. M. & Sheen, J. A Central Integrator of Transcription Networks in Plant Stress and Energy Signalling. *Nature* **448**, 938–942 (7156 2007).
323. Teng, S., Keurentjes, J., Bentsink, L., Koornneef, M. & Smeekens, S. Sucrose-Specific Induction of Anthocyanin Biosynthesis in Arabidopsis Requires the MYB75/PAP1 Gene. *Plant Physiology* **139**, 1840–1852 (2005).



Appendix



Supplemental information

Table S1: Size of chloroplasts of *P. patens* and *A. thaliana*. n = 4 from 4 different cells.

species	length [μm]	wide [μm]
<i>P. patens</i>	9.85	7.53
	7.76	5.66
	8.09	6.29
	6.41	4.90
<i>A. thaliana</i>	8.21	7.49
	8.72	7.22
	9.63	7.91
	10.86	8.87

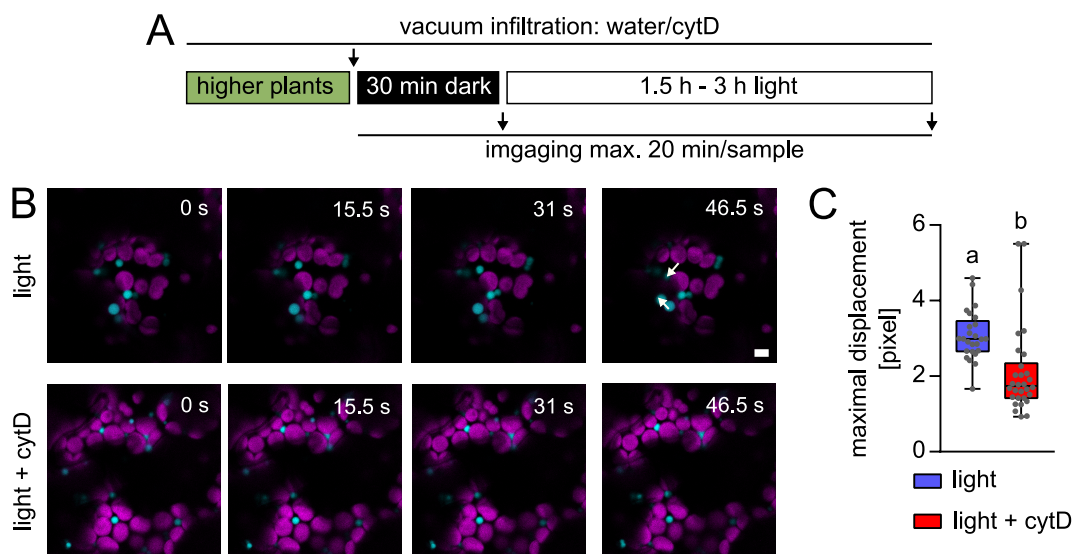


Figure S1: Movement analysis of peroxisomes using the cytoskeleton inhibitor cytD in *A. thaliana*.

A Experimental setup: light treatment was performed at $20 \mu\text{mol photons m}^{-2} \text{s}^{-1}$ for 1.5-3 h after a dark adaption. cytD ($20 \mu\text{M}$) was used to depolymerise the actin filament. Time series were recorded in 30 time stacks over 2 min. **B:** Representative CLSM time series of light (control) and light + cytD treated cells showing an overlay of chlorophyll autofluorescence (magenta) and a peroxisomal marker (cyan). px-ck [186] was used as *A. thaliana* peroxisomal CFP marker line. The arrows show examples of moving peroxisomes. **C:** Quantification of the peroxisomal movement in *A. thaliana*. The quantification process was performed using Icy [184]. The maximal peroxisomal displacement was detected in a time frame of 2 min. $n \geq 25$ in 5 or 3 cells for light or cytD, respectively. Data are shown as box plot Min to Max showing all points, whereby each point represents individual peroxisomes. Significant differences were calculated according to an unpaired t-test.

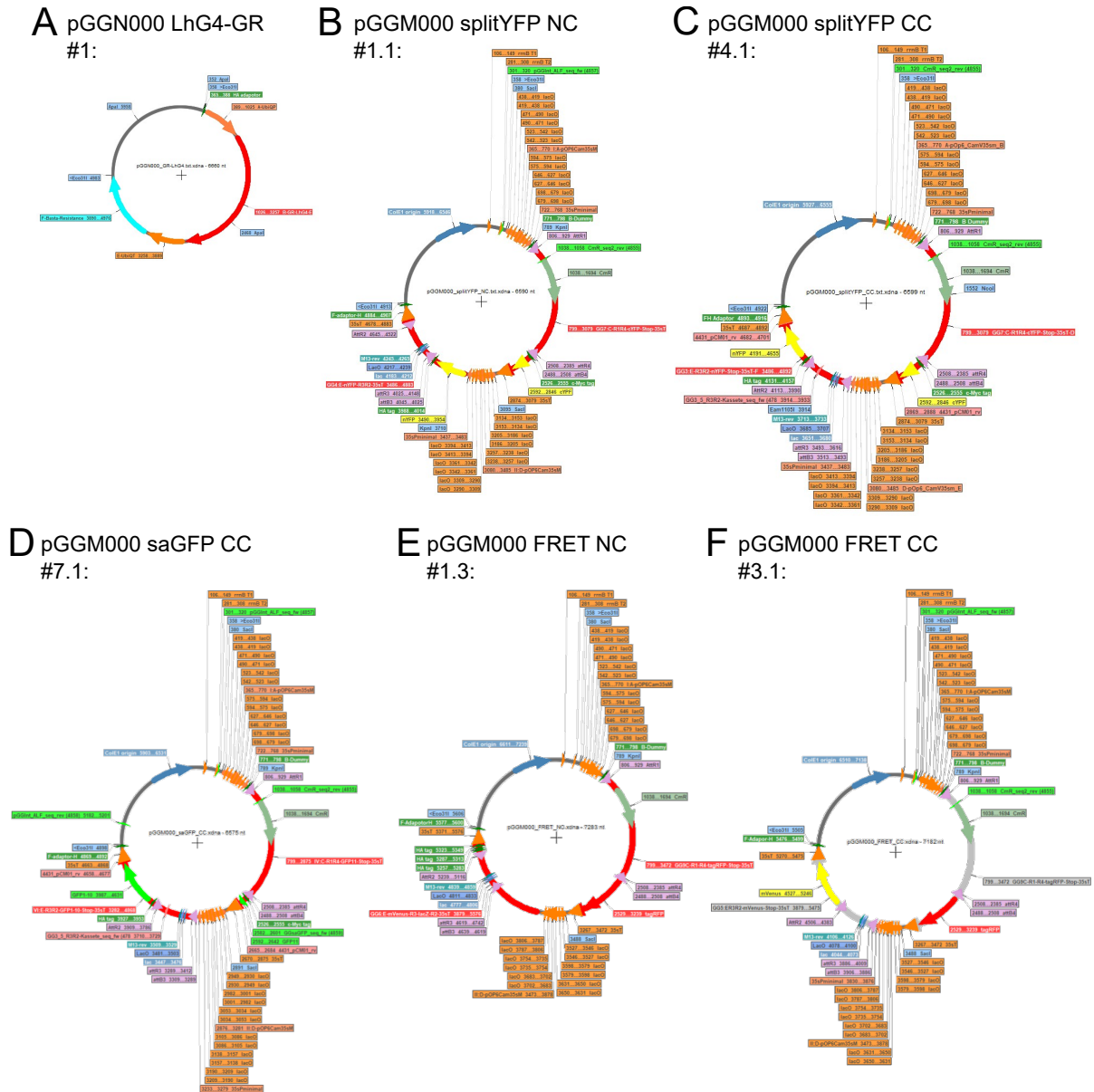


Figure S2: Vector maps of successfully cloned intermediate vectors of the 2in1 pInd system. Enzymes, which were used for the digest (figure 32), are marked in each vector map (KpnI, ApaI, SacI and Eco31I (BsaI)).

SUPPLEMENTAL INFORMATION

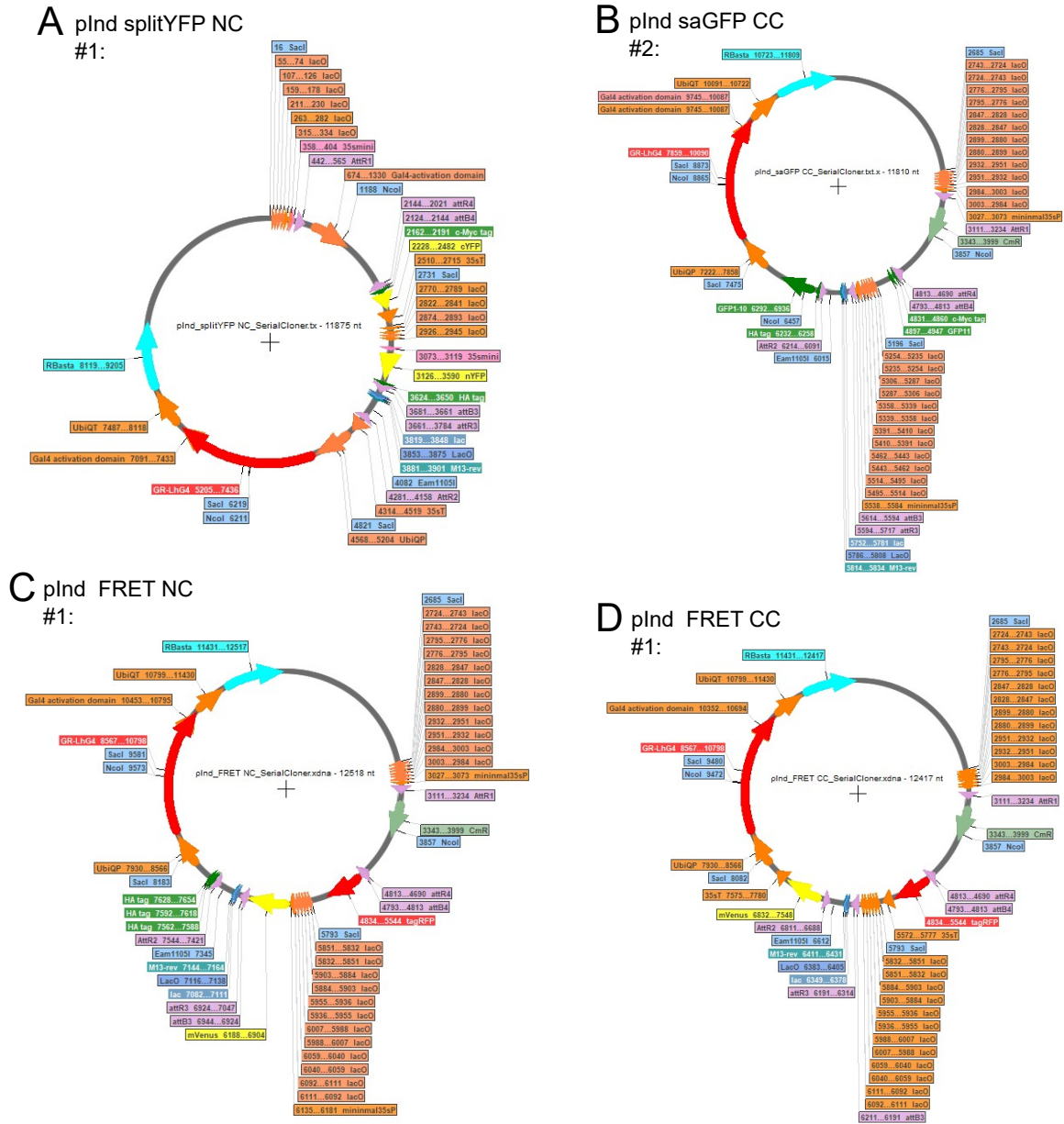


Figure S3: Vector maps of successfully cloned destination vectors of the 2in1 pInd system. Enzymes, which were used for the digest (figure 32), are marked in each vector map (KpnI, ApaI, SacI and Eco31I (BsaI)).

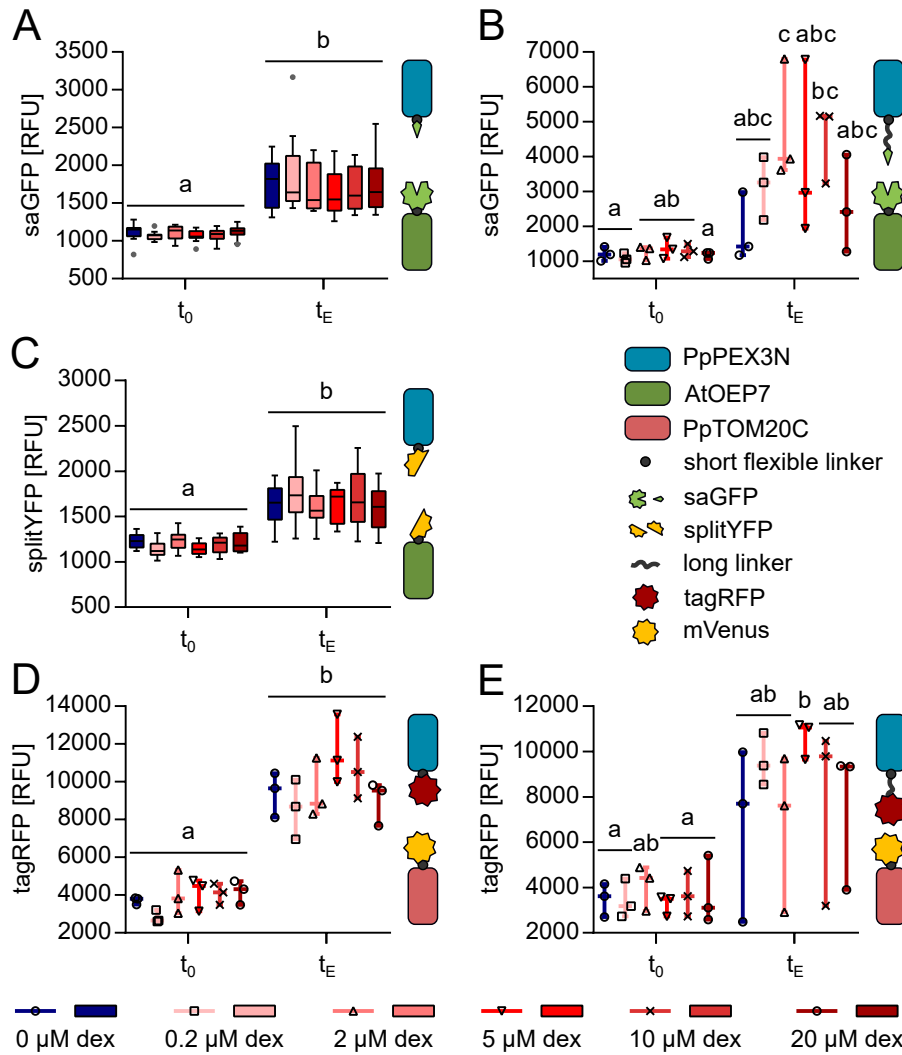


Figure S4: *In vivo* verification of dexamethasone inducible pInd vector system verified by the respective sensor fluorescence in the transient system of *N. tabacum*.

N. tabacum leaves were infiltrated with saGFP (A, B), splitYFP (C) and FRET (D, E) sensor constructs. *N. tabacum* leaf discs were submerged in wells of a 96-well plate prefilled with assay medium. After about 1 h of dark incubation, assay medium was exchanged by fresh medium with different concentrations of dexamethasone (t_0). The relative fluorescence unit (RFU) of the respective fluorescent sensor was detected over time by the plate reader. The graphs represent the respective relative fluorescence unit (RFU) of t_0 and the endpoint of the plate reader experiment (t_E : 20.2 h (A), 38.6 h (B, D, E), 24.2 h (C)). $n = 3$ (of one infiltrated leaf) (B, D, E); $n = 12$ (of three infiltrated leaves, 4 discs per leaf) (A, E). Data are represented as grouped box plot with median and Tukey whiskers. Significant differences were calculated according to 2-way ANOVA with Tukey's multiple comparisons test. Excitation: 482 nm (saGFP, splitYFP), 540-20 nm (tagRFP); emission: 530-20 nm (saGFP), 540-20 nm (splitYFP), 580-20 nm (tagRFP).

SUPPLEMENTAL INFORMATION

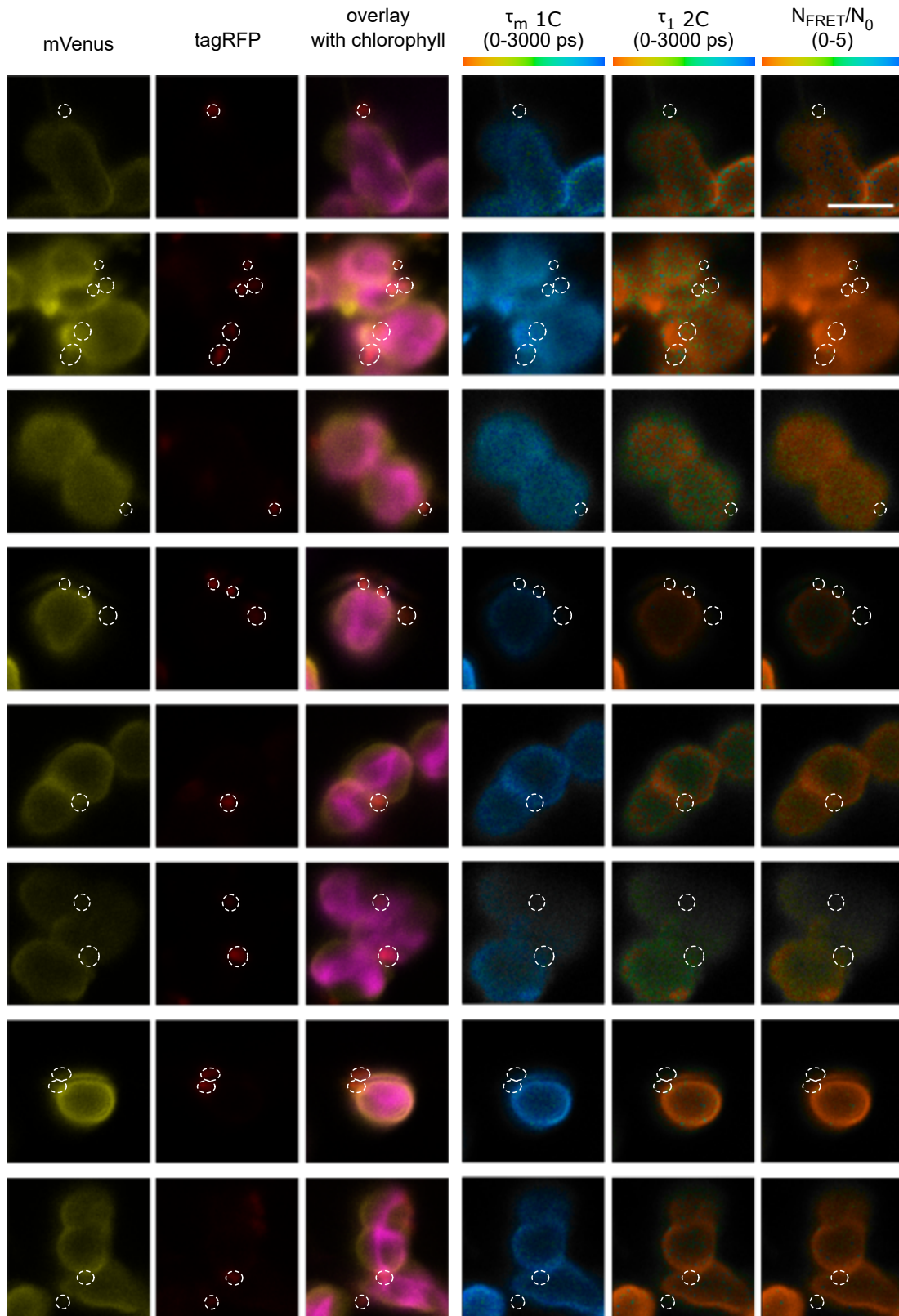


Figure S5: FRET-FLIM-based proximity sensor between outer envelope (OE) and peroxisomal membrane (PerM) with longer linker under light conditions and cytD treatment transient in *Nicotiana tabacum*, (AtOEP7:mVenus PpPEX3N:tagRFP, 48#1).

mVenus is fused C-terminal to AtOEP7 and localised to OE, whereas the acceptor tagRFP is fused C-terminal to a truncated version of PpPEX3 with short linker and localised to PerM. The bridging distance of this construct between both membranes is ≤ 22.08 nm + the Förster radius. The donor mVenus would perform Förster resonance energy transfer (FRET) and concomitant decrease in fluorescence lifetime τ_m when approaching the distance of the Förster radius (~ 5.7 nm) with the tagRFP. As indication for FRET a local decrease in τ_m and the appearance of quenched donor lifetime values (τ_1) are expected. N_{FRET}/N_0 visualise the ratio of quenched donor (τ_1) to unquenched donor (τ_2). Leaf discs were vacuum infiltrated in 20 μ M cytD (cytochalasin D) and incubated at 20 μ mol $m^{-2} s^{-1}$ for minimum 1.5 h. Maximum time of imaging per sample was 20 min. Scale = 2.5 μ m.

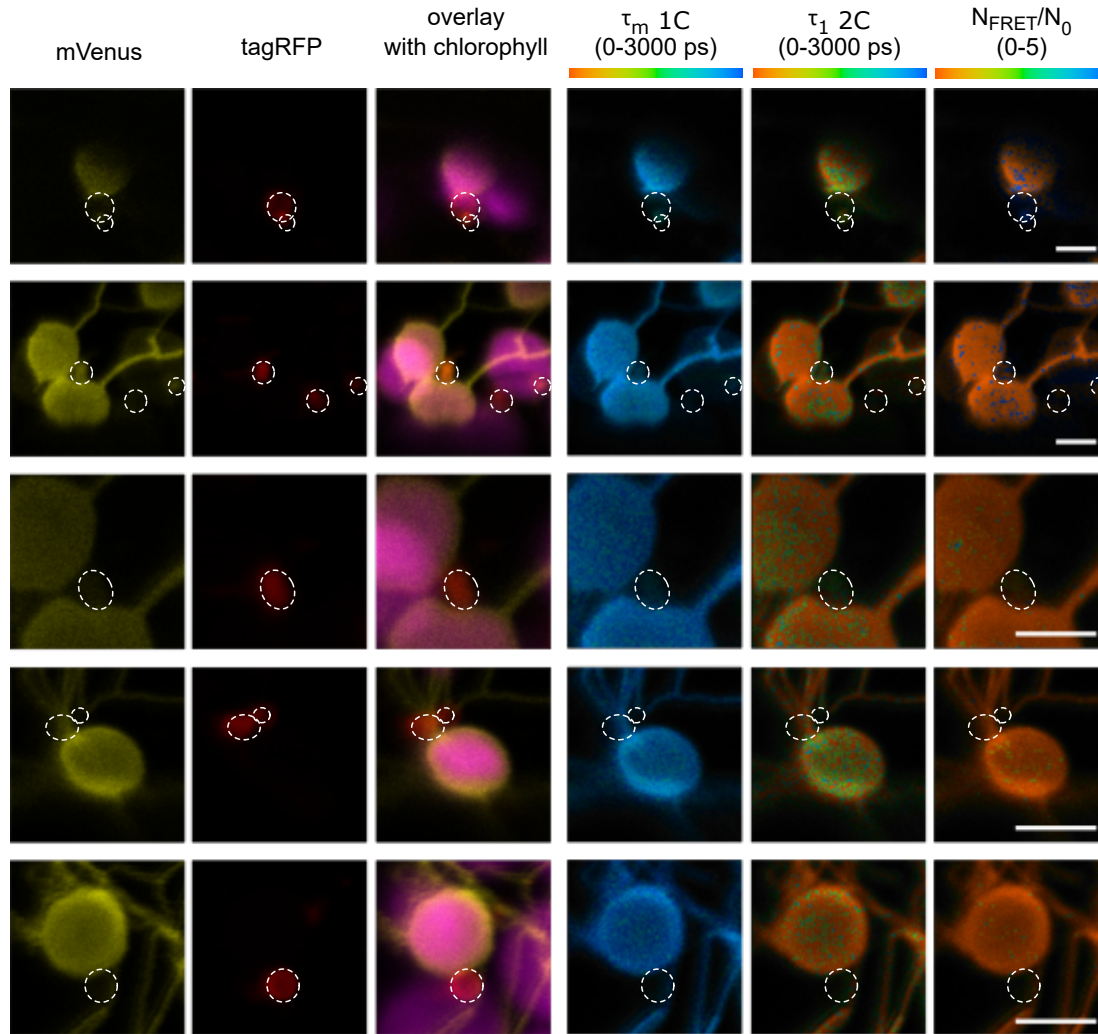


Figure S6: FRET-FLIM-based proximity sensor between outer envelope (OE) and peroxisomal membrane (PerM) with longer linker under light conditions and cytD treatment transient in *Nicotiana tabacum*, (AtOEP7:mVenus PpPEX3N(GGSGG)₁₃:tagRFP, 84#2). mVenus is fused C-terminal to AtOEP7 and localised to OE, whereas the acceptor tagRFP is fused C-terminal to a truncated version of PpPEX3 with a (GGSGG)₁₃ linker and localised to PerM. The bridging distance of this construct between both membranes is ≤ 45.48 nm + the Förster radius. The donor mVenus would perform Förster resonance energy transfer (FRET) and concomitant decrease in fluorescence lifetime τ_m when approaching the distance of the Förster radius (~ 5.7 nm) with the tagRFP. As indication for FRET a local decrease in τ_m and the appearance of quenched donor lifetime values (τ_1) are expected. N_{FRET}/N_0 visualise the ratio of quenched donor (τ_1) to unquenched donor (τ_2). Leaf discs were vacuum infiltrated in 20 μ M cytD (cytochalasin D) and incubated at 20 μ mol m⁻² s⁻¹ for minimum 1.5 h. Maximum time of imaging per sample was 20 min. Scale = 2.5 μ m.

SUPPLEMENTAL INFORMATION

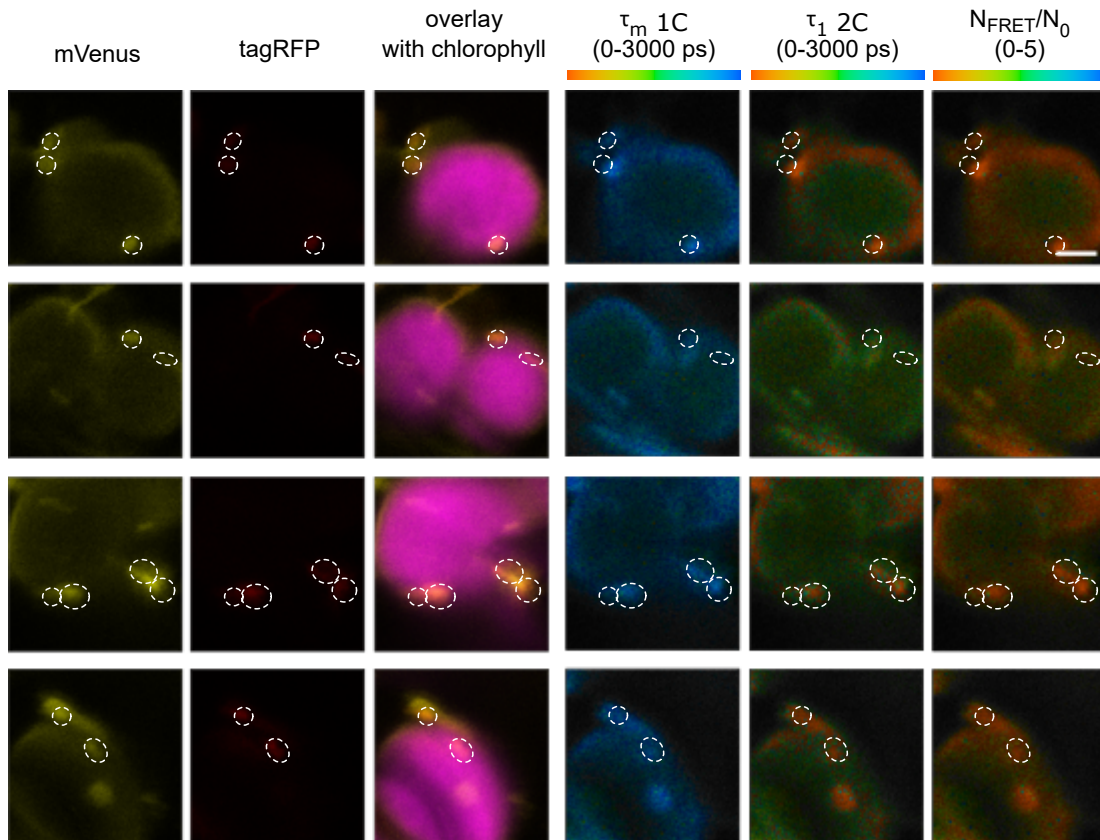


Figure S7: FRET-FLIM-based proximity sensor between outer envelope (OE) and peroxisomal membrane (PerM) with longer linker under light conditions in stable Arabidopsis line (px-ck AtOEP7:mVenus PpPEX3N:tagRFP #21; 48#1 #21).

mVenus is fused C-terminal to AtOEP7 and localised to OE, whereas the acceptor tagRFP is fused C-terminal to a truncated version of PpPEX3 with short linker and localised to PerM. The bridging distance of this construct between both membranes is ≤ 22.08 nm + the Förster radius. The donor mVenus would perform Förster resonance energy transfer (FRET) and concomitant decrease in fluorescence lifetime τ_m when approaching the distance of the Förster radius (~ 5.7 nm) with the tagRFP. As indication for FRET a local decrease in τ_m and the appearance of quenched donor lifetime values (τ_1) are expected. N_{FRET}/N_0 visualise the ratio of quenched donor (τ_1) to unquenched donor (τ_2). Leaf discs were vacuum infiltrated in water and directly imaged or incubated at $20 \mu\text{mol m}^{-2} \text{s}^{-1}$. Maximum time of imaging per sample was 20 min. Scale = $2.5 \mu\text{m}$.

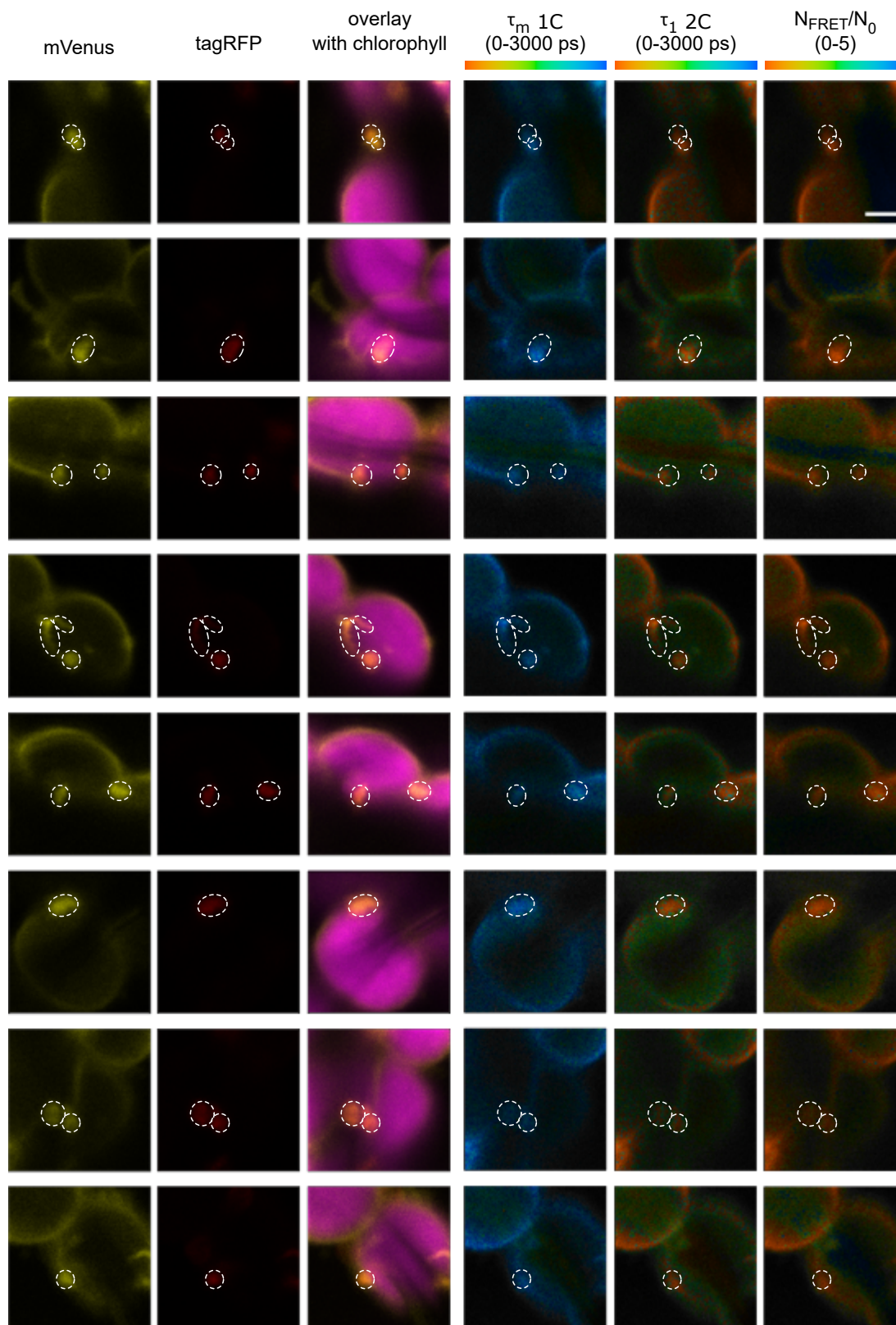


Figure S8: FRET-FLIM-based proximity sensor between outer envelope (OE) and peroxisomal membrane (PerM) with longer linker under light conditions and cytD treatment in stable Arabidopsis line (px-ck AtOEP7:mVenus PpPEX3N:tagRFP #21; 48#1 #21).

mVenus is fused C-terminal to AtOEP7 and localised to OE, whereas the acceptor tagRFP is fused C-terminal to a truncated version of PpPEX3 with short linker and localised to PerM. The bridging distance of this construct between both membranes is ≤ 22.08 nm + the Förster radius. The donor mVenus would perform Förster resonance energy transfer (FRET) and concomitant decrease in fluorescence lifetime τ_m when approaching the distance of the Förster radius (~ 5.7 nm) with the tagRFP. As indication for FRET a local decrease in τ_m and the appearance of quenched donor lifetime values (τ_1) are expected. N_{FRET}/N_0 visualise the ratio of quenched donor (τ_1) to unquenched donor (τ_2). Leaf discs were vacuum infiltrated in 20 μ M cytD (cytochalasin D) incubated for minimum 1.5 h at 20 μ mol $m^{-2} s^{-1}$. Maximum time of imaging per sample was 20 min. Scale = 2.5 μ m.

SUPPLEMENTAL INFORMATION

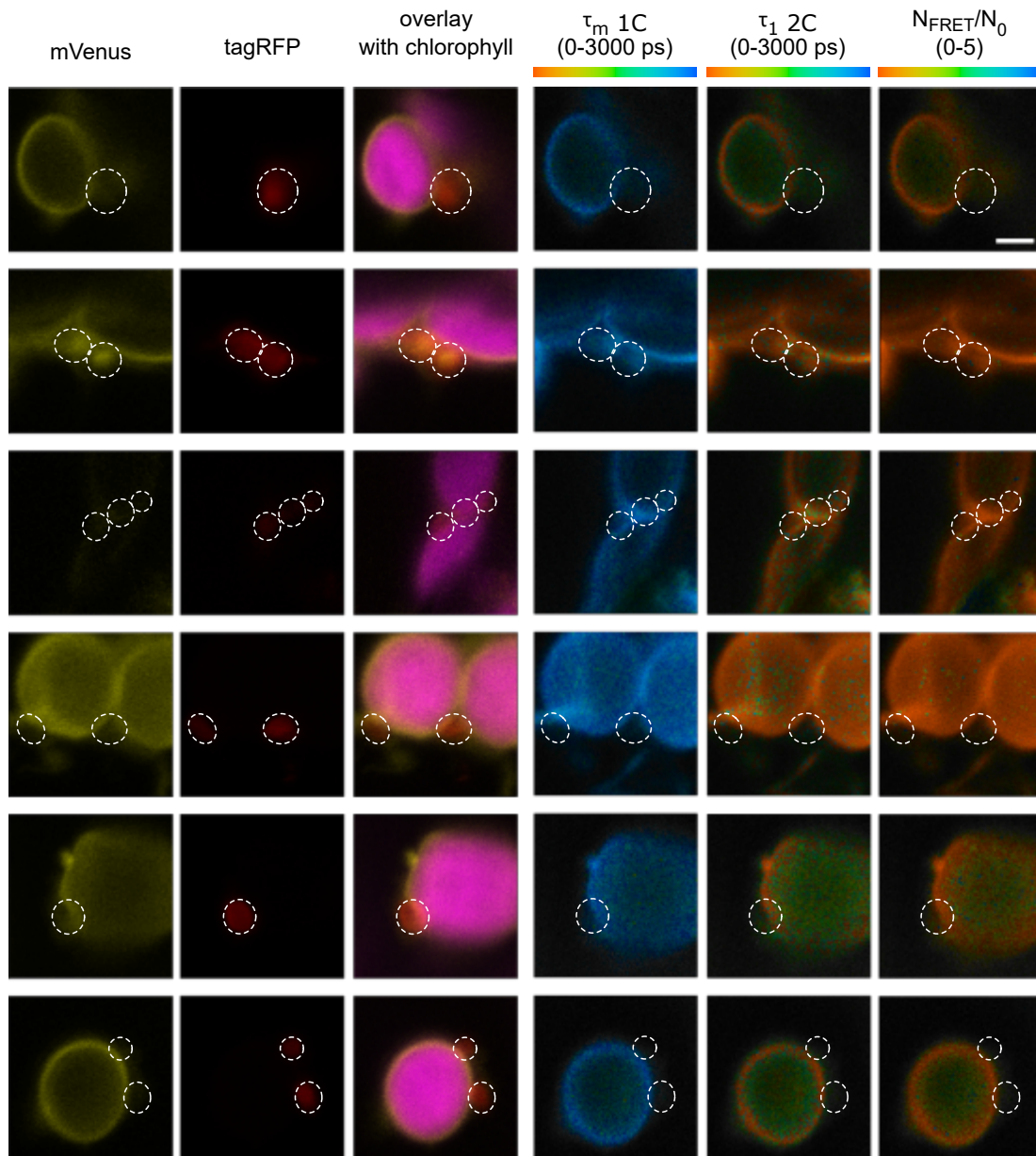


Figure S9: FRET-FLIM-based proximity sensor between outer envelope (OE) and peroxisomal membrane (PerM) with longer linker under light conditions in stable Arabidopsis line (Col-0 AtOEP7:mVenus PpPEX3N(GGSGG)₁₃:tagRFP #12; 84#2 #12).

mVenus is fused C-terminal to AtOEP7 and localised to OE, whereas the acceptor tagRFP is fused C-terminal to a truncated version of PpPEX3 with a (GGSGG)₁₃ linker and localised to PerM. The bridging distance of this construct between both membranes is $\leq 45.48 \text{ nm} +$ the Förster radius. The donor mVenus would perform Förster resonance energy transfer (FRET) and concomitant decrease in fluorescence lifetime τ_m when approaching the distance of the Förster radius ($\sim 5.7 \text{ nm}$) with the tagRFP. As indication for FRET a local decrease in τ_m and the appearance of quenched donor lifetime values (τ_1) are expected. N_{FRET}/N_0 visualise the ratio of quenched donor (τ_1) to unquenched donor (τ_2). Leaf discs were vacuum infiltrated in water and directly imaged or incubated at $20 \mu\text{mol m}^{-2} \text{ s}^{-1}$. Maximum time of imaging per sample was 20 min. Scale = $2.5 \mu\text{m}$.

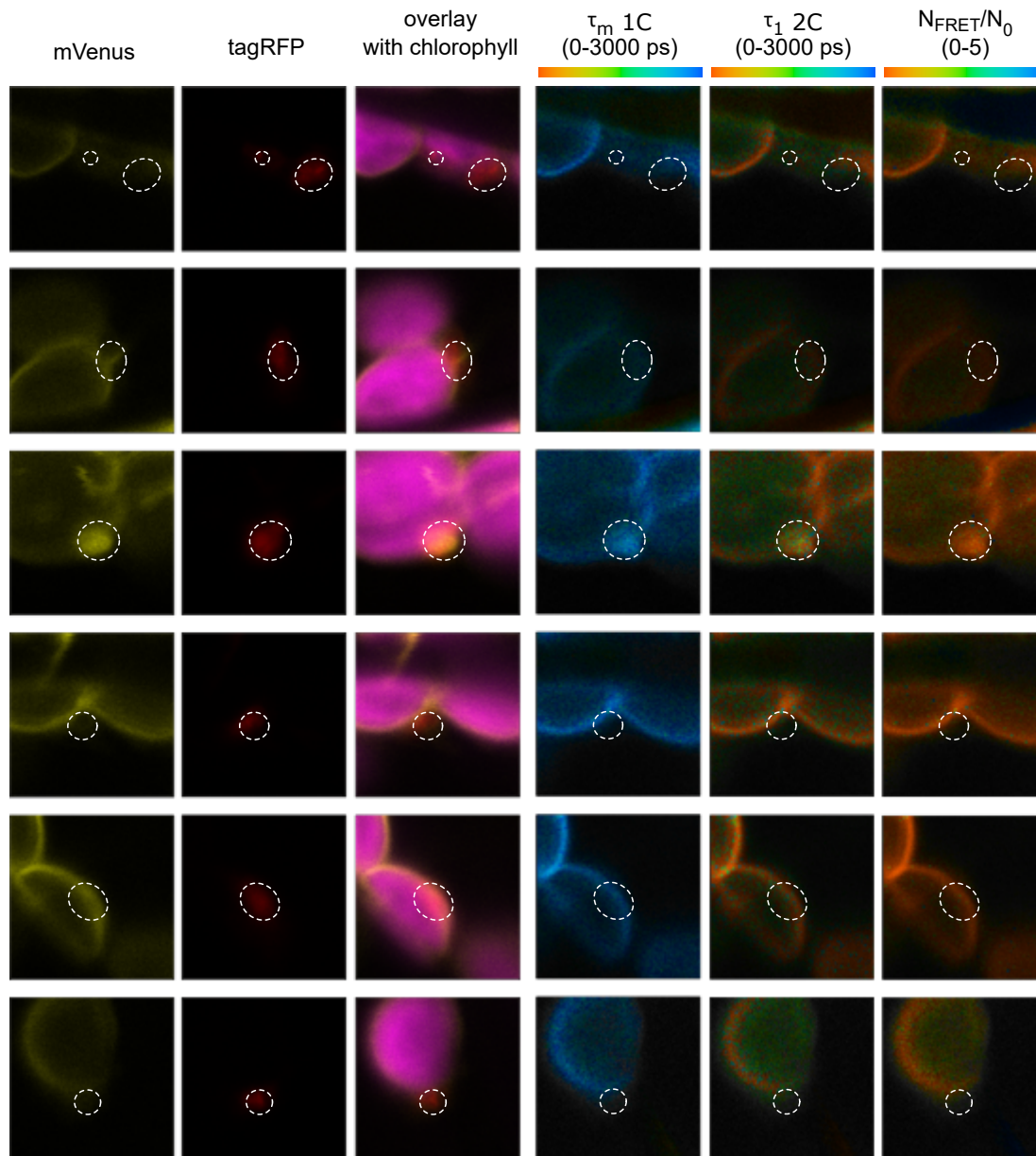


Figure S10: FRET-FLIM-based proximity sensor between outer envelope (OE) and peroxisomal membrane (PerM) with longer linker under light conditions in stable Arabidopsis line (Col-0 AtOEP7:mVenus PpPEX3N(GGSGG)₁₃:tagRFP #15; 84#2 #15).

mVenus is fused C-terminal to AtOEP7 and localised to OE, whereas the acceptor tagRFP is fused C-terminal to a truncated version of PpPEX3 with a (GGSGG)₁₃ linker and localised to PerM. The bridging distance of this construct between both membranes is $\leq 45.48 \text{ nm} +$ the Förster radius. The donor mVenus would perform Förster resonance energy transfer (FRET) and concomitant decrease in fluorescence lifetime τ_m when approaching the distance of the Förster radius ($\sim 5.7 \text{ nm}$) with the tagRFP. As indication for FRET a local decrease in τ_m and the appearance of quenched donor lifetime values (τ_1) are expected. N_{FRET}/N_0 visualise the ratio of quenched donor (τ_1) to unquenched donor (τ_2). Leaf discs were vacuum infiltrated in water and directly imaged or incubated at $20 \mu\text{mol m}^{-2} \text{ s}^{-1}$. Maximum time of imaging per sample was 20 min. Scale = $2.5 \mu\text{m}$.

SUPPLEMENTAL INFORMATION

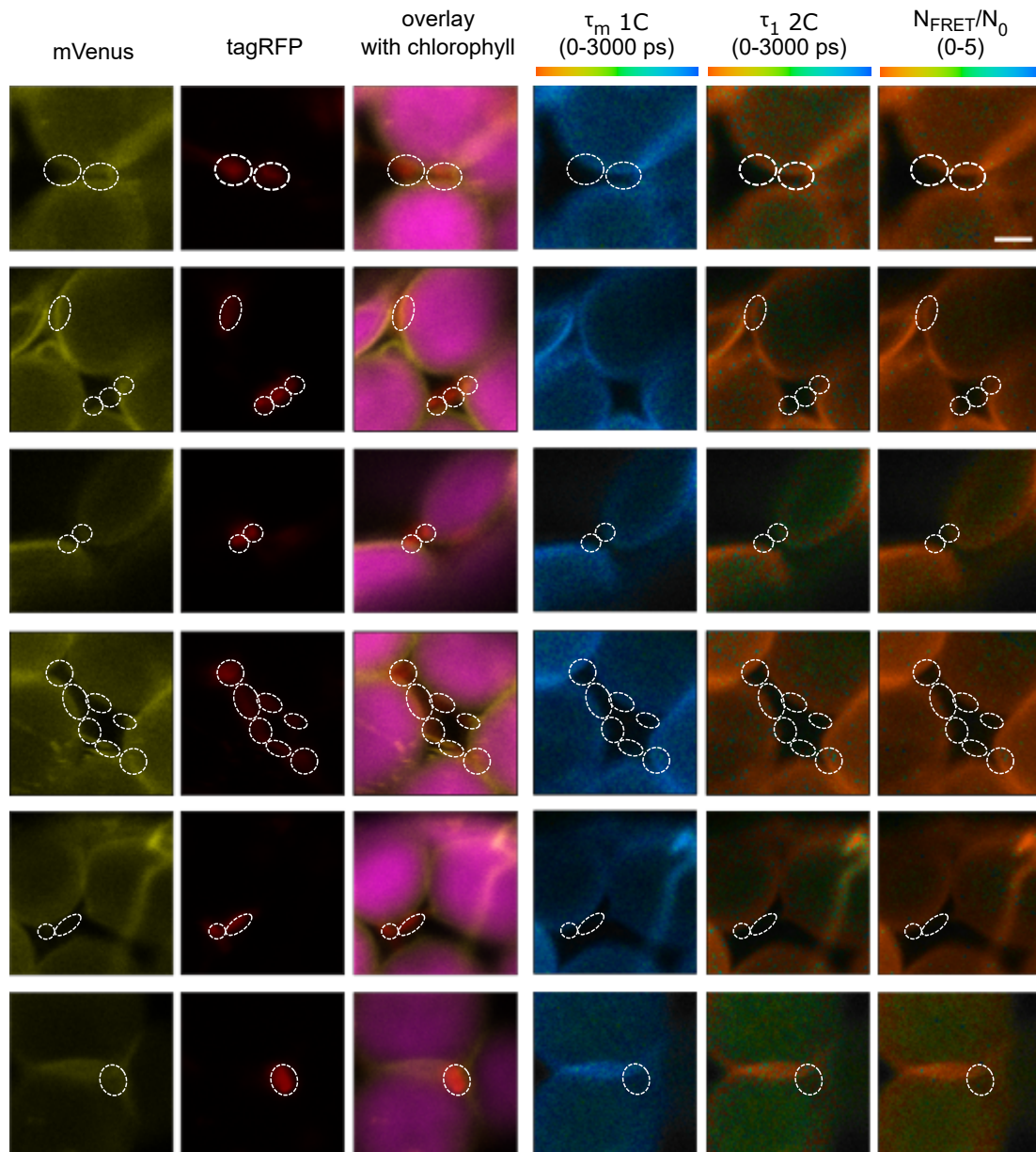


Figure S11: FRET-FLIM-based proximity sensor between outer envelope (OE) and peroxisomal membrane (PerM) with longer linker under light conditions in stable Arabidopsis line (px-ck AtOEP7:mVenus PpPEX3N(GGSGG)₁₃:tagRFP #35; 84#2 #35).

mVenus is fused C-terminal to AtOEP7 and localised to OE, whereas the acceptor tagRFP is fused C-terminal to a truncated version of PpPEX3 with a (GGSGG)₁₃ linker and localised to PerM. The bridging distance of this construct between both membranes is ≤ 45.48 nm + the Förster radius. The donor mVenus would perform Förster resonance energy transfer (FRET) and concomitant decrease in fluorescence lifetime τ_m when approaching the distance of the Förster radius (~ 5.7 nm) with the tagRFP. As indication for FRET a local decrease in τ_m and the appearance of quenched donor lifetime values (τ_1) are expected. N_{FRET}/N_0 visualise the ratio of quenched donor (τ_1) to unquenched donor (τ_2). Leaf discs were vacuum infiltrated in water and directly imaged or incubated at $20 \mu\text{mol m}^{-2} \text{s}^{-1}$. Maximum time of imaging per sample was 20 min. Scale = $2.5 \mu\text{m}$.

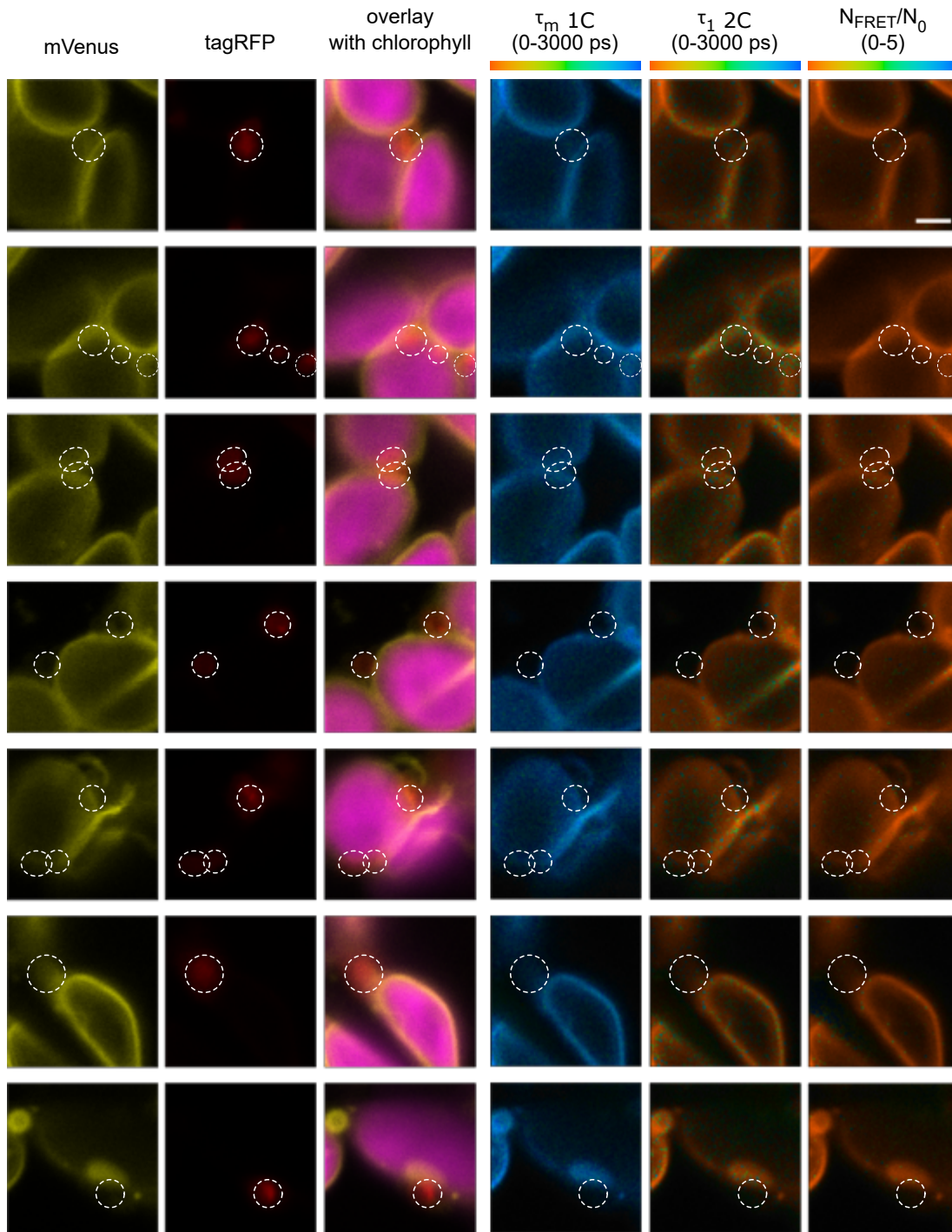


Figure S12: FRET-FLIM-based proximity sensor between outer envelope (OE) and peroxisomal membrane (PerM) with longer linker under light conditions and cytD treatment in stable Arabidopsis line (Col-0 AtOEP7:mVenus PpPEX3N(GGSGG)₁₃:tagRFP #12; 84#2 #12).

mVenus is fused C-terminal to AtOEP7 and localised to OE, whereas the acceptor tagRFP is fused C-terminal to a truncated version of PpPEX3 with a (GGSGG)₁₃ linker and localised to PerM. The bridging distance of this construct between both membranes is $\leq 45.48 \text{ nm} +$ the Förster radius. The donor mVenus would perform Förster resonance energy transfer (FRET) and concomitant decrease in fluorescence lifetime τ_m when approaching the distance of the Förster radius ($\sim 5.7 \text{ nm}$) with the tagRFP. As indication for FRET a local decrease in τ_m and the appearance of quenched donor lifetime values (τ_1) are expected. N_{FRET}/N_0 visualise the ratio of quenched donor (τ_1) to unquenched donor (τ_2). Leaf discs were vacuum infiltrated in $20 \mu\text{M}$ cytD (cytochalasin D) incubated for minimum 1.5 h at $20 \mu\text{mol m}^{-2} \text{ s}^{-1}$. Maximum time of imaging per sample was 20 min. Scale = $2.5 \mu\text{m}$.

SUPPLEMENTAL INFORMATION

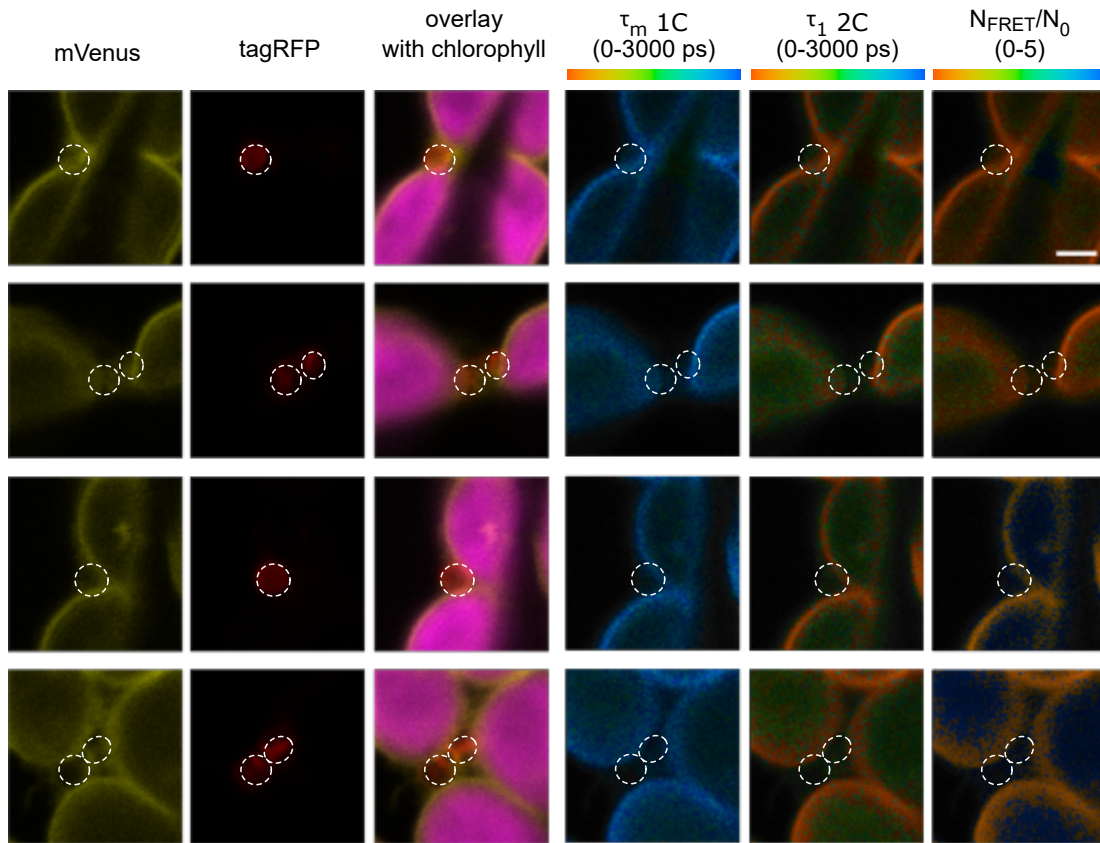


Figure S13: FRET-FLIM-based proximity sensor between outer envelope (OE) and peroxisomal membrane (PerM) with longer linker under light conditions and cytD treatment in stable Arabidopsis line (Col-0 AtOEP7:mVenus PpPEX3N(GGSGG)₁₃:tagRFP #15; 84#2#15).

mVenus is fused C-terminal to AtOEP7 and localised to OE, whereas the acceptor tagRFP is fused C-terminal to a truncated version of PpPEX3 with a (GGSGG)₁₃ linker and localised to PerM. The bridging distance of this construct between both membranes is $\leq 45.48 \text{ nm} +$ the Förster radius. The donor mVenus would perform Förster resonance energy transfer (FRET) and concomitant decrease in fluorescence lifetime τ_m when approaching the distance of the Förster radius ($\sim 5.7 \text{ nm}$) with the tagRFP. As indication for FRET a local decrease in τ_m and the appearance of quenched donor lifetime values (τ_1) are expected. N_{FRET}/N_0 visualise the ratio of quenched donor (τ_1) to unquenched donor (τ_2). Leaf discs were vacuum infiltrated in $20 \mu\text{M}$ cytD (cytochalasin D) incubated for minimum 1.5 h at $20 \mu\text{mol m}^{-2} \text{ s}^{-1}$. Maximum time of imaging per sample was 20 min. Scale = $2.5 \mu\text{m}$.

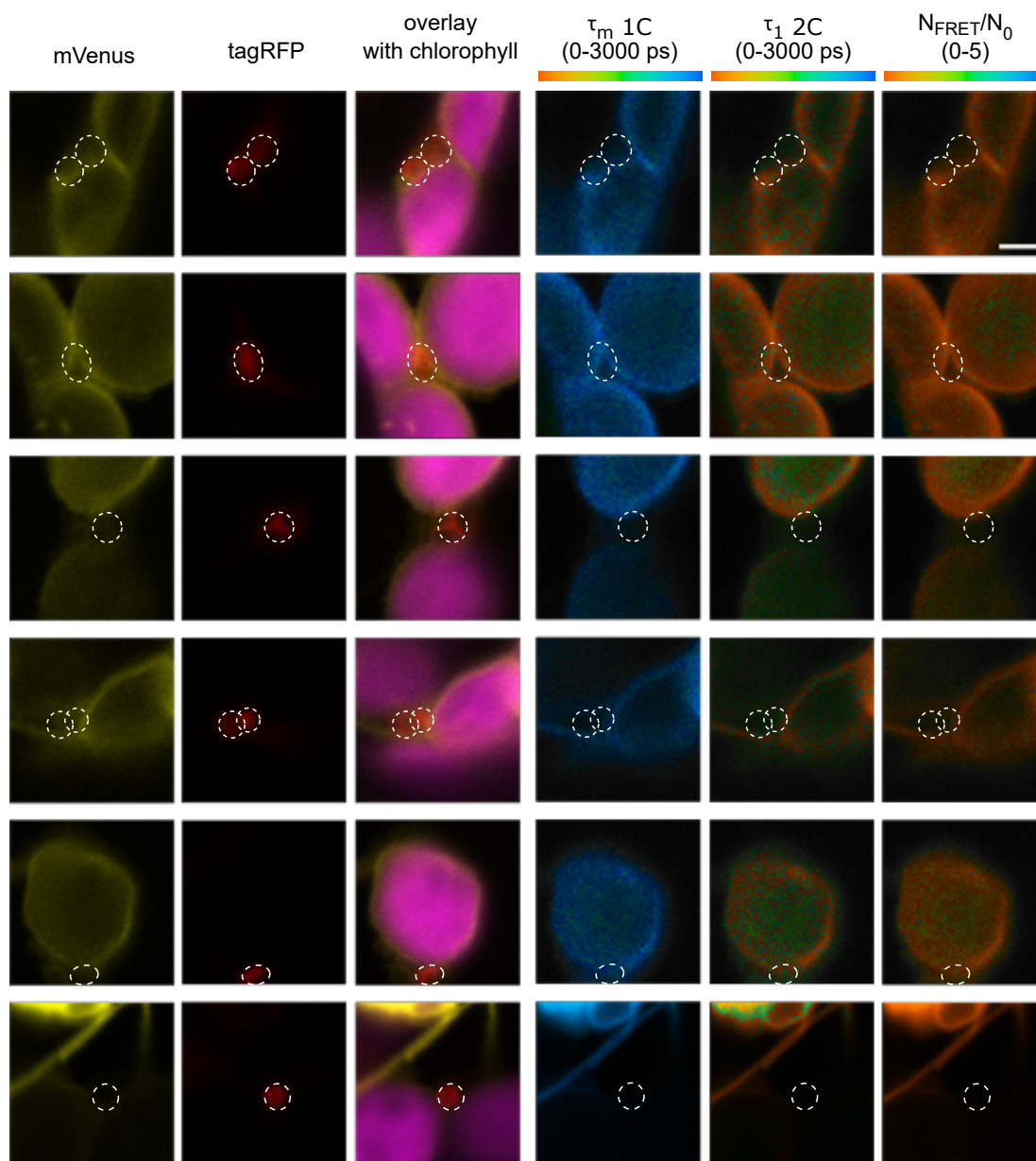


Figure S14: FRET-FLIM-based proximity sensor between outer envelope (OE) and peroxisomal membrane (PerM) with longer linker under light conditions and cytD treatment in stable Arabidopsis line (px-ck AtOEP7:mVenus PpPEX3N(GGSGG)₁₃:tagRFP #35; 84#2 #35).

mVenus is fused C-terminal to AtOEP7 and localised to OE, whereas the acceptor tagRFP is fused C-terminal to a truncated version of PpPEX3 with a (GGSGG)₁₃ linker and localised to PerM. The bridging distance of this construct between both membranes is ≤ 45.48 nm + the Förster radius. The donor mVenus would perform Förster resonance energy transfer (FRET) and concomitant decrease in fluorescence lifetime τ_m when approaching the distance of the Förster radius (~ 5.7 nm) with the tagRFP. As indication for FRET a local decrease in τ_m and the appearance of quenched donor lifetime values (τ_1) are expected. N_{FRET}/N_0 visualise the ratio of quenched donor (τ_1) to unquenched donor (τ_2). Leaf discs were vacuum infiltrated in 20 μ M cytD (cytochalasin D) incubated for minimum 1.5 h at 20 μ mol m⁻² s⁻¹. Maximum time of imaging per sample was 20 min. Scale = 2.5 μ m.

SUPPLEMENTAL INFORMATION

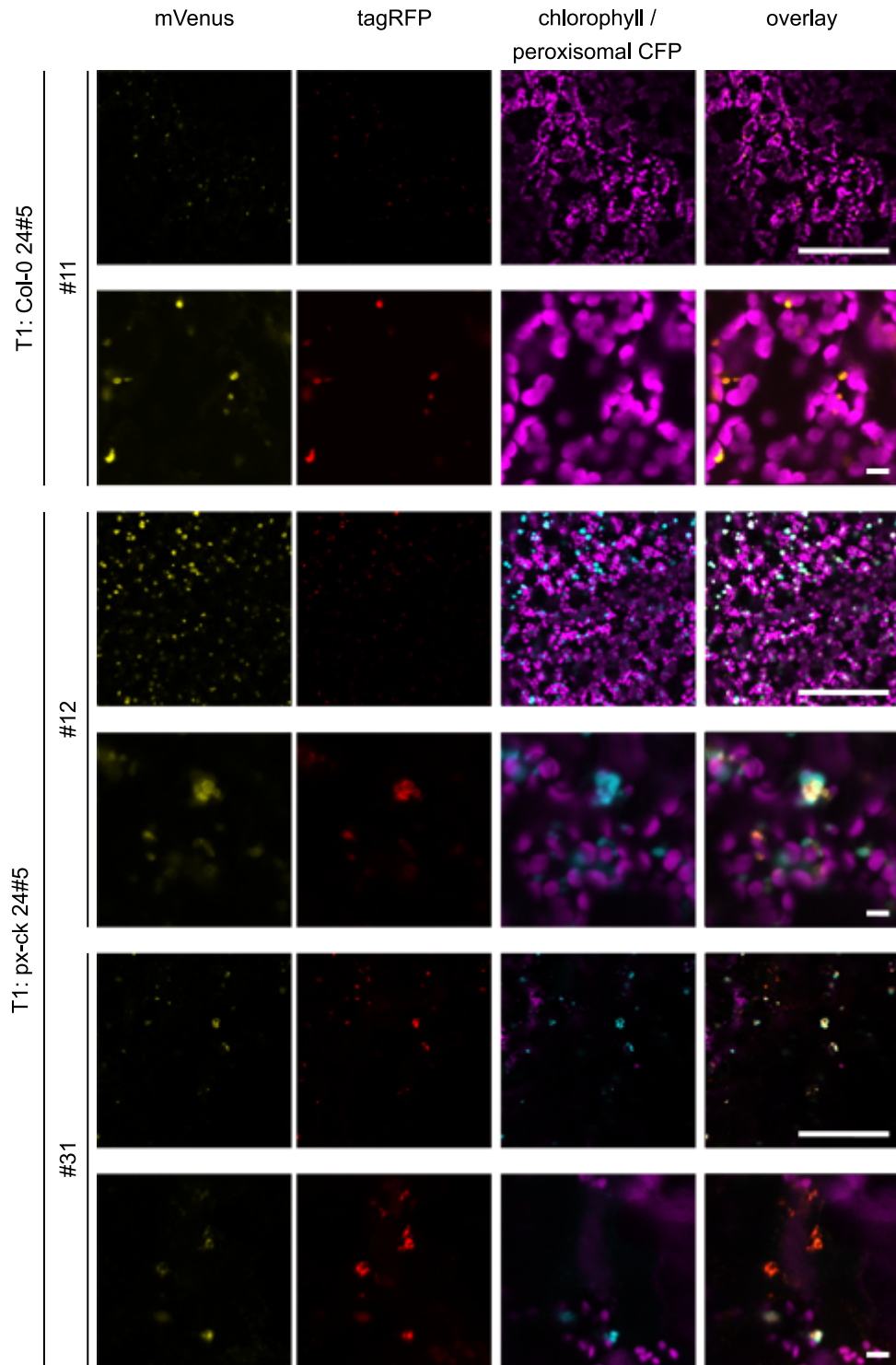


Figure S15: Representative CLSM images of independent Arabidopsis T1 (first generation) lines expressing the tether construct 24#5 (PpPEX3N:tagRFP:mVenus:PpTOM20C) under the constitutive promoter CaM35sP.

The tether construct was transformed in two different WT backgrounds Col-0 and px-ck, where the last one is a Col-0 line with peroxisomal CFP (CFP-SKL) marker ([186]). Col-0 24#5 #11, px-ck 24#5 #12 and px-ck 24#5 #31 were used for the following experiments. Chlorophyll autofluorescence is depicted in magenta, whereas the peroxisomal CFP is shown in cyan. Scale bar = 5 μ m.

Table S2: Raw data for the quantification ratio of alive and dead pollen.

Pollen were stained with Alexander staining solution, whereby the cytoplasm of alive and viable pollen is coloured in magenta-red surrounded by the green coloured envelope. Dead pollen lost their cytoplasm, thus they have only a green envelope left.

Genotype	Plant	Alive	Dead	Total	%
Col-0	1	987	38	1025	3.7
	2	1214	31	1245	2.5
	3	1317	17	1334	1.3
	4	637	12	649	1.8
	5	735	7	742	0.9
Col-0 24#5 #11C	1	549	291	840	34.6
	2	886	267	1153	23.2
	3	409	227	636	35.7
	4	773	520	1293	40.2
	5	938	67	1005	6.7
	6	247	100	347	28.8
px-ck	1	1095	14	1109	1.3
	2	1227	19	1246	1.5
	3	1312	34	1346	2.5
	4	1028	20	1048	1.9
	5	777	17	794	2.1
px-ck 24#5 #12B	1	755	21	776	2.7
	2	884	9	893	1.0
	3	1330	53	1383	3.8
	4	799	34	833	4.1
	5	950	40	990	4.0
px-ck 24#5 #31F	1	1890	165	2055	8.0
	2	1170	115	1285	8.9
	3	1091	55	1146	4.8
	4	653	50	703	7.1
	5	624	32	656	4.9

List of Figures

1	Schematic representation of putative MCS proteins and their functions. . . .	3
2	Schematic overview of known organellar interaction in plants.	6
3	Simplified schemata of photorespiratory metabolism.	10
4	Putative techniques for the identification and characterisation of organelle- organelle interaction.	13
5	Schemata of topology assay using the splitYFP reporter system after Zamyatnin Jr <i>et al.</i> [165].	17
6	Principle of time-correlated single photon counting (TCSPC) and the fluores- cence lifetime (FLIM) analysis.	22
7	Plate design for Basta selection on plates.	31
8	Leaves covered individually in aluminium foil for senescence assay.	36
9	Parameter file for the Python-based analysis pipeline.	61
10	Maximum intensity projection (MIP) of representative z-stacks used for a chloroplast-peroxisome proximity analysis in three different species and un- der different photosynthetic conditions.	69
11	Segmentation of chloroplasts and peroxisomes: Procedure and setting optim- isation based on the example of an <i>A. thaliana</i> mesophyll cell.	70
12	Segmentation of chloroplasts and peroxisomes by self-developed Python- based analysis pipeline with optimised filter settings and in three different spe- cies.	71
13	Maximum intensity projection (MIP) of representative cells transformed with artificial or synthetic tether constructs between chloroplasts and peroxisomes.	73
14	Quality control of self-developed Python-based proximity analysis between chloroplasts and peroxisomes in <i>N. tabacum</i> pavement cells.	74
15	Quality control of self-developed Python-based analysis pipeline for the prox- imity analysis between chloroplasts and peroxisomes in <i>A. thaliana</i> mesophyll cells.	75
16	Proximity analysis between chloroplasts and peroxisomes under different pho- tosynthetic conditions.	77
17	Schematic overview of fusion protein candidates for BiFC and FRET/FLIM re- porter systems	79
18	Verification of cytosolic expression control.	80

19	Localisation and topology control of ER membrane protein candidates.	82
20	Localisation and topology control of PM protein candidates.	83
21	Localisation and topology control of outer envelope (OE) protein candidate of the chloroplast.	84
22	Localisation and topology control of mitochondria outer membrane (MOM) protein candidates.	85
23	Localisation and topology control of peroxisomal membrane (PerM)protein candidates.	86
24	Schematic overview of the proximity BiFC (bimolecular fluorescence complementation) reporter using the example of splitYFP and the expected signal distribution.	88
25	Signal distribution of splitYFP proximity reporter using PpPEX3N and PpTOM20C as fusion partners in the transient system of <i>N. tabacum</i>	89
26	Quantification of BiFC signal under light and dark conditions using PpPEX3N and PpTOM20C as fusion partners in the transient system of <i>N. tabacum</i>	91
27	Signal distribution of splitYFP proximity reporter using PpPEX3N and OEP7 as fusion partners in the transient system of <i>N. tabacum</i>	92
28	Signal distribution of splitYFP proximity reporter bridging two different distances between the outer envelope (OE) and the peroxisomal membrane (PerM) in the transient system of <i>N. tabacum</i>	93
29	Comparison of splitYFP and saGFP signal using using PpPEX3N:(GGSGG) ₁₃ and OEP7 as fusion partners in the transient system of <i>N. tabacum</i>	95
30	Signal distribution of splitYFP proximity reporter using VAP27-1 and SYT1C as fusion partners in the transient system of <i>N. tabacum</i>	97
31	Cloning strategy for dexamethasone inducible 2in1 reporter system.	100
32	Verification of successfully cloned intermediate and destination vectors of the 2in1 pInd system by usage of restriction enzymes.	102
33	<i>In vivo</i> monitoring of dexamethasone induction of pInd FRET vector system verified by the respective sensor fluorescence in the transient system of <i>N. tabacum</i>	104
34	<i>In vivo</i> monitoring of dexamethasone induction of pInd BiFC vector system verified by the respective sensor fluorescence in the transient system of <i>N. tabacum</i>	107
35	Visualisation of induced saGFP fluorescence using the OEP7 and PpPEX3N:(GGSGG) ₁₃ as fusion partners and transient in <i>N. tabacum</i>	108
36	Determination of FLIM detection range in <i>Nicotiana benthamiana</i> pavement cells.	110
37	Imaging setup adaption for dynamic FRET-FLIM measurements in <i>N. tabacum</i> leaf cells.	112

LIST OF FIGURES

38	FRET-FLIM-based proximity sensor between outer envelope (OE) and peroxisomal membrane (PerM) with short and long linker under light conditions and cytochalasin D (CytD) treatment transient in <i>N. tabacum</i>	113
39	FRET-FLIM-based proximity sensor between outer envelope (OE) and peroxisomal membrane (PerM) with short and long linker under light conditions in stable <i>A. thaliana</i> lines.	115
40	FRET-FLIM-based proximity sensor between outer envelope (OE) and peroxisomal membrane (PerM) with short and long linker under light conditions and cytochalasin D (CytD) treatment in stable <i>A. thaliana</i> lines.	116
41	Perturbing organellar interaction by transient expression of the synthetic tether construct 24#5 (PpPEX3N:tagRFP:mVenus:PpTOM20C) in <i>N. benthamiana</i>	118
42	Overexpression of tether construct PpPEX3N:tagRFP:mVenus:PpTOM20C (24#5) lead to peroxisomal cluster formation in leaf cells of transgenic <i>A. thaliana</i> lines (T ₃ generation).	121
43	Signal distribution of the synthetic tether construct PpPEX3N:tagRFP:mVenus:PpTOM20C (24#5) in transgenic T ₃ <i>A. thaliana</i> lines in leaf and root tissue.	123
44	Organelle morphology of <i>A. thaliana</i> wild type (px-ck) and T ₃ synthetic tether lines (PpPEX3N:tagRFP:mVenus:PpTOM20C; 24#5) in mesophyll cells.	124
45	Germination rate of <i>A. thaliana</i> wild type background lines (Col-0, px-ck) and T ₃ synthetic tether lines (PpPEX3N:tagRFP:mVenus:PpTOM20C; 24#5) under standard growth conditions on plates.	126
46	Root development of <i>A. thaliana</i> wild type background lines (Col-0, px-ck) and T ₃ synthetic tether lines (PpPEX3N:tagRFP:mVenus:PpTOM20C; 24#5) under standard growth conditions.	127
47	Comparison of <i>A. thaliana</i> wild type background lines (Col-0, px-ck) and T ₃ synthetic tether lines (PpPEX3N:tagRFP:mVenus:PpTOM20C; 24#5) under standard growth conditions on soil.	129
48	Leaf morphology and mesophyll cell size of <i>A. thaliana</i> wild type px-ck and T ₃ synthetic tether lines (PpPEX3N:tagRFP:mVenus:PpTOM20C; 24#5).	130
49	Dark-induced senescence of 4-week-old <i>A. thaliana</i> wild type background lines (Col-0, px-ck) and T ₃ synthetic tether lines (PpPEX3N:tagRFP:mVenus:PpTOM20C; 24#5).	131
50	Inflorescence and flower morphology of <i>A. thaliana</i> wild type background lines (Col-0, px-ck) and T ₃ synthetic tether lines (PpPEX3N:tagRFP:mVenus:PpTOM20C; 24#5) under standard growth conditions.	132

51	Silique morphology and seed development of <i>A. thaliana</i> wild type background lines (Col-0, px-ck) and T ₃ synthetic tether lines (PpPEX3N:tagRFP:mVenus:PpTOM20C; 24#5) under standard growth conditions.	133
52	Pollen grains and stamina development of <i>A. thaliana</i> wild type background lines (Col-0, px-ck) and T ₃ synthetic tether lines (PpPEX3N:tagRFP:mVenus:PpTOM20C; 24#5) under standard growth conditions.	134
53	Pulse Amplitude Modulation (PAM) fluorometry analysis of 9-week-old <i>A. thaliana</i> wild type background lines (Col-0, px-ck) and T ₃ synthetic tether lines (PpPEX3N:tagRFP:mVenus:PpTOM20C; 24#5) under standard conditions on soil.	135
54	Analysis of respiration of <i>A. thaliana</i> wild type px-ck and T ₃ synthetic tether lines (PpPEX3N:tagRFP:mVenus:PpTOM20C; 24#5) under standard growth conditions on soil.	136
55	Root development of <i>A. thaliana</i> wild type background lines (Col-0, px-ck) and T ₃ synthetic tether lines (PpPEX3N:tagRFP:mVenus:PpTOM20C; 24#5) after heat stress on plates.	137
56	Comparison of 2-week-old <i>A. thaliana</i> wild type px-ck and two T ₃ synthetic tether lines (#12B, #31F) containing the synthetic tether construct PpPEX3N:tagRFP:mVenus:PpTOM20C (24#5) under high light stress conditions on soil.	140
57	Comparison of 5-week-old <i>A. thaliana</i> wild type background lines (Col-0, px-ck) and T ₃ synthetic tether lines (PpPEX3N:tagRFP:mVenus:PpTOM20C; 24#5) under high light stress conditions on soil.	141
58	Main findings of this study investigating contact sites with FP-based sensors, putative underlying reasons and ways to improve FP-based proximity sensors.	149
59	Main findings and putative underlying mechanisms investigating perturbation of the spatial organisation by introducing a synthetic tether.	158
S1	Movement analysis of peroxisomes using the cytoskeleton inhibitor cytD in <i>A. thaliana</i>	XVII
S2	Vector maps of successfully cloned intermediate vectors of the 2in1 pInd system	XVIII
S3	Vector maps of successfully cloned destination vectors of the 2in1 pInd system.	XIX
S4	<i>In vivo</i> verification of dexamethasone inducible pInd vector system verified by the respective sensor fluorescence in the transient system of <i>N. tabacum</i>	XX

LIST OF FIGURES

S5 FRET-FLIM-based proximity sensor between outer envelope (OE) and peroxisomal membrane (PerM) with longer linker under light conditions and cytD treatment transient in *Nicotiana tabacum*, (AtOEP7:mVenus PpPEX3N:tagRFP, 48#1). XXI

S6 FRET-FLIM-based proximity sensor between outer envelope (OE) and peroxisomal membrane (PerM) with longer linker under light conditions and cytD treatment transient in *Nicotiana tabacum*, (AtOEP7:mVenus PpPEX3N(GGSGG)₁₃:tagRFP, 84#2). XXII

S7 FRET-FLIM-based proximity sensor between outer envelope (OE) and peroxisomal membrane (PerM) with longer linker under light conditions in stable *Arabidopsis* line (px-ck AtOEP7:mVenus PpPEX3N:tagRFP #21; 48#1 #21). . . XXIII

S8 FRET-FLIM-based proximity sensor between outer envelope (OE) and peroxisomal membrane (PerM) with longer linker under light conditions and cytD treatment in stable *Arabidopsis* line (px-ck AtOEP7:mVenus PpPEX3N:tagRFP #21; 48#1 #21). XXIV

S9 FRET-FLIM-based proximity sensor between outer envelope (OE) and peroxisomal membrane (PerM) with longer linker under light conditions in stable *Arabidopsis* line (Col-0 AtOEP7:mVenus PpPEX3N(GGSGG)₁₃:tagRFP #12; 84#2 #12). XXV

S10 FRET-FLIM-based proximity sensor between outer envelope (OE) and peroxisomal membrane (PerM) with longer linker under light conditions in stable *Arabidopsis* line (Col-0 AtOEP7:mVenus PpPEX3N(GGSGG)₁₃:tagRFP #15; 84#2 #15). XXVI

S11 FRET-FLIM-based proximity sensor between outer envelope (OE) and peroxisomal membrane (PerM) with longer linker under light conditions in stable *Arabidopsis* line (px-ck AtOEP7:mVenus PpPEX3N(GGSGG)₁₃:tagRFP #35; 84#2 #35). XXVII

S12 FRET-FLIM-based proximity sensor between outer envelope (OE) and peroxisomal membrane (PerM) with longer linker under light conditions and cytD treatment in stable *Arabidopsis* line (Col-0 AtOEP7:mVenus PpPEX3N(GGSGG)₁₃:tagRFP #12; 84#2 #12). XXVIII

S13 FRET-FLIM-based proximity sensor between outer envelope (OE) and peroxisomal membrane (PerM) with longer linker under light conditions and cytD treatment in stable *Arabidopsis* line (Col-0 AtOEP7:mVenus PpPEX3N(GGSGG)₁₃:tagRFP #15; 84#2 #15). XXIX

S14 FRET-FLIM-based proximity sensor between outer envelope (OE) and peroxisomal membrane (PerM) with longer linker under light conditions and cytD treatment in stable *Arabidopsis* line (px-ck AtOEP7:mVenus PpPEX3N(GGSGG)₁₃:tagRFP #35; 84#2 #35). XXX

S15 Representative CLSM images of independent Arabidopsis T1 (first generation) lines expressing the tether construct 24#5 (PpPEX3N:tagRFP:mVenus:PpTOM20C) under the constitutive promoter CaM35sP	XXXI
---	------

List of Tables

2	Publications using Bimolecular fluorescence complementation (BiFC) for the investigation of organellar interaction.	19
3	Overview of publications using Bimolecular fluorescence complementation (BiFC) to study different distances at MCS.	20
4	Technical equipment	25
5	Enzymes used in this study	27
6	Specific materials and kits used in this study.	27
7	Software used in this study.	28
8	Segregation pattern of all tested independent Arabidopsis lines in T ₂ generation on plates with Basta selection.	32
9	Segregation pattern of independent Arabidopsis lines in T ₃ generation on Basta plates.	33
10	Bacteria strains.	38
11	Stock and working concentrations of antibiotics	39
12	Primers for Gateway cloning	41
13	Primers for Greengate cloning.	46
14	Primers for Q5 mutagenesis ccdB gene.	46
15	Primers for DNA sequencing, colony PCR or gentyotyping only.	47
16	Phusion PCR thermocycler conditions.	48
17	Two step PCR thermocycler conditions.	48
18	Taq DNA polymerase PCR thermocycler conditions.	49
19	Individual pEntry modules for Greengate cloning of 2in1 pInd vector system.	50
20	Greengate reaction conditions.	52
21	2in1 pInd destination vectors, which were generated in this study.	52
22	Gateway vectors used as donor or destination vector.	53
23	Proteins or protein domains used for 2in1 FP-based sensor systems as candidates.	54
24	Generated Gateway expression clones for FP-based sensor systems.	55
25	Calculation of FP-based reporter sizes.	59
26	Python packages used for the proximity Python-based analysis pipeline.	62

27	Segregation on plates with Basta selection of independent <i>A. thaliana</i> T ₂ synthetic tether lines expressing the synthetic tether construct 24#5 (PpPEX3N:tagRFP:mVenus:PpTOM20C) under the constitutive promoter CaMV35S.	119
28	Segregation on plates with Basta selection of <i>A. thaliana</i> synthetic tether lines expressing the synthetic tether construct 24#5 (PpPEX3N:tagRFP:mVenus:PpTOM20C) in the third generation (T ₃).	120
29	Comparison of the experimental settings for the proximity analysis between Oikawa <i>et al.</i> 2015 [26] and our work.	146
30	Comparison of linker length to investigate MCS via Bimolecular fluorescence complementation (BiFC) from Cieri <i>et al.</i> [151], T. Li <i>et al.</i> [152] and our study.	155
S1	Size of chloroplasts of <i>P. patens</i> and <i>A. thaliana</i>	XVII
S2	Raw data for the quantification ratio of alive and dead pollen.	XXXII

Acknowledgements

Ich möchte mich von ganzem Herzen bei allen bedanken, die mich auf meinem Weg zur Fertigstellung meiner Doktorarbeit unterstützt haben. Ohne Eure Hilfe und Unterstützung, wäre ich nicht da, wo ich jetzt bin.

Ein ganz besonderer Dank gilt meiner Betreuerin Stefanie Müller-Schüssele, die mich nicht nur fachlich, sondern auch menschlich durch diese anspruchsvolle Zeit begleitet hat. Steffi, ganz herzlichen Dank für deine Motivation, deine Unterstützung und dass du auch nie vergessen hast, den Menschen hinter der Arbeit zu sehen. Ich konnte viel von dir lernen!

Auch Andreas Meyer möchte ich meinen besonderen Dank aussprechen. Danke für den wissenschaftlichen Austausch, deine Unterstützung und dass du die Rolle als mein zweiter "erster" Betreuer übernommen hast.

Ich möchte mich auch bei Ute Vothknecht bedanken für die Übernahme als Zweitgutachterin und für die hilfreichen Ideen während der "Mitochondria in New Light" Meetings. Des Weiteren möchte ich mich auch den beiden weiteren Promotionskommissionsmitgliedern für ihre Zeit bedanken.

Besonders möchte ich meinen Labor-Buddies danken: Danke Finja, Alina, José und Luca, dass ihr mir nicht nur wissenschaftlich, sondern auch emotional zur Seite gestanden habt. Unseren gemeinsamen Mittagessen, Kaffee-/Teepausen und Gesangseinlagen im Labor haben mir viel Kraft gegeben. Ein großer Dank geht auch an Andi, Alexa, Malte, Maria und Lisa für die tolle Unterstützung im Labor. Liebe Jutta, lieber Philippe, danke für Eure Unterstützung und die guten Gespräche. Ich habe die gemeinsame Zeit mit euch allen genossen und bin froh, in dieser Zeit einige gute Freundschaften dazugewonnen zu haben.

Natürlich möchte ich mich bei allen meinen Freunden bedanken, dass ihr immer ein offenes Ohr hattet. Ihr habt mich auch in stressigen Zeiten zum Lachen gebracht und mir damit wieder neuen Antrieb gegeben. Ohne euch hätte ich das nicht geschafft.

Das gleiche gilt auch für meine Familie. Ich danke euch ganz, ganz herzlich. Ihr habt mich immer ermutigt und unterstützt, wenn ich es gebraucht habe. Danke, dass ihr so geduldig zugehört habt und mir einen Halt gegeben habt.

Ich bin unglaublich dankbar für all die Unterstützung und Freundschaft, die ich während dieser Zeit erfahren durfte. Vielen, vielen Dank!



General statement

Name: Falz
Vorname: Anna-Lena
Titel der Dissertation: Keeping in Touch: Visualising and Perturbing
Photorespiratory Organelle Proximity in Plants

Hiermit erkläre ich durch meine Unterschrift an Eides statt:

1. Die von mir eingereichte Dissertation habe ich selbstständig und ohne unzulässige fremde Hilfe verfasst. Hierbei habe ich weder Textstellen von Dritten oder aus eigenen Prüfungsarbeiten noch Grafiken oder sonstige Materialien ohne Kennzeichnung übernommen.
2. Es sind ausschließlich die von mir angegebenen Quellen und Hilfsmittel verwendet worden.
3. Sämtliche wörtliche und nicht wörtliche Zitate aus anderen Werken sind gemäß den wissenschaftlichen Zitierregeln kenntlich gemacht.
4. Die von mir vorgelegte Arbeit ist bisher noch nicht oder an der nachstehend aufgeführten Stelle vollständig/auszugsweise veröffentlicht. (s. Anlage)
5. Die von mir vorgelegte Arbeit ist bisher noch in keiner Form als Bestandteil einer Prüfungs-/Qualifikationsleistung vorgelegt worden.
6. Ich bin nicht zweimal in einem Promotionsverfahren an einer deutschen Hochschule aufgrund einer Ablehnung der Dissertation oder nicht bestandener Prüfungsleistungen gescheitert.
7. Die von mir eingereichte Dissertation habe ich unter Beachtung der Grundsätze zur Sicherung guter wissenschaftlicher Praxis erstellt.
8. Über die Bedeutung und die strafrechtlichen Folgen einer falschen eidesstattlichen Erklärung gemäß § 156 StGB bin ich mir bewusst.
9. Meine Angaben entsprechen der Wahrheit und ich habe diese nach bestem Wissen und Gewissen gemacht.

Ort, Datum

Unterschrift der*des **Doktorand*in**